PHOTONIC STUDIES OF DEFECTS AND AMORPHIZATION IN ION BEAM DAMAGED GaAs SURFACES

by

Ashok K. Vaseashta

Dissertation submitted to the Faculty of the
Virginia Polytechnic Institute and State University
in partial fulfillment of the requirement for the degree of

Doctor of Philosophy

in

Materials Engineering Science

APPROVED:

Prof. L. C. Burton, Chairman

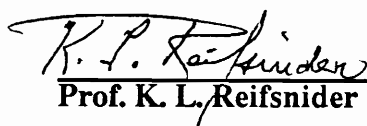

Prof. K. L. Reifsnider

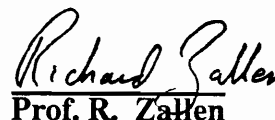

Prof. R. Zallen

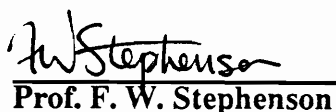

Prof. F. W. Stephenson

Prof. S. Onishi

January, 1990
Blacksburg, VA 24061

LD
5655
V856
1990
V373
Spec

PHOTONIC STUDIES OF DEFECTS AND AMORPHIZATION IN ION BEAM DAMAGED GaAs SURFACES

by

Ashok K. Vaseashta

(ABSTRACT)

In the present investigation, a comprehensive photonic characterization and analysis of low energy Ar^+ ion beam processed GaAs surfaces is presented. The purpose of this investigation was to evaluate the damage and amorphization introduced at the surface and sub-surface regions by ion bombardment. Ar^+ ion beam etching was selected in order to rule out the possibility of producing any additional effects at the interface due to chemical reactions in the case of reactive ion etching.

After a brief review of the concepts and underlying physics, several photonic structures are introduced. The basic theory governing the photovoltaic devices and photoconductive samples is discussed. The preparation and characterization techniques of ion beam processed GaAs samples are described. An automated photovoltaic materials and devices (PVMD) system was developed. Asyst, a Forth based scientific software was selected to write the source codes for data acquisition and reduction. The inherent fast execution times of the software allows data acquisition in real time, ensuring the quasi-steady state condition. The electrical and optical evaluation procedures developed and employed for the present investigation are discussed.

One of the striking features of the ion beam bombardment on semi-insulating (SI) GaAs samples was the observation of persistent photoconductivity. A phenomenological model for optically generated ion beam induced metastable defect state formation was proposed to explain the persistent photoconductivity. Presence of two or more exponential curves in the relaxation mode indicates the distributed nature of the traps within the band gap. A conjectural flat-band energy diagram was introduced to elucidate the proposed model. The observed dark and photoconductivity response model was based on the

distributed lumped electrical components analysis. Fundamental transport equations were employed in the analysis of the lumped electrical components model.

Metal-Insulator-Semiconductor (MIS) type Schottky barrier diodes and photodiodes were fabricated employing both thermal and anodic oxides. Diode parameters were evaluated as a function of ion-beam energy. An increase in reverse saturation current density accompanied by an increase in the ideality factor was observed, indicating the presence of trap-assisted tunneling and a region of high recombination. The effective barrier height was generally lowered; however, no monotonic correlation with the ion energy was observed. It is proposed that the mechanisms described in previous studies (e.g. tunneling, stoichiometry effects, ion penetration depth) were dominated by the effect of Fermi level pinning at the electronic states of process-induced defects. Deep level transient spectroscopy (DLTS) indicated the presence of at least two distinct deep trap levels, at 0.32 eV and at 0.52 eV below the conduction band edge, as a consequence of ion beam etching. The EL2 peak was evident in the virgin sample and vanished in the ion beam etched samples and such observation is in agreement with our proposed model. The photovoltaic response was characterized using illuminated current-voltage (I-V) and spectral response measurements. The ratio of external quantum efficiencies of IBE devices to unetched device indicates the regions and relative extent of the damage. Since the damage has a impact on the band-bending due to excess carrier generation, the sub-bandgap photon absorption response reveals the degree of disorder. XPS results indicated an increased surface sensitivity and change in Ga/As ratio as a function of ion beam energy.

The modelling of ion-beam-processed samples was considered and several computer programs which simulate their operation are described. The depth of amorphization was calculated using the Lindhard-Scharff-Schiøtt (LSS) theory and the standard projected range and straggle parameters, and experimental parameters. A large difference was observed in the values calculated using LSS theory and experimentally measured values, using optical probes. The difference was explained in light of the Collision-Cascade model.

ACKNOWLEDGEMENTS

The author expresses his debt of gratitude and immense appreciation towards his thesis advisor, Prof. L. C. Burton for providing invaluable guidance and support throughout the course of this investigation. His moral support, inspiration and invaluable information concerning research and teaching will establish new directions in the author's future professional career. Sincere thanks are due to Prof. F. W. Stephenson for providing unrestricted access to Hybrid Microelectronics Laboratory. Mrs. Barbara and Prof. Burton, and Mrs. Sally and Prof. Stephenson are greatly acknowledged for providing unparalleled and everlasting friendship. Much indebtedness are due to Prof. R. Zallen for providing conceptual enrichment of Solid State Physics. Constant interactions with Dr. S. Onishi on thin film deposition and vacuum system design provided many useful directions for the experiments. Thanks are due to Prof. K. L. Reifsnider for his moral support and providing inspiration for the program. Thanks are due to Dr. June Epp for her time and efforts expanded towards ion bombarding the samples; to Prof. J. Dillard for providing XPS and AES facilities; to Prof. A. El-Shabini Riad for enlightening discussions; to Dr. S. Vernon of Spire Corporation for providing gratis MOCVD deposited GaAs samples; to Dr. P. Uppal of Martin Marietta Laboratories and Dr. A. Geissberger of ITT-GTC for generously providing MBE grown GaAs samples. Thanks are due to Mr. A. Siochi, Dr. J. Feng, Mr. C. Turman, Mr. P. Johnson, Mr. Z. Chen, Mr. I. K. Yoo, and Dr. E. Cole of George Mason University, for friendship and sharing information regarding the present investigation. Many friends generously contributed their time and efforts. Just to name a few: Mr. Monty Hayes for equipment and software, Mr. S. Sen for DLTS measurements and recurrent discussions, Mr. K. Muthukrishnan for help in the mask development and anodic oxidation, Ms. Uma Kommineni for literature survey and duplication, Ms. Lynn Hellbaum and Mr. Keith Kasprak for efficiently cutting the rubylith masks and artwork photoreduction, Mr. Michael Gunther and Mr. Bernd Zimmerman for Fiber Optics accessories... and the list

goes on. Many thanks are due to Mr. Frank Cromer and Mr. Eric Ellis for their technical assistance to the program. To all others who inadvertently may have been omitted, the author wishes to extend many thanks and owes his deepest gratitude. They have shared with the author and helped make possible the excitement of new discoveries and understanding in a fascinating field of science.

Ankur merits an exceptional recognition for sacrificing his numerous and inestimable hours of attention. God bless him. Finally, author wishes to extend special appreciation to his parents for their love and moral encouragement.

The research was funded in part by Texas Instruments, DuPont and Virginia's Center for Innovative Technology.

Table of Contents

Acknowledgments

List of Figures ix

List of Tables xiv

Chapter 1: Introduction 1

1.1 Semiconductor GaAs: An Overview 5

1.2 Ion Beam Etching: An Applications Review 11

1.3 Literature Review and Research Objectives 15

Chapter 2: Unifying Theoretical Concepts 19

2.1 Ion Bombardment and Collision Cascade 19

2.2 Metal Semiconductor Contact and Schottky Effect 22

2.2.1 Unified Defect Model and Mid-Gap Energy Theories 26

2.2.2 Present Understanding of MS Schottky Diodes 27

2.2.3 Ohmic Contacts to GaAs 32

2.3 Dark and Photoconductivity 33

2.3.1 Optical Processes in Semiconductors 36

2.3.2 Slow-Relaxation Effects: Persistent Photoconductivity and Thermally Stimulated Conductivity 40

2.4 Photovoltaics 43

2.4.1 Metal Insulator Semiconductor Solar Cells 46

2.4.2 Schottky Barrier Height Characterization 49

Chapter 3: GaAs Sample Preparation and Characterization Techniques 52

3.1 Sample Preparation 52

3.1.1 Gap Cell Configuration Conductivity Sample Preparation 53

3.1.2 Contact Formation Techniques 56

3.1.3 Oxidation of GaAs Samples. 58
3.1.4 Schottky Diode Fabrication 62
3.2 Automated Characterization System 65
3.2.1 Experimentation Philosophy 67
3.2.2 Software Selection Criterion 70
3.2.3 Photovoltaic Materials and Devices Measurement System 76
3.3 Characterization Techniques 78
3.3.1 Dark and Light Current-Voltage Characteristics 78
3.3.2 Spectral Response 80
3.3.3 Dark and Photoconductivity Measurements 83
3.3.4 Deep Level Transient Spectroscopy (DLTS) 84
3.3.5 X-ray Photoelectron Spectroscopy (XPS) 86
Chapter 4: Results and Discussion 90
4.1 Dark and Photoconductivity 90
4.1.1 Spectral Conductivity 98
4.1.2 Persistent Conductivity, Relaxation and Fatigue 101
4.1.3 Thermally Stimulated Conductivity 113
4.2 Diode and Photodiode Characteristics 115
4.2.1 Dark Current-Voltage (I-V) Characteristics 115
4.2.2 Light Current-Voltage (I-V) Characteristics 124
4.2.3 Capacitance-Voltage (C-V) Characteristics 124
4.3 Spectral Response and Quantum Efficiency 133
4.3.1 Subband Gap Absorption and Internal Photoelectric Emission . . . 135
4.4 Deep Level Transient Spectroscopy, (DLTS) 135
4.4 X-ray Photoelectron Spectroscopy, (XPS) 141
Chapter 5: Computer Simulation and Device Analyses 146
5.1 Physical Model of the Damage 146

5.2 Calculation of the depth of IBE Induced Damage in GaAs 149
5.3 Modelling Optical Effects - Photogeneration Rate 155
5.4 Effect of IBE on the Conductivity of GaAs 159
Chapter 6: Summary, Conclusion and Future Recommendation 168
6.1 Summary and Conclusion 168
6.2 Future Recommendation 170
Appendices:
Appendix A: Fabrication Procedures and Process variables
A.1 Substrate Cleaning 173
A.2 Lift-Off Process 173
A.3 Chemical Etching 173
A.4 Oxidation 174
A.5 Contact Formation 174
Appendix B: Photovoltaic Materials and Devices Characterization: Software ... 175
Appendix C: Grid Design for Schottky Barrier Photodiodes 195
References: 198
Curriculum Vitae
List of Publications

List of Figures

1.1 Operating characteristics of several silicon and GaAs digital logic families 3

1.2 (a) Lattice structure of GaAs. (b) The first Brillouin zone of the reciprocal lattice for GaAs. 6

1.3 (a) Energy band structure of GaAs as calculated using an empirical Non-Local Pseudo-potential scheme. (b) Electron energy as a function of reduced wave vector for energies close to the top of the valence band and the bottom of the conduction band. 8

1.4 (a) Implementation of dry processing in semiconductor process development. (b) Location of the substrate and end product of the dry processes. 12

1.5 Schematic of an ion-beam gun. 14

2.1 (a) Scheme of the main displacement processes that lead to surface damage. (b) Mechanism of collision cascade and Energy Dissipation for an incoming ion of mass M_I and energy E_o, E_o = Kinetic energy of the incoming ion, E_e = energy dissipated through electron excitation, E_T = Transfer energy, and E_d = displacement energy. 20

2.2 Stopping power of an ion as a function of energy. 23

2.3 (a) Energy band diagram of metal-semiconductor under two limiting cases; (a) ideal condition ie. no surface states, and (b) surface states density large enough to dominantly influence the barrier height. (c) Detailed Energy-band diagram of an Metal-Semiconductor contact with an interfacial layer of the order of atomic distances. 25

2.4 (a) The energy level diagram for the advanced Unified Defect Model , (b) Energy band diagram for a semiconductor showing the screening and delocalization effect. 28

2.5 (a) Characteristic types of optical transitions shown both for the flat-band

model and for E vs. k plot. (1) excitation from the valence band to higher lying conduction bands. (2) excitation across the band gap, (3) exciton forming, (4) excitation from imperfections. (5) free-carrier excitation. (b) A model for the absorption from the valence band tails. 37

2.6 (a) A generic schematic of a diffused junction solar cell. (b) Flat band diagram representation of the generic cell. (c) Electric field and excess charge distribution in the generic cell. 44

2.7 Measured and computed spectral response of generic silicon solar cell showing contribution due to various regions. 48

3.1 Grid-pattern layout for (a) Schottky photodiode and (b) Four equally spaced conductivity probes... 54

3.2 Dicing, scribing, ion beam bombardment, and whisker bonding of the devices.. 57

3.3 Angular evaporation mask arrangements used for contact formation 59

3.4 (a) Gridline formation problems. (b) Schematic of the lift-off process 60

3.5 Carrier concentration vs. depth of a representative MBE grown sample. 64

3.6 (a) Conceptual schematic representing the exchange of information between computer and external world via domain converters. (b) Schematic of unity gain and transimpedance amplifier used as buffer. 68

3.7 (a) Flow chart of software strategy. (b) Flow chart of a representative program. . 72

3.8 (a) Schematic of the hardware layout of the characterization system. (b) Schematic of the low thermal inertia cryostat designed for measurements. .. 79

3.9 (a) Schematic of the hardware layout of (a) Spectral response measurement system. (b) DLTS measurement system. 82

3.10 PHI model 10-360 hemispherical capacitor energy analyzer. 87

4.1 Inverse temperature vs. log conductivity for virgin, 1 KeV etched and 3 KeV etched SI-GaAs samples in dark (lower curves) and under 1.19 eV optical excitation (upper curves). 91

4.2 Inverse temperature vs. log conductivity for virgin, 1 KeV etched and 3 KeV etched SI-GaAs samples under 2.06 eV optical excitation. 92

4.3 Dark and photoconductivity (under white light, 901.5 nm., 600 nm., and 420 nm. illumination) versus inverse temperature for 50 KeV Si implanted and unannealed, (a) (100), and (b) (211) GaAs. 94

4.4 Dark and photoconductivity (under white light, 901.5 nm., 600 nm., and 420 nm. illumination) versus inverse temperature for 50 KeV Si implanted and annealed, (a) (100), and (b) (211) GaAs. 95

4.5 Activation energy of SI-GaAs samples as a function of ion beam energy. 96

4.6 Detection of shallow traps in ion beam etched GaAs. 97

4.7 Spectral conductivity (current per incident photons) for (a) virgin, and (b) 1 KeV etched samples at 77 K, under 5 sec., 15 sec., and 30 sec. of monochromatic light soak. Also, shown are spectral conductivity after white light soak; 1/2 hr. and 1 hr. for virgin, and 1/2 hr. for 1 KeV etched sample. 99

4.8 Spectral conductivity for 3 KeV etched sample at 77 K under 5 sec., 15 sec., and 30 sec. monochromatic illumination soak. Also shown is the spectral conductivity for virgin, 1 KeV, and 3 KeV etched samples at 77 K (30 sec.) light soak at each wavelength. 100

4.9 Time dependence of photocurrent for virgin, 1 KeV etched, and 3 KeV etched samples at 77 K for (a) 0.8 eV , (b) 1.19 eV, and (c) 2.06 eV monochromatic excitation. 102

4.10 Waveform of photconductivity occurring with primary light irradiation ($h\nu_1 \approx 2.06$ eV) subsequent to secondary light irradiation ($h\nu_2 \approx 0.954$ eV) for (a) virgin sample, (b) 1 KeV etched. 105

4.10 (contd.) (c) 3 KeV etched, and (d) 4 KeV etched. Sample temperature held at 77 K and Sample type was LEC SI-GaAs (100). 106

4.11 Phenomenological model of the optically generated metastable defect state

formation by ion beam etching. 109

4.12 (a) i(t) of Virgin, 1 KeV etched, and 3 KeV etched, SI GaAs upon IR-filtered white light optical excitation. (b) Same as (a) but on expanded time scale. 111

4.13 (a) i(t) of virgin, 1 KeV etched and 3 KeV etched SI-GaAs upon termination of white light excitation, (b) Same as (a) on expanded time scale. 112

4.14 Comparison of thermal cycle of Virgin, 1 KeV etched, and 3 KeV etched SI (100) GaAs, (a) Under dark, and (b) Under monochromatic light absorption relaxation: Thermally stimulated conductivity. 114

4.15 Characteristics of Virgin, 1 KeV, 3 KeV and 4 KeV etched MIS Schottky diodes, as a function of ion beam energy, (a) Thermally grown oxide, and (b) Anodically grown oxides. 117

4.16 Comparison of MIS Schottky diode with thermal and diode oxide at 270 K. 119

4.17 ln (I_f/T^2) vs. q/kT or activation energy method to determine the barrier height for (a) Thermally grown oxides, and (b) Anodically grown oxide, as a function of ion beam energy. 120

4.18 Conductance variation as a function of temperature for Virgin, 1 KeV etched , 3 KeV etched, and 4 KeV etched MIS Schottky barrier diodes, (a) Thermally grown oxides, and (b) Anodically grown oxides. 122

4.19 Conductance variation as a function of temperature for virgin diodes fabricated on MBE grown materials. 123

4.20 Schottky diode characteristics under AM1 (simulated), as a function of ion beam energy; Virgin, 1 KeV, 3 KeV, and 4 KeV, Ar^+ Ion etched. 125

4.21 $1/C^2$ vs. reverse voltage characteristics of virgin, 1 KeV, and 3 KeV etched Schottky diodes, (a) Thermally grown oxides, and (b) Anodically grown oxides.. 128

4.22 Capacitance vs. frequency for virgin, 1 KeV, 3 KeV, and 4 KeV etched Schottky diodes with thermally grown oxides at (a) zero bias, and (b) at -1 V.... 129

4.23 Capacitance vs. frequency for virgin, 1 KeV, 3 KeV, and 4 KeV etched

Schottky diodes with anodically grown oxides at (a) zero bias, and (b) at -1 V.... 130

4.24 (a) External quantum efficiency of MIS Schottky barrier photodiodes as a function of ion beam etch energy (virgin, 1 KeV, 3 KeV, and 4 KeV), (b) Ratio of external quantum efficiency of 1 KeV, 3 KeV, and 4 KeV etched photodiodes to external Q.E. of virgin diode. 134

4.25 (a) Plot of ln(QE) vs. photon (subbandgap) energy for virgin and 1 KeV MIS Schottky photodiodes. (b) Square root of the collection efficiency as a function of photon energy for virgin and 1 KeV MIS Schottky photodiodes. 136

4.26 DLTS spectrum of the MIS Schottky diodes fabricated on virgin, 1 KeV, 3 KeV, and 4 KeV Ar^+ etched surfaces, (a) Thermally grown oxides, (b) Anodically grown oxides. 138

4.27 XPS spectra for oxide grown on Ar^+ ion etched GaAs using water vapor saturated oxygen at room temperature. 142

4.28 Hypothetical representation of oxides formation on an IBE GaAs surface, (b) Side view of the above model for clear representation. 144

5.1 Physical model of the ion beam damaged GaAs surface and subsurface region.. 148

5.2 Computed plot of depth of ion induced damage in the host lattice 152

5.3 (a) Optical Constants of GaAs. (b) Optical penetration depth in c-GaAs and a-GaAs. 157

5.4 (a) Proposed model of the parasitic absorption at the interfacial region of IBE GaAs structures. (b) Optical generation rate in GaAs substrates. 160

5.5 (a) A theoretical, two dimensional model for carrier-pair generation in the photoconductivity element. (b) Lumped electrical component equivalent of Schottky diodes and photoconductivity element. 165

C.1 (a) A Units of (1) parallel grid lines, (2) parallel grid lines with one bus bar, (c) rectangular mesh grid, and (4) circular grid. (b) current flow considerations in the grid fingers, and (c) lateral current flow at short circuit................. 196

List of Tables

1.1 GaAs constants at room temperature. 10

2.1 Basic conduction processes in MIS structures. 31

2.2 Intrinsic semiconductor parameters effecting the photovoltaic device response . 47

3.1 Summary of device fabrication processes. 66

3.2 Benchmark test comparisons for Quick-basic, C and Asyst Softwares. 74

3.3 XPS Sensitivity factors. 88

4.1 Ratio of steady state photoconductivity to dark conductivity.. 103

4.2 Typical photodiode parameters. 126

4.3 Diode parameters as a function of ion beam energy - (a) Thermal Oxides, (b) Anodic oxides. 132

4.4 Location and density of traps as a function of ion beam energy - Thermal oxides and Anodic oxides. 139

4.5 Ga and As oxide ratios as a function of ion beam energy for (a) Thermal oxides, (b) Anodic oxides. 143

5.1 Theoretical and experimental parameters used for the calculation of depth of ion beam induced damage in GaAs host lattice. (a) conditions of Ar^+ ion beam milling. (b) Parameters used for the calculation of the depth of damage. 153

5.2 Depth of damage comparison computed from the LSS theory and the experimental parameters, and from UV reflectivity measurements for Ar^+ ion bombarded GaAs. 154

Chapter 1

Introduction

From a commercial standpoint, gallium arsenide (GaAs) is currently the leading member of the III-V compound family. The initial thrust of GaAs application was towards the high powered lasers and light emitting diodes (LEDs). In view of its rapidly maturing technology, the interest is currently aimed at microwave monolithic integrated circuits (MMIC), millimeter microwave integrated circuits (MIMIC), analog ICs for light weight transmitters and receivers, and digital ICs. Very high speed and high frequency electronic devices, and digital and analog integrated circuits have been realized with ion-implanted field effect transistors (FETs), selectively doped heterostructure transistors (SDHTs) and heterostructure bipolar transistors (HBTs). The ternary materials of GaAs, such as $Al_xGa_{1-x}As$ have larger bandgap and have excellent lattice match with GaAs and are the basis of modulation doped field effect transistors (MODFETs). In quaternary alloys, it is possible to vary the bandgap and lattice constant independently. Such ability to tailor the band structure leads to enhanced performance heterostructures, especially for fiber-optics transmission systems.

The diverse characteristics of Ga and As atoms in GaAs pose severe problems in device fabrication. Conventional semiconductor processing techniques, such as solid state diffusion, oxidation etc. are not applicable to GaAs. A poor quality of unstable native oxide on GaAs and a high density of surface states at the GaAs/insulator interface makes it difficult to realize the GaAs metal-oxide-semiconductor FETs (MOSFETs) or the MISFETs. Schottky barrier metal semiconductor field effect transistor (MESFETs) or junction field effect transistors (JFETs) are examples of practically used GaAs FETs. Often these devices are fabricated by direct implantation into a GaAs semi-insulating substrate. Ion implantation offers unique advantages to fabricate GaAs devices. Since its

first realization in late 1970s, when selective direct ion implantation of active device elements intrinsically provided electrical isolation between active and passive circuit elements, the current evolution of GaAs technology was demonstrated in the laboratory for high speed digital integrated circuits and MIMICs. The higher speed, reduced power, and radiation hardness of this direct bandgap semiconductor has led the scientific community to actively contribute to its research since the successful insertion of GaAs technology promised quantum improvements in the future ultra-fast computers, microwave radar, communication system and electro-optical data transmission systems. GaAs offers several advantages over its leading contender - Silicon. The principal advantage are the higher electron mobility (the higher electron mobilities of GaAs transistors result in faster electron transit times across their active regions and hence shorter gate propagation delays for comparable dimensions and lower dissipation than in silicon devices), higher saturated drift velocity, and its availability in the semi-insulating form. Such performance characteristics allow GaAs to operate in high frequency regimes (≈ GHz) in a true monolithic configuration. Excellent device isolation with reduced parasitic capacitance also help GaAs devices to operate at microwave frequencies, a regime in which most of the defense communication systems operate. The performance differences between several types of silicon and GaAs transistor technologies are indicated in Figure 1 (of [1]). It is observed that more advanced technologies, relying on enhancement- and depletion-mode GaAs FET have demonstrated 52-psec switching delays at 0.55-mW power dissipation. In high electron mobility transistors (HEMT) switching delays as low as 12.2-psec are reported, with a speed-power product of approximately 13.7 fJ (1.12-mW power dissipation). Commercial and military GaAs integrated circuits are thus becoming available which can be operate at gigahertz clock rates. Current application for military applications focuses on MIMIC and digital radio frequency memory (DRFM) which is an A/D converter and a scratchpad memory having a sampling capacity of over 1 giga-samples per second. For biomedical research the application is towards studying the reaction

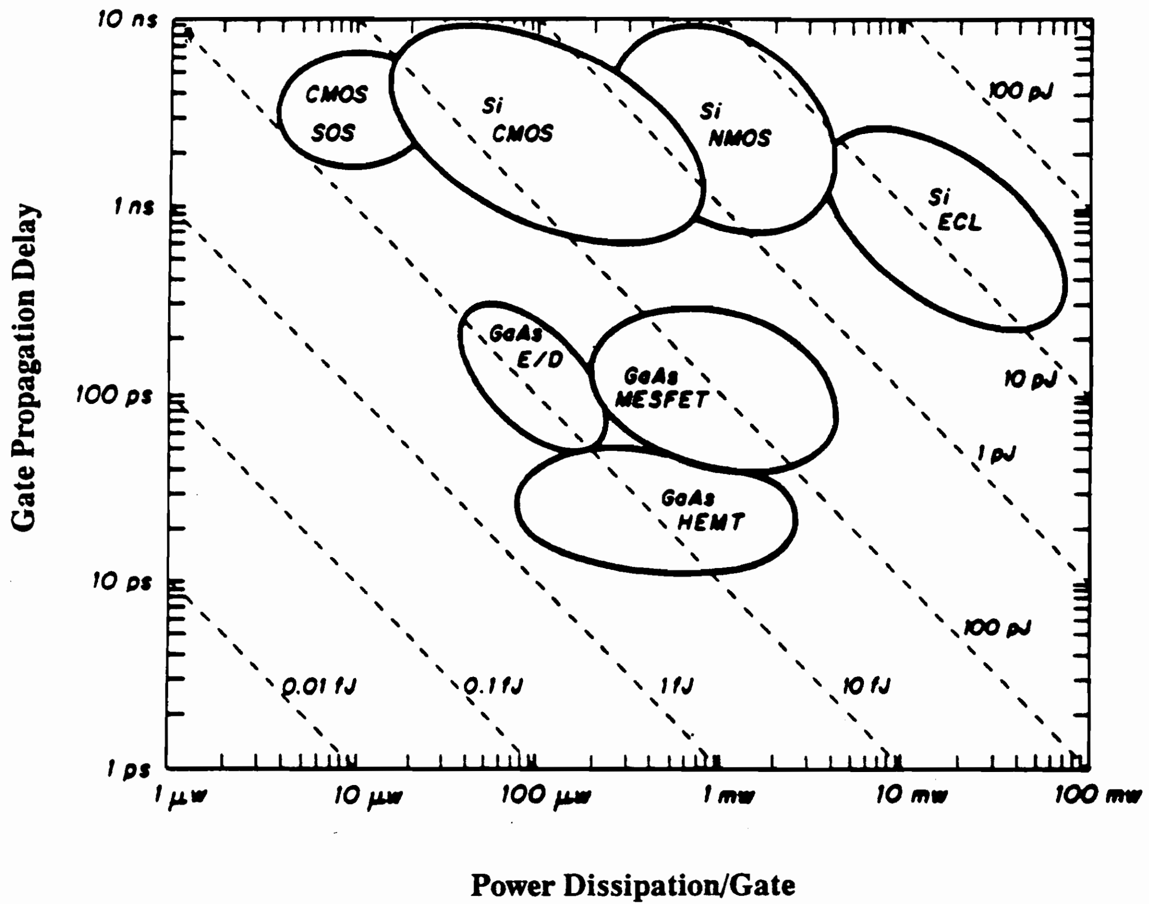

Figure 1.1 **Operating characteristics of several silicon and GaAs digital logic families.**

kinetics of molecules. This is true of several physical phenomena where relaxation occurs over a few nano to pico seconds. Hence transient response can be analyzed for trap locations within the bandgap of the material. For signal processing applications, research is focussed towards error detection and correction (EDAC) circuitry. By processing several points, the signal could be improved leading to better resolution. It appears probable that very large scale integration (VLSI) technology of silicon, will be employed to fabricate very dense components, such as microprocessors, and generic signal, and data processing modules, while system implementation tasks fulfilled by gallium arsenide integrated circuits will be quite different from and complementary to those of silicon VLSI.

One of the key elements in the successful fabrication of most GaAs based devices is dry plasma processing. A key driving force for the use of dry processing is the high degree of control, and anisotropy, that can be maintained while etching small features. The advantage of inert ion beam milling has resulted in the production of specialized devices which have particularly demanding etch needs - such as, to etch submicrometer structures in high frequency transistors, thin magnetic heads, bubble memories, and fine pattern master glass masks. However, the exposure of the wafer to a variety of energetic ions, electrons, and photons during the etch process may cause damage, which often adversely affects device characteristics. Ion bombardment produces an amorphous layer at the near surface region containing defects and implanted ions causing degradation in the device performance. The purpose of this investigation is study the effects of the ion bombardment on the device performance. In the literature, several techniques, such as low energy electron diffraction scattering (LEEDS) [2], Rutherford back-scattering (RBS) [3,4], X-ray photoelectron spectroscopy (XPS) [5-7], Raman spectroscopy [8,9], thermally stimulated current [10,11], photoluminescence [12,13], etc. are reported to evaluate the depth and extent of such damage. In all of these techniques the probe depth is a few hundred Angstroms deep into the bulk. Since the damage is concentrated at the surface, most techniques employed in the present investigation are surface sensitive probes and probe depth is

comparable to the depth of the damage.

1.1 Semiconductor GaAs: An Overview

GaAs is a direct band gap semiconductor which crystallizes into the zinc blende structure. The primitive cell of the structure consists of two equivalent, interpenetrating sublattices with face-centered cubic (fcc) translational symmetry. The two sublattices are separated by 2.44793 Å along the body diagonal of the unit cube whose side length is 5.6532 Å at 300 K, Figure (1.2a). The first Brillouin zone has the same shape as that of the fcc lattice, a truncated octahedron. The lines of the first Brillouin zone with important symmetry considerations are shown in Figure (1.2b). The space group of the zinc-blende structure is T^2d and lacks inversion symmetry. A marked consequence of such phenomena reveals in the presence of dissimilar atoms and hence difference in chemical activity of the opposite (111) crystal faces in GaAs. Various chemical etches show orientation selectivities and as a result of this, the properties of GaAs devices strongly depend upon the gate orientation of the substrate. When mechanically stressed at 300 K, a crystal wafer cleaves most easily in the (110) plane. A shift in valence band charge from gallium to arsenic atom produces a mixed (ionic/covalent) bond, which has a significant effect on the electronic band structure, such as increase in bond strength. The valence electron configuration of the Ga and As atoms are $4s^2 4p^1$ and $4s^2 4p^3$, respectively. In GaAs structure, sp^3 covalent bonding is employed where each atom of one kind is surrounded by the other kind. This is an admixture of ionic and covalent bonding, primarily covalent.

The optical and electronic properties of GaAs can well be described within the context of the electronic band theory of solids. A simplified description of the band structure can be obtained by assuming an ideal periodic crystal in the frame of the nearly free electron model and decoupling the effect of vibrations about their equilibrium positions as perturbations. A more accurate calculations of the energy band structure, however are based on the 'Non-local Pseudopotential' method[14], and are shown in Figure

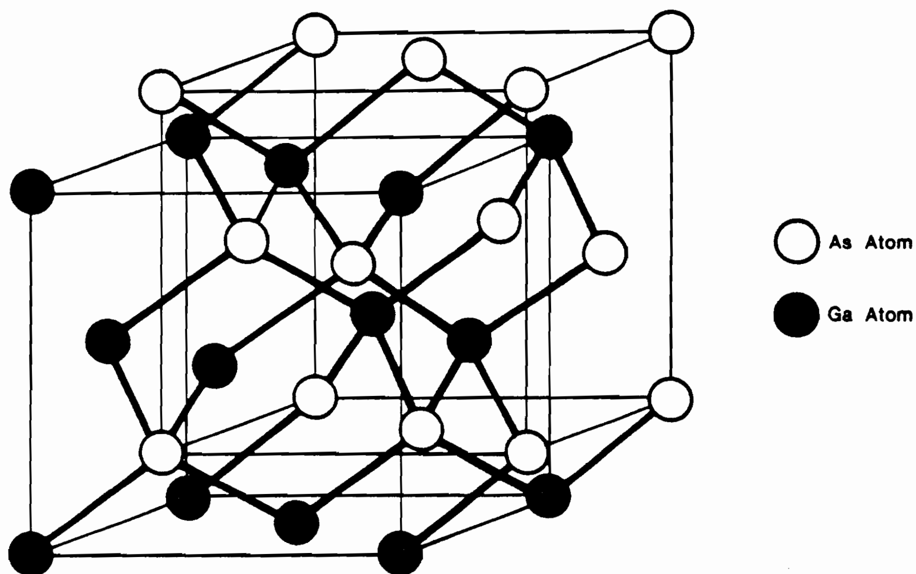

(a)

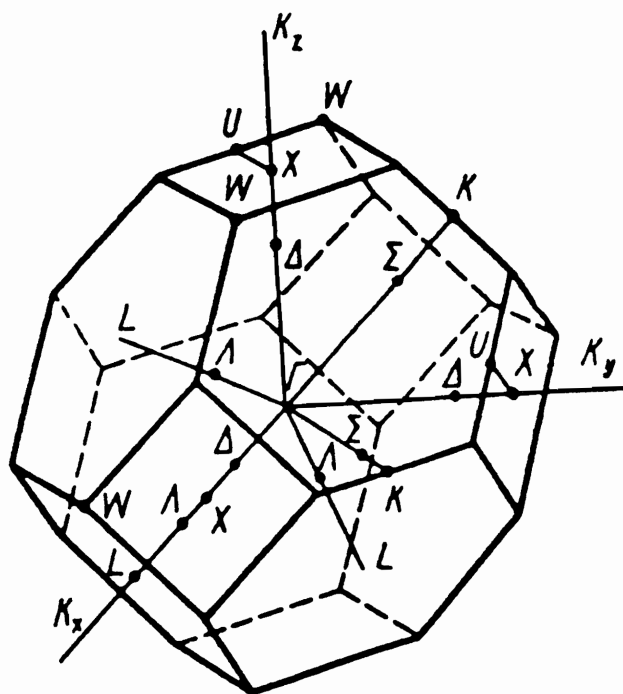

(b)

Figure 1.2 **(a) Lattice structure of GaAs. (b) The first Brillouin zone of the reciprocal lattice for GaAs.**

1.3 (a). Figure 1.3 (b) shows the part on the band structure near the bottom of the lowest conduction band and near the top of the highest valence band. The highest valence band in Figure 1.3a is the curve with the label $L_{4.5}$ and the lowest conduction band is the one with the one label L_6. The bottom 'split-off' valence band is lower by about 0.34 eV owing to the spin-orbit splitting. The valence band maximum, and the minimum allowed energy for the conduction band occur at the zero wave-vector point (Γ), rendering GaAs a direct band gap material with bandgap, E_G = 1.423 eV. The electron transition from valence to conduction band are entirely photon assisted without any change in the momentum vector. Direct bandgap semiconductors are ideal candidates for electro-luminescent devices, viz. laser diode, because the radiative recombination is a first order transition process and the quantum efficiency is much higher than that of for an indirect gap semiconductor, where both a phonon and a photon are involved in the transition. This property of GaAs is extremely important for the photonic applications.

Thermal generation of carriers (electron and holes) across the gap at 300 K, thus produce lower steady-state carrier densities in the GaAs ($\approx 10^{16}/cm^3$), hence more highly insulating materials, and superior device isolation capabilities are achievable with GaAs. Under the plane wave approximation for free electrons, the mass of particles can be determined by the second order differential equation of energy with respect to momentum, $d^2E/dk^2 = \hbar^2/m^*$, where m^* = 'curvature' effective mass, and a parabola is generated in E-k dispersion curve. The conduction band energy varies rapidly with wave vector (momentum) at the Γ point in GaAs. This results in an electron effective mass to rest mass ratio (m_e^*/m_0) of 0.067 for GaAs as compared to 0.98 for Si. Application of an electric field therefore accelerates electron to a higher saturated velocity in GaAs than in Si, since the scattering processes are of similar magnitude. Hence low-field electron mobility in GaAs ($\mu \approx 8500$ cm^2/V-s) is higher than silicon ($\mu \approx 400$ cm^2/V-s), indicating that n-type unipolar devices are the most advantageous structures in GaAs. It is evident from the energy band structure of GaAs that there is finite probability of inter-valley scattering via

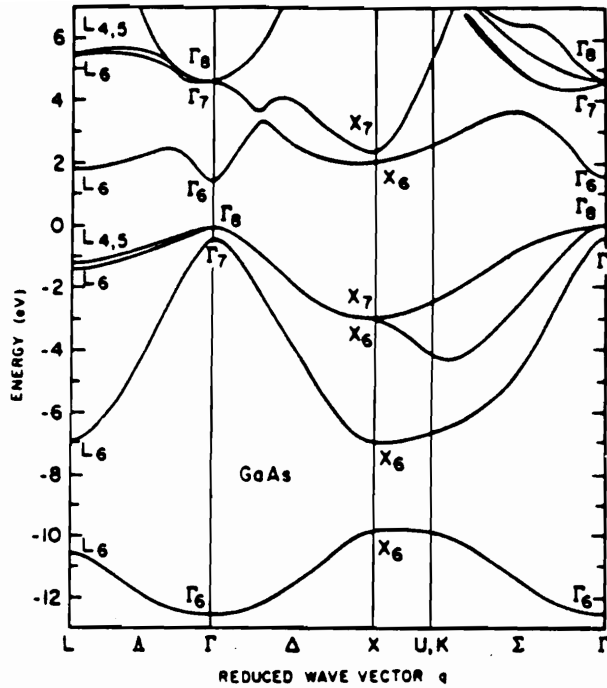

(a)

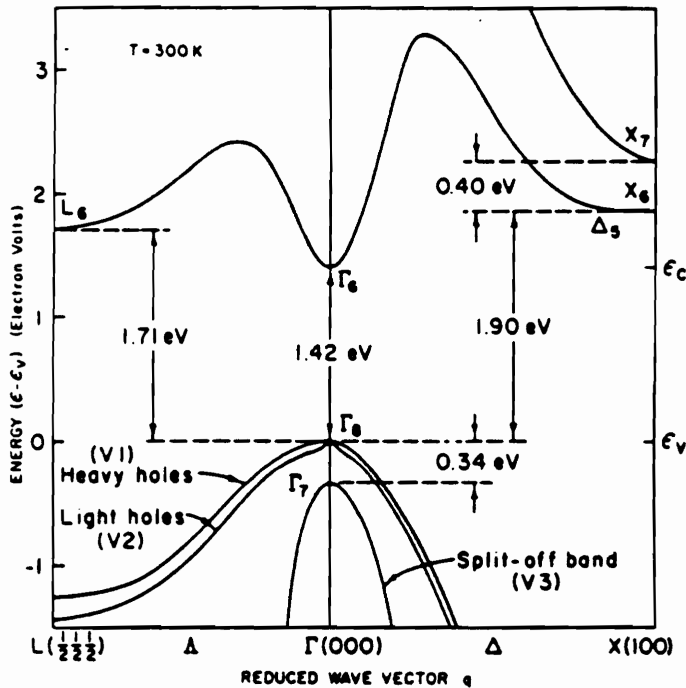

(b)

Figure 1.3 **(a) Energy band structure of GaAs as calculated using an empirical Non-Local Pseudo-potential scheme. (b) Electron energy as a function of reduced wave vector for energies close to the top of the valence band and the bottom of the conduction band.**

phonon interaction. The characteristic is termed as transferred electron effect and is used in the generation of microwaves by transferred electron devices (TED). Since in GaAs, $m_e^* = 0.067m_o$ and $m_h^* = [(m_{lh}^*)^{3/2} + (m_{hh}^*)^{3/2}]^{2/3} = 0.53m_o$, the effective densities of state in the conduction band ($\approx 4.2x10^{17}/cm^3$) is much less than in the valence band ($\approx 9.6x10^{18}/cm^3$), so both the density of state terms and the band gap difference suppress the intrinsic carrier concentrations in GaAs ($\approx 2x10^{10}/cm^3$). In order to produce intrinsic quality GaAs, a particular impurity or defect species need to be controlled to better than 1 part in 10^{16}, hence realization of isolation advantage in GaAs is generally achieved by incorporation of defects. Such defects create deep electronic states near the center of the band gap and pin the position of the Fermi level close to its intrinsic position (ie. within a few tens of millivolts from the middle of the gap). The electron occupancy of the crystal is thereby controlled by the deep state and the Fermi level is pinned to the neighborhood of the defect state energy. Substitutional chromium atoms on the gallium sites produce a deep state near the center of the gap, which controls the resistivity, and is located 0.76 eV below the conduction band. EL2 is generally attributed to an As_{Ga} antisite or As cluster defect[15-18], although its origin is yet conjectural. Since EL2 plays a vital role in GaAs technology, many research laboratories are actively involved in studying its origin. Table 1.1 lists various constants of GaAs at room temperature.

Bulk GaAs is grown in crystal ingots by two principal methods, viz. horizontal Bridgman, and liquid-encapsulated Czochralski (LEC) techniques. The latter technique has serious drawbacks - a high density of dislocations due to thermal stresses are generated in the crystal during and after growth, and the vertical and the radial temperature gradients. Improvisations in LEC technique such as liquid-encapsulated Kyropolous[19] (LEK) and magnetic LEC (MLEC) growth [20], are reported in literature, providing GaAs wafers with reduced etch pit density (EPD).

The most significant feature of GaAs technology is the ability to form thin-film lattice-perfect heterojunction structures with GaAlAs, either abrupt to a single atomic

Table 1.1 GaAs Constants at room temperature .

STRUCTURAL

Crystal Structure: Zincblende
Lattice Constant [a_0] = 5.64 Å
Molecular Density = 2.2139×10^{22} cm^{-3}

PHYSICAL

E_g = 1.423 eV
Δo = 0.341 eV
M_{Ga} = 69.720 amu M_{As} = 74.922 amu
m_c = 0.063 m_o
m_{hh} = 0.50 m_o m_{lh} = 0.088 m_o m_{sah} = 0.15 m_o
Debye Temperature = 360 K
Density = 5.32 gm./cm^3
ϵ_0 = 12.85 , ϵ_∞ = 10.88
Melting Point = 1238 ° C
Vapor pressure = 100 Pa at 1050° C
= 1 Pa at 900° C

ELECTRICAL

Breakdown field = 4×10^5 (V/cm)
Conductivity (intrinsic electrical) = 3.0×10^{-9} Ω^{-1} cm^{-1}.
Dielectric Constant = 13.1
Electron Affinity, χ = 4.07 V
Effective Density of States
in Conduction Band, N_c = 4.7×10^{17} cm^{-3}
in Valence Band, N_v = 7.0×10^{18} cm^{-3}
Minority Carrier Lifetime (τ) = 10^{-8} sec.
Mobility (electron) = 8500 cm^2/(V-s)
(hole) = 400 cm^2/(V-s)

MECHANICAL

Bulk Modulus = 7.55×10^{11} dyne/cm^2
Linear Expansion Coefficient, α = 5.73×10^{-6} K^{-1}

† Effective masses are identified from the different electronic energy band curvatures near the Γ point in Fig. 1.1: c = Conduction, hh = heavy hole, lh = light hole, sah = split off hole.

plane or graded over any arbitrary distance. The recent development of multiple-quantum wells and superlattices, where the periodic potential structure of the semiconductor crystal is under direct control in one dimension, has important bearing on high speed heterojunction devices. The most common fabrication techniques for the such thin layers are molecular beam epitaxy (MBE), organo-mettalic chemical vapor deposition (MOCVD) and atomic layer epitaxy (ALE). The major advantage of such techniques is in the control of material production and realization of changes that can be introduced at the atomic level.

1.2 Ion Beam Etching: An Applications Review

Ion implantation offers unique advantages for controllably and reproducibly introducing shallow conductive layers into bulk grown semi-insulating substrates. Within the limitation of ion range statistics, the depth and concentration of implanted species can be controlled individually, by adjusting the energy and dose of an implanted species. Another potential offered by ion implantation as a doping technique is that, multiple doping levels can be selectively achieved, such as buried active layer formation. It is also used for selectively isolating active regions by ion beam amorphization. Ion implantation processing offers a potential for attaining a high degree of automation for large scale fabrication of GaAs devices and has technical, economical, and environmental advantages.

It is often necessary to process GaAs semiconductors in a low energy environment. Depending upon dose, ions, and energy range, the process is appropriately termed as ion beam etching (IBE), ion beam milling or reactive ion beam etching (RIBE). A key driving force for the use of dry processing is the higher degree of control that can be achieved over etch profiles and dimensions. Various ways in which dry processing is implemented in process development is shown schematically in Figure (1.4a) while Figure (1.4b) lists appropriate location of the substrate and end products of the processes. Many similarities exist between dry etching for the fabrication of Si and III-V compounds. However, the

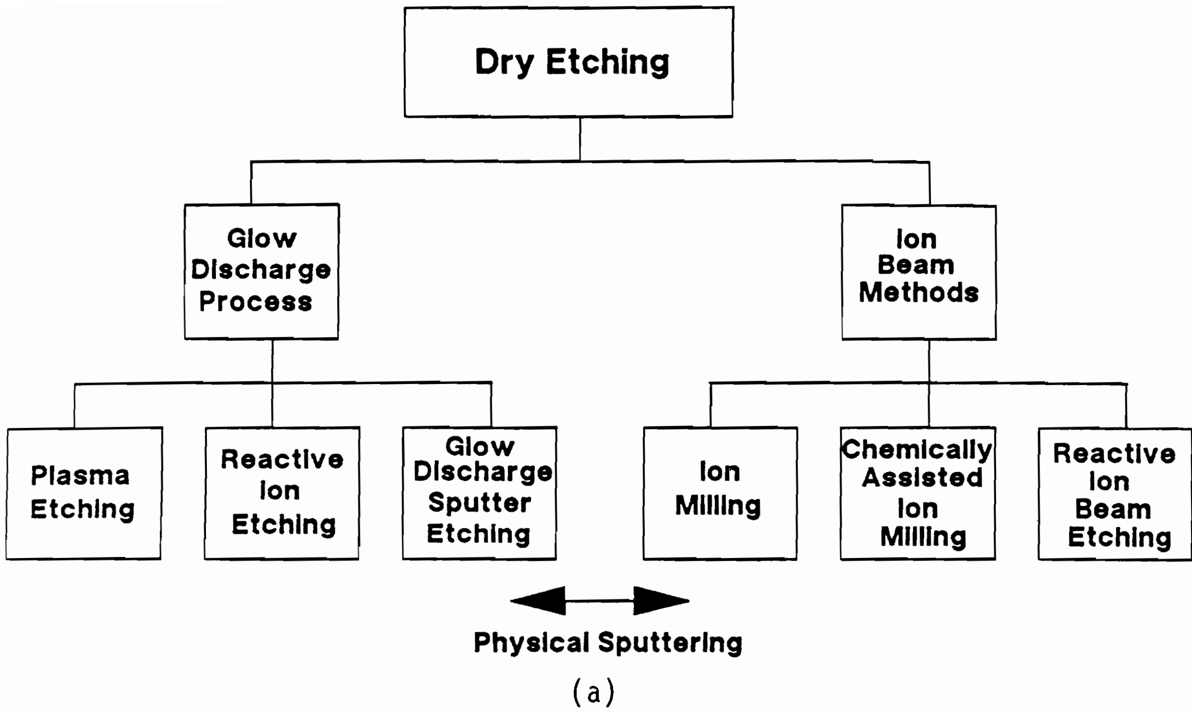

Method	Gas	Wafer Location	Etch Products
Glow Discharge Sputter Etching	Inert (eg Ar)	Powered Electrode	Involatile
Reactive Ion Etching	Reactive (eg. CF_4)	Powered Electrode	Volatile
Plasma Etching	Reactive (eg. CF_4)	Grounded Electrode	Volatile

Method	Gas A	Gas B	Etch Products
Ion Milling	Inert (eg Ar)	None	Involatile
Reactive Ion Beam Etching	Reactive (eg. CF_4)	None	Volatile Usually
Chemically Assisted Ion Milling	Reactive (eg. CF_4)	None	Volatile

(b)

Figure 1.4 (a) Implementation of dry processing in semiconductor process development. (b) Location of the substrate and end product of the dry processes.

diverse nature of Ga and As atoms in GaAs add another dimension of complexity and challenge for the development of a successful dry etch process.

A generalized schematic of an ion beam etching system is shown in Figure (1.5). IBE is simply the bombardment of the target with a highly collimated beam of energetic gas ions of various species, energies and fluences. Ion beam etching produces surface and lattice changes in the material, due to several processes. One such process is sputtering (ejection of surface ions and neutrals into the surrounding vacuum) which is caused by sufficient energy being transferred to a surface atoms to overcome its binding energy. Physical sputtering effects occur even at low energy ($\approx$ 100 eV) incident particle energies. Hence, an appropriate selection of parameters such as energy, reactive ions to neutral ions flux ratio, surface orientation to produce desired effect is essential.

IBE offers several advantages over alternate etching techniques. Among these advantages are the independent yet simultaneous control over etch parameters, directional controllability of the ion beam, increased uniformity, and repeatability. Modification of surfaces by ion bombardment depends largely upon the substrate and etching parameters, and hence find tremendous applications. In the context if III-V compounds, the applications requiring the shaping of III-V semiconductors can be separated into three basic categories. For applications requiring macroscopic features for material selective, fast, and anisotropic etching, the processes include via hole through-the-chip interconnections, chip separation, and selectively etched wells in heterostructures. For applications requiring optically smooth surfaces for light propagation in the semiconductor and well controlled etched profiles, the processes include formation of mirror facets, integral lenses and etched gratings. For electronic surfaces the applications range from surface cleaning, sensitization, mesa formation for restricting the p-n junction area, to more important applications for the gate metallization of MESFETs. Other applications include uniform delineation, and high vertical walling in the fabrication of bubble memories, precise formation of the channel shape in surface acoustical devices, and optical waveguides. Due

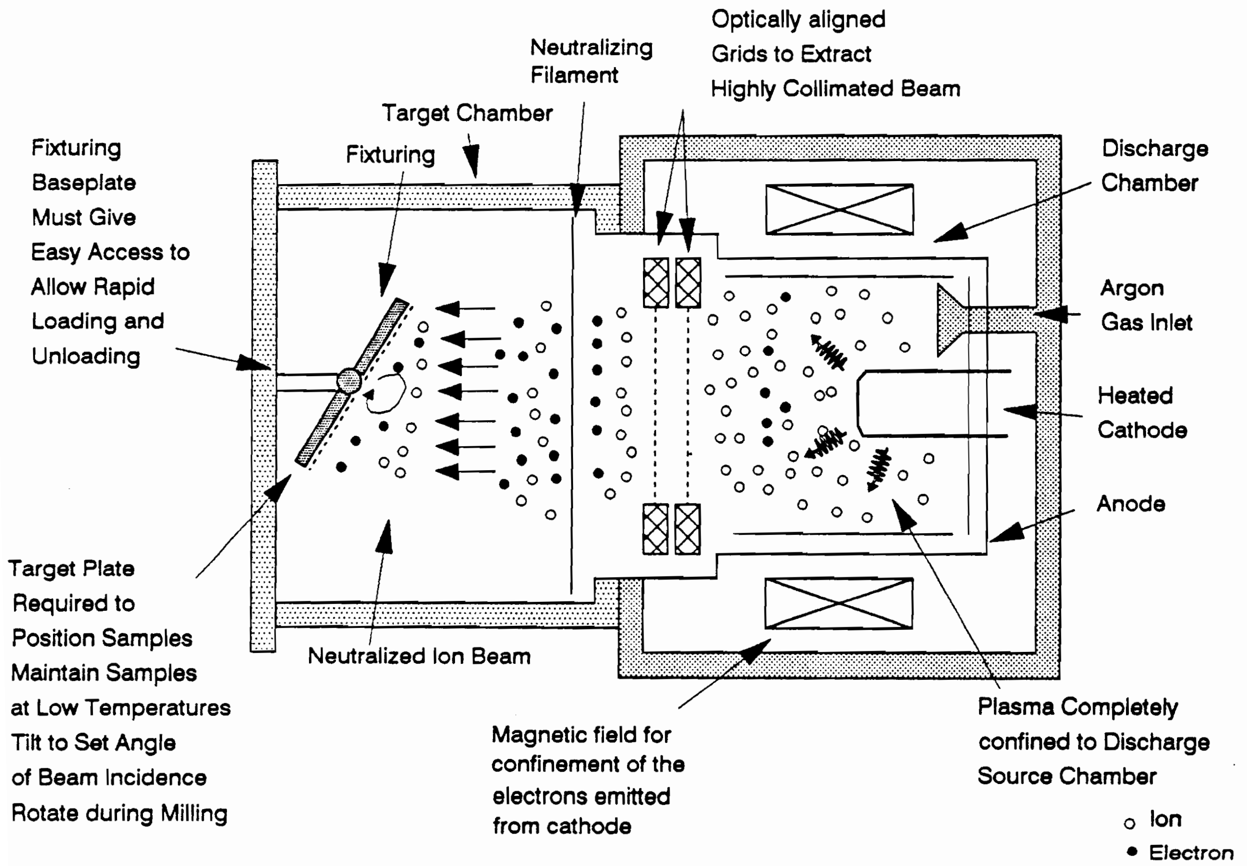

Figure 1.5 A Schematic of an ion-beam gun.

to the fast development of GaAs field effect transistors (FET's) for microwave communication systems, there is considerable interest in obtaining reproducible and reliable properties of the most important electrode in these devices, the Schottky gate contact. The standard technology for producing Schottky contact is still represented by wet chemical preparation of the surface and deposition of a highly conductive metal, usually Al, by means of thermal evaporation in a vacuum chamber. Optimized processing, in general meets the requirement of electrical properties and results in barrier heights $\approx$ 0.8 eV and an ideality factor of nearly one. In recent years several promising techniques have been proposed as alternatives to the conventional procedure, due to the difficulty of reproducing constant surface conditions. Dry surface cleaning techniques such as sputter, ion beam or reactive ion etching are superior to wet processing in view of the uniformity across the wafer, etch rate control, and reproducibility from wafer to wafer. Above all, they can be followed in situ by metal deposition thus avoiding formation of an interfacial layer. Associated with these numerous advantages are some disadvantages of the ion beam etching, such as radiation induced damage to the host crystal and ion-channeling. Such damage introduced into the host lattice is detrimental to the quality of the devices prepared on IBE surfaces. From the devices point of view it is extremely essential to understand the nature and extent of ion damage.

1.3 Literature Review and Research Objectives

There exists a vast literature on ion-implantation and its effects on the crystal structure. Most of these studies indicate that the host lattice suffers radiation induced damage. Ion beam induced damage can be classified into several distinct and broad categories viz. physical, chemical, and electrical damage, and ion-channeling, in the substrate materials. The latter can be reduced by adjusting the angle of the incident beam. The physical defects include structural defects, randomization or formation of an amorphous layer in the top region, with amorphicity increasing as a function of ion beam

energy, dislocations, loops, vacancies, interstitials, and interstitail-vacancy complex [21,22]. The chemical effects include change in stoichiometric composition, alteration in surface reactivity [23,24], contamination from metallic impurity form within the ion beam chamber, introduction of Ga vacancies, As and Ga antisites, etc. Electrical damage includes ion-induced deep trap levels [25-39], and surface region damage resulting in lower drift mobility. It is believed that IBE results in the formation of a damaged layer at or near the semiconductor surface which consists of a donorlike traps[40] distributed exponentially from the surface, causing enhanced tunneling of electrons through the barrier [41,42]. Recent studies on the effect of the ion-bombardment on the I-V behavior of GaAs-Schottky contacts, indicated a lack of correlation between ion energy and Schottky barrier height [43].

As mentioned previously, most of the previous studies probe surfaces a few hundred to a micron deep into the bulk. At low ion beam energies the damage primarily resides at the surface. The photonic characterization would be a most appropriate choice because maximum absorption of the photons takes place in the surface region. Literature concerning the photonic investigation is practically non-existant. A review of some pertinent previous investigations is, however, presented below.

Some studies have been reported [44-58] in the literature on ion beam processed metal/semi-conductor and MIS-Schottky barrier diodes and photodiodes fabricated on (100) n-GaAs. The diode parameters exhibited strong dependence upon processing parameters and clearly indicate some of the more common conclusions, such as reduction in barrier height, increase in reverse saturation current and ideality factor. Schottky contacts showed no correlation in between ion energy and Schottky barrier height[43].

Slow-relaxation effects were observed by several investigators [59-71] in SI GaAs, however, there is no mention of such observations in ion beam processed GaAs surfaces. The interest in such studies stems primarily due to increased utilization of dry processing in defining high resolution patterns in integrated circuits and opto-electronic devices for use in optical signal communication, having submicron size geometries. It will be shown in the

latter part of the thesis that the studies of slow-relaxation effects in ion beam processed surfaces led to an important observation of the persistent photoconductivity[64]. Some of the earlier observed phenomenon were explained in light of this observation. The spectral conductivity at low temperature, and time-dependence measurements resulted in a new model of the generation of defects in ion-beam processed surfaces.

Photovoltaic response, especially spectral response, is typically measured to study the relative contribution of photons of different energy to the short-circuit photo-current, and is strongly influenced by the structure and the history of the cell. Spectral response under normal operating conditions yields interface recombination information, while the sub-band gap absorption results in current collection due to the internal photo-electric emission of carriers over the junction barrier. No such information is available in literature on IBE devices. The tail-state absorption is typically measured by either photoconductivity, or quantum efficiency measurements, due to sub-bandgap photons in disordered materials, such as a:Si:H alloys [72-76], to get an estimate of the disorder in valence band tail states.

Low frequency capacitance dispersion was observed[9,27,47,48], in Schottky barrier diodes, arising as a result of ion beam etching. DLTS studies on the IBE devices indicated introduction of some deep traps [41-43]. The results were, somehow, inconsistent and no direct correlation of deep trap levels and density could be established, with the ion beam energy. XPS [5,6,9,23,46], UV reflectivity [10,77], and Raman Spectroscopy [10,78], studies on GaAs samples bombarded under identical conditions indicated different depth of damage. In light of such a discrepancy, a rigorous theoretical computer modelling was considered based on LSS theory[79], the ion range statistics, and experimental parameters, to accurately predict the depth of the damage.

It is evident from the above brief review that very little information exists in the literature concerning this rather unique and useful processing step. For a successful implementation of dry processing, its electrical consequences must properly be understood. Hence, the present study is intended to investigate the effects of IBE on GaAs surfaces and

verify the observations using physical and electrical models. It is the aim of this study to characterize the effect of ion beam induced damage as a function of ion beam energy, ($\lesssim$ 4 KeV; at 10^{16} fluence) in terms of electrical and optical behavior of the n-GaAs Schottky contacts and also in the dark, and photoconductivity of semi-insulating (SI) GaAs samples. Ar^+ ion beam etching was chosen in order to rule out the possibility of producing any additional effects at the interface due to chemical reactions in the case of reactive ion etching and thus making the interpretation and comparison with the other techniques studied in the present investigation more ambiguous.

For the present investigation, the study primarily concentrated on the following different but directly associated areas:

1. To develop surface sensitive inspection devices and experimental methods to accurately discern the effects in the disordered surface regions.
2. To characterize the IBE substrate and evaluate the distribution of the traps in the band gap, introduced as a consequence of ion beam processing.
3. To gain understanding of the process, by proposing phenomenological physical and equivalent electrical models of the effects of ion beam induced damage.

In order to achieve these goals, an automated electro-optical test station was developed and source-codes written to acquire the data in real time. Several new test structures were introduced and characterized to study the effects introduced as a result of ion beam bombardment on GaAs surfaces.

— ¤ —

Chapter 2

Unifying Theoretical Concepts

To accomplish the research objectives outlined in Chapter 1, it was necessary to review critical areas of background physics. By way of introduction, a brief review of the ion implantation processes and collision-cascade mechanisms of ion movement into the host lattice is presented. The reasons for implementing photovoltaic (viz. Schottky barrier photodiode) and photoconductive studies as the diagnostic tools for the ion beam bombarded surfaces, are elaborated by providing the basic theory of structures from the fundamental standpoint. The advantages of the characterization schemes adopted in this investigation are presented.

2.1 Ion Bombardment and Collision Cascade

If a surface is subjected to irradiation by energetic particles, several effects, such as backscattering, sputtering, desorption of surface layer, emission of electrons and photons, etc. occur, with a consequent modification in surface structure, and topography. The incident particles,-usually monoatomic ions-suffer a series of energy loss collisions; an example being the collisions between the ions and the substrate atoms (nuclear collision). Figure 2.1 (a), and (b) illustrate some of the processes that can occur when a particle of energy E_o impinges upon a surface. Figure 2.1 (a) shows a cascade of displaced atoms originating due to collision between the implanted ion and the lattice atom. During its path, the implanted ion may initiate many similar displacement cascades, within a volume surrounding the ion track. Figure 2.1 (b) shows various mechanisms of energy dissipation for an incoming ions of mass, M_1 and energy, E_o. The maximum amount of energy, $T_{max.}$ that can be transferred from the primary ion to an atom, at rest in the target can be represented as [80].

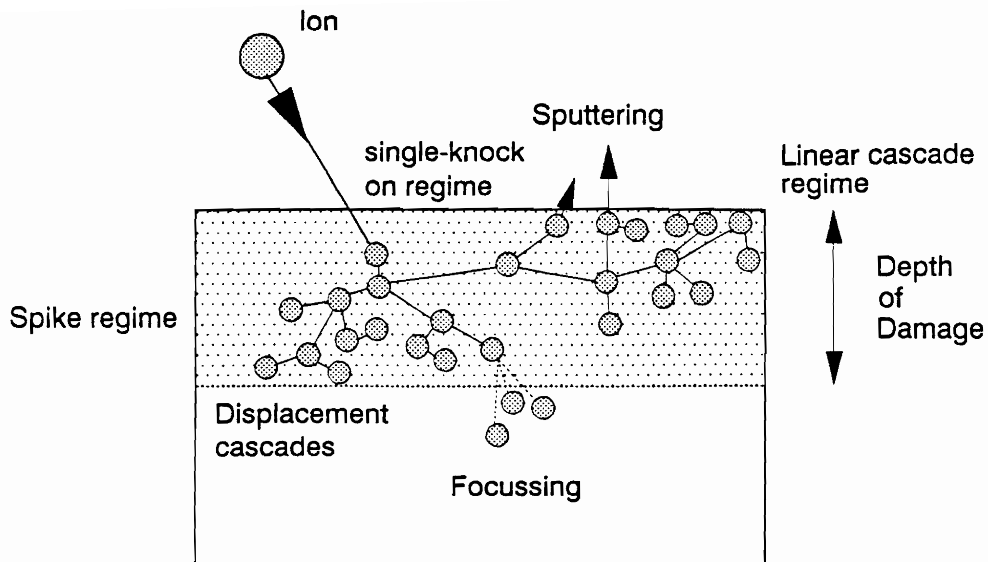

(a)

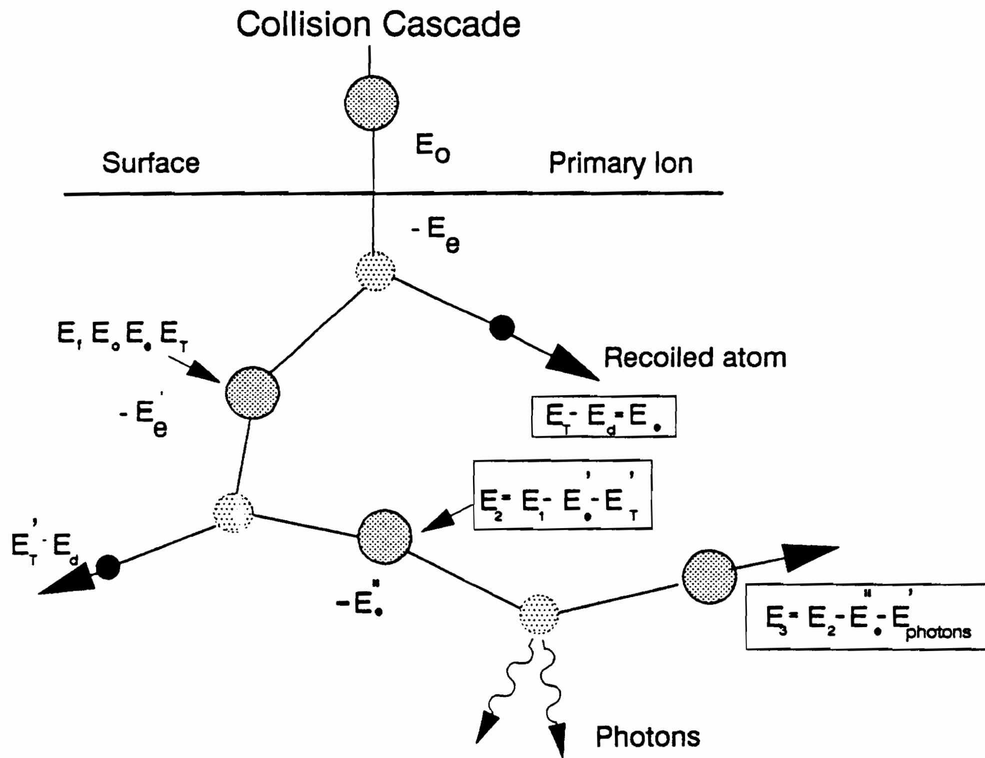

(b)

Figure 2.1 **(a) Scheme of the main displacement processes that lead to surface damage. (b) Mechanism of collision cascade and Energy Dissipation for an incoming ion of mass M_I and energy E_0, E_0 = Kinetic energy of the incoming ion, E_e = energy dissipated through electron excitation, E_T = Transfer energy, and E_d = displacement energy.**

$$T_{max.} = \gamma\ E_0 = \left[\frac{4M_1 M_2}{(M_1 + M_2)^2} \right] E_0 \qquad (2.1)$$

where γ is the maximum energy transfer factor, M_1 and M_2 are the respective atomic masses. When energy transfer is sufficient to break the host molecular bond, lattice damage results. The other energy losses are due to collisions with the electrons (electronic collision). The statistical nature of nuclear and electronic energy-loss collisions ensures that ultimate ion-depth distribution follows a Gaussian form, where the peak corresponds to the most probable (projected) ion range. Linear cascade theory can be employed to generate the expected spatial distribution of a displaced atom from a knowledge of the energy deposited into nuclear collision process. The number of displaced atoms per incident ion, N_d is given by [81].

$$N_d = 0.42\ \nu(E)/E_d \qquad (2.2)$$

where $\nu(E)$ is the nuclear component of the ion energy loss which contributes to atomic displacements, and E_d is the mean displacement energy for lattice atoms. Two types of annealing take place during implantation: viz. (a) dynamic annealing of damage produced by single ion, and (b) thermal or bulk annealing of damaged layers due to a rise in temperature during ion bombardment. The inability of linear cascade theory to accurately predict damage level for low temperature ion bombardment has been attributed to the effects of thermal and displacements spikes. The observed damage is the result of the competing disordering and annealing processes, at temperatures above absolute zero.

One of the processes, known as sputtering, is the ejection of surface ions and neutrals into the surrounding vacuum and is caused by sufficient energy being transferred to a surface atom, to overcome its binding energy. Two types of sputtering can occur: physical and chemical sputtering. A general expression of the sputtering yield can be represented by[82],

$$Y = \frac{0.42}{U^{be}} \alpha \frac{(M_t)}{M_i} \sigma(E_i, Z_i, Z_t) \qquad (2.3)$$

for orthogonal incidence, where E, M, and Z are the energy, mass, and charge of the ion, i and the target, t respectively. α describes the efficiency of the momentum transfer, σ_n is the nuclear stopping cross-section, and U_b is the binding energy. At high projectile velocities, the energy loss to electrons dominate the slowing down of the ion, while scattering by electrons is a minor effect. Therefore, the stopping cross-section dominates the sputtering yield. Figure 2.2 [Ref. #80], shows schematically a pertinent survey. At lower velocities, nuclear stopping dominates. At higher velocities, for $| v \lesssim Z_1^{2/3} e^2/\hbar |$, electronic stopping takes over. In this regime, termed as Lindhard and Scharff, the projectile is neutral. Beyond the stopping power maximum, the Bethe regime is approached where the projectile is stripped. In the relativistic regime, the stopping power goes through a broad minimum and increases in the extreme relativistic regime. One model interprets the target temperature dependence, in terms of annealing via vacancy migration at the periphery of direct impact induced amorphous zones [83]. Among other effects of the ion bombardment are: erosions which generally develop into topographical features such as facets, terraces, blisters, cones and pyramids etc. The bombarding ions can also become trapped into the surface layers, altering the surface chemistry of the target.

2.2 Metal Semiconductor Contact and Schottky Effect

Metal-Semiconductor (MS) junctions form an integral part of the integrated circuit technology; they also serve as a test vehicle to understand the fundamental physics of surface and interfaces in many practical systems. Depending upon the materials parameters the MS junction behaves either as Schottky (rectifying) or as Ohmic (linear) contact. When a metal is brought in close proximity to a semiconductor, a potential barrier results from the difference in work function of the two substrates. Two limiting cases are presented in Figure 2.3. The energy band diagram of a metal of work function Φ_m and an n-type

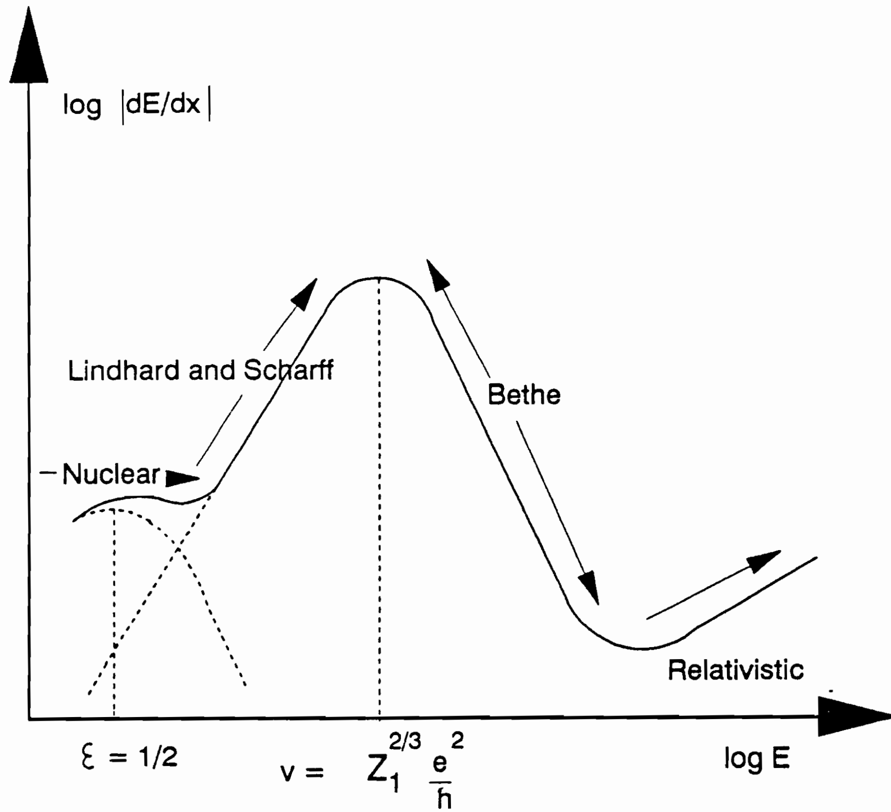

Figure 2.2 Stopping power of an ion as a function of energy.

semiconductor of work function Φ_{sc} system, ($\Phi_m > \Phi_{sc}$) is shown in Figure 2.3 (a) in absence of the surface states. The Schottky-Mott barrier height, $q\Phi_B$, is given by;

$$q\Phi_B = q(\Phi_m - \chi_{sc}) \tag{2.4}$$

when metal is in intimate contact with the semiconductor or the separation is comparable to the interatomic distance. An electric field is established from the semiconductor to metal due to the positive charge of ionized donors in the semiconductors, and a thin sheet of negative charge in the metal, contained within the Thomas-Fermi screening distance from the interface ($\approx$ 0.5 Å).

For ($\Phi_m < \Phi_{sc}$), the electron energy bands bend, such that Fermi level in the semiconductor is raised by an amount (Φ_{sc} - Φ_m), leaving behind a positive charge on the metal and an accumulation of electrons on the semiconductor, confined to a thickness of the order of a Debye length, and is essentially a surface charge. There is no potential barrier to electron flow from either side. The electron concentration is increased in the region near the interface, resulting in an ohmic contact.

In practice, a large density of surface state is present in the semiconductor surface, as shown in Figure 2.3 (b). If the density of surface state is very large, altering of the occupational level E_F is independent of the metal work function and the phenomenon is termed as 'Fermi-level pinning'. Several researchers have attempted to explain the 'Fermi-level pinning'[84-101], however, a limited understanding exists about the role of interface formation on the electrical performance of a practical Schottky-barrier junction. A brief review of the existing models proposed in the literature for Schottky-barrier formation is presented in the following section and is discussed in the context of the Schottky-barrier lowering mechanism. It is instructive to know that the Schottky effect is the image-force-induced-lowering of the potential energy for charge carrier emission when an electric field is applied.

Most practical MS contacts have a thin interfacial layer of the order of atomic

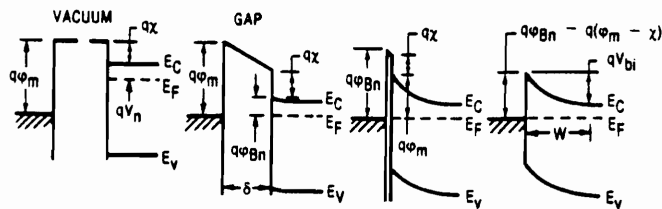

(a)

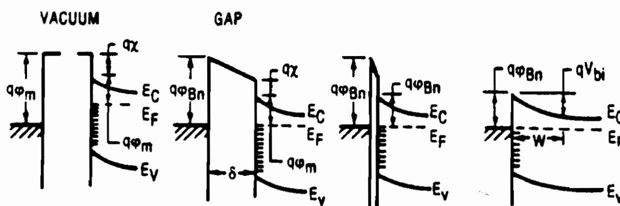

(b)

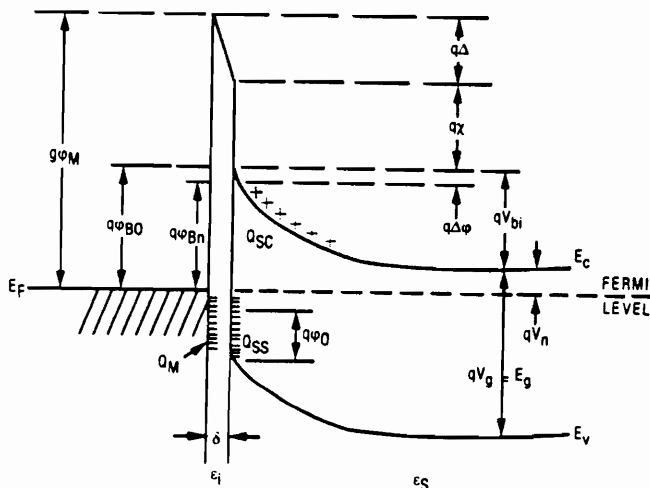

φ_M - WORK FUNCTION OF METAL
φ_{Bn} - BARRIER HEIGHT OF METAL - SEMICONDUCTOR BARRIER
φ_{B0} - ASYMPTOTIC VALUE OF φ_{Bn} AT ZERO ELECTRIC FIELD
φ_0 - ENERGY LEVEL AT SURFACE
$\Delta\varphi$ - IMAGE FORCE BARRIER LOWERING
Δ - POTENTIAL ACROSS INTERFACIAL LAYER
χ - ELECTRON AFFINITY OF SEMICONDUCTOR
V_{bi} - BUILT-IN POTENTIAL
ε_S - PERMITTIVITY OF SEMICONDUCTOR
ε_i - PERMITTIVITY OF INTERFACIAL LAYER
δ - THICKNESS OF INTERFACIAL LAYER
Q_{SC} - SPACE-CHARGE DENSITY IN SEMICONDUCTOR
Q_{SS} - SURFACE-STATE DENSITY ON SEMICONDUCTOR
Q_M - SURFACE-CHARGE DENSITY ON METAL

(c)

Figure 2.3 **(a) Energy band diagram of metal-semiconductor under two limiting cases; (a) ideal condition ie. no surface states, and (b) surface states density large enough to dominantly influence the barrier height. (c) Detailed Energy-band diagram of an Metal-Semiconductor contact with an interfacial layer of the order of atomic distances.**

distance, present at the surface, as shown in Figure 2.3 (c). The interfacial layer is assumed to be independent of the electrons and can withstand a potential across it. Concepts germane to this investigation are introduced in a later section.

2.2.1 Unified Defect Model and Mid-Gap Energy Theories

The mechanism of Schottky-barrier formation is receiving considerable amount of attention and many models have been proposed. The central feature of most of the models has been some conformation of Fermi level pinning, indicating that the position of the Fermi level (E_F) relative to the semiconductor band gap, at the interface, is insensitive to the Schottky metal. Spicer and co-workers [84-87,92,93,101] have suggested that the states pinning E_F are associated with the native defects in the semiconductor, in their unified defect model (UDM). According to the UDM, depositing sub-monolayer coverage of a metal or oxygen on freshly cleaved surfaces, moved the Fermi level into the gap. The consequent 'pinning' was attributed to the native defects induced into the semiconductor, antisite being the key native defect in the UDM. As Weber [102] pointed out the As_{Ga} antisite is a double donor, hence it must have a 'spectator' minority acceptor defect, in order for the Fermi level to be pinned. This spectator defect was identified as the Ga_{As} antisite, which provides two acceptor levels between the 0.5 eV level of the As_{Ga} antisite and the valence band maximum (VBM), as shown in Figure 2.4 (a). Of particular importance of this advanced UDM (AUDM) is its ability to explain the changes in the Schottky barrier height for Al and Au on GaAs due to thermal annealing and to relate these changes to interfacial chemistry.

In an attempt to explain the controversial dipole effect in terms of the fundamental properties of the interface, Haine [103] proposed that the dominant source of interface charge comes from the metal induced gap states (MIGS). According to the theory, E_F is pinned by states intrinsic to MS interface. Tersoff [104] further proposed that MIGS penetrate several layers into the semiconductor, and hence first few layers of the semiconductor must be locally metallic. The Fermi level is hence pinned at that energy

which gives local charge neutrality. Fermi energy must fall at or near the energy E_B, where gap states cross from predominantly valence to conduction band character. Experimentally, the principle challenge to verify the theory lies in quantitatively characterizing the states present in the semiconductor gap, at the interface.

More recently, Ludeke and co-workers [88-91,100] have explained an anomalous movement of the Fermi level after the semiconductor was thought to be pinned near the onset of metallic behavior, in terms of a new effect called the 'screening and delocalization effect' in Schottky barrier formation. The delocalization is based on the notion that a localized defect or impurity state on the surface of the semiconductor becomes delocalized in the presence of a metallic overlayer. A detailed discussion of the delocalization and screening effect is beyond the scope of this thesis; however it is evident from the Figure 2.4 (b), that Γ is the full width at half maximum (FWHM) of broadened resonance following the interaction of the defect level with the metallic states.

It is emphasized that each theory has its own merit and none ubiquitously explains the Fermi level pinning phenomenon adequately. The models described above have been taken into consideration by several authors in calculating Φ_B by thermionic emission and in computing the quantum-mechanical transmission probabilities of electron tunneling through the potential barrier.

2.2.2 Present Understanding of the MS Schottky Diodes

It is evident from the above discussion that much controversy exists over these rather apparently simple systems. In an ideal MS system, no interfacial layer exists and the potential energy barrier to the flow of charge carriers is primarily determined by the work function difference between the metal and the semiconductor. The four mechanisms by which carrier transport can occur in Schottky barriers are thermionic emission over the potential barrier, carrier tunneling through the potential barrier, carrier recombination and/or generation in the depletion region, and carrier recombination in the neutral region of the semiconductor, which is equivalent to minority carrier injection. The dominant

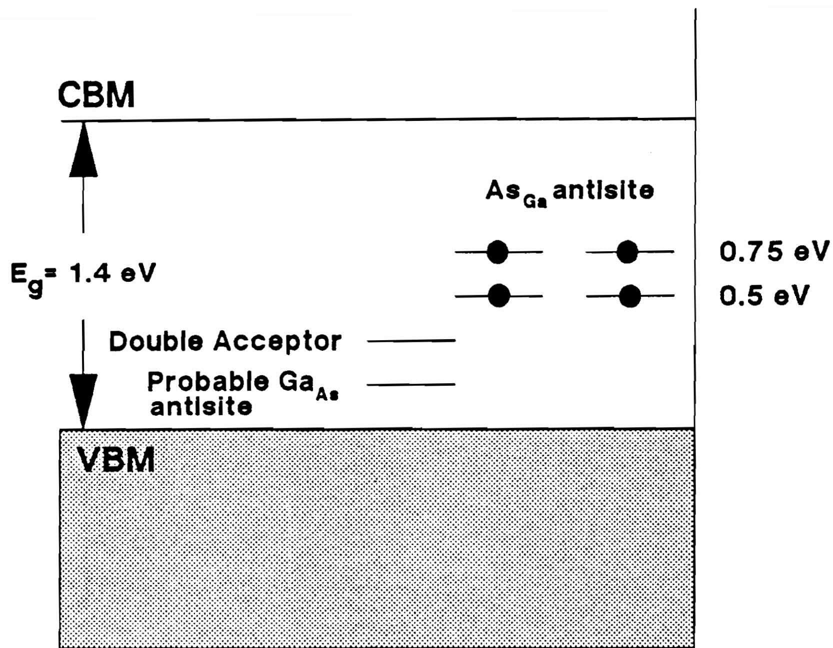

Advanced Unified Defect Model

(a)

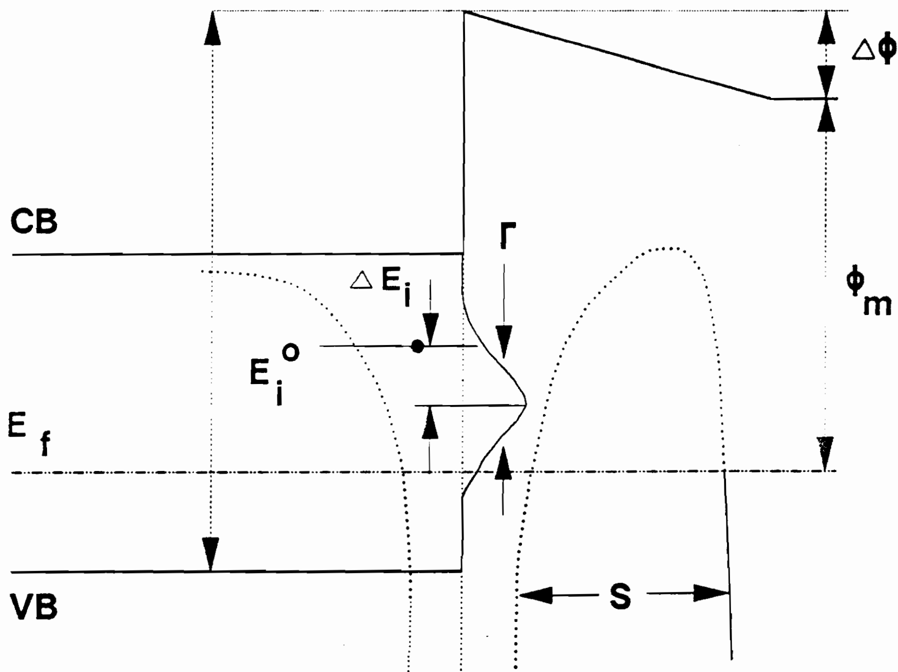

(b)

Figure 2.4 (a) The energy level diagram for the advanced Unified Defect Model , (b) Energy band diagram for a semiconductor showing the screening and delocalization effect.

mode of the current flow in most Schottky barriers in Si and GaAs is through thermionic emission and tunneling. In practical MS systems, the interface electric field plays a critical role in controlling the barrier height. Schottky barrier height (SBH) variable through the entire bandgap of GaAs has been demonstrated in atomically clean Al-GaAs systems deposited in-situ in an MBE reactor [105].

An expression for the diode IV characteristics based on a modified Bethe's thermionic emission theory, considering electron energy distribution influenced by quantum -mechanical tunneling and reflection, is given by:

$$I = AA^{*} T^{2} \exp(-\Phi_B/kT)(\exp qV/nkT - 1) \quad (2.5)$$

A being the area, A^* is the effective Richardson constant, T is the absolute temperature, Φ_B is the SBH, V is the voltage applied to the junction and n is a non-ideality parameter higher than unity.

$$A^{*} = f_p \, f_Q \, (4\pi m^{*} q k^{2}/h^{3}) \quad (2.6)$$

where f_p is the probability of an electron reaching the metal without being scattered by an optical phonon after having passed the top of the barrier, f_Q is the transmission coefficient and m^* is the effective mass.

Depending upon preparation conditions, the MS interface may exhibit a complex morphology, characterized by disorder, and the presence of various reaction products. Compound semiconductors display a disconcerting richness of chemistry and hence interfaces may be inhomogeneous. The SBH that is measured, due to complexity of the interface morphology, may not be a true barrier height but some transport property. Determinations of the SBH can only be assessed if interface obeys a set of stringent conditions. Large deviations and anomalies have been observed and explanations are suggested in literature [106-109]. Presence of large surface states and thin interfacial oxide layer alter the SBH and Φ_B has some bias dependence, according to the Bardeen's model,

and is expressed by;

$$\Phi_B = \Phi_{B0} - \alpha E_{max} \tag{2.7}$$

$$\text{where, } \alpha = \frac{\delta \varepsilon_s}{\varepsilon_i + q^2 \delta D_s}$$

where ε_s is the semiconductor permittivity, ε_i is the insulator permittivity, δ is the insulator thickness, D_s is the density of surface states, and Φ_{B0} is the flat-band barrier height.

For highly doped semiconductors, the Schottky barrier becomes so thin that electron near the top of the barrier can tunnel through the barrier. The current-voltage characteristics in such case of thermionic field emission (TFE) is determined by the competition between the thermal activation and tunneling, and is given by;

$$j = j_{stf} \exp(qV/E_o) \tag{2.8}$$

where $E_o = E_{oo}$ Coth(E_{oo}/kT) and, $E_{oo} = h/4\pi\ (N_D/m^* \varepsilon_s)^{1/2}$. The pre-exponential term was calculated by Crowell and Sze:

$$J_{stf} = \left[\frac{A^* \ T\ [\pi E_{oo} q(\Phi_b - V - \xi)]^{\frac{1}{2}}}{k \ \mathrm{Cosh}(E_{oo}/kT)}\right] \exp\left[\frac{-q\xi}{kT} - \frac{q}{E_o}(\Phi_b - \xi)\right] \tag{2.9}$$

Here, $\xi = (E_c - E_{Fn})/q$

At low temperatures ie. in the field emission (FE) regime, $E_o \approx E_{oo}$, and the slope of the ln(I) vs. V plot is temperature independent.

Hole injection or recombination in the neutral region essentially constitutes the minority carrier current in a metal/n-GaAs Schottky contact. Since the Schottky barrier diode is a majority carrier device, there is a negligible contribution of hole injection to the total current. Other effects, such as tunneling at states as the interface and field crowding at contact edges have been observed to effect the current-voltage characteristics. A

Table 2.1 Basic Conduction processes in MIS structures.

Process	Expression[a]	Voltage and Temperature Dependence[b]
Schottky Emission	$J = A^{*}T^{2} \exp\left\{ -\frac{q[\varphi_B - (qE/4\pi\varepsilon_i)^{1/2}]}{kT} \right\}$	$\approx T^{2} \exp[+a(V^{1/2})/T]$
Frenkel-Poole Emission	$J \approx E \exp\left\{ -\frac{q[\varphi_B - (qE/\pi\varepsilon_i)^{1/2}]}{kT} \right\}$	$\approx V \exp[+2a(V^{1/2})/T]$
Tunnel or Field Emission	$J \approx E^{1/2} \left[-\left(\frac{8m^{*}\varphi_B{}^{3}/3hq}{3} \right)^{1/2} \right]$	$\approx V^{2} \exp(-b/V)$
Space-Charge Limited	$J = (8/q)\varepsilon_i \mu E^{2}/d$	$\approx V^{2}$
Ohmic	$J \approx E \exp(-\Delta_{ae}/kT)$	$\approx V \exp(-cT)$
Ionic Conduction	$J \approx E/T \exp(-\Delta_{ai}/kT)$	$\approx V/T \exp(-d'/T)$

[a] A^{*} is the effective Richardson constant; φ_B, is the barrier height; E, the electric field; ε_i, the insulator dynamics permittivity; m^{*}, the effictive mass; d, the insulator thickness; ΔE_{ae}, the activation Energy of electrons; and ΔE_{ai}, the activation energy of the ions.

[b] V =Ed. a, b, c, d´ are positive constants independent of V or T.

summary of the basic conduction processes in MIS structures is presented in Table 2.1

2.2.3 Ohmic Contacts to GaAs

By definition, an ohmic contact is a perfect source or sink of both carrier types and has no tendency to inject or collect preferentially either electrons or holes. For most applications, ohmic contacts, alternatively can be defined as a source of carriers with negligible internal resistance compared with the semiconductor bulk, which obey Ohm's law, $V = IR$, for the current densities of interest. Due to the presence of inhomogeneous native oxide layer, high surface state density and changing requirements of contact dimensions for device structures, there is no standard ohmic contact to GaAs. To quantify an ohmic contact, 'figure of merit' such as specific contact resistivity, and/or normalized contact resistance or specific transfer resistance must be stated. In a metal-semiconductor (MS) contact, the metal → semiconductor electron current component remains unchanged to a first approximation. The contact property can therefore be altered by controlling the semiconductor → metal electron current component. In GaAs, Φ_B cannot be made small by proper choice of metal, evidently because of a high surface state density, effectively pinning the semiconductor Fermi level. The alternative is then to reduce the depletion layer width with consequent increase of electron tunneling current. The tunneling probability for electrons at the depletion edge is expressed by the familiar WKB approximation. Assuming a parabolic barrier, the tunneling or the field-emission current can be approximated as,

$$j(\text{tunnel}) \propto \exp\left[q(V - V_{bi})/\xi_{oo}\right] \qquad (2.10)$$

where,

$$\xi_{oo} = \frac{hq}{4\pi}\left[\frac{N_D}{\varepsilon m^*}\right]$$

Also, by way of comparison,

$$j\ (\text{thermionic}) \propto \exp\left[qV - \Phi_B)/kT\right] \qquad (2.11)$$

Therefore, if $\xi_{00} >> kT$, the tunneling current will dominate. For GaAs, $\xi_{00} \simeq 2.0 \times 10^{-11} N_D^{1/2}$ eV, where N_D is in cm^{-3}. Therefore, $\xi_{00} >> kT$ at room temperature for $N_D \gtrsim 1.6 \times 10^{18}$ cm^{-3}. Thermionic-field-emission current, which require electrons to be thermally excited over part of the barrier from where they can tunnel through the barrier, produces an ohmic contact.

The most widely investigated metallization is composed of Au, Ge and Ni [110-125]. The specific contact resistivity for these contact systems, however is much higher for a given N_D, than predicted by the tunnel contact model [126]. Such deviation from the tunneling model was attributed to formation of several new complexes at the surface. One such effect being the formation of spikes of highly doped materials, protruding into the GaAs [115], and the current transfer through the protrusions which can be modeled as hemispheres of finite dimensions [127]. It is believed that Ge diffusion into GaAs leads to Ge_{Ga} donor formation, which makes the required n^+ layer. A Ni overlayer inhibits the 'balling-up' of the AuGe by 'wetting' the surface for increased adhesion. There is also evidence that Ge not only produces an n^+ layer but also lowers Φ_B by inducing disorder [128]. The enhanced tunneling and barrier lowering may be able to explain the deviation from the tunnel contact model.

More recent techniques involve deposition of ohmic contact by epitaxial growth of layers of semiconductor materials having either an electron affinity greater than the metal work function or has surface states which pin the Fermi level near the conduction band. By further tailoring of the gap of the deposited layers, the electrons can be made to move easily between the metal and semiconductor.

2.3 Dark and Photoconductivity

Electrical conductivity of a semiconductor depends upon the number of mobile charge carriers, the distribution of thermal velocities, and on the change from an equilibrium distribution provoked by an applied electric field. For an intrinsic or near

intrinsic conductor, the ambipolar, weak field electrical conductivity expression is given by:

$$\sigma = q(n\mu_n + p\mu_p) \qquad (2.12)$$

based upon the Boltzamann transport equation. The terms have their usual meanings. The electron mobility as a function of temperature depends upon the electron gas degeneracy, E(k) at the lowest conduction band states, and the dominant scattering processes. The most common scattering process are acoustic and optical phonons, ionized impurities, and dislocations. In covalent semiconductors, the electrons are scattered predominantly by longitudinal acoustic (LA) phonons. The lattice scattering mobility can be expressed as:

$$\mu_l \approx (m^*)^{-5/2}\ T^{-3/2} \qquad (2.13)$$

Departure from a precisely $T^{-3/2}$ dependence from lattice scattering mobility occurs commonly and is attributed to a variety of competing effects, including the nonspherical shapes of constant energy surface for conduction electrons. The mobility from ionized impurities can be expressed as:

$$\mu_i \approx (m^*)^{1/2}\ N_I^{-1}\ T^{-3/2} \qquad (2.14)$$

where N_I is the ionized impurity density. At lower temperature, when the phonon population is depleted, the mean free path is controlled by ionized-flaw scattering. The combined mobility is, $\mu = (1/\mu_l + 1/\mu_i)^{-1}$. For polar semiconductors, optical-phonon scattering is significant and can be approximated by

$$\mu \approx (m^*)^{-3/2}\ T^{1/2} \qquad (2.15)$$

Several other scattering mechanisms such as inter-valley scattering, (a) in which an electron is scattered within an energy ellipsoid, and (b) electron scattered from the vicinity of one minimum to another minimum, also effect the mobility. Electron can be scattered

when objects of atomic size interrupt the periodicity of the lattice. Conductivity follows a relationship of the form, $\sigma = \sigma_o \exp(-E_A/kT)$, where σ_o is the minimum metallic conductivity and E_A is the activation energy. An Arrehenius plot results in activation energy and dominant scattering mechanism as a function of temperature.

Photoconductivity is a useful probe for the defect structure of solids. The conductivity of the sample is measured in presence of an optical excitation. The electrical response of semiconductor to sub-bandgap photon is treated in a later section, however for simplicity, the carrier generation due to an optical source of $h\nu > E_g$ is considered here. The generation rate in a semiconductor, in presence of an optical excitation can be expressed by, $G = G_L + G_{th}$, where G_{th} is the thermal generation rate and G_L is the electron hole pair generation due to the optical excitation. The direct recombination rate can be expressed as;

$$R = Bnp = B(n_o+\Delta n)(p_o+\Delta p) \qquad (2.16)$$

where B is the probability coefficient and Δn , and Δp are the carrier densities in excess of equilibrium carrier densities, $n_o = p_o$, respectively.

Under steady state illumination, R = G, and

$$\therefore G_L = R - G_{th} - U \qquad (2.17)$$

where U is the net recombination rate. Recognizing, that $G_{th} = R_{th} = Bn_op_o$,

$$\therefore G_L = B(n_o + \Delta n)(p_o + \Delta p) - Bn_op_o \qquad (2.18)$$

Under low level injection conditions, $\Delta p = G_L\tau = U\tau$, where τ is the carrier lifetime. In presence of traps, defects or recombination center of density N_t and energy E_t, the carrier lifetime is given by $\tau_p = 1/(c_p N_t)$, where c_p is the capture cross section of the minority carrier.

The general equation describing the rate of change of excess carriers after

termination of an optical excitation mechanism is;

$$\frac{d\Delta p}{dt} = G_L - U$$
$$= G_L - \frac{\Delta p}{\tau_p} \qquad (2.19)$$

The steady state excess carrier concentration is $\Delta p = G_L \tau_p$ at $t \leq 0$. Using this as the boundary condition;

$$\Delta p = G_l \tau_p \exp(-t/\tau_p) \qquad (2.20)$$

The analysis of the transient response for the indirect recombination is more involved, as the solution is not a simple single exponent. It will be seen later that the transient response of ion beam etched samples show a two or more exponent decay mechanism response.

2.3.1 Optical Processes in Semiconductors

The interaction of optical excitation with semiconductor produces essentially two types of response functions which are categorized as the lattice vibrational response and the electronic response. The lattice vibrational excitations have characteristic excitation energies on the order of 10 meV or 10^{-2} cm^{-1}, and therefore the spectral features appear in the far-infra-red region. The phonon dispersion relation provides information which is pertinent to crystal structure. The most direct and perhaps the simplest method for probing the electronic band structure is the fundamental absorption edge (lowest energy absorption edge). Such measurements yield the minimum energy separation between the valence band and the conduction bands and the nature (allowed, forbidden, direct, indirect etc.) of transitions involved. Figure 2.5 (a) shows schematically the absorption processes in solids. The transitions indicated by [1] are electron transitions from the valence band to higher lying conduction band, characterized by continuous high absorption process with structure

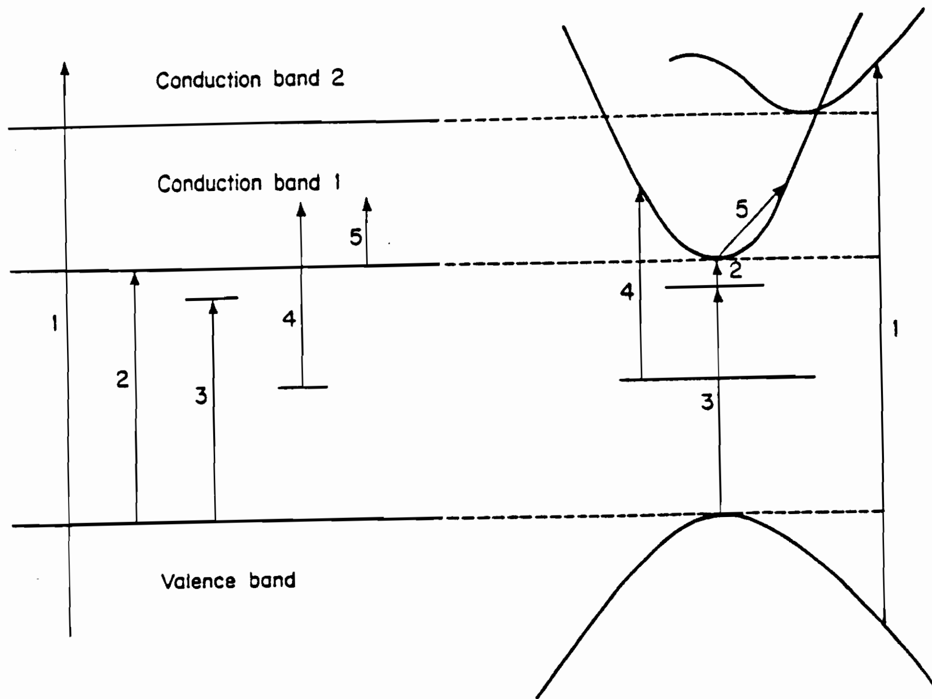

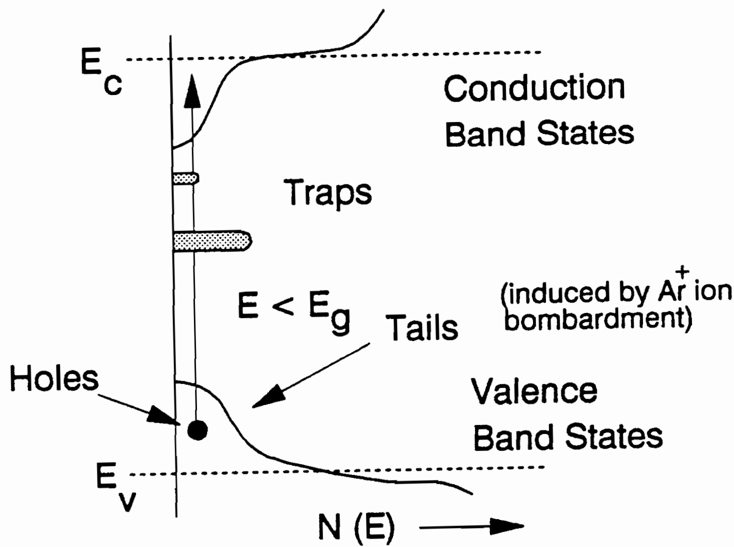

Figure 2.5 (a) Characteristic types of optical transitions shown both for the flat-band model and for E vs. k plot. (1) excitation from the valence band to higher-lying conduction bands. (2) excitation across the band gap, (3) exciton forming, (4) excitation from imperfections. (5) free-carrier excitation. (b) A model for the absorption from the valence band tails.

variations depending on the density of states distributions in the bands involved.

If, in the Brillouin zone of a semiconductor, the valence band maximum occurs at the same momentum value as the lowest lying conduction band minimum, an electron transition as indicated by a [2] from valence to conduction band conserves momentum. Such a transition is called 'Direct', and if the transition probability for a direct transition is calculated using the quantum theory, a characteristic dependence, expressed below, is found:

$$\hbar\omega_{pt} \propto (\hbar\omega_{pt} - E_{gd})^{\frac{1}{2}} \qquad (2.21)$$

Here, $\hbar\omega_{pt}$ is the photon energy and E_{gd} is the direct band gap. In some materials quantum selection rules forbid direct transitions at $k=0$, so that a transition from the top of the valence band to the bottom of the conduction band requires a change of both energy and wave-vector. In an indirect transition, conservation of energy is satisfied by;

$$\Delta E = \hbar\omega_{pt} \pm \hbar\omega_{pn} \qquad (2.22)$$

$\hbar\omega_{pn}$ being the energy of a phonon that is absorbed simultaneously with the absorption of the photon. Transition probability for an indirect transition using quantum theory shows a characteristic dependence of

$$\alpha \propto (\hbar\omega_{pt} - E_{gid})^{2} \qquad (2.23)$$

Here the phonon energy is assumed small compared to the photon energy. A more accurate expression consists of two terms, one for optical absorption together with phonon absorption and the second term corresponds to the optical absorption together with the phonon emission. Transitions indicated by [3], transport energy from one location to the another, without transport of net charge by a free electron-hole pair, termed an Exciton. Energy less than the band gap is required to create a bound electron-hole pair. The allowed states from the exciton can be described in terms of a hydrogenic model.

If imperfections are present in the crystal, they create energy levels that lie in the forbidden gap. Transitions shown by [4] correspond to the optical excitation of an electron from an imperfection level to the conduction band. A quite similar transition can be drawn corresponding to the optical excitation of an electron from the VB to an impurity level. Since the specific energy levels associated with the imperfections are localized energy levels, the imperfection levels exist only in relatively small regions of space around the imperfections. The absorption due to an imperfection (point imperfection-defects, point imperfection-impurities and structural imperfections-dislocations, or grain boundaries) consists of a narrow peaked band, with maximum at the energy separation between the two levels. The absorption constant for a transition to the CB from an electron-occupied imperfection level in the forbidden gap, or to a hole-occupied imperfection level in the gap from the valence-band, can be represented in a simple way,

$$\alpha = S_{op} N_{im} \qquad (2.24)$$

where S_{op} is the optical cross-section of the imperfection, and N_{im} is the density of imperfections available for absorption.

Free carriers absorption due to electron is indicated by transition [5]. Absorption of photons by free carrier, causes a transition to higher energy state within the same band or higher bands. It involves the absorption of both photons and phonons since both energy and $|k|$ must be changed in the transition. Optical absorption due to free carriers acting collectively as a kind of 'electron gas' is known as plasma resonance absorption.

For direct transition, no absorption below the energy gap is expected. In highly doped or compensated and disordered semiconductors the density of states in the conduction and valence bands tail exponentially into the forbidden gap. Consequently the absorption coefficient falls off exponentially as the photon energy decreases below the bandgap. This is known as the "Urbach Rule" and the exponential absorption edge of GaAs correlates quite well with the transitions involving the band tails. A model for the

absorption from valence band tails is shown in Figure 2.5 (b). The absorption coefficient is proportional to the product of the densities of initial and final states integrated over the position transitions for a given $h\nu$ [129]:

$$\alpha(h\nu) = Æ \int_{\xi}^{h\nu-\xi} |E_V|^{\frac{1}{2}} \exp \frac{E}{E_o} \, dE \qquad (2.25)$$

Æ is constant, E_V is the energy of state corresponding to the parabolic valence band, ξ is the Fermi level position, and E_o is an empirical parameter having the dimension of energy. After a set of suitable mathematic manipulations, the slope of the absorption edge on a semilogarthimic plot yields:

$$E_o = \left[\frac{d(\ln \alpha)}{d(h\nu)} \right]^{-1} \qquad (2.26)$$

The quantity E_o can be correlated with the degree of disorder in an IBE GaAs surface and will be seen in the next chapter.

2.3.2 Slow-Relaxation Effects: Persistent Photoconductivity and Thermal Stimulated Conductivity.

The fundamental requirement of a relaxation process is that the system be removed from thermodynamic equilibrium and exist in a transitory state which requires the reactants to surmount a free energy barrier until the reestablishment of equilibrium. For the present context, three relaxation types are discussed. The first is the photosensitive quantity which does not vanish with the interception of irradiation, but has a long tail. The excess free carrier density decays via recombination with small capture cross-section; the phenomenon being termed as the ‘persistent photoconductivity’ (PPC). In the second phenomena, the photosensitive quantity rapidly increases with the onset of irradiation, after which it

gradually decreases, even if the irradiation is continued; this phenomena is termed as 'photoelectric fatigue' or quenching. The third is so called thermally stimulated relaxation (TSR) process, where the system is in contact with a thermal reservoir that provides the thermal energy and the relaxation towards thermal equilibrium proceeds via thermal release of carriers from the traps into the bands and subsequent recombination with the recombination centers. An example where such measurements lead to trap spectroscopy information is called thermally stimulated conductivity (TSC).

An unusual slow-relaxation phenomena in semi-insulating GaAs[66-68,70], TSC in SI-GaAs[130-135], PPC in SI-GaAs[136], and $Al_{1-x}Ga_xAs$ alloys[136-138], and optical quenching in GaAs[139,140], have been reported in literature. Early reports indicate that oxygen impurity introduces defect levels, and the slow-relaxation effect was associated with a complex center, such as donor-acceptor pair $(D^{+}A^{-})^{o}$. Much of the present literature supports interplay of EL2 for such an observation[141-150]. In $Al_{1-x}Ga_xAs$, the effect of PPC is usually linked to 'DX' centers, consisting of a simple donor (D), and an unknown defect (X), and was postulated by Lang et al[151]. Several theories have been proposed in past few years and a synthesis of these observations draws two important conclusions: (a) The electron capture and emission kinetics of the DX center imply that the deep donor level derives its symmetry almost entirely from the L point. (b) The DX center is linked to the phenomenon of localized resonant donor levels in compound semiconductors.

The DX center has also been observed in GaAs with the application of hydrostatic pressure which modifies the band structure in much the same way as increasing the AlAs mole fraction does. Hence, above a critical pressure, the DX level, which moves with the L minimum of the CB, is pushed below the Γ minimum. Thermally activated capture behavior, a characteristic feature of DX center, was observed. Recently, extended X-ray absorption fine structure (EXAFS) studies suggest a very small bond length change upon charge localization by the donor, producing large energetic relaxation of the lattice.

Another study indicates that a small donor displacement with a polaron-like distortion of the surrounding lattice, results in a large energetic relaxation. A most probable physical explanation for the DX center is indicated by the configuration coordinate model. The electronic charge distribution of the defect atom is changed when it is excited from the ground into an excited state. The bonding with the nearest neighbors in the lattice is influenced, in that the electronic configuration of the neighboring ions becomes unstable: the ions take up new equilibrium positions. Part of the excitation energy is thus transferred to the lattice. This process takes a long time compared with the electronic transition. One can assume that the latter occurs while the lattice configuration is still unchanged (Frank-Condon Principle). The electronic transition back to the ground state takes place under the new lattice configuration. The ground state is not therefore reached immediately. The electronic transition is instead followed by a rearrangement of the ions into the original configuration. Since energy has then been given up twice to the lattice, the electron recombintion energy is less than the excitation energy. Hence compared with the absorption spectrum, the emission spectrum is displaced to longer wavelength. Yet another model is proposed by Levinson[152], which deals with the charge state controlled electrostatic interaction between two or more defects. According to his model, the minimization of electrostatic and lattice strain energy causes a transformation between the two possible configurations of the complex. It will be seen later that a new observation of PPC was made in IBE samples. Several hypotheses were suggested to explain the phenomena. The phenomena of the photoelectric fatigue can be ascribed to the specific properties of the main deep center.

The thermal cycle experiment indicate the thermal activation energies involved in the relaxation. The TSC spectrum usually consists of a number of (more or less) resolved peaks of electrical conductivity vs. temperature, which may be attributed to a species of traps. In general, various different types of traps and recombination centers may be present and their involvement in the reaction kinetics process will greatly change with temperature.

Development of electron kinetic model for TSC based on electron and holes traps, and trap recombination center pair has been reported [135,153] in the literature and is beyond the scope of the thesis.

2.4 Photovoltaics

Photovoltaics deals with the conversion of photons directly into electrical energy. The photovoltaic cell (solar cell) is basically a diode with provision of admitting photon excitation having energy $h\nu$, where h is the Planck's constant, and ν is the frequency; $\nu \geq \nu_0 = E_g/h$, where E_g is the bandgap of the semiconducting material. Electron-hole pairs are generated in the proximity of a photovoltaic junction or barrier. There exists a vast literature describing the photovoltaic device operation [154-156] and characterization techniques[157-165]. For the sake of continuity, a brief discussion germane to assess material, interface and device parameters is presented here. Figure 2.6 shows a schematic of a typical diffused junction solar cell, comprised essentially of five regions or sub-regions: an emitter, a depleted photovoltaic barrier (p-n junction space-charge layer, Schottky barrier or metal/insulator/semiconductor Schottky barrier), low doped base layer or absorber, a highly doped back ohmic contact region (formed either by intentional introduction of impurity or by alloying of back contact material) and a high-low junction region to reflect the minority carriers[161]. Figure 2.6 also shows the energy-band diagrams, electric field and minority carrier concentration profile throughout bulk of the solar cell.

For a practical solar cell, the I-V characteristics can be written as;

$$I = I_s\{\exp[q\,(V - IR_s)/kT] - 1\} - I_L \qquad (2.27)$$

I_L is the light generated current. From Eq.2.27, the open-circuit voltage ($I = 0$):

$$V_{oc} = (kT/q)\ln(I_L / I_s + 1) \qquad (2.28)$$

The output power is given by;

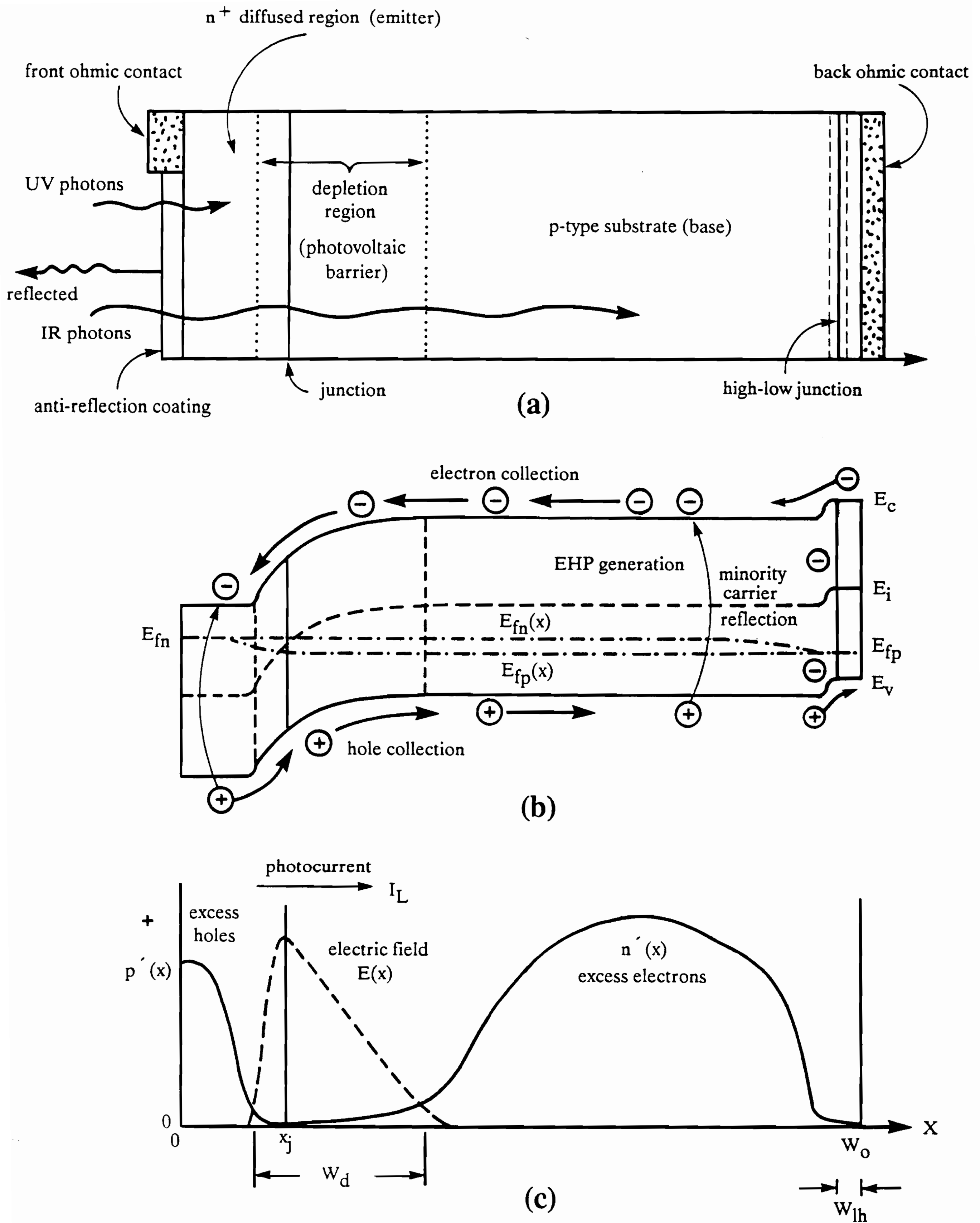

Figure 2.6 **(a) A generic schematic of a diffused junction solar cell. (b) Flat band diagram representation of the generic cell. (c) Electric field and excess charge distribution in the generic cell.**

$$P=|IV|= I\left[\left[\frac{kT}{q} \ln \left[\frac{I\ I_L}{I^S}\right] + 1\right] + IR\right] \quad (2.29)$$

The condition for maximum power can be obtained when ($dP/dV = 0$), or

$$I_m = I_s\ \beta V_m \exp\ (\beta V_m)$$

$$\approx I_L\ \{1 - 1/\beta V_m\} \quad (2.30)$$

$$V_m = 1/\beta\ \ln\ [(I_L/I_s + 1)/(1 + \beta V_m)]$$

$$\approx V_{oc} - 1/\beta\ \ln\ (1 + \beta V_m) \quad (2.31)$$

where ($\beta = q/kT$). The maximum power output P_m is then;

$$P_m = V_m\ I_m$$

$$\approx I_L\ [V_{oc} - 1/\beta\ \ln\ (1 + \beta V_m) - 1/\beta]$$

$$= I_L\ (E_m\ /\ q) \quad (2.32)$$

E_m corresponds to the energy per photon delivered to the load at the maximum power point. The power conversion efficiency is given by

$$\eta = (I_m\ V_m/P_{in}) = (F.FI_{sc}V_{oc}/Pin) \quad (2.33)$$

Where the fill factor (F.F) = (I_mV_m/I_LV_{oc}). When a monochromatic light of wavelength λ, is incident on the front surface, the number of carriers collected per incident photon at each wavelength is termed as the spectral response (SR). Solving, in general for the generation rate of electron-hole pairs, as a function of distance from the semiconductor surface and one-dimensional, steady state continuity equation, under low level injection conditions, the total photocurrent at a given wavelength can be written as:

$$J(\lambda) = J_p(\lambda) + J_n(\lambda) + J_{dr}(\lambda) \quad (2.34)$$

The SR, then equals this sum divided by $qF(\lambda)(1 - R)$ for the internal quantum efficiency.

$$\therefore\ SR(\lambda) = \frac{J(\lambda)}{qF(\lambda)(1 - R(\lambda)} \qquad (2.35)$$

where n, p and dr represent n-type, p-type and depletion regions, F is the incident flux and R is the reflection coefficient. Table 2.2 lists the intrinsic parameters fro some photovoltaic materials. Based upon the spectral data of Bird and Hulstrom, the measured and calculated external quantum efficiency of standard silicon solar cell are shown in Figure 2.7. It is instructive to note that response due to various regions can be identified. Hence a mere ratio of spectral responses of a device with a standard or control devices can indicate the region of reduced response due to nonlinearities. In IBE devices, since the damage resides mostly at the interface, the spectral response is an important diagnostic tool.

2.4.1 Metal Insulator Semiconductor Solar Cells

The Schottky barrier photovoltaic device offers several advantages which include, (1) low-temperature processing, (2) high current output and good spectral response, (3) high radiation resistance due to high electric field near the surface. Light with energy greater than the barrier height can be absorbed in the metal and excite holes over the barrier into the semiconductor, primarily used in photoelectric measurements of barrier height. The two major contributions to the spectral response comes from the depletion region and the base neutral region. The high field in the depletion region will sweep the photogenerated carriers out before they can recombine, leading to a photocurrent:

$$J_{dr} = q\ T(\lambda)F(\lambda)[1 - \exp(-\alpha W)] \qquad (2.36)$$

$T(\lambda)$ being the transmission coefficient, W being the width of the depletion region, and α is the absorption coefficient. The contribution from the base region is simplified to

$$J_n = qT(\lambda)F(\lambda)[\alpha L_n/(\alpha L_n+1)]\exp(-\alpha W) \qquad (2.37)$$

Table 2.2 **Intrinsic semiconductor parameters effecting the photovoltaic device response.**

Property → / Semiconductor ↓	Gap Transition	Bandgap @ 300°K (eV)	Mobility ($cm^2V^2 sec^{-1}$) electron	hole	χ (eV)	Lattice Constant a (A°)	Temperature Coefficient Expansion @ 300°K (*10^{-6} °C^{-1})
Elemental							
Si(Diamond)	Indirect	1.11	1350	480	4.01	5.431	2.33
Ge(Diamond)	Indirect	0.66	3600	1800	4.13	5.658	5.75
Compound							
GaAs(Zincblende)	Direct	1.43	8300	300	4.07	5.654	5.8
InP (Zincblende)	Direct	1.27	4500	100	4.38	5.869	4.5
CdS(Wurtzite,hex)	Direct	2.42	340	-	4.5	4.135	4.0
CdTe(Wurtzite)	Direct	1.44	700	65	4.28	6.477	-
Zn_3P_2(Tetragonal)	Direct	1.50	-	20	3.8	c=11.4	-
$CdSiAs_2$(p-type)*	Direct	1.55	-	300	3.85	5.884	-
$ZnSnP_2$ (p-type)*	-	1.66	-	55	4.25	5.651	-

* Chalcopyrite

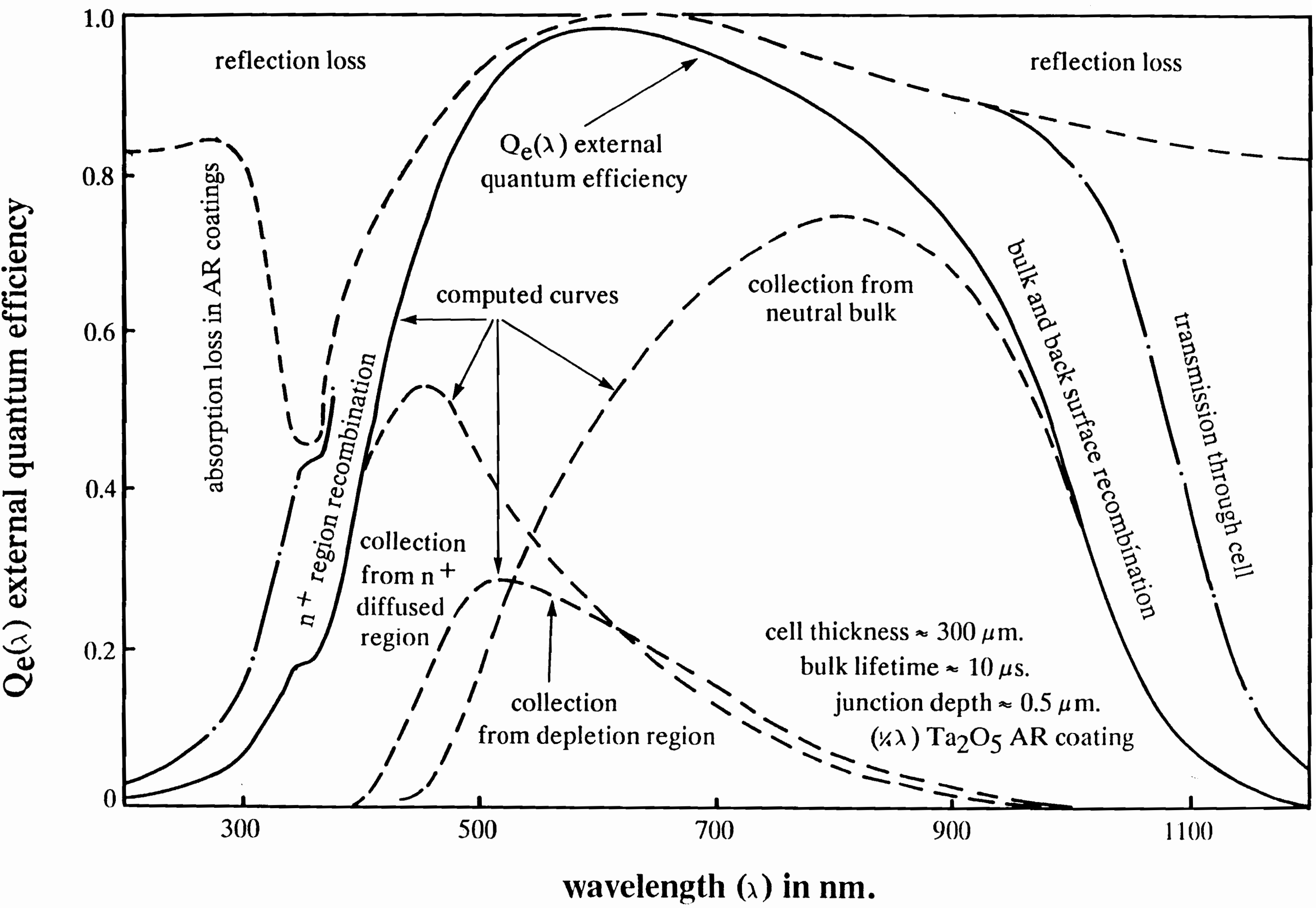

Figure 2.7 **Measured and computed spectral response of the silicon solar cell showing contribution due to various regions.**

The above two terms can be summed to produce the total photocurrent. In an MIS solar cell, a thin insulating layer is formed between the metal and the semiconductor substrate. The saturation current density is similar to that for Schottky barrier with an additional term

$$J_s = A^{**}T^2 \exp(-q\Phi_b/kT)\exp[-(q\Phi_T)^{\frac{1}{2}}\delta] \quad (2.38)$$

where $q\Phi_T$ in eV is the average barrier height presented by the insulating layer and δ in Å is the insulator thickness. An expression for V_{oc} can be written as[186];

$$V_{oc} = nkT/q[\ln(J_L/A^{**}T^2) + q\Phi_b/kT + (q\Phi_T)^{\frac{1}{2}}\delta] \quad (2.39)$$

An increase in V_{oc} is observed with insulator thickness 'δ', the short circuit current decreases, causing reduction in efficiency. As an optimum, a thin tunneling oxide layer is introduced. The beneficial role of the interfacial layer has been described in the literature[66-172] and include enhancement in open circuit voltage, and Φ_b, and reduced reverse saturation current.

2.4.2 Schottky Barrier Height Characterization Techniques

There are essentially four methods used to measure the barrier height of the metal-semiconductor junction: Current-voltage[173], capacitance-voltage[173], activation energy[173], and photoelectric method[174]. For $V >> kT/q$, the Schottky diode equation can be expressed as,

$$\ln(J) = \ln(J_s) + qV/nkT \quad (2.40)$$

Hence a plot of ln (J) as a function of V should result in a straight line having slope (q/nkT) and intercept ln (J_s).

$$\therefore \text{ slope} = dV/d(\ln J) = q/nkT$$

and,

$$\Phi_B = kT/q \ln(A^{**} T^2/J_s)$$

The value of Φ_B is not very sensitive to the choice of A^{**}. As an example, a 100% increase in A^{**} will cause an increase of about 0.018 eV in Φ_B. For uniformly doped substrates a plot of $1/C^2$ vs. V will yield a straight line with intercept V_i on the voltage axis. The barrier height can be determined from;

$$\Phi_{Bn} = V_i + V_n + kT/q - \Delta\Phi \qquad (2.41)$$

where V_n is the depth of the Fermi level below the conduction band, and $\Delta\Phi$ is the Schottky barrier lowering. The disadvantage of the technique lies in the fact that the technique applies only for the uniformly doped substrates.

The activation energy technique requires no knowledge of the diode area, but certainly requires that measurement be made at several temperatures. Hence measurements are performed on a suitable temperature controlled test apparatus at several temperatures. The diode current at a forward bias can be written as;

$$\ln(I/T^2) = \ln(A\, A^{**}) - q/kT(V_{bi} - V_f/n) \qquad (2.42)$$

where the subscript f has been attached to the forward voltage to emphasize that it remains fixed in this measurement (such that $V_f >> 3kT/q$). A plot of the quantity I/T^2 as a function of 1/T then gives a straight line having slope = $q/kT\ (V_{bi} - V_f/n)$. The quantity $q(V_{bi} - V_f/n)$ is the activation energy. This is unfortunately one equation in two unknowns (V_{bi} and n). If n is determined, however by an alternate technique, V_{bi} can accurately be determined.

The photoelectric measurement is an accurate and direct method for Schottky barrier height determination. When monochromatic light is incident upon a metal surface, the light can generate excited electrons in the metal if $h\nu > \Phi_b$, and also in the semiconductor if $h\nu > E_g$. The photocurrent per absorbed photon, η, as a function of the photon energy,

$h\nu$, is represented by Fowler's theory, which under an appropriate set of conditions reduces to;

$$\eta \approx (h\nu - h\nu_0)^2 \quad \text{for, } h(\nu - \nu_0) > 3kT, \quad \text{or}$$

$$\sqrt{\eta} \approx h(\nu - \nu_0)$$

Hence if the square root of the photoresponse is plotted as a function of the photon energy, a straight line should be obtained, and the extrapolated value on the energy axis should give directly the barrier height.

— ¤ —

Chapter 3

GaAs Sample Preparation and Characterization Techniques

Photonic devices operate in either photovoltaic, photoconductive, or luminescence mode. The present investigation is aimed at the former two categories and hence the sample preparation involved design of front contact grid in both type of devices, allowing the incident radiation to interact with the semiconductor. The grid pattern layout and process development was selected primarily to study the effects of ion induced damage in GaAs. Similar considerations are, in principle, true of most other types of semiconductor materials and photonic devices. A series of tests were developed and an automated photovoltaic materials and devices (PVMD) system was designed, as a part of this investigation. The photonic devices were subjected to a series of both conventional and non-conventional tests. This chapter deals with the design consideration, and fabrication procedure specifically developed to prepare the samples. The characterization procedures developed during the course of the investigation are presented. Basic evaluation experimental setup and merits of the techniques are also discussed.

3.1 Sample Preparation

Two structures, viz. photovoltaic, and photoconductive were considered. In both the cases carriers generated due to photoionization in the front surface region contribute to the current flow in the external circuit. The photonic structures are versatile for the present investigation because the electrical traps and structural damage induced by the ion beam are in close proximity to the surface and hence can readily be detected. For the photoconductivity measurements a standard, four equally spaced conductor probe type pattern was designed. The photodiodes, however, require front and back contacts to provide current in the external circuit. While the back ohmic contact may be a thick and

uniform ohmic conductor layer, the front contact layer in the Schottky diodes has a dual purpose to serve. It should be fairly conducting and must simultaneously be transparent to the visible spectrum. A second grid is usually placed over the thin transparent conductor to collect carriers from the thin Schottky metal layer. The lateral series resistance of the second metal layer should be negligible and must cover only a small fraction of the active area. Such conflicting requirements are usually satisfied through the use of a grid of narrow conductors spread across the surface having a bond pad to establish contact with the external circuit. The masks layout are shown schematically in Figure 3.1. The masks were designed and artwork drawn using computer-aided design (CAD) instrumentation and AutoCAD™ software. To achieve sharp and precise edge definition, the metal masks were prepared using photoreduction and chemical etching of a 3 mil. stainless steel #304 shim. [A list of procedures developed for sample preparation, chemical etching, oxidation procedures, photolithography artwork exposure and developing, etc. are provided in Appendix A].

3.1.1 Gap Cell Configuration Conductivity Sample Preparation

For conductivity measurements, undoped SI GaAs wafers were procured from Morgan Semiconductors. All wafers were liquid-encapsulated Czochralsky (LEC) grown, having (100) crystal orientation, cut 2° off (110). The electron mobility of these wafers was on the order of 7500 cm^2/V-Sec. The wafers were scribed and diced into 8 m.m. x 8 m.m. platelets and marked for crystal orientation. Due to surface sensitive nature of the inspection devices a great deal of caution was exercised to produce atomically clean, continuous, and isotropic surfaces. Samples were thoroughly degreased in organic solvents (see Appendix A) and chemically etched in a H_2SO_4(conc.):H_2O_2(30%):H_2O 8:1:1 (by vol.) solution, a diffusion-limited reaction containing a high concentration of the oxidizing agent. For a diffusion-limited solution the etching rate depends upon the mechanical agitation induced turbulence and is independent of the orientation [175]. This procedure etched approximately 1.2 μm/min. [176]. A standard five minute etch, at a mechanical

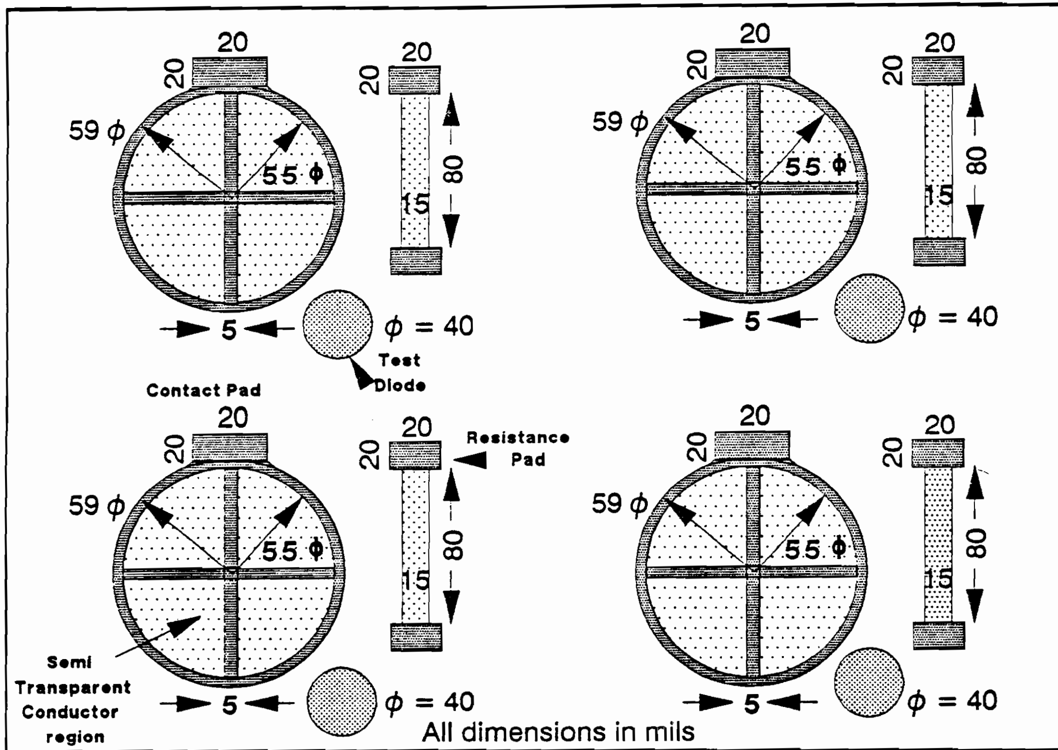

(a)

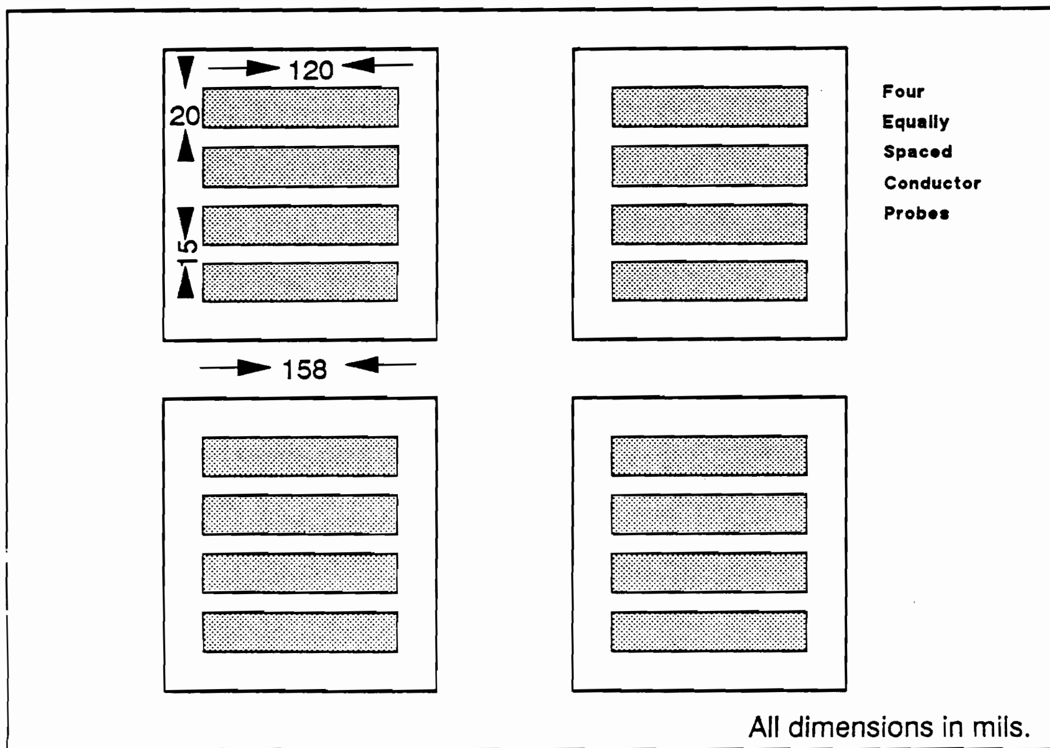

(b)

Figure 3.1 Grid-pattern layout for (a) Schottky photodiode and (b) Four equally spaced conductivity probes.

rotation (≈ 22 rpm), ensured removal of lattice damage arising from the mechanical grinding, lapping and polishing operation. The wafers had a mirror-like appearance after the chemical etch. The wafers were rinsed in warm deionized (DI) water (10 MΩ resistivity), in between inorganic cleaning and etch procedures. The samples were then placed in warm (45° C) HCl(conc.):H_2O) 1:1 (by vol.) solution to etch the unstable oxides (Ga_2O_3, As_2O_3, etc.) present on the surface, followed by DI water rinse. The wafers were dried using dry, pre-purified nitrogen jet stream. Four Au-Ge (88:12) [Eutectic preforms, procured from Materials Research Corporation], stripe contacts, approximately 2200 Å thick were then evaporated in a Denton Vacuum Inc. evaporator, model #503 onto each sample, followed by a nickel evaporation, without exposing the samples to the atmosphere in between two evaporations. The vacuum prior to evaporation was better than $1x10^{-6}$ torr. The liquid nitrogen cold trap prevents emission of hydrocarbon into the chamber. The thickness of the deposited materials were monitored by a Varian quartz crystal thickness monitor, model Kronos # QM-311 (by setting appropriate materials parameters) and controlled by a shutter operated via an angular motion rotary feed-through. Ohmic contacts were obtained by furnace annealing the samples for two minutes at 440°C in forming gas (90% N_2, 10% :H_2) ambient in a quartz tube. A single zone Lindberg furnace was employed for annealing purposes, with the temperature being controlled by an Omega temperature controller. The gas flow was regulated using rotameters from Matheson.

Ion bombardment: This was carried out in a Perkin Elmer model 5300 XPS system equipped with a model 04-300 differentially pumped ion gun, mounted at 45° with respect to a line perpendicular to the specimen surface. The samples were then cleaned with HCl(Conc.):H_2O solution (1:1 by vol.) at room temperature for 10 minutes to remove surface oxide and were loaded into the main chamber, through a load-lock chamber. After proper centering of the specimen by x-y micromanipulator and angle adjustment to reduce the channeling, the samples were bombarded with Ar^+ ions. Ar^+ ion bombardment was carried out at 1 KeV, 3 KeV, and 4 KeV energies using a 1 cm^2 raster

beam with ion-current in the range of 0.2 - 40.0 μA (measured using a Keithley 610A Electrometer). The time of ion bombardment was adjusted to give fluences of 10^{16} ions/cm^2. Specimen surfaces were oriented such that ion bombardment was in the (111) direction. The base pressure, before ion-bombardment was 3x10^{-6} Pa. or less. Chamber pressure during ion bombardment was generally about 1x10^{-5} Pa.

Ar^+ ion bombarded samples were then mounted onto a Kovar, TO-8 IC header with Si-based thermally conducting and electrically insulating epoxy from Omega Engineering. To ensure absolute insulation, an alumina pallet, cut into 8 m.m. x 8 m.m. size was inserted between the sample and IC header. Electrical contacts were established using 3 mil. thick gold whisker leads bonded with silver epoxy #H20E from Epo-Tek, and furnace (Thermolyne) cured at 120° C, for 20 mins., under a forming gas ambient maintained in a quartz tube. Figure 3.2 shows schematically the dicing, scribing, ion-beam bombardment and whisker-lead bonding schemes.

3.1.2 Contact Formation Techniques:

For the pattern generation on the samples, two main approaches were followed: a) evaporation through a photoetched metal mask, and b) a lift-off process.

a) In the evaporation using photo-etched metal mask, the contact metal is deposited using resistive heating evaporation onto the sample which is in line-of-sight with the evaporation boat. The intercepting metal mask defines the pattern on the sample. The films needed for the Schottky photodiodes were on the order of 60 Å thick. A precise control over the thickness was desired and was monitored in-situ.

It is generally expected that the interaction between the surface of the condensed phase and the individual atoms about to evaporate depends upon the direction into which the particles will be emitted. Such emission is statistical in nature and is contingent upon assumption about the energy states of molecule at the instant of evaporation. Based upon standard assumptions, such as isothermal enclosure, infinitesimal small opening, Maxwellian speed distribution, etc., the number of particles within a small solid angle are

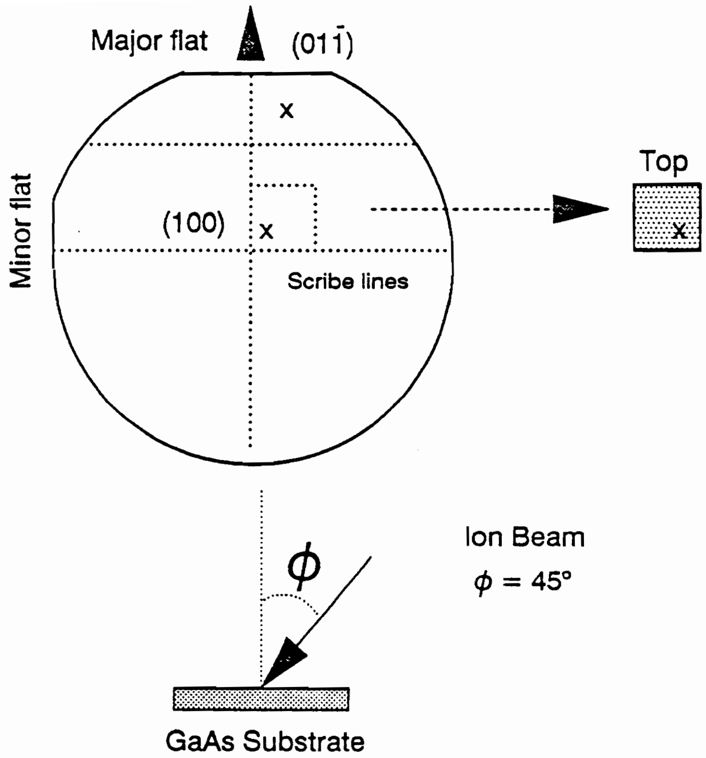

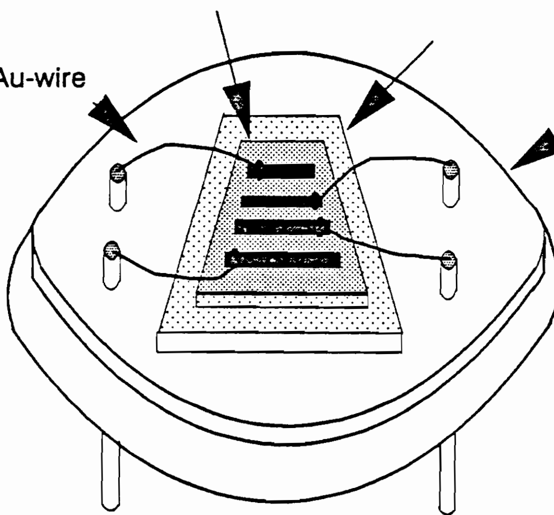

Figure 3.2 **Dicing, scribing, ion beam bombardment and whisker lead bonding of the devices .**

expressed by Cosine law of emission[177]. Hence based upon the cosine law of emission a special angular deposition jig was designed, where the angle of the impinging molecules can be changed easily, hence providing control over the thickness of the film, as shown in Figure 3.3. The film thickness was calibrated using a laser and a photodetector, knowing the absorption coefficient of the thin absorbing film at the wavelength (633 nm.) of the emission line of He-Ne laser.

b) For applications requiring exact evaluation of the device parameters, the pattern generation was realized employing a lift-off process [178]. For the development of small pattern geometries and processes yielding high dimensional accuracy, photoresist masking is commonly used. Some of the disadvantages related to the conventional photoresist masking are 'wing tips' and metal tear-off due to the bridging in between the photoresist and the metal, and are illustrated in the Figure 3.4(a). To avoid the 'wing tips' and metal tear-off, photoresist was purposely modified by the addition of the Monazoline® (a trade mark of Mona Industries, N. J.), which is basically a five cornered imidazole ring [179]. To develop the fine line pattern needed for the present work, lift-off or image reversal process was optimized by developing an appropriate procedure of exposure and development, as described in the Appendix A and is shown in Figure 3.4(b).

3.1.3 Oxidation of GaAs Samples:

The growth of a thin interfacial oxide layer has improved the open circuit voltage and efficiency by upto 60% in GaAs metal-semiconductor photovoltaic devices. It is also believed that deposition of metal layers on atomically clean surfaces alters the chemical state of the surfaces and hence a thin passivating, tunneling oxide layer helps improve the reproducibility in the Schottky barrier contact formation. In contrast with silicon whose native oxide, SiO_2, possesses extremely good bulk properties and near ideal interfacial characteristics, the native oxide of GaAs suffers from distinct limitations. The compound nature of the GaAs produces a different surface chemistry for each constituent, and the oxides have low decomposition temperature. Oxidation of GaAs has been the focus of

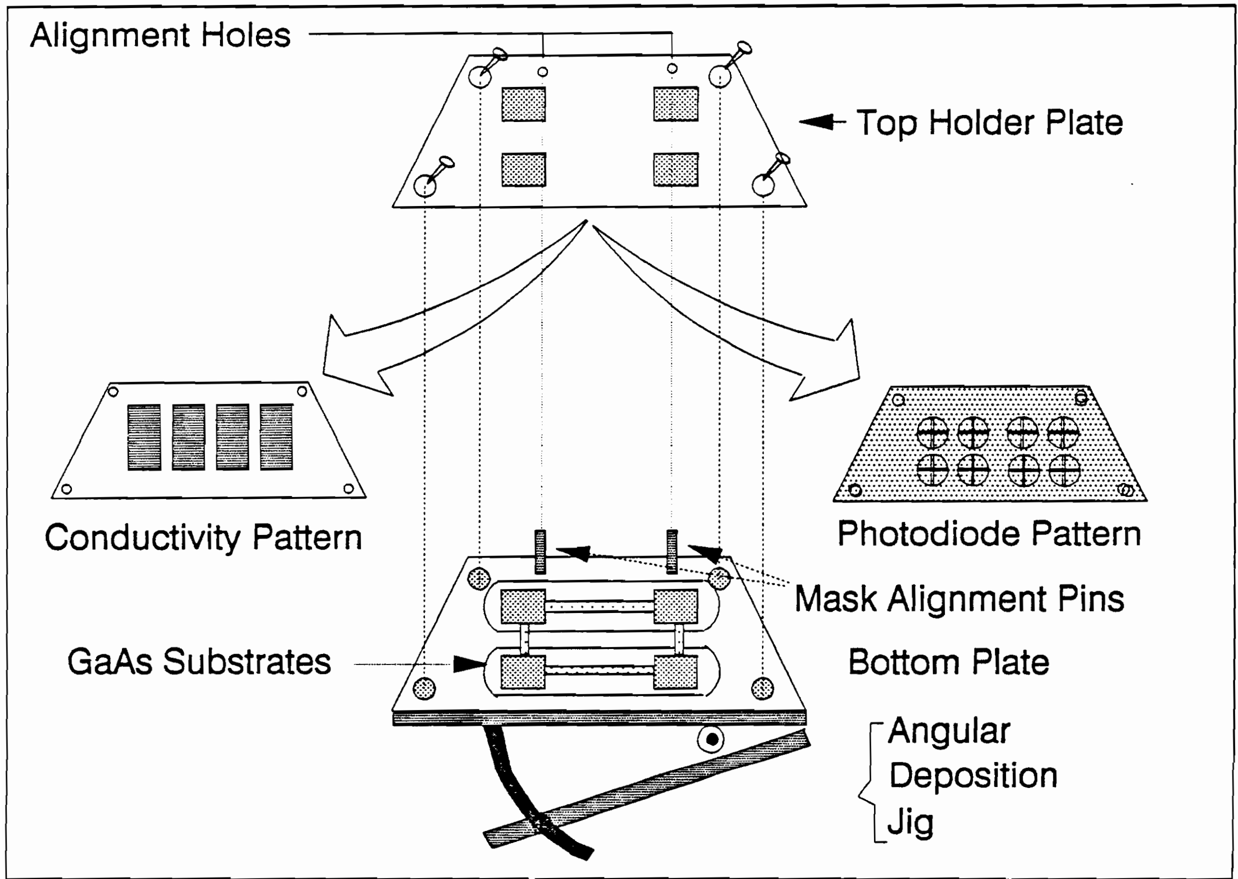

Figure 3.3 Angular evaporation mask arrangements used for contact formation.

- To have better area resolution and less shadow loss, it is necessary to avoid metal `wing tips'.

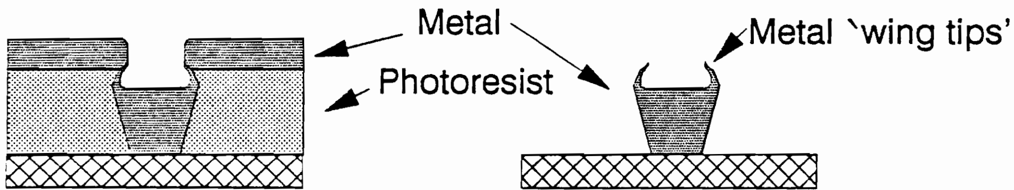

- Metal tear off can also occur with this type of photoresist profile when overlying metal films form a continuos sheet down one side of the window and up the other.

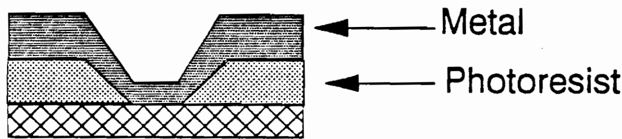

(a)

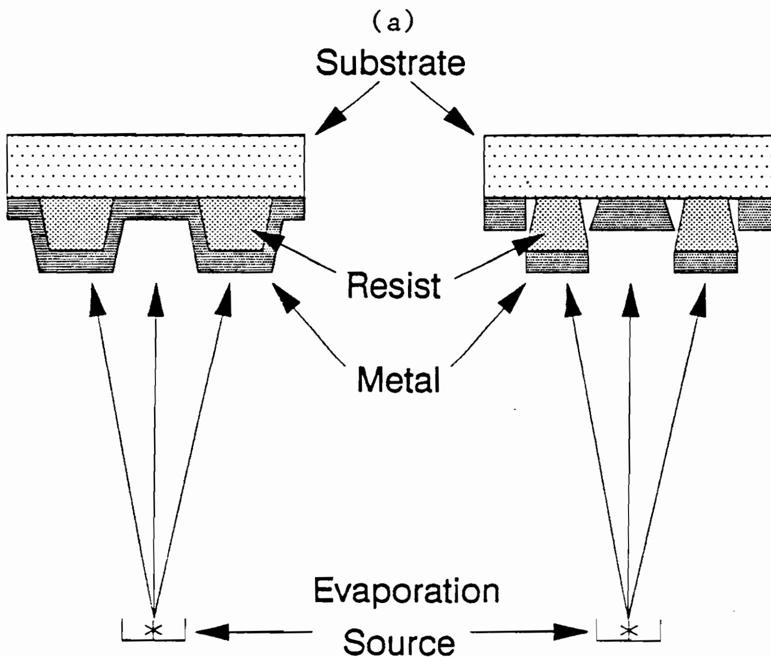

- In left-hand profile a continuos metal layer is formed The under cut in right-hand profile isolates the regions and hence the top metal can be lifted.

(b)

Figure 3.4 (a) Gridline formation problems. (b) Schematic of the lift-off process.

considerable attention for several years and most of these studies have dealt with the oxidation of the GaAs (110) surface [180-184]. To investigate the initial stages of oxidation, studies by many analytical techniques are used, including Auger Electron Spectroscopy (AES), X-ray Photoelectron Spectroscopy (XPS), Ultra-violet Photoelectron Spectroscopy (UPS), Low-energy electron diffraction (LEEDS), Electron energy loss spectroscopy (EELS), Reflection high energy electron diffraction (RHEED), High resolution electron energy loss spectroscopy (HREELS), Extended X-ray absorption fine structure (EXAFS), Thermal desorption spectroscopy (TDS), Ion scattering spectroscopy (ISS), and Secondary ion mass spectroscopy (SIMS), primarily to establish the mechanism responsible for adsorption, the chemical composition of the oxides formed, the local atomic structure of the oxides, and the relationship between the chemical composition and local atomic structure of the oxides. Most studies indicate that such oxides primarily consist of amorphous Ga_2O_3 and As_2O_3. The high vapor pressure of the column V elements mitigates against homogeneous growth.

Several approaches were followed to produce thin, controlled, reproducible layers of oxides of Ga and As, having Ga/As ratio of unity. It is well known that the chemically etched GaAs surface has a native oxide of approximately 18-20 Å thickness, and since only approximately 10 Å of additional oxide needs to be grown, the role of native oxide is not evident. It is for this reason that acid stripping of the initial native oxide layer was considered immediately prior to the oxidation. The oxidation procedures are described below.

a):Thermal Oxidation: Thin layers of oxides of GaAs were grown at room temperature by flowing water vapor saturated oxygen over freshly etched GaAs substrates placed in a quartz tube. Due to different chemical nature of the constituent atoms, the equilibrium thermodynamic products and rate-controlling processes cannot be accurately predicted. As slow as the process is, it takes approximately 60 hrs. to achieve a desired thickness, and it is still much faster than some of the room temperature thermal activation assisted oxidation

processes.

b):Anodic Oxidation: The growth of the anodic oxide of GaAs is quick and is relatively easy to accomplish. The anodic oxidation is carried out near room temperature, and the oxidation is field assisted. The process is modeled by field-aided diffusion, as compared to the energy barrier diffusion model for thermal oxidation. An acqueous electrolytic solution of 10 gm. of ammonium pentaborate, in a 100 ml. of ethylene glycol was prepared. With a constant voltage of approximately 15 V (GaAs as cathode) and an adjustable external series resistance, growth rate and time were adjusted to obtain a desired thickness.

c):Evaporation: Perhaps the simplest of all deposition procedures is thermal evaporation. Thin layers of antimony oxide were deposited; however lack of control of thickness prevented its further use.

More recently molecular beam epitaxy has been examined for dielectric preparation and offers an attractive option. More exotic processes include organo-metallic Chemical vapor deposition (MOCVD)[185], and Langmuir-Blodgett films[186] for deposition of thin dielectric films on III-V compounds.

Ellipsometry or polarimetric spectroscopy is the measurement of reflection of the state of polarization of light. Ellipsometry can easily be applied to the surface of films throughout the thickness range from partial monoatomic coverage upto a few microns and hence was applied to determine the refractive index and extinction coefficient of the ion beam bombarded samples. A Gaertner Scientific Corp. model #L116A-85F dual-mode ellipsometer, automated using HP-85 was used to monitor the thickness of the oxide layer on GaAs samples.

3.1.4 Schottky Diode Fabrication

The MIS Schottky barrier structure was chosen, as contrasted to the M/S Schottky barrier structures due to the following reasons.

a). To prevent inter-diffusion of metal into the semiconductor, which otherwise may alter the semiconductor surface.

b). To increase the barrier height due to the insulating layer.

The samples for the Schottky diodes and photodiodes consisted of two substrate categories. The first set of substrates were the LEC grown n-type (100) GaAs cut 2° off (110), with 2-3x10^{17}/cm^3 base doping, procured from Morgan Semiconductors. The other set of samples were prepared at Martin Marietta laboratories, by depositing a 2 micron thick n^--layer (5x10^{16}/cm^3) of GaAs by Molecular Beam Epitaxy (MBE), on n^+-type (2x10^{18}/cm^3) (100) GaAs, cut off 2° off (110), substrates. The MBE apparatus, a Perkin Elmer PHI-425B is equipped with 8 furnace zones and attains a vacuum base pressure of 10^{-11} torr, preventing cross-contamination in the subsequent layers. A representative dopant profile was measured at Martin Marietta laboratories, using a Bio-Rad Polaron model# PN 4200, an automatic electrochemical C-V dopant profiler and is shown in Figure 3.5.

Initial scribing, dicing and organic degreasing steps were common for both the categories. The LEC samples were subjected to a 5 min. chemical etch in a 8:1:1 (by vol.) H_2SO_4(conc.):H_2O_2(30%):H_2O with rotational mechanical agitation, followed by several warm/cold DI water rinses and nitrogen jet stream dry. Ohmic contacts were evaporated on the back surface of GaAs samples by blanket evaporation of 2200 Å of Au-Ge (88%-12%) eutectic preforms followed by 700 Å of Nickel, using the evaporation unit described before. The samples were then annealed at 440° C in forming gas ambient to form the ohmic contacts. After the ohmic anneal the samples were etched in 1:1:100 (by Vol.) H_2SO_4(conc.):H_2O_2(30%):H_2O reaction-limited solution, etching approximately 60 Å/min. of GaAs (for amorphous GaAs the rate was different $\approx$ 55 Å/min.). The samples were then thoroughly rinsed in warm/cold DI water baths. Prior to ion bombardment, the native oxide was acid stripped in 1:1 (by Vol.) HCl(Conc.):H_2O solution for about 10 min. followed by thorough rinse in DI water and nitrogen jet stream dry. The sample was mounted on a stainless steel probe and immediately transferred to the XPS chamber for ion bombardment. The ion bombardment conditions were identical to those described before.

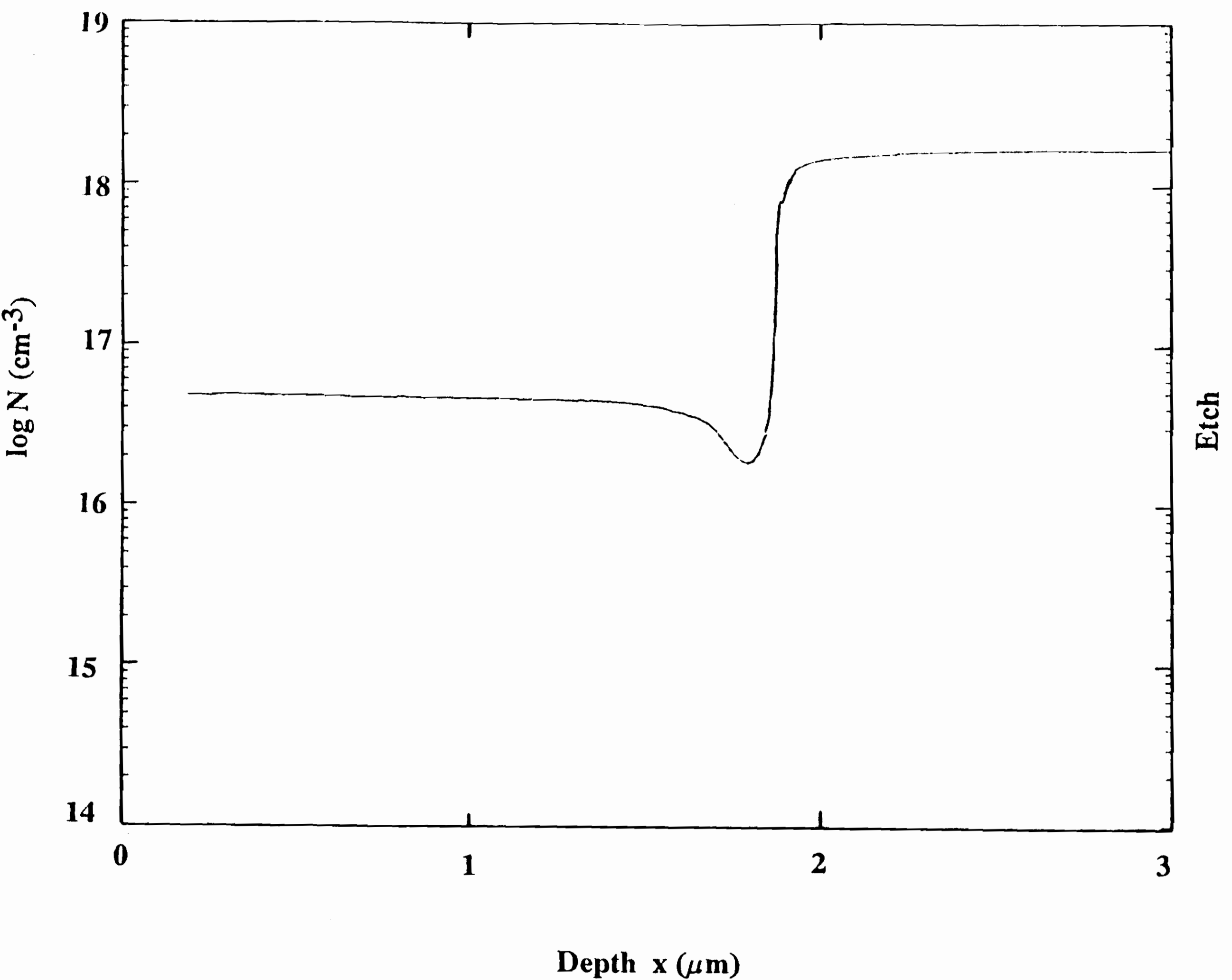

Figure 3.5 Carrier concentration vs. depth of a representative MBE grown sample.

The native oxide was once again etched as described above and then the samples were immediately transferred to an oxidation quartz tube furnace. The samples were then oxidized for 60 hrs. in water vapor saturated ambient maintained by bubbling ultra-pure oxygen at 200 sccm through the DI water heated to 45° C.

Thin (≈ 60 Å) Schottky metal (Gold) film was deposited on the oxidized sample, using the same evaporation system. For most of the photo-diode fabrication, evaporation through the metal mask was employed in conjunction with angular deposition jig. For diode fabrication, thick (≈ 2500 Å) Schottky metal (Aluminum or Gold) was deposited using a lift-off process. The edge definition was enhanced using a modified photo-resist using amidazole based chemical, as described before. A summary of the preparation steps used for sample preparation is provided in Table 3.1.

3.2 Automated Characterization System

Computerized data acquisition systems offer several useful features, among which are improved data organization standards, greater ability to process large quantities of data, better data analysis, and enhanced data presentation. A key component of the automated data acquisition is the software which controls and supervises accurately the flow of information between the digital world (host computer) and the analog world (external phenomena), acquires the data, performs analysis and presents information in a reduced and organized way. Figure 3.6(a) represents the process of domain conversion between the physical phenomena and the host computer via a transducer.

There is a growing need to characterize photonic devices employing computers due to complex and multiple controls in the characterization systems. Domain conversion is usually accomplished using a 12 bit Metra Byte, 16 channel A/D converter and 2 channel D/A converter, a 12 bit Analog Devices 4 channel D/A converter and a 12 bit Metra Byte IEEE-488 protocol data acquisition board. An IBM-PC/AT computer consisting of a 16 bit variable-size segmented memory 80286 CPU, 80287 math co-processor and with a 640K

Table 3.1 **Summary of device fabrication processes.**

Treatment	Technique	Parameters
1. Pretreatment:		
Scribe and Dice		
Organic Degrease		at 45° C
Inorganic clean		at 40° C
Oxide removal		at 40° C
Chemical Etch		8:1:1 (SHH)
2. Conductivity Samples:		
Front ohmic contact	Au-Ge/Ni(88:12)	$p = 1 \times 10^{-7}$ torr. t = 2400 Å/ 800 Å
Sinter	Furnace	at 450 ° C $N_2:H_2$ = (90:10)
Chemical etch		
Ion beam etch	Bombardment	Ar^+ ion $p = 4\text{-}5 \times 10^{-6}$ torr E = 1, 3 and 4 KeV
3. Schottky Diodes Fabrication:		
Back Ohmic contact	Au-Ge/Ni(88:12)	$p = 1 \times 10^{-7}$ torr t = 2400 Å / 800 Å
Sinter	Furnace	at 450 ° C $N_2:H_2$ = (90:10)
Chemical etch		
Ion beam etch	Bombardment	Ar^+ ion $p = 4\text{-}5 \times 10^{-6}$ torr E = 1, 3 and 4 KeV
Schottky metal deposition	Al, Au	$p = 1 \times 10^{-7}$ torr t = 60-65 Å
Pattern Generation	Lift-off	+ve photoresist Exposure = 6.5 sec Develop = 90 sec.

motherboard memory is used. The buffer interface between the device and the computer is designed and fabricated to protect the domain converters from application of inadvertent hazardous voltages, and is shown schematically in Figure 3.6(b).

3.2.1 Experimentation Philosophy

To dynamically characterize solid state devices in terms of functional and performance parameters, it is often critical to observe their response in real-time. Considerable attention has been dedicated to the development of various high-level languages for real-time data acquisition and process control applications. With the exception of Forth, most classical programming languages used for real time data acquisition applications are either extensions of languages devised for use on large computers, or are written in the assembler language of microprocessors. Most programming languages assume time-independent and synchronizable asynchronous processes running on a single processor, with the shared memory imposing severe real-time constraints. Recently developed Laboratory Information Management Systems (LIMS), with appropriate software to control the operation of the instrument and Data Base Management Systems (DBMS) to exchange well-indexed library data, provide a certain level of productivity. Data acquisition in such a divided attention environment, however, cannot support precision timing, as commands which could directly read or write from I/O channels are not allowed. The pre-emptive, priority-driven scheduling of recent multitasking operating systems permit real-time data acquisition, but only for the events which occur at precise intervals of time, hence extremely time-critical events cause appreciable interrupt latencies. Also, real-time data acquisition and analysis with instruments having either limited or no data storage capability is difficult, as it involves a complex interaction between highly time-dependent tasks on the same computer. Most laboratory-type stand alone data acquisition systems employing commercial software packages, often lag in observing real-time response because of excessive software overheads due to complex architecture of the measuring instrumentation and multiple task

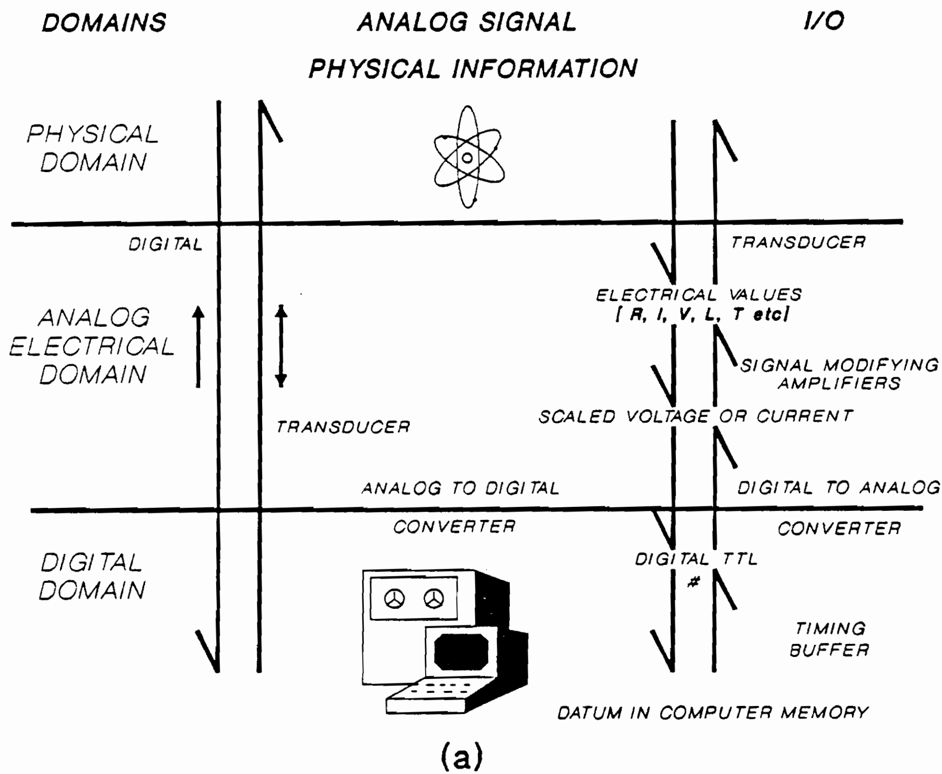

(a)

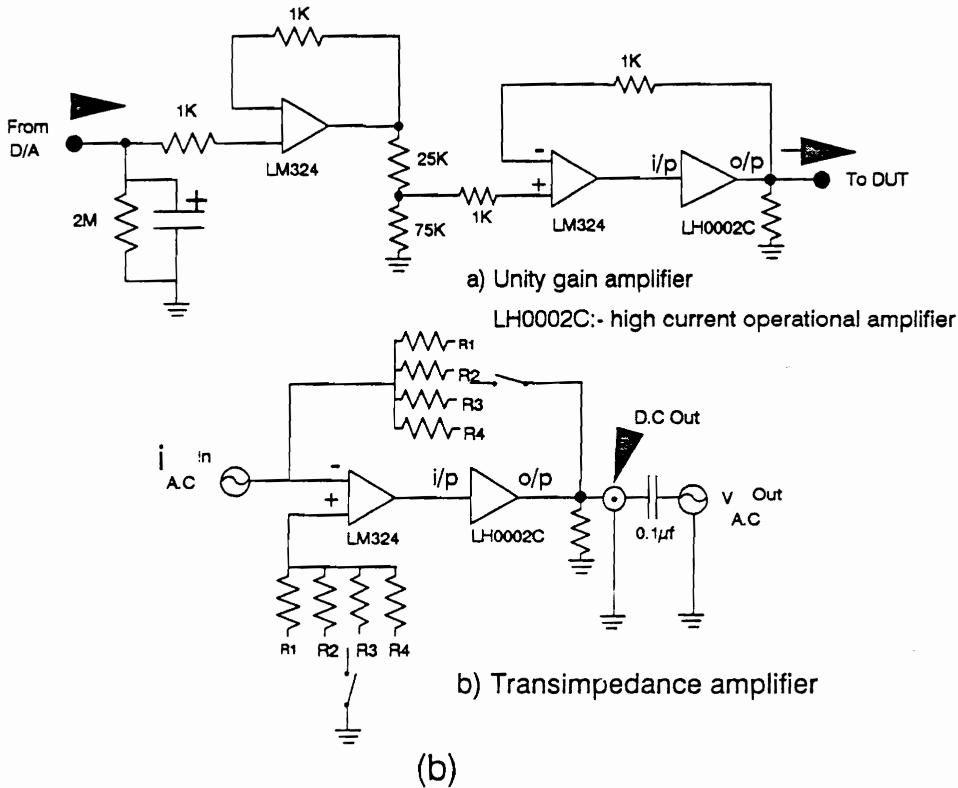

(b)

Figure 3.6 (a) Conceptual schematic representing the exchange of information between computer and external world via domain converters. (b) Schematic of unity gain and transimpedance amplifier used as buffer.

assignment. Asyst, written in Forth, is a programming software that is well suited for process control applications. It has certain unique features which are uncommon in most other conventional languages such as BASIC, FORTRAN and Pascal. Asyst has the eloquence of a high level language and still enjoys intimacy with the machine hardware helpful for time sensitive applications. Hence, the main emphasis was placed to perform data acquisition in real time.

Multi-vendor Data Acquisition boards

Both analog and digital instruments are utilized in the this characterization system. Asyst supports up to 8 data acquisition boards. At a given instant of time only one task can be performed, i.e. only one board is the controller. A finite time is involved in transferring control from one board to the another and depends upon both the hardware and the software. As the data-acquisition system becomes complex, the need to provide support for concurrency, synchronization and bidirectional information transfer become paramount, necessitating optimization of software overhead time. The latter can usually be minimized using predefined templates in compiled colon definitions. Since board drivers written in Asyst utilize assembly language, Asyst has the capability to run data acquisition and control tasks in the background mode within few tenths of microseconds of the foreground task. In such a foreground/background mode, the computer operates asynchronously, though in a time sequential manner in the foreground mode. The concurrent processing operates on the PC's clock, which intercepts the foreground activity at a specified interval of time to transfer its control to the background activity. Hence all time sensitive tasks can be performed in the background with minimal software overheads. Although direct memory access and block transfer modes can be used for fast data acquisition, multi-tasking is essentially used for its flexibility. The main disadvantage of the multi-tasking is its slow acquisition mode, as multi-tasking is driven by interrupts generated by the system controller's real time clock. At each interrupt stage, the foreground is temporarily halted, the pointer location is stored and after the interrupt is serviced, the pointer returns back to

where it left the operation to continue with the foreground activity. Such a transfer of control consumes considerable valuable time and results in lower data throughput. Applications needing higher conversion rates may not use multi-tasking effectively because as background task assignments increases, software spends more and more time servicing interrupts and less and less time in execution of the foreground operation, which can lead to loss of the concurrent environment.

3.2.2 Software Selection Criterion

Attributes of a "Good" Laboratory Automation Software

A "good" laboratory automation language should have some desirable semantic and syntactic features. Syntactically the language should have provision for piecewise constructs such as procedures, monitors, functions, etc. Such abstractions provide greater control over the complexity of the system. Desirable semantic features of the laboratory languages are mentioned extensively in the literature[187-190]. Some of the features worth mentioning are multitasking, exception handling, portability, modularity, structured programming such as conception and coding of modules from top down, etc. Good user/user communication is not really measurable, however can be related to simplicity, good documentation and popularity. Support for concurrency is considered important for most languages, as real-time software must efficiently deal with devices and externally generated events under rigid time constraints.

Forth provides most of the logical constructs of a modern structured programming language and is stack-oriented which is useful in debugging the source codes. The 'last in first out'(LIFO) stack is used for passing parameters to predefined words. Forth uses post-fix notation which is more efficient for linking words together without call statements. It also provides for scalars (value) parameters, such as data type constants and variables (location) parameters, which can be initialized at the time of declaration. It is possible to define new words which, when put together, can help create words having new defining actions. Forth has an assembly language capability such that it can handle most

time-sensitive control functions directly. Compiled definitions are time efficient, as they are memory resident, and no disk access latencies are involved. Compiled source code are just string of addresses and execution consists of passing control successively to each address in turn by the threaded code interpreter. Provision also exits for incorporating assembly level codes, providing an intimate control of the computer hardware. Any memory location can easily be accessed and manipulated. Forth is portable, modular and is a real-time multi-tasking language, having all the attributes of a "good" laboratory language, and is implemented as a threaded code interpreter. The compiled program is just string of addresses, each pointing towards at the lower level. A real-time multitasking language, Polyforth II developed by Forth Inc., is widely used in distributed process control.

Software Performance And Speed Comparison

A speed comparison of some I/O operations was performed to get estimate of the rate of data acquistion. The program logic, Figure 3.7(a, b) is organized such that data is accessed in an array and data manipulation, e.g. computation or box-car averaging, is done at a later time, unless instrumentation warrants concurrent control based on the previous data. It is, however extremely difficult to compare the speed of several software fairly by writing standard benchmarks, because this is not the only criterion by which a language or a compiler is evaluated[191]. Several functional dependencies must be taken into consideration prior to comparing languages on a one-to-one basis. For example;

- File parsing: Programming languages such as BASIC, Pascal, FORTRAN and C include an algebraic expression parser such that expressions were written in the infix notation, whereas languages such as LISP and Prolog employ a prefix algebraic expression parser. The syntax in which most computers operate is postfix. Forth employs a postfix algebraic expression parser which conserves time required in parsing an expression to infix or prefix to postfix notation.

- Compilers/Interpreters/linkers: In the interpreted form an executable machine code module is not created directly from the source code and hence at execution time each

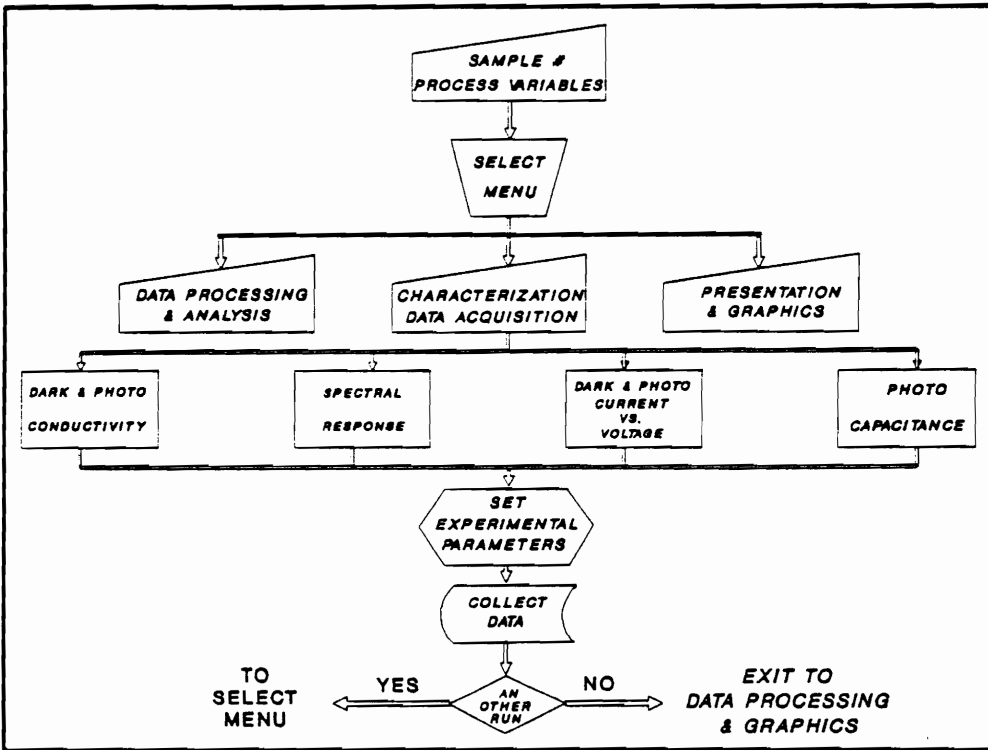

(a)

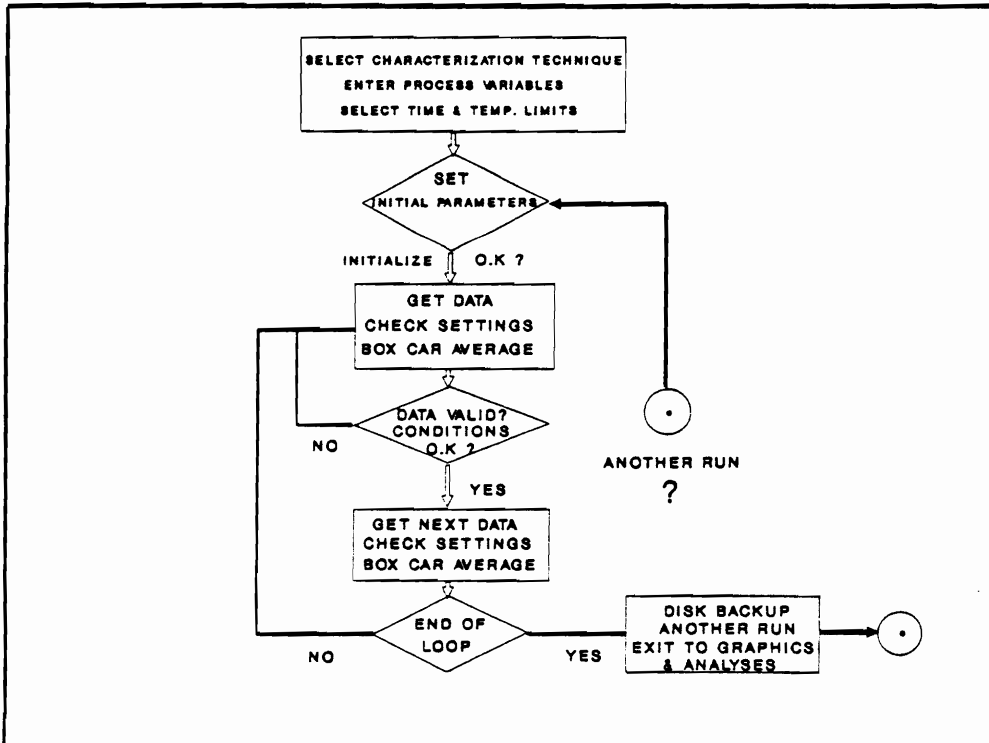

(b)

Figure 3.7 (a) Flow chart of software strategy. (b) Flow chart of a representative program.

program statement is interpreted in a way that leads to an executable set of machine instructions, leading to very slow execution speeds. In compiled form the entire executable module of machine instructions forms the user's source code thus reducing execution time manifolds. Factors such as availability of dynamic storage allocation and pointer variable also effect the speed.

Two popular benchmarks for evaluating speed are to observe the computing time to run the sieve of Eratosthenes, and the prime number generators. Most compilers are optimized for pure mathematical computations, hence for laboratory automation and data acquisition purposes, some meaningful tests may comprise string handling, file I/O, etc. Specific to this study, experiments to evaluate the time to acquire data in various modes, and the time involved in switching control from one board to the other, are useful. Synchronization of the task initialization time is crucial in all the tests. Table 3.2 lists some benchmark test comparisons between languages Quickbasic Rev. 3.0, Asyst Rev. 2.1 and C. All the tests were performed on a standard IBM-PC/AT with IBM DOS Rev.(3.3). For each test the RAM was initialized. All memory resident programs were temporarily deleted, as many TSRs intercept the timer, causing delays. All the benchmark programs were stored and initialized from the hard disk drive to minimize large mechanical and DOS related floppy disk access latencies. The hard disk organization was optimized to reduce any delay because of fragmentation. A normal timer function was used in all the benchmarks. The tests for an IEEE board were performed on X7R-type capacitors using an HP 4192A low-frequency impedance analyzer. Initialization procedures, such as self-test and lead compensation, were performed prior to all individual speed evaluation tests. For A/D boards a slowly varying (≈50-100 Hz) sinusoidal voltage was fed to one of the channels of the DASH-16 distribution board. It is observed that using Asyst in a multi-vendor board environment (specific to this set-up) a 100 point (@ 10 data point box-car average each) experiments can be performed in about 17.7 seconds as compared to the 214.06 second in Quickbasic. Time can further be adjusted by reducing resolution in

Table 3.2: Banchmark test comparisons for quick-basic, C, and Asyst softwares

Test performed	Quickbasic	C	Asyst
Read 10 data points from A/D board	0.0600589	† 0.00767700[3]	0.00282707[1] 0.10036800[2]
Read 10 data points from IEEE board	1.8125314	≳ 1.59	0.16597340
Read 10 data points from A/D, switch to IEEE and read 10 data points	2.140625	†	0.17765900[3]
Read an array with 2000 data points, multiply with a single precision number and assign to another array	0.667	0.981	0.25479

1. Buffered mode
2. Multitask mode
3. Concurrent mode

† Drivers programming beyond the scope of this thesis.
* Time in seconds.

terms of less data points or a narrower window interval in the box-car average routine, to ensure real-time response of the device.

Asyst was a useful choice of software for laboratory data acquisition and device analysis. By creating an integrated environment of Forth in a multitasking mode , faster execution times for the time sensitive experiments were achieved. As Asyst software supports multi-vendor data acquisition boards accepting different protocols, it was possible to conduct experiments involving a variety of instrumentation. The ability to define new words due to threaded-code interpretation resulted in several common procedures which interactively can be utilized in any typical data acquisition program. The user defined compiled colon definitions stay memory resident and can be recalled instantly.

The drawbacks of Asyst were, e.g. the postfix notation was initially difficult to adapt to, Lack of a GOTO... statement to transfer control (typically, such transfer of control is useful in handling error conditions and creating jump situations), minimal error-checking and negligible computer security procedures, etc. Also, most of the new colon definitions, or words, stay memory resident, even after redefining. This not only may cause stack overflow but programming got tricky at times, especially while manipulating the pointer in memory locations. Editing small test programs was a minor inconvenience, in that, while defining new colon definitions, if by accident a wrong command is entered, the whole program had to be rewritten. The discussion above is device and computer specific and hence may operate only under identical conditions. As a final note, the role of consistency verification by ancillary and independent measurements cannot be overemphasized.

The system discussed below contains source codes, developed and used successfully to characterize several types of photovoltaic materials and devices, including;

(1) Current-voltage measurements as a function of intensity, spectral content and temperature;

(2) Spectral response as a function of light bias and voltage, and

(3) Dark and photoconductivity of semi-insulating and doped materials.

By comparison with the other softwares, Asyst provides fast and accurate access to the data and is employed in the characterization facility to evaluate devices and materials.

3.2.3 Photovoltaic Materials and Devices Measurement System

The photovoltaic system consists of a GE Gemini 300 Arc lamp, powered by a highly stabilized D.C. GE, model #9768Y4070 power supply, which simulates the solar spectrum and is calibrated at 100 mW/cm^2 (air mass 1, or AM1) using a Solarex standard cell. To determine the exact color temperature on the Gemini Lamp, chromaticity test were performed using a Minolta, Model # CS-100, Colorimeter. White light from the lamp is allowed to impinge upon a white non-fluorescent sheet and using the colorimeter, the color coordinates are recorded as a function of illuminance in nits. The color temperature of the Gemini 300 lamp is then computed using CIE 1931 (x,y)-Chromaticity diagram showing isotemperature lines, on the mired scale [192]. Spectrum locustrac yields spectral irradiance or spectral power distribution. This simulated spectrum is incident on a device and the response is recorded as a function of sweeping voltage generated by the D/A converter. Current is observed using a 617 Keithley programmable electrometer. A total of 50 data points (each point box-car averaged 5 times) is acquired for a typical run in approximately 10 seconds. No significant deviation from the pre-set operating conditions was observed during the data acquisition time, ensuring quasi-steady state response. Data points are then computed to yield device parameters, such as maximum open circuit voltage, short circuit current, fill factor, power conversion efficiency, series and shunt resistance.

Spectral response measurements are performed either under D.C. conditions or at very low frequencies, such as 7 or 13 Hz (eliminating any component of the line frequency or its subharmonics). Monochromatic excitation was obtained from the combinations of the Gemini 300 Arc lamp, by a Jarrell Ash half meter Ebert monochromator (with 1200 grooves/mm grating blazed at 250 nm.) model # Monospec 50 with compumotor, model # 2100 series indexer for precise positioning of the grating, and with the appropriate filters.

The monochromator is flooded with dry nitrogen gas to eliminate the H_2O - related fine structure appearing in the excitation spectrum. To eliminate the EMI noise due to extraneous signal pick up by long leads, a Princeton Applied Research, lock-in amplifier model #124A is preceded by a notch-filter. The frequency of the lock-in amplifier and intercepting Stanford Research System optical chopper, model # SR450 are monitored using an HP Dynamic Signal Analyzer, model # 3561A, having resolution of 2 mHz in a span of 2 Hz. It is used to detect the noise spectrum. Signal brushing is accomplished using analog filtering (a low pass or line notch filter) in the input circuit of a phase sensitive (synchronous rectification) detector, providing an input component that is coherent with the reference frequency as a D.C. signal at the output. Spectral response measurement involves constant interaction of the experimenter, and hence the source code is written in an interrupt-driven mode. Also, due to large mechanical latencies caused by ramping and deramping the monochromator motor, a precise data acquisition time cannot be predicted. By creating a synchronized foreground/background environment, a significant reduction in data-acquisition time is achieved. A possible source of error in such an experiment was fluctuation in the lamp intensity. Capacitance of the devices is measured using a Schlumberger impedance gain/phase analyzer Solatron model# 1260, as a function of white light and voltage bias and frequency. An average data acquisition run takes approximately 3.5 seconds for 20 data points.

Basic transport characteristics include measurements of steady state and transient conductivity. Electromagnetic Interference (EMI) was reduced by using the minimum transmission distance, and shielded and low-noise coaxial and triaxial cables in a balanced input configuration mode. The input signal, being very small, was prone to adventitious noise. Small signal measurements are performed in a floating potential mode. The device is mounted on the cold finger of a shielded, variable temperature, optical cryostat having high thermal inertia, and evacuated to prevent moisture condensation and to eliminate any air-borne shunting path. Temperature of the specimen holder is measured using a platinum

resistance detector (RTD) because of its exceptional stability and fast response time. The variation in temperature is measured as variation in voltage and data fit into a resistance temperature transfer function defined by the Callendar-Van-Dusen equation. To measure dark conductivity, the sample is initially cooled down to liquid nitrogen temperature, and is then heated gradually. At specific and small intervals of temperature, voltage is measured using a Keithley 617 programmable electrometer having input-impedance on the order of $10^{14}\ \Omega$. For a temperature excursion of approximately 350°, 300 data points are taken in an average of 90 minutes. Photoconductivity is measured as a function of temperature and photon energy. In all the experiments, the data points are stored in respective arrays and at the end of data acquisition run, mathematical computations were performed to infer the specific information. Figure 3.8 (a) shows a schematic of the hardware layout of the characterization system and Figure 3.8 (b) shows the low thermal inertia cryostat designed for the measurements.

3.3 Characterization Techniques

The primary objective of the characterization of the ion bombarded samples was to determine the nature and extent of the damage, introduced by the energetic Ar^+ ions. Electrical, electro-optical, and chemical analysis characterization techniques were employed for the present investigation. In the following sections, the essential features of the characterization techniques and the procedures to interpret the results are presented.

3.3.1 Dark and Light Current-Voltage (J-V) Characteristics

From basic p-n junction theory, the dark current-voltage characteristics for a diode is represented by,

$$J = J_{o1}\ [\exp(qV/AkT) - 1] \qquad (3.1)$$

where J_{o1} is the dark reverse saturation current density which results primarily from the generation and recombination in the depletion layer, q is the electronic charge, V the

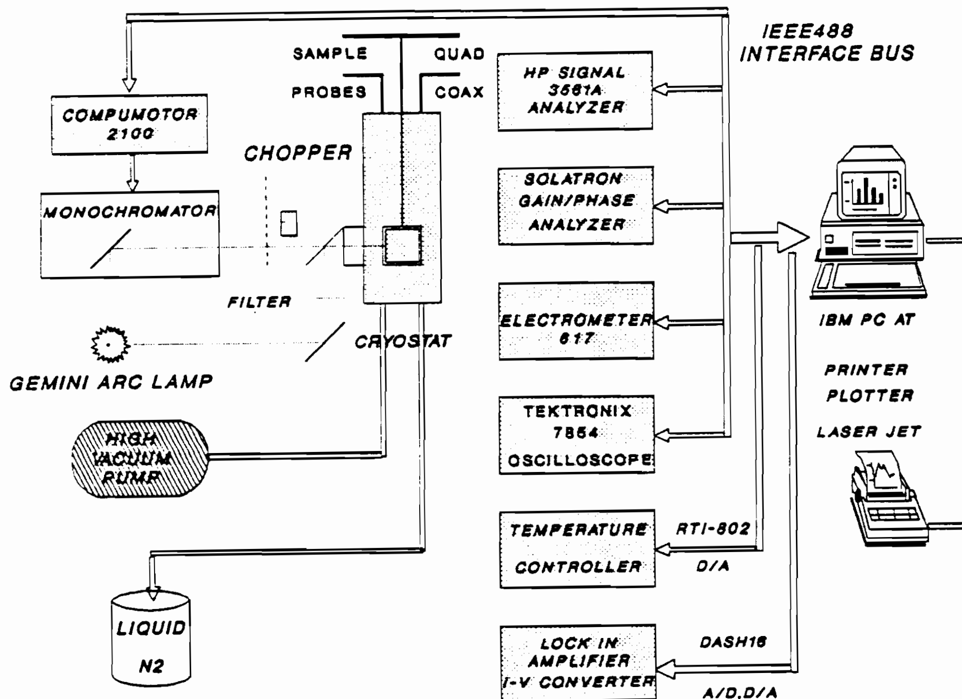

(a)

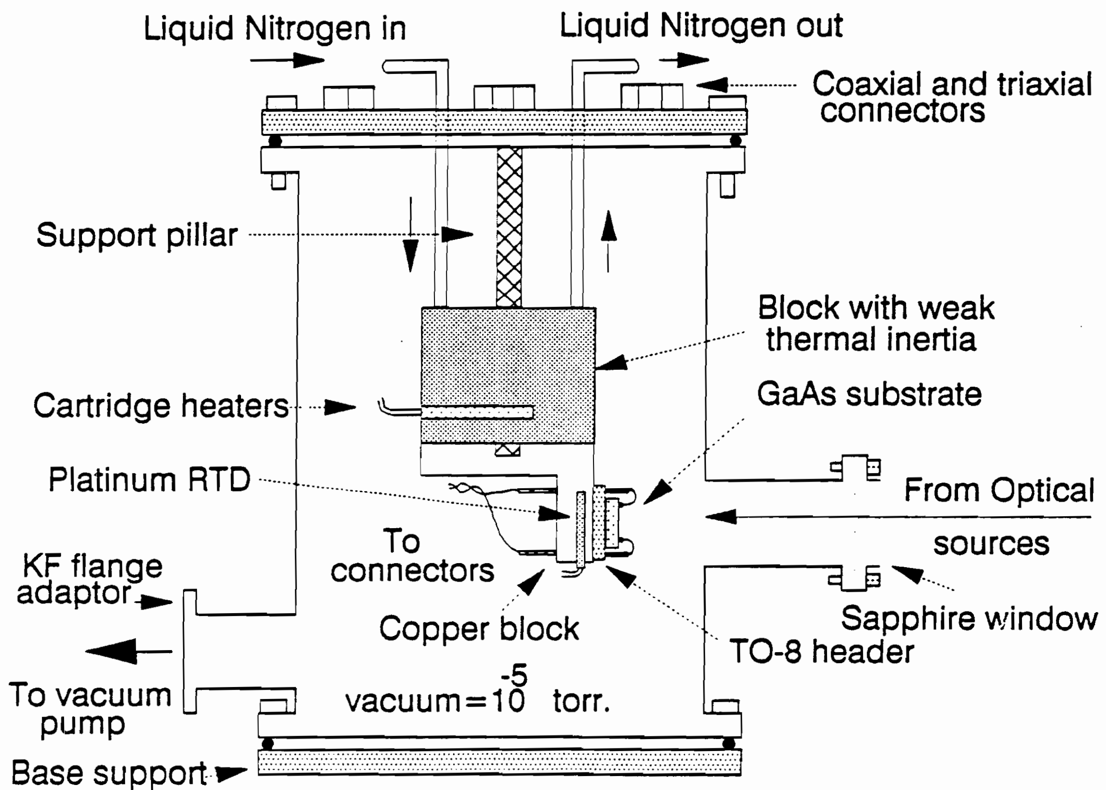

(b)

Figure 3.8 (a) Schematic of the hardware layout of the Characterization System. (b) Schematic of the low thermal inertia cryostat designed for measurements.

voltage, A is the diode ideality factor, typically > 1.0, k is the Boltzamann constant and T is the temperature. Hence, parameters such as ideality factor, reverse saturation current, barrier height etc. are evaluated from the basic dark diode characteristics.

The photovoltaic response is measured by placing the device under AM1.5 simulated illumination by a GE Gemini 300 arc lamp and tracing the I-V plot. The intersection of the curve with voltage and current axis yield V_{oc} and I_{sc}, respectively. The power conversion efficiency is computed at the maximum power point (V_m , I_m) from the illuminated I-V curve as, $\eta = (V_m * I_m) / P_{in}$ where P_{in} is the incident optical power. The series and shunt resistances are computed by calculating slopes near the V_{oc} and I_{sc} points respectively.

3.3.2 Spectral Response

Solar cell spectral response is a powerful tool for the characterization of photovoltaic devices, yielding information such as quantum efficiency, internal photoelectric emission [164], collection length[162], minority carrier diffusion length[156], spectrum selectivity and layer-by-layer response of a completed device. Trap saturation in top disordered surface layers, provides mobility information. Quantum efficiency is defined as the number of photogenerated electrons passing through an external load per incident photon.
Mathematically, it is expressed as

$$QE(\lambda) = \frac{I(\lambda)}{q \text{ x number of incident photons}(\lambda)} \qquad (3.2)$$

Typically, solar cells are operated in the short circuit current mode to measure spectral response . The short circuit current density is represented as

J_L = q {(no. of incident photons $E > E_g$) x (probability of transmission into the device) x (probability of absorption by the cell) x (collection probability)}

$$J_L = qF(\lambda)(1 - R)(1 - e^{-\alpha l})\eta_{co} \qquad (3.3)$$

where, $F(\lambda)$ is the number of incident photons with $E > E_g$, R and α are reflection and absorption coefficients respectively and η_{co} represents the collection efficiency. The total short circuit current can be calculated by adding contributions from the three regions of the cell and integrating over the available spectrum. The continuity equations for low level injection can be solved with appropriate assumptions and boundary conditions to provide the expressions for the contribution from emitter and base regions, $J_n(\lambda)$ and $J_p(\lambda)$ respectively. Expressions for the current contributions have been calculated and are reported with and without the back surface field [161].

To find the depletion region contribution, one can assume that lifetime is long compared to the carrier transit time and that all of the carriers created in depletion region are collected. Then

$$J_{dep} = qF(\lambda)(1-R)\exp(-\alpha x_j)[1-\exp(-\alpha w)] \quad (3.4)$$

for a given wavelength. Since w is usually small, J_{dep} is sometimes neglected. The quantum efficiency can be calculated as follows

$$SR(\lambda) = \left[\frac{J_p(\lambda) + J_n(\lambda) + J_{dep}(\lambda)}{qF(\lambda)[1-R(\lambda)]}\right] \quad (3.5)$$

(The subscripts n and p refer to the parameters relative to the electrons and holes, respectively). Hence, by measuring the solar cell short circuit current as a function of wavelength reveals a wealth of information about the device. Spectral response beyond the intrinsic absorption region is used to determine the internal photo-emission barrier height by extrapolating a plot of the square root of normalized response vs. photon energy. Mid-gap defect electrons can be excited from the localized defect site to the conduction band using sub-band gap photons, and can be observed by the exponential photo-current response as a function of photon energy. A schematic of the hardware layout of the spectral

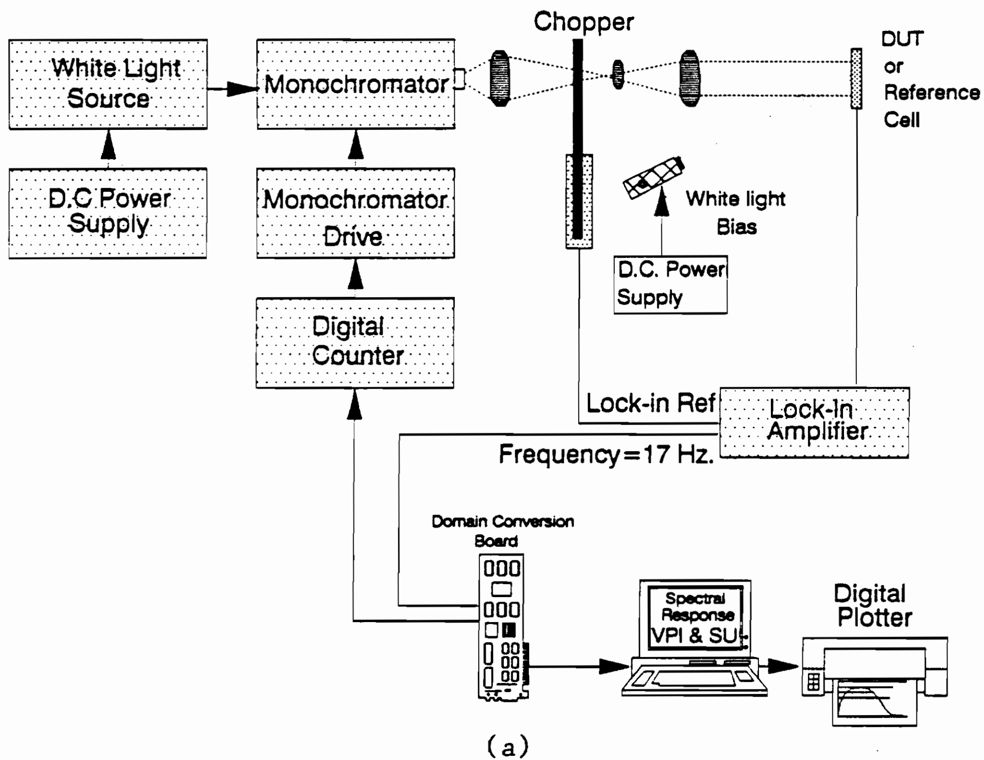

(a)

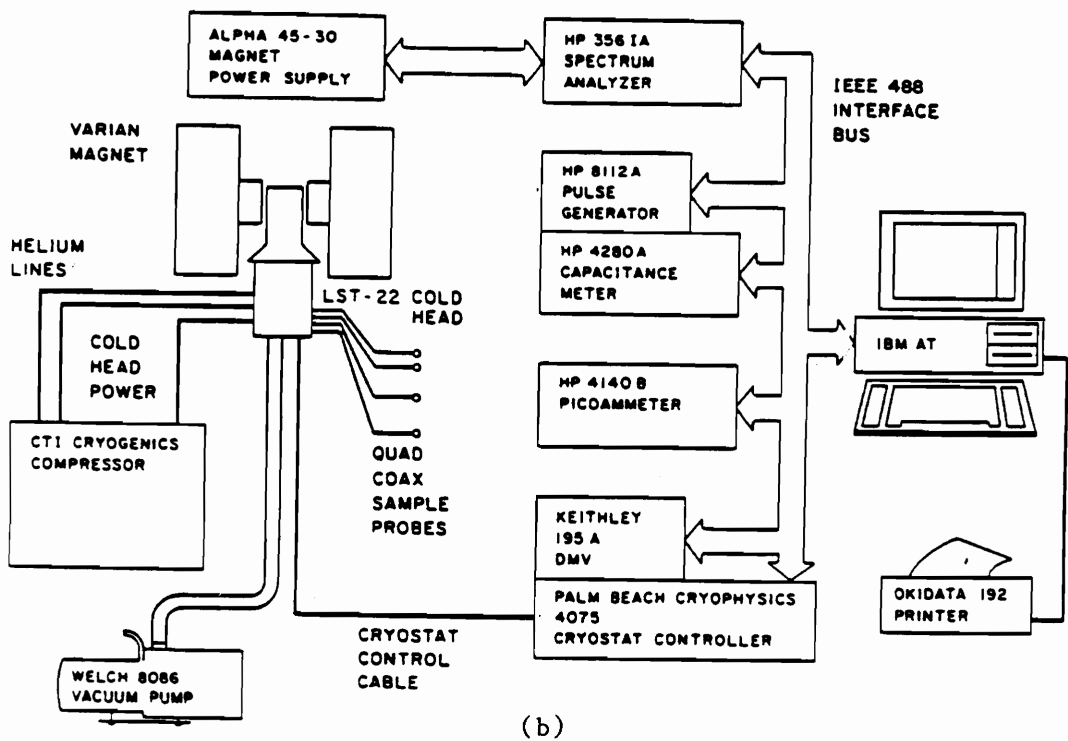

(b)

Figure 3.9 (a) Schematic of the hardware layout of (a) Spectral response measurement system. (b) DLTS measurement system.

response system is shown in Figure 3.9(a). Reliable spectral response data provides accurate calculation of device efficiency, diffusion length, and with the addition of a white light bias, voltage dependence of the light-generated current and its effect upon fill factor.

In an illuminated photovoltaic device, the entire photo-current is opposed internally by the forward bias current in open-circuit condition. Hence, spectral dependence of the photocapacitance provides information related to the junction behavior. Depletion-layer capacitance provides information about the built-in potential of the junction while forward-biased or self-biased (photovoltage) capacitance provides a determination of the lifetime and diffusion length[193]. Energy positions and photoionization characteristics of deep levels in GaAs solar cells can be determined using wavelength-modulated photo capacitance spectroscopy[194].

3.3.3 Dark and Photoconductivity Measurements

When incident photons interact with a photoconductor, conduction electrons are generated either by band-to-band transition (intrinsic) and by transitions involving forbidden-gap energy levels (extrinsic), resulting in an increase in conductivity. Photoconductivity is a useful probe for identifying the defect structure of solids, as the photoexcitation of carriers reveal some fundamental transport parameters, example being recombination lifetime, trap energy and depth distribution. For an intrinsic or near intrinsic semiconductor, the (weak field) ambipolar conduction expression accounts for the contribution of both electron and hole mobilities and is customarily based on Boltzamann transport. Upon illumination, denoting n as the electron concentration in the material and L as the number of photons absorbed per unit volume per unit time in the material, the rate of change of electron concentration can be represented as;

$$dn/dt = L - An(n + N) \qquad (3.6)$$

where N is the trap density. This equation can be solved for steady state photo-conductivity and for the response time. Photoconductivity is particularly sensitive in the

infra-red region of the spectrum and reveals defect-related information for disordered materials.

The response of a photoconductor to a time varying excitation may be employed as an efficient tool to unravel the kinetics of the generation of carriers, their interaction with traps, and their recombination. Relaxation and Fatigue measurements were conducted on ion etched samples, as reported by Nojima et al[66-68]. Two optical excitation wavelengths were considered, one above the band gap and other below the band gap. The above band gap excitation consists of a Spectra-Physics He-Ne laser at emission wavelength at 6253 Å and below the band gap excitation was a semiconductor heterojunction laser diode form Laser Diode Inc. with emission line at 1300 nm and full-width at half maximum (FWHM) of approximately 10 nm. The power is supplied by a Laser Diode current supply, LCS 200/R with variable current adjustment capability. The laser diode is mounted on a thermo-electric cooler for constant temperature operation. A fiber optic pig-tail directs the beam to a selected spot.

The response of the device was observed under an optical excitation and in dark as a function of time. A constant voltage is applied through a D/A converter and the current response is measured on a Keithley electrometer model #617. The temperature of the sample was maintained at 77 K throughout the measurements.

Spectral conductivity was measured for the samples, using the monochromatic excitation, using Jarrell Ash Monochromator and a Gemini 300 Arc lamp. Due to the presence of slow relaxation effects in IBE samples, the device was soaked for a finite period of time prior to measuring its response. Time dependence of the IBE samples was also measured under different optical excitation.

3.3.4 Deep Level Transient Spectroscopy, (DLTS)

DLTS is essentially the capacitance monitored as a function of time, obtained by reverse biasing a diode and pulsing it a zero bias. Upon application of the pulse, the traps get filled in the reduced space charge region and then the trapped electrons are released

exponentially at a rate dependent upon the sample temperature. The thermal release rate for the electrons is given by,

$$\alpha = \nu \exp\left[-(E_C - E_T)/kT\right] \qquad (3.7)$$

where ν is the release frequency. A DLTS spectrum is achieved by monitoring the capacitance as a function of time at varying sample temperatures at an appropriate rate window. The spectrum indicates the magnitude of the capacitative transient versus temperature, where majority carrier traps are indicated by negative peaks in the spectrum. The magnitude of the peaks may be used to determine the trap density through the relation

$$\frac{\Delta C}{C} = -\frac{N_T}{2N_D}\left[1 - \frac{2\lambda}{W(V)}\left[1 - \frac{C(V)}{C(0)}\right] - \left[\frac{C(V)}{C(0)}\right]^2\right] \qquad (3.8)$$

where λ is the so-called edge region thickness, W the space charge thickness, N_T the trap density, C the reverse biased capacitance and ΔC the transient capacitance given by

$$\Delta C = C(t_1) - C(t_2) \qquad (3.9)$$

where t_1 and t_2 are the boxcar integrator times. If the edge region neglected then the trap density N_T can be found from the relation

$$N_T = 2\ N_D\ |\Delta C/C| \qquad (3.10)$$

assuming $\Delta C << C$. DLTS is more sensitive to traps located near the edge of the space charge layer. The trap energy may be determined using an Arrehenius plot of log of the transient decay rate vs. 1/T. This was implemented in DLTS by scanning the rate window which in turn changes the peak temperature accordingly. A simpler calculation show that for a rate window at 50/sec, the trap energy can be represented by; $E_T = 23.7kT_M$, for, $\nu = 10^{12}$/sec. and T_M is the peak temperature. Figure 3.9(b) shows a hardware layout of DLTS characterization facility.

3.3.5 X-ray Photoelectron Spectroscopy, (XPS)

The surface analysis was carried out using a Perkin Elmer PHI model 5300 XPS system. X-ray generation occurs in the PHI model 04-500 X-ray source equipped with both Mg and Al anodes. Mg K_{α} radiation was utilized in these studies with the anode power set at 250 watts. Photoelectrons emitted from samples are focussed into the spectrometer input slit and at the appropriate kinetic energy by the PHI model 10-360 Precision Energy Analyzer (Figure 3.10), a concentric hemispherical analyzer. The electron signals are detected by a position sensitive detector that consists of two 2.5 cm. diameter channel electron multiplier arrays.

Photoelectrons were produced using Mg K_{α} radiation ($h\nu = 1253.6$ eV) as the excitation source. The analysis chamber pressure was less than $3x10^{-6}$ Pa. Spectra were acquired at 90° and 15° take-off angle (toa) measured as the angle between the sample surface and the photoelectron analyzer. Compositional analysis as a function of depth was carried out for some samples in which case the toa was varied between 90° and 15°. The most signal of the observed photoelectron signal arises from a layer $3\lambda \sin\Theta$, where λ is the mean free path of the photoelectron and Θ is the take off angle. For Ga 3d and As 3d core levels λ is approximately 22 Å, therefor the analysis depths are approximately 66 Å and 17 Å for 90° and 15° toas, respectively.

The photopeaks are analyzed by subtracting the X-ray source line width (deconvoluting), smoothing, and curve-resolving the data using the software routines available with PHI 5300 system. The atomic concentrations were evaluated from the photopeak areas using the sensistivity factors listed in Table 3.3. Smoothing was utilized to reduce noise in the spectra. The smoothing routine in the PHI 5000 series software is accomplished using the Savitzky-Golay convolution algorithm, which is an expanded calculation of a moving average. A 15-point smooth was used in this study.

The peak positions, FWHMs, and areas were determined using the curve-fitting routine. Standard Gaussian peaks were superimposed on the deconvoluted and smoothed

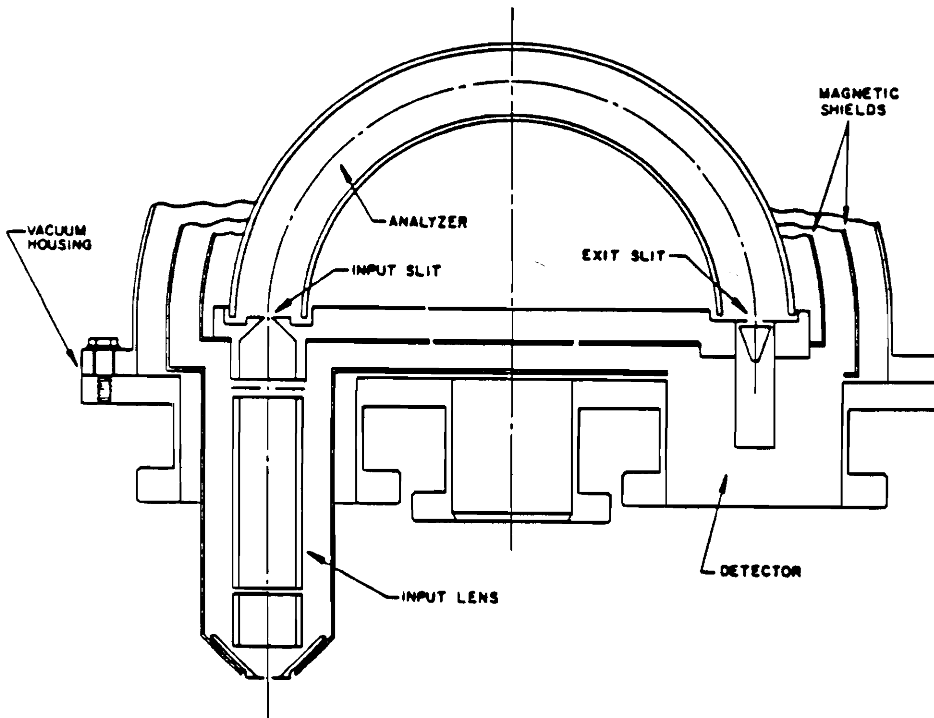

Figure 3.10 PHI model 10-360 hemispherical capacitor energy analyzer.

Table 3.3 XPS Sensitivity factors.

Level	Sensitivity Factor (σ)
Ga 3d	0.31
As 3d	0.53
O 1s	0.66
Ar 2p	0.96
N 1s	0.42

data after a background subtraction in the integrated mode was performed. Peak heights, widths, and positions were adjusted to simulate the peak structure of the experimentally obtained peaks. Peak widths and positions were obtained from the standard oxide measurements and were used to assist in curve-fitting. Curve-fits were obtained by manual manipulation of the photopeaks so as to keep reasonable widths and positions for peaks.

Atomic concentrations were determined using the following expression:

$$\%\ \text{AC for species X} = \frac{\text{Area}(X)/\sigma(X)}{\sum_{i=1}^{n} \text{Area}(i)/\sigma(i)} \times 100 \quad (3.11)$$

where n is the number of chemical species (ie. Ga(GaAs), As(GaAs), Ga(Ga_2O_3), As(As_2O_3), etc.), i is the peak area determined from the curve-fit routine, and σ is the sensitivity factor.

— ¤ —

Chapter 4

Results and Discussion

The experimental results of IBE surfaces of semi-insulating and doped GaAs are presented in this chapter. Wherever applicable, a comparison with the results reported in the literature is mentioned. Pertinent discussion accompanies each of the figure, providing additional information, analysis and reasons for any apparent discrepancies.

4.1 Dark and Photoconductivity

Dark and photoconductivity response, as a function of inverse of temperature for virgin, 1 KeV etched and 3 KeV etched LEC SI-GaAs (100) samples is shown in Figure 4.1. The most prominent features of the curves were: (a) The photoconductivity under sub-bandgap photon energy illumination increased exponentially with 1/T for all samples at temperature about 125 K, with the same activation energy. This indicated, according to Bube et al.[149], the presence of Shockley-Read recombination mechanism at a center located at about 0.26 eV above the Fermi level. It is interesting to note that this level is not influenced significantly by the ion etch. (b) There is evidence for three distinct segments on the virgin curve as the temperature decreased. Two segments have activation energies of 0.78 eV, and 0.47 eV, and the third segment shows temperature dependence with an "effective (negative) activation energy" of 0.26 eV. As the ion beam energy increases, the 0.47 eV segment is substantially reduced and is totally eliminated by 3 KeV etch. Figure 4.2 shows the log conductivity response vs. inverse temperature as above, in the presence of above band-gap illumination, 600 nm. using Jarell Ash monochromator. These curves essentially show a similar response, except for the fact that 0.47 eV segment was not observed at all. This indicates that above band gap photons create electron-hole pairs, which come to a rapid thermal equilibrium. However, in the case of below band gap

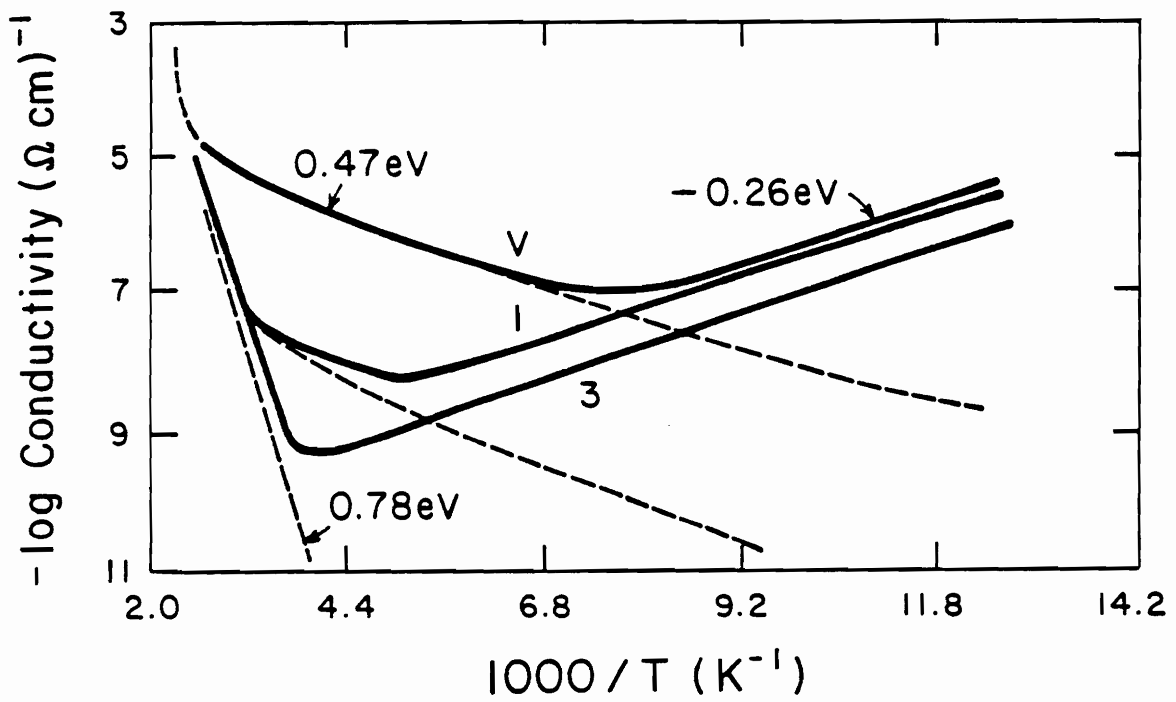

Figure 4.1 Inverse temperature vs. log conductivity for virgin, 1 KeV etched and 3 KeV etched SI-GaAs samples in dark (lower curves) and under 1.19 eV optical excitation (upper curves)

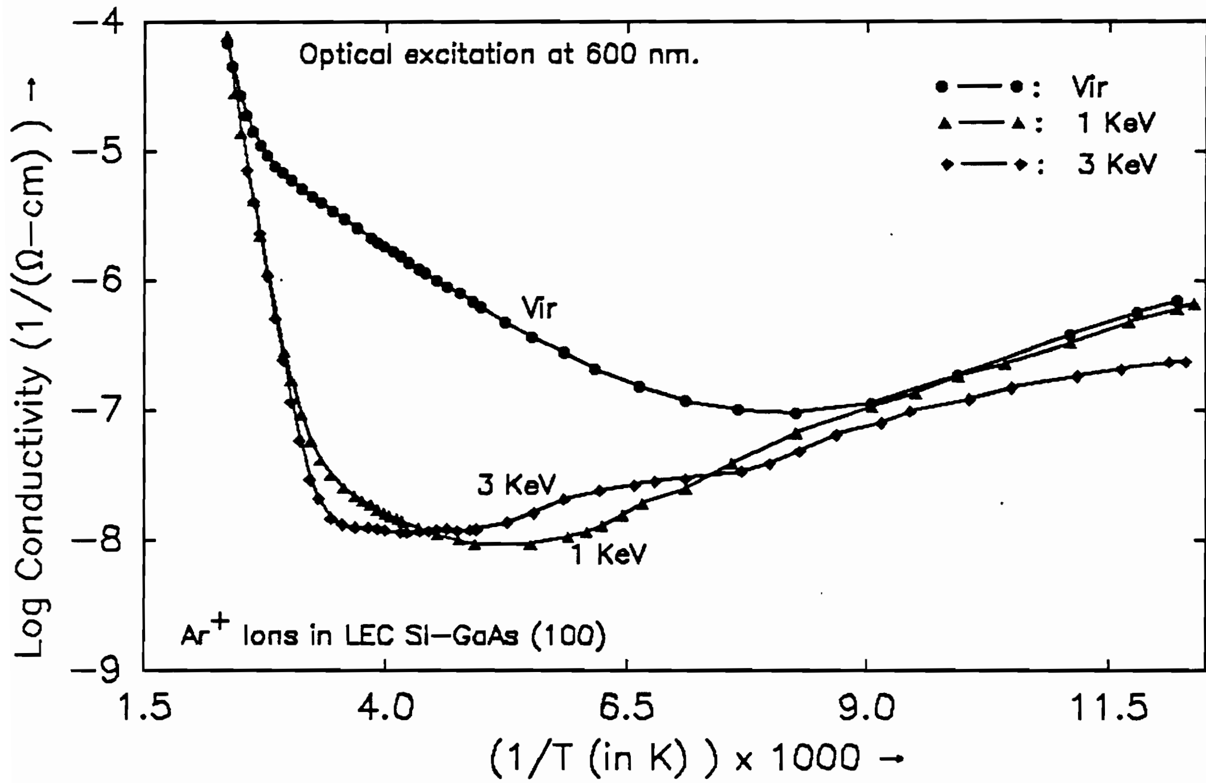

Figure 4.2 Inverse temperature vs. log conductivity for virgin, 1 KeV etched and 3 KeV etched SI-GaAs samples under 2.06 eV optical excitation.

photons, the transition of carriers is via the defect level at 0.47 eV. Figure 4.3 shows the dark and photoconductivity measurement performed on Si-implanted at 50 KeV and unannealed samples for (100) and (211) orientation. Similar measurements were performed on samples, rapid thermal annealed at 850 C for 30 secs., for electrically activating the dopants. For the unannealed case, the dark and white light illuminated results are somewhat similar , with the (211) orientation having a slightly higher resistance. A striking difference was observed between (211) and (100) curves, for IR illuminations at 0.9 μm. The minor change in the (211) curve from its dark value may be due to the fact that the photoconductnace changes for this orientation are due, predominantly to the photoexcitation near the surface; the 0.9 μm. photons are absorbed deeper. It was not clear why the (100) and (211) cases are so different under 0.9 μm. illumination, since the Raman measurements indicated near identical damage profiles[195]. However, the trap distribution that provides the carriers for photoconductivity may be significantly different throughout the damaged, unannealed layers for the two orientations. The large difference in the photoconductivity for the two orientations was totally removed by annealing, as shown in Figure 4.4. The (100) orientation shows higher conductivity than (211), for all illumination and temperature conditions investigated.

Figure 4.5 shows the activation energy, calculated at room temperature from Arrhenius plots, shown in Figure 4.1. Increasing activation energy indicates the increased amorphicity of IBE layers. Regions of log conductivity vs. inverse temperature plots were expanded and several slopes were observed on the plot. Figure 4.6 shows one such plot, where two levels, one at 0.31 eV and other shallow level at 0.035 eV were observed. As will be seen later in the chapter, the level at 0.31 eV was also detected using DLTS. The activation energy of some other levels found were 0.52 eV, 0.41 eV, 0.36 eV, 0.27 eV, 0.22 eV, 0.18 eV and 0.056 eV. The levels at 0.31 eV and 0.52 eV were observed to be arising due to ion beam etching.

Figure 4.3 **Dark and photoconductivity (under white light, 901.5 nm., 600 nm., and 420 nm. illumination) versus inverse temperature for 50 KeV Si implanted and unannealed, (a) (100), and (b) (211) GaAs.**

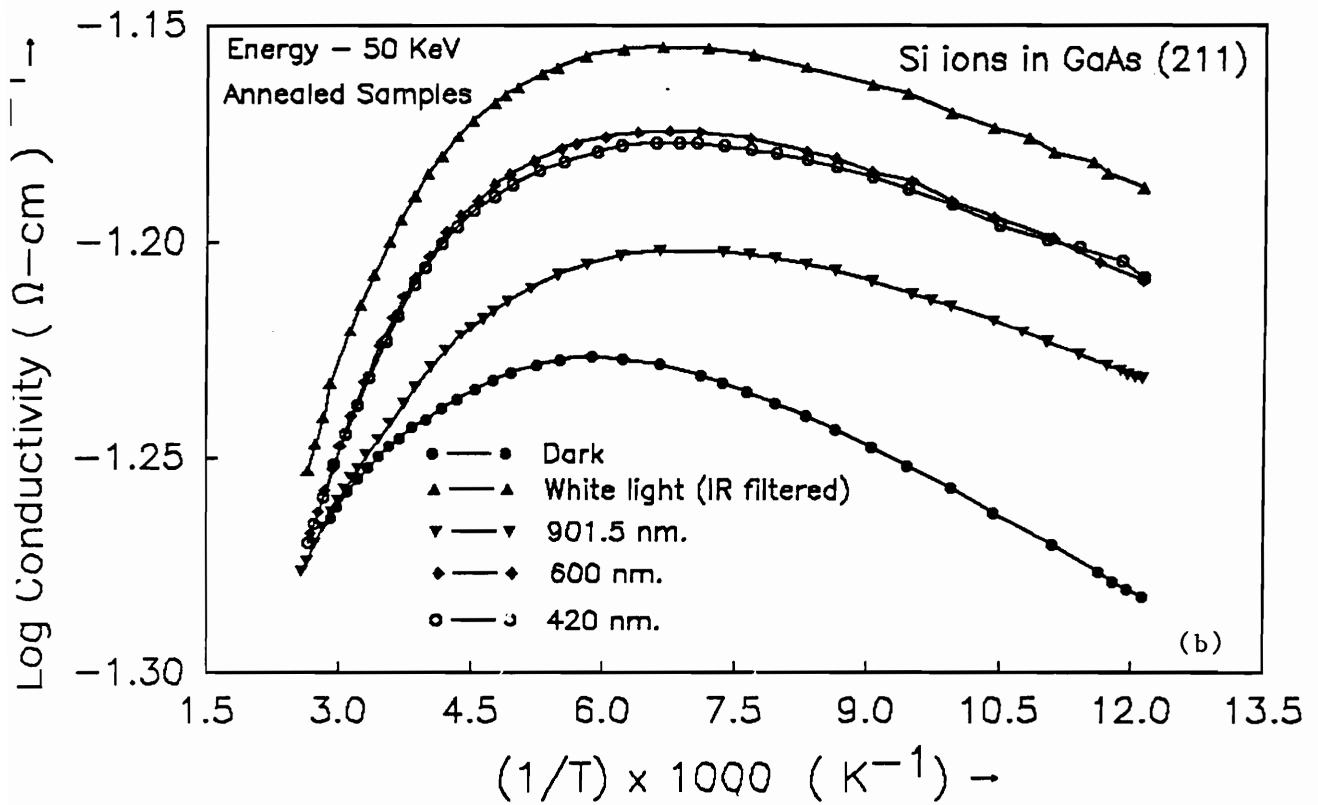

Figure 4.4 **Dark and photoconductivity (under white light, 901.5 nm., 600 nm., and 420 nm. illumination) versus inverse temperature for 50 KeV Si implanted and annealed, (a) (100), and (b) (211) GaAs.**

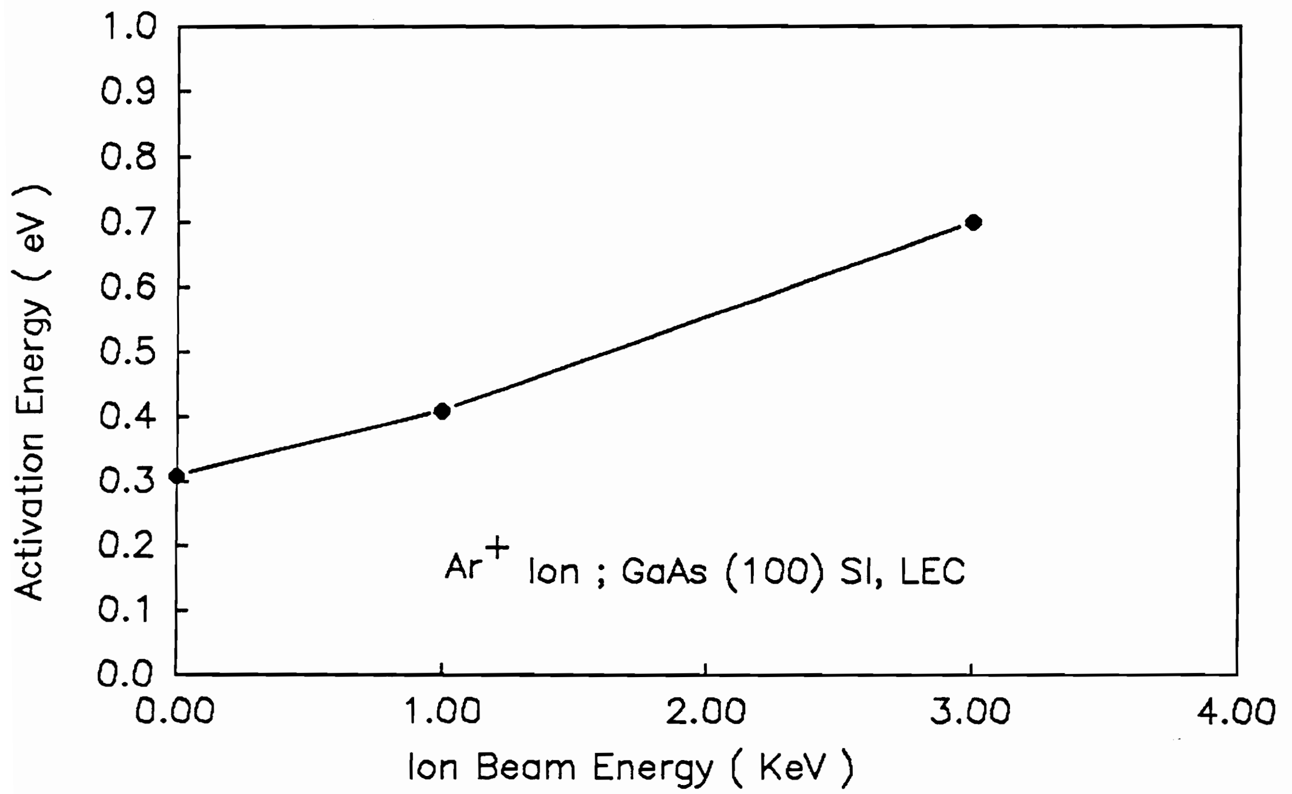

Figure 4.5 **Activation energy of SI-GaAs samples as a function of ion beam energy**

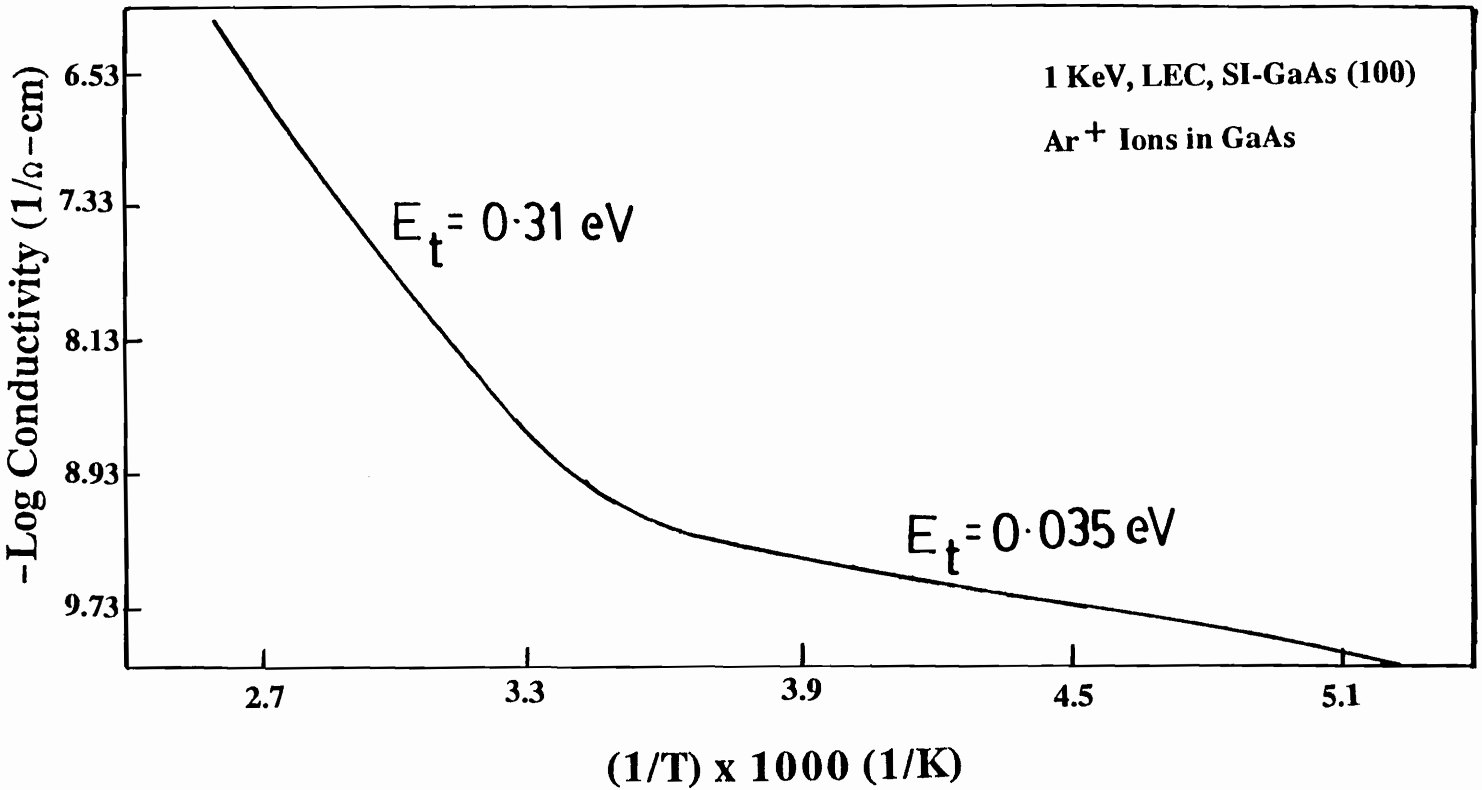

Figure 4.6 Detection of shallow traps in ion beam etched GaAs.

4.1.1 Spectral Conductivity

The photoconductive response depends strongly upon time, wavelength and temperature, these all being dependent on ion-etch energy (virgin, 1 KeV and 3 KeV). D.C. spectral conductivity response curves are shown in Figure 4.7 and 4.8. The unquenched spectra for virgin and ion-etched samples show a rather narrow peak at about 0.75 eV, a broad central peak from 0.9 eV to 1.5 eV and a fairly flat region beyond 1.6 eV. The shift in the broad central peak indicates that time-dependent quenching occurs for photons in the 0.9 eV to 1.4 eV range, which is later described in terms of optically generated metastable defect-state formation. The narrow peak at 0.75 eV was not much altered by the ion-etch. These results were in accordance with the results reported by Nojima [66-68].

For 1 KeV and 3 KeV IBE samples, the spectral dependence could be quenched after 1/2 hr. of IR filtered white light soak, while the virgin sample still showed spectral dependence after 1/2 hr. soak. Even after a white light soak of 1 hr., the virgin sample showed spectral dependence of 0.75 eV. The broad central peak was observed to be completely quenched.

The electroabsorption data are rich in information but the interpretation is difficult, since several mechanisms are involved. The results described above are in agreement with those of Vincent et al.[71] and Bube et al.[149]. Observation of photoconductance in IBE samples makes this study unique. Based upon the experience of the previous authors and observations of this study, a phenomenological model of electroabsorption in IBE samples is presented. Figure 4.8 (b) shows the spectral conductivity for virgin, 1 KeV and 3 KeV samples at 77 K where the samples were soaked at monochromatic irradiation for 30 sec. before taking the data. In these curves, several features deserve special mention: (a) The unquenched spectra were similar for ion-etched and virgin samples, (b) The broad central peak was affected by pre-illumination or the light soak. For energies greater than the 1.0 eV, the magnitudes of the peaks were a function of the duration of the pre-illumination.

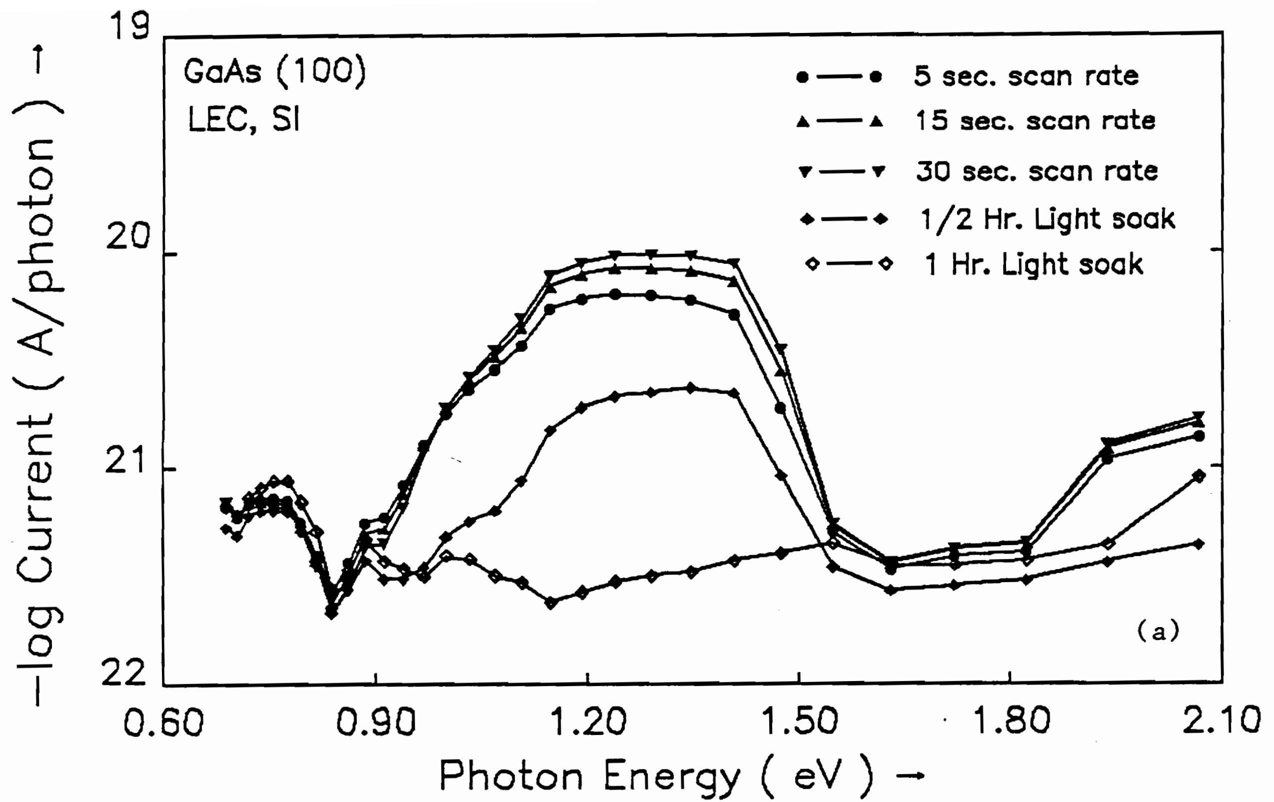

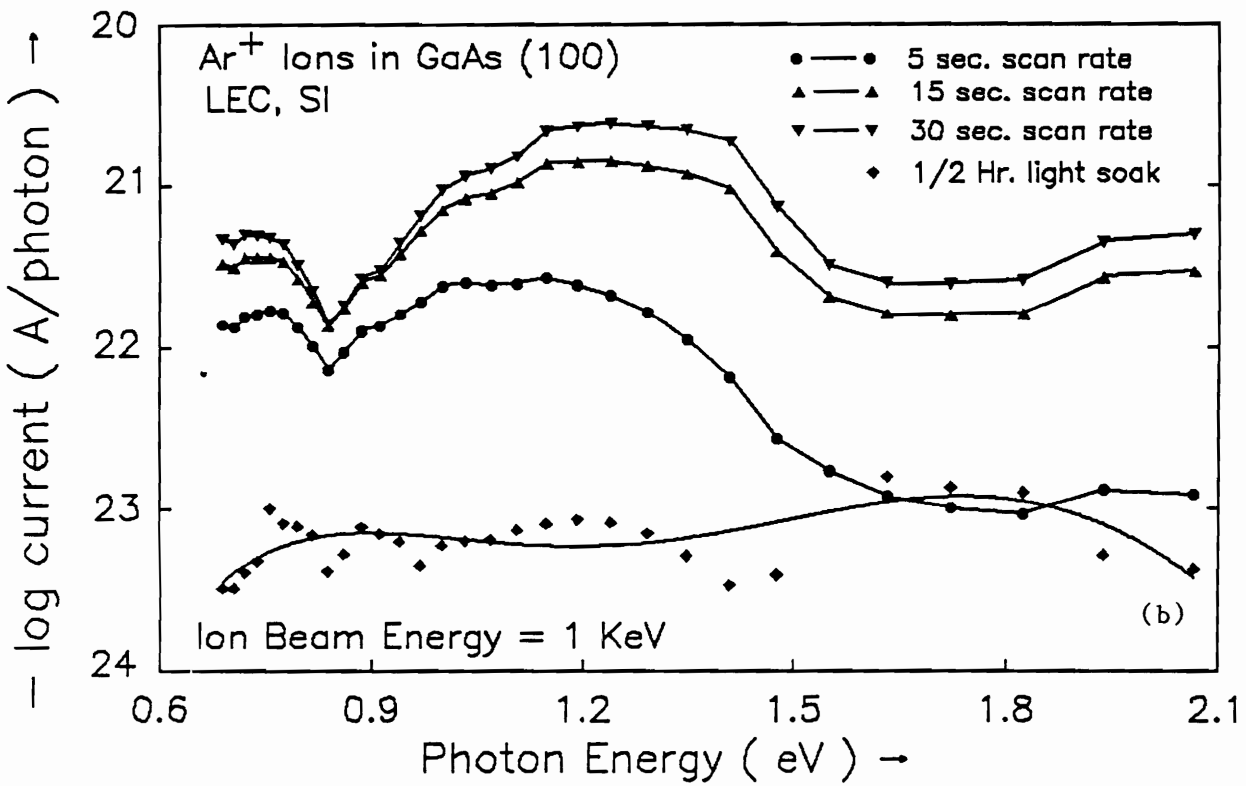

Figure 4.7 Spectral conductivity (current per incident photons) for (a) virgin and (b) 1 KeV etched samples at 77 K, under 5 sec., 15 sec., and 30 sec. of monochromatic light soak. Also, shown are spectral conductivity after white light soak; 1/2 hr. and 1 hr. for virgin, and 1/2 hr. for 1 KeV etched sample.

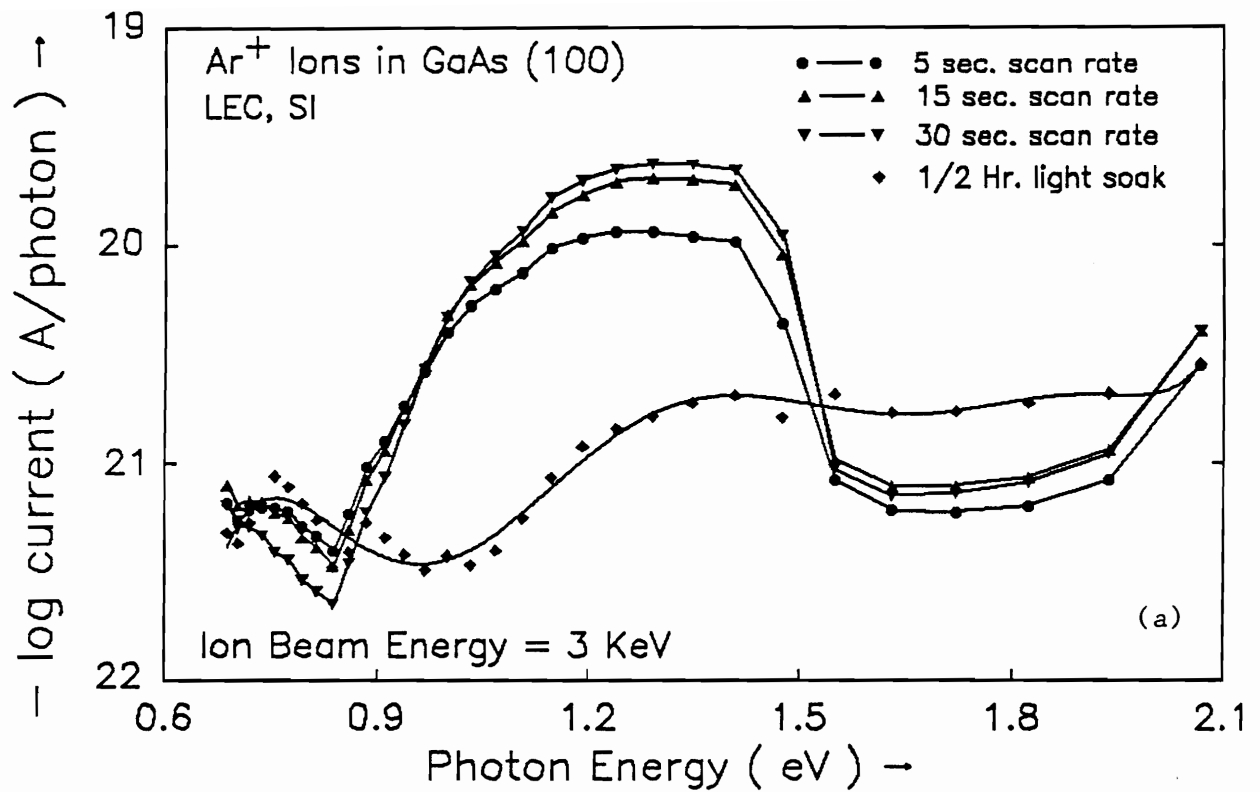

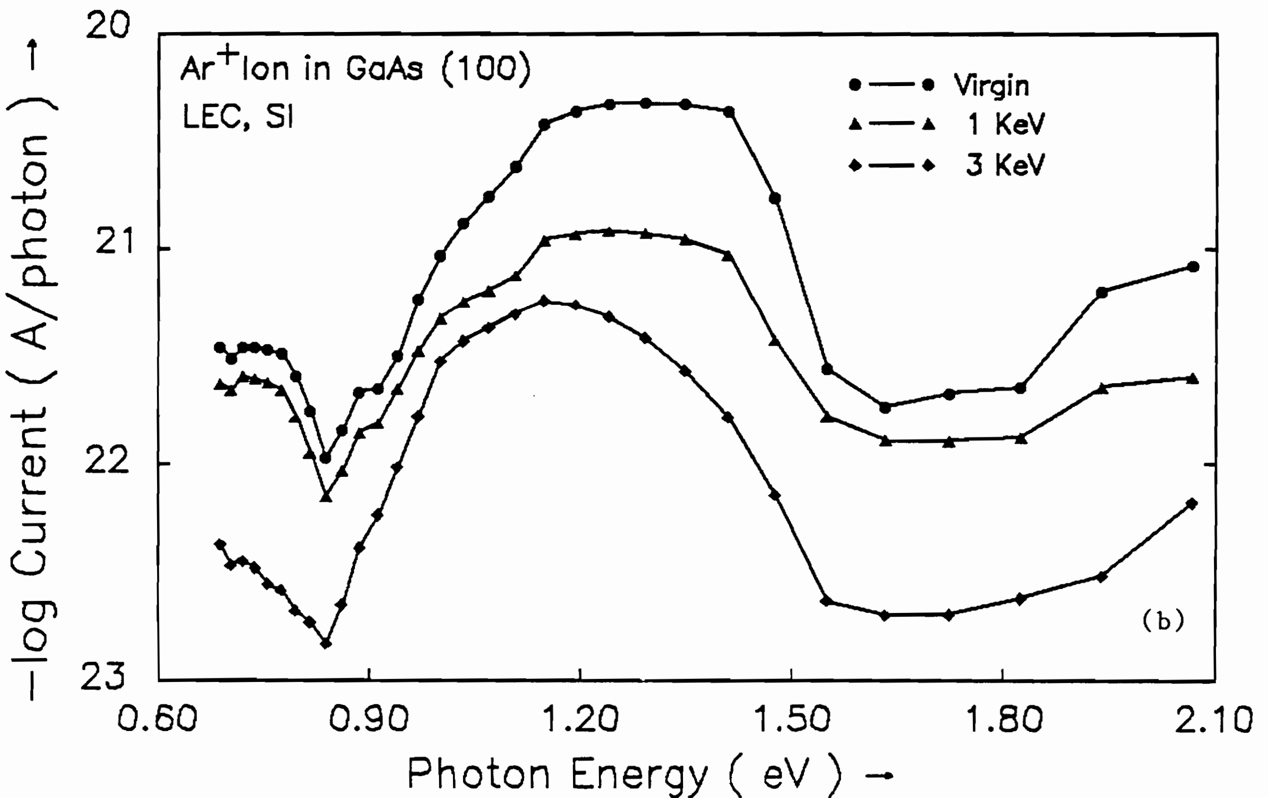

Figure 4.8 Spectral conductivity for 3 KeV etched sample at 77 K under 5 sec., 15 sec., and 30 sec. monochromatic illumination soak. Also shown is the spectral conductivity for virgin, 1 KeV, and 3 KeV etched samples at 77 K (30 sec.) light soak at each wavelength.

From Figure 4.7 (a) for virgin sample, a stationary state is obtained after almost one hour of pre-illumination. It will be shown later that recovery of the initial conditions requires an annealing at a temperature of about 120 K. The same is true in IBE samples, however the stationary state is reached much earlier.

The complex experimental sequences and the difficulty in the interpretation of the electroabsorption of IBE samples cannot permit a simple explanation of all these observations, but there is no contradiction.

4.1.2 Persistent Conductivity, Relaxation, and Fatigue

Time dependent characteristics at 77 K are shown in Figure 4.9, and exhibit several interesting features.

a): A rather slow rise in photo-current at sub band-gap energy at (0.80 eV , 1550 nm), (1.19 eV , 1040 nm), and the rapid increase for above band-gap excitation at (2.06 eV, 600 nm) are strikingly similar to the results reported by Desnica and Santic[196]. The sharp rise for the 2.06 eV curve was attributed to the rapid equilibrium of electron-hole pair generation. The slow rise of the 1.19 eV curves can be attributed to the slower generation of free carriers due to EL2 photoionization. The unetched sample, however shows a slight decrease in photoconductivity at 0.8 eV, indicating competition between mid-gap level transitions, as proposed by Lin and Bube[149], and possible reduced absorption by the EL2 center[148].

b): The degree of photosensitivity was increased by the ion-etch. This increased photosensitivity was due the increase in dark resistivity, by about 5 orders of magnitude. The light to dark conductivity ratio increases by approximately 3000 at 1.2 eV, as compared to 10^5 at 2.1 eV in IBE samples, clearly indicating the interplay of traps. In presence of optical excitation, the traps fill up, increasing the drift mobility and the photoconductivity to the virgin sample value. Table 4.1 lists activation energies and the ratios of steady state photo-to-dark conductivity ratio.

c): There is a considerable persistent photoconductivity (PPC) evident in the

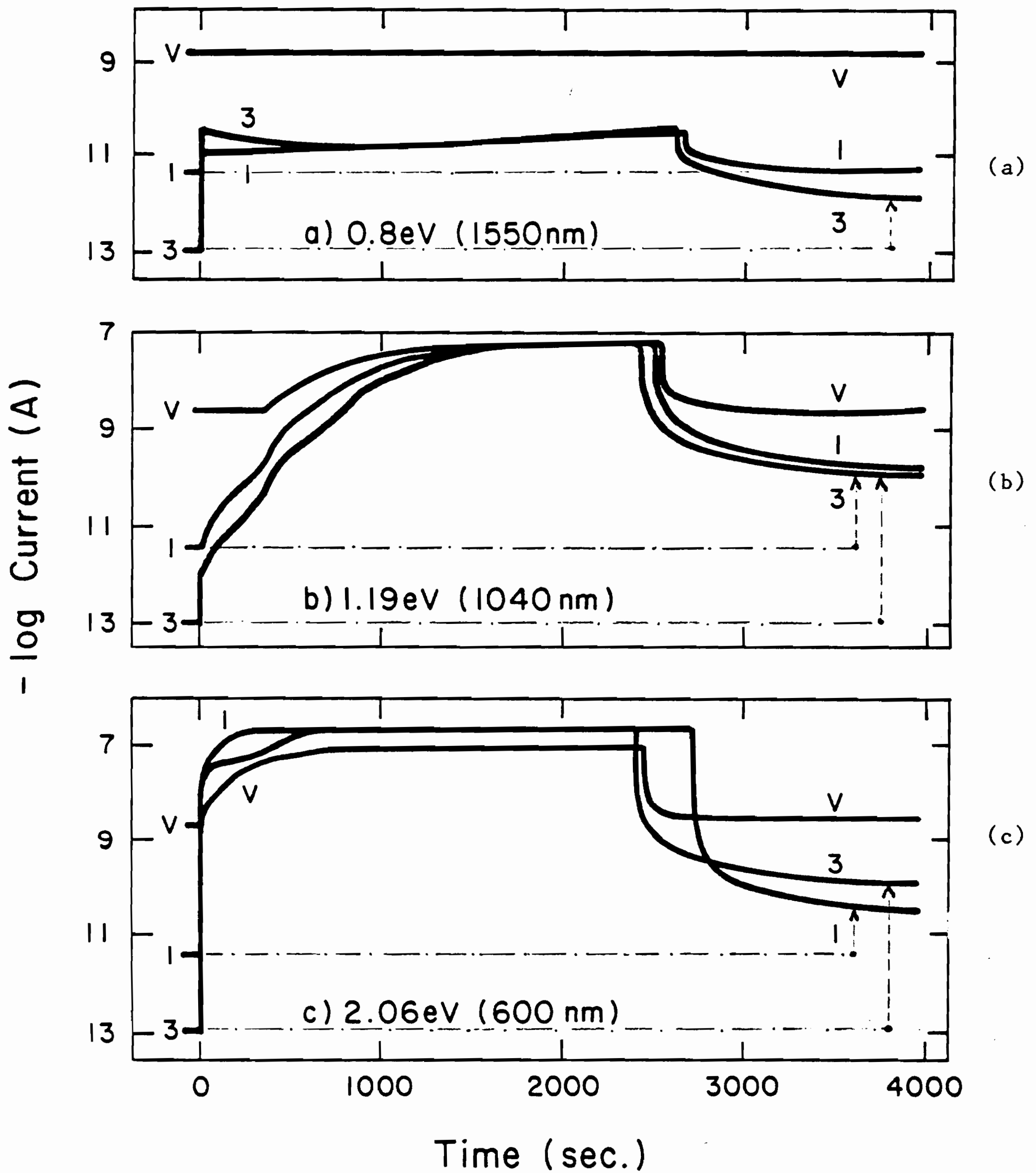

Figure 4.9 Time dependence of photocurrent for virgin, 1 KeV etched, and 3 KeV etched samples at 77 K for (a) 0.8 eV , (b) 1.19 eV, and (c) 2.06 eV monochromatic excitation.

Table 4.1 Ratio of steady state photoconductivity to dark conductivity.

Sample Description	Activation Energy (eV)	Current in Dark (A)	Ratio at 0.80 (eV)	Ratio at 1.20 (eV)	Ratio at 2.10 (eV)
SI-virgin	0.326	1.38×10^{-9}	0.471	0.261×10^{2}	0.303×10^{2}
1 Kev IBE	0.42	4.68×10^{-13}	0.130×10^{2}	0.131×10^{5}	0.281×10^{5}
3 KeV IBE	0.68 - 0.70	1.12×10^{-14}	0.914×10^{2}	0.937×10^{5}	0.239×10^{7}

ion-etched samples, with non evident for the virgin samples. PPC is a clear signature of the ion-etch, with memory existing for an extended period of time. PPC has also been observed in SI-GaAs, and in $Al_{1-x}Ga_xAs$, in addition to the present observation for ion bombarded samples. The relaxation rates differ considerably for these samples. However, no single model proposed in the literature so far satisfactorily explains the slow-relaxation phenomena in these materials.

Based on this observation of persistent photoconductivity in IBE samples and experiments of Nojima[66-68], Tajima[70], and Mita[69], photoconductivity experiments using sequential double irradiation for IBE SI-GaAs were performed, and the waveforms of photoconductivity occurring simultaneously with irradiation ($h\nu_1 \approx 1.958$ eV) subsequent to primary light irradiation ($h\nu_2 \approx 0.954$ eV) for a virgin and ion beam etched samples at 77 K are shown in Figure 4.10. Photons of above and below band gap energies were selected, because striking features of the phenomena were seen in the experiments mentioned above. The main feature of the primary light induced phenomena was the gradual increase to steady state photoconductivity. This initial increase in photoconductivity was observed to be the same as observed in the previous experiments (barring individual sample dependencies). With the interception of the primary excitation, all the curves show an exponentially decaying i(t) response and the photosensistive quantity had a long tail or shows persistent photoconductivity. Another phenomena where photosensitive quantity rapidly increased with the onset of incident radiation, after which it gradually decreased even if the irradiation were continued is the 'photoelectric fatigue' or 'quenching'. Both these phenomena were ascribed to the specific properties of the main deep center, EL2. Upon irradiation with the secondary light ($h\nu_2 \approx 0.954$ eV) photoelectric fatigue was observed. After a brief period of interception of light, if the sample was irradiated with the primary light, the equilibrium was reached much earlier than the first time irradiation. Photoelectric fatigue was observed in all the samples under secondary light irrespective of previous illuminations. Important features for such observations are summarized as

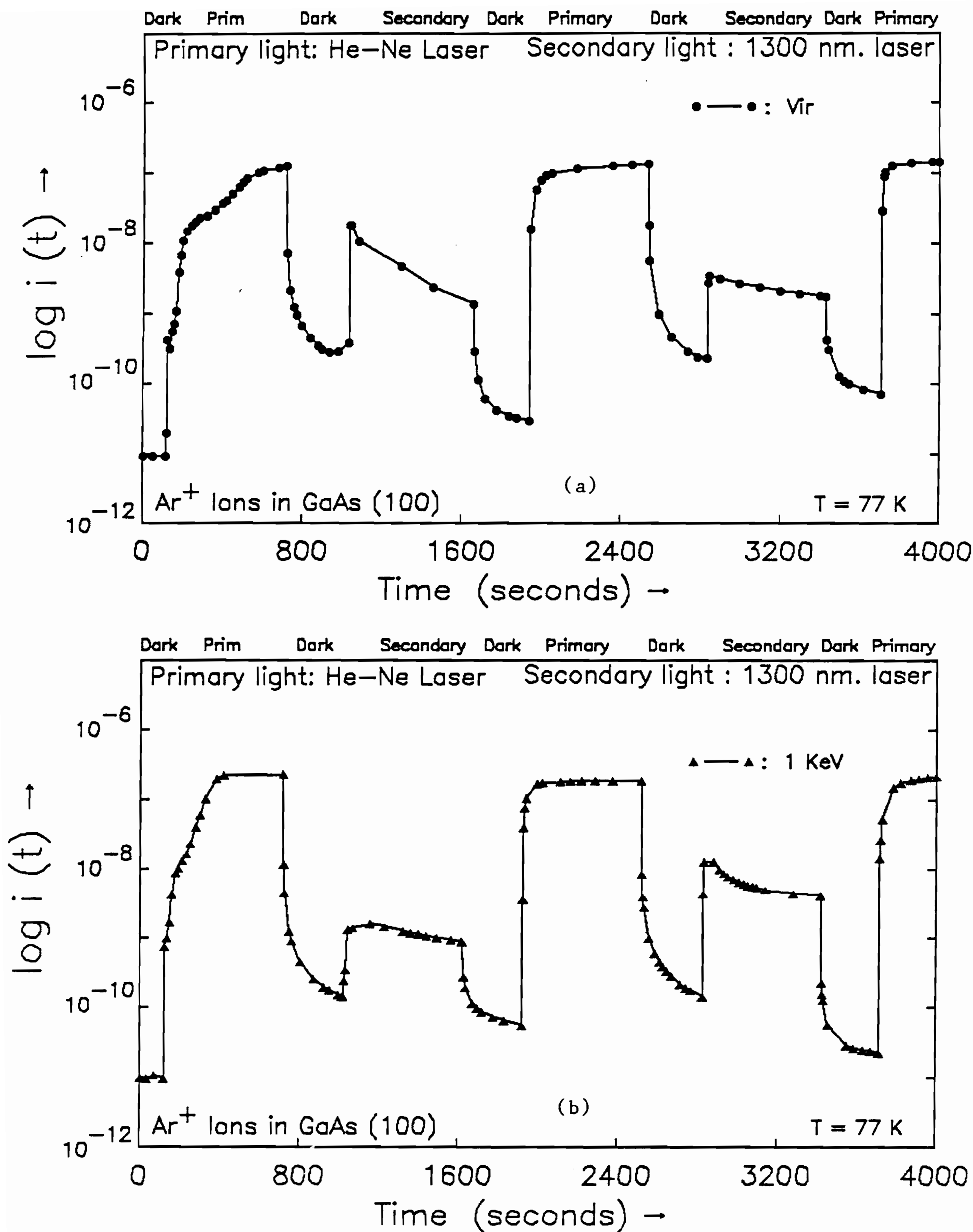

Figure 4.10 Waveform of photoconductivity occurring with primary light irradiation ($h\nu_1 \approx 2.06$ eV) subsequent to primary-light irradiation ($h\nu_2 \approx 0.954$ eV) for (a) virgin sample, (b) 1 KeV etched,

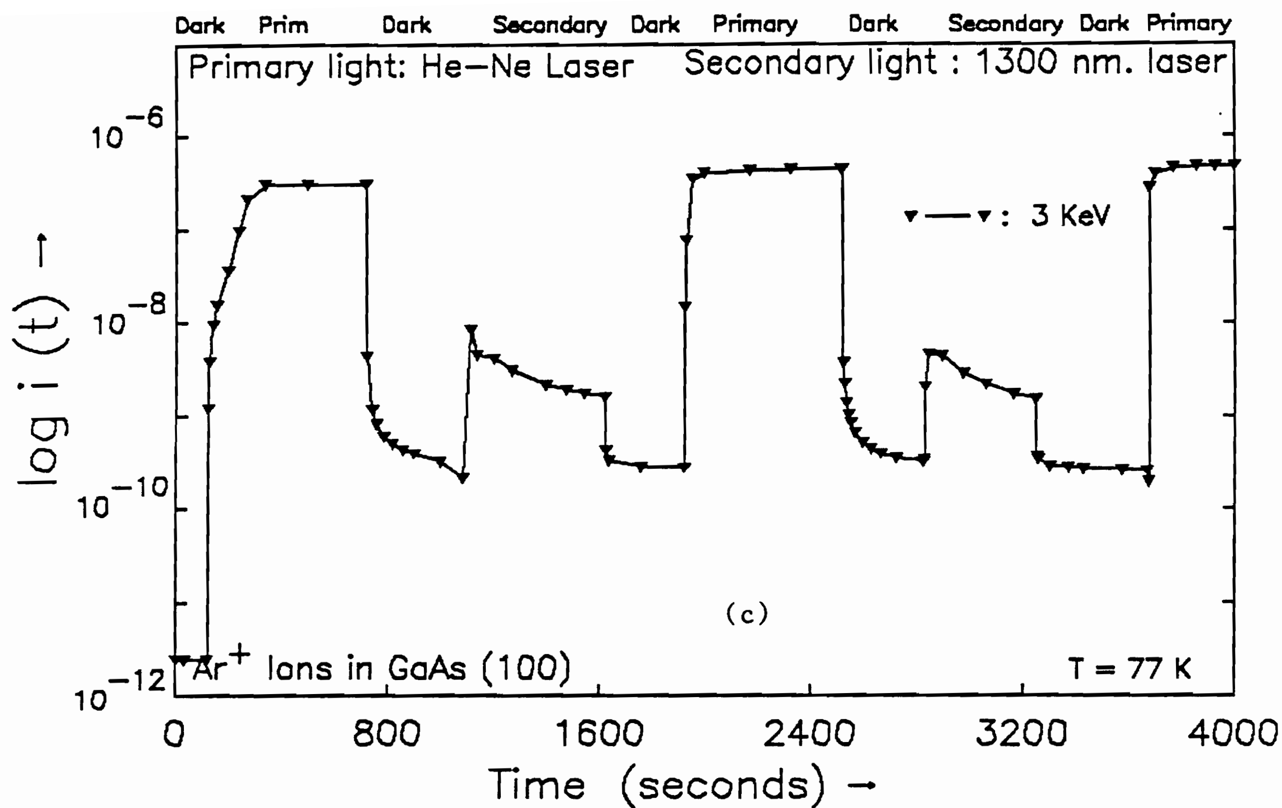

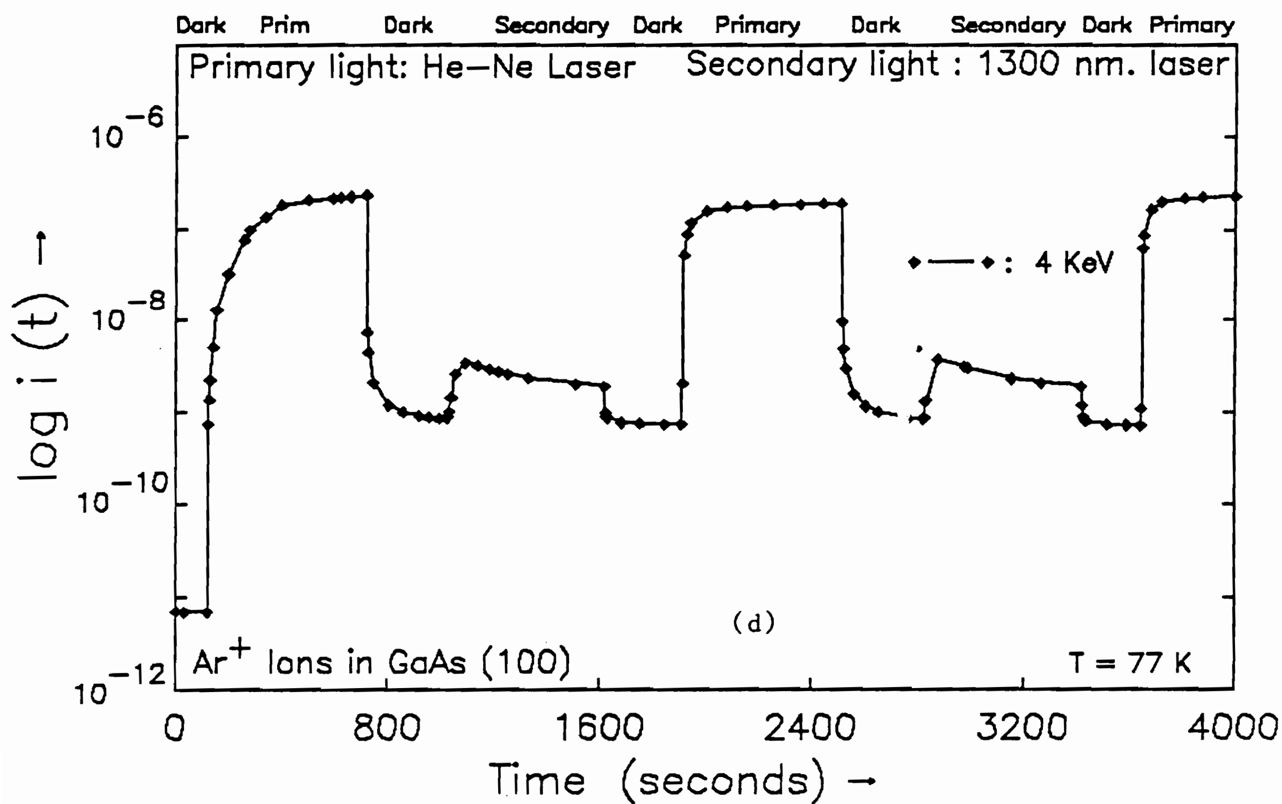

Figure 4.10 (contd.) (c) 3 KeV etched, and (d) 4 KeV etched. Sample temperature was held at 77 K and the substrate was LEC SI-GaAs (100).

follows.

(a): Irradiation of secondary light subsequent to primary light induces a rapid increase to certain maximum level followed by a gradual exponential decrease.

(b): Irradiation of secondary light saturates the defects and hence stationary photoconductivity level is reached faster than without prior irradiation with secondary light.

In virgin samples, photosensitivity relates to the overall optoelectronics quality of an individual crystal. The gradual increase or decrease in photoresponse in IBE was due to the interplay of deep center with the defects induced by ion beam etching, in addition to the individual property of the crystal.

The pronounced feature of the observation can be explained by the dynamical transition of electrons in the conduction band (CB), the valence band (VB), a main deep center 'X', and its metastable excited state 'X^*', which depicts a defect state with large lattice relaxation in a configuration coordinate (CC) model. The metastable state X^* can be classified into two kinds of states, X_a^* and X_b^* according to whether the electronic transition $X^* \Rightarrow X$, due to irradiation with the photon energy near $\approx$ 0.9 eV, is allowed or forbidden. It is also assumed that the concentration of these states satisfies the relation $N(x_a^*) << N(x_b^*)$. Hence, the fatigue is induced by the electronic transition, $X \Rightarrow X^*$, that occurs during relaxation after primary light irradiation. Hence, the spike phenomena occurring sequentially is explained by electronic transition of the type, $X_a^* \Rightarrow X \Rightarrow CB$, which induces a spike like waveform of the photocurrent. In order to explain the persistent photoconductivity, several explanations were presented. It is well known that IBE introduces discrete trap centers over a region deeper than the ion range predicted by the LSS range distribution theory [79]. A possible mechanism for the PPC is the existence of longer lifetime electron traps in the damaged and partly-amorphous near-surface region. At temperatures lower than 120 K, such traps become filled with electrons during optical excitation. Upon terminating the excitation source, the EL2 - generated hole current

dominates for an extended period of time, which depends on the electron trap kinetics. (This is consistent with p-type behavior that has been reported). These could be the same electron traps which result in the low frequency capacitance-dispersion reported elsewhere for ion-beam etched Schottky diodes[27,46,47]. (Analogous to the persistent photoconductance, no significant dispersion was seen for diodes fabricated on unetched material).

A second mechanism could be the photogeneration of metastable states which have smaller capture cross-sections for electrons, with PPC arising due to a dynamical transition of electrons between trap levels with large relaxation times. PPC can be associated with the complex of an ordinary donor [D] and another defect [X] , possibly an arsenic vacancy, and can be explained by the Defect Configuration Coordinate model[136]. The defect center has a very strong coupling between electronic and vibronic systems. At low temperatures, there is insufficient energy for the center to capture an electron and hence contribute to the conductivity, which is a characteristic feature of the PPC effect. IBE introduces discrete shallow traps within the bandgap of the semiconductor. It is possible that EL2 transforms into its metastable configuration $EL2^*$, inducing capture of a shallow defect. In the absence of optical excitation, electronic transitions to the conduction band or from the valence band to the new defect configuration are forbidden, resulting in a larger relaxation time. Thermal activation at $T \geq 125$ K provides enough energy for a transformation to the original stable EL2 state. Such a transformation can be represented as follows:

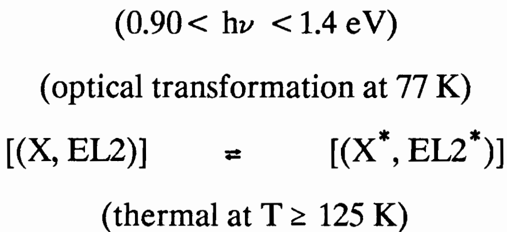

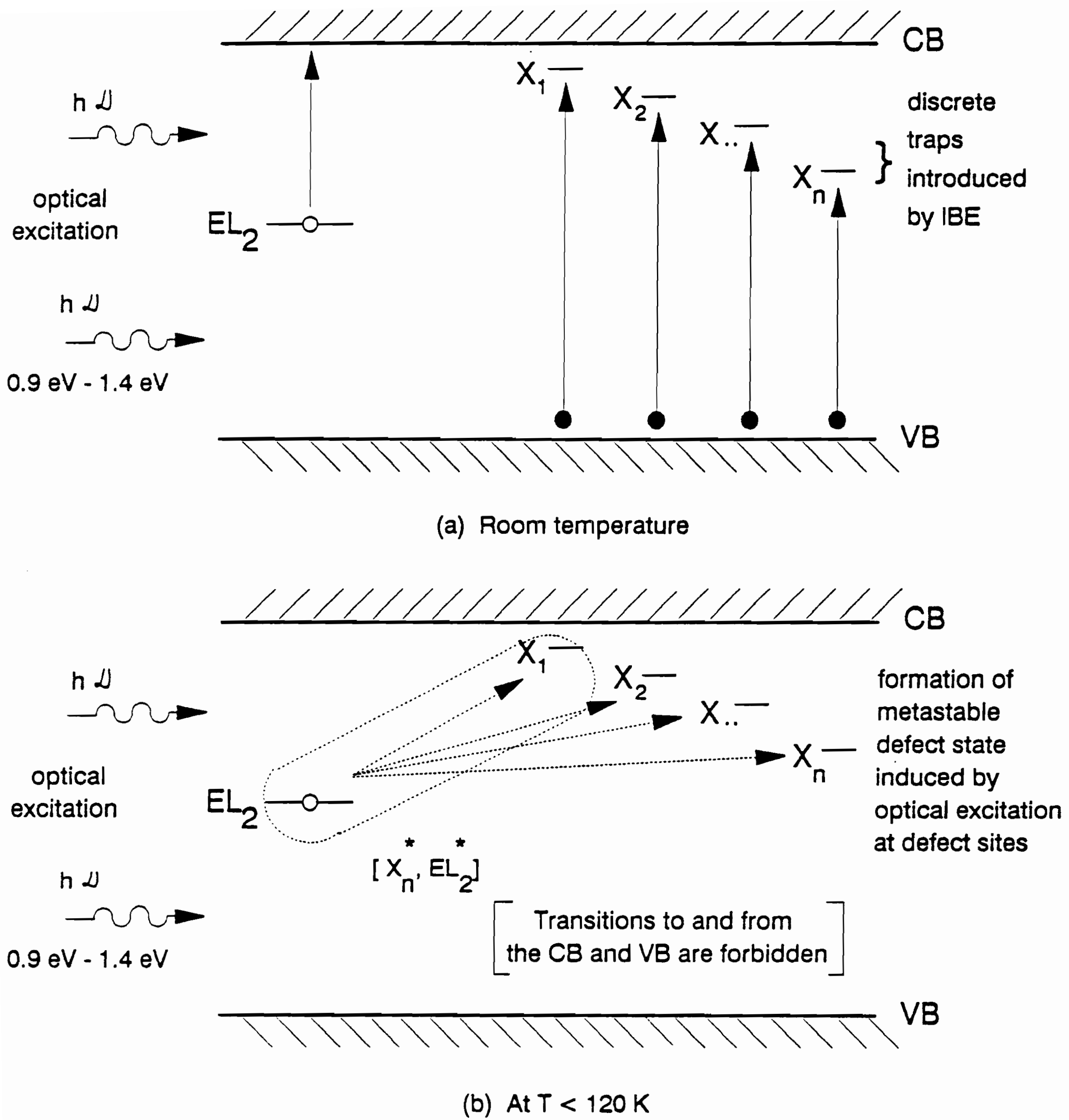

Figure 4.11 Phenomenological model of the optically generated metastable defect state formation by ion beam etching.

where the complex $[(X^*, EL2^*)]$ is a metastable defect-state. This assumption is supported by the physical model proposed by Levinson [152], which deals with the charge state controlled electrostatic interaction between two or more defects, and is shown schematically in Figure 4.11. According to this model, the minimization of electrostatic and lattice strain energy causes a transformation between the two possible configurations of the complex.

The rate equation for such a transition is proposed by Tajima et. al.[70] and is given by;

$$dN(t)/dt = - k_q N(t) + k_r (N_o - N(t)) \quad (4.1)$$

where N_o is the initial EL2 state, N(t) is the number of EL^* states at time t, k_q is the rate constant for the $EL2 \Rightarrow EL2^*$, and k_r is for the $EL2^* \Rightarrow EL2$.

A solution of the above rate equation can be represented by:

$$N(t) = C \exp\left[-(k_q + k_r)t \right] + \frac{k_r}{k_r + k_q} N_o \quad (4.2)$$

where C is a constant. Substituting for the initial condition ie. $N(0) = N_o$;

$$N(t) = \frac{k_r}{k_r + k_q} N_o \left[1 - \exp\left[-(k_q + k_r) t \right] \right] (4.3)$$

knowing the time constants and the saturated level, the rate constants can be determined.

Fatigue under IR filtered white light illumination was also observed in the virgin and IBE samples. Figure 4.12 (a) shows i(t) vs. time for virgin and IBE samples under white light and is considered to be due to several competing processes. Figure 4.12 (b) shows the same effect on the expanded time scale. Figure 4.13(a) shows the i(t) response of the above samples after interception of the optical excitation and Figure 4.13 (b) shows the same effect on time expanded scale.

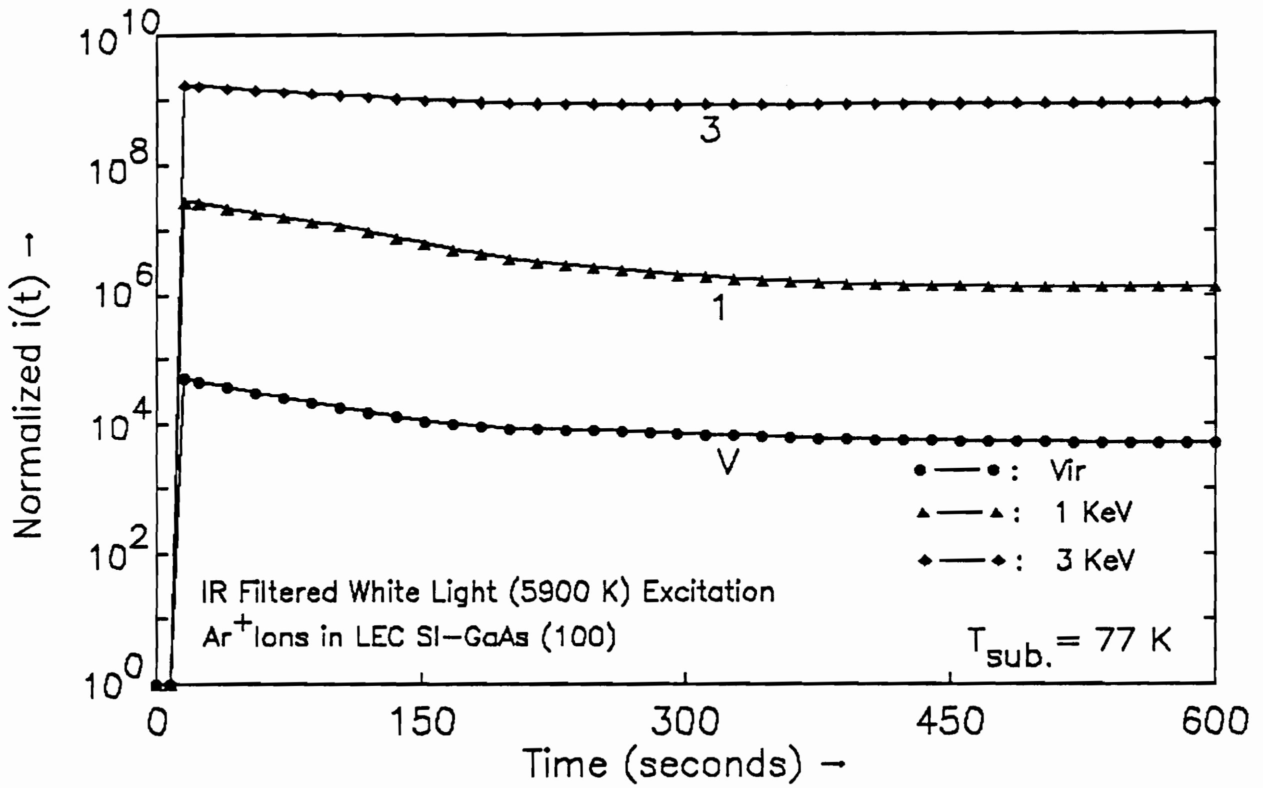

(a)

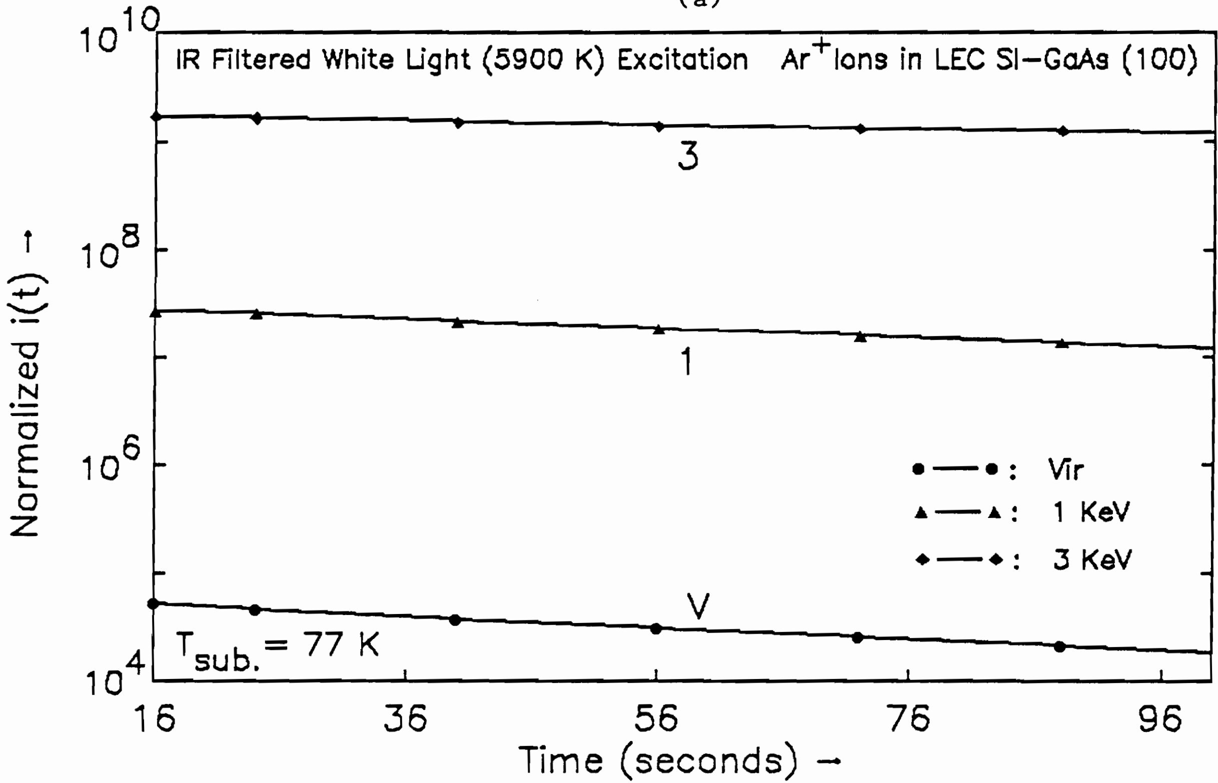

(b)

Figure 4.12 (a) i(t) of Virgin, 1 KeV etched and 3 KeV etched SI GaAs upon IR-filtered white light optical excitation. (b) Same as (a) but on expanded time scale.

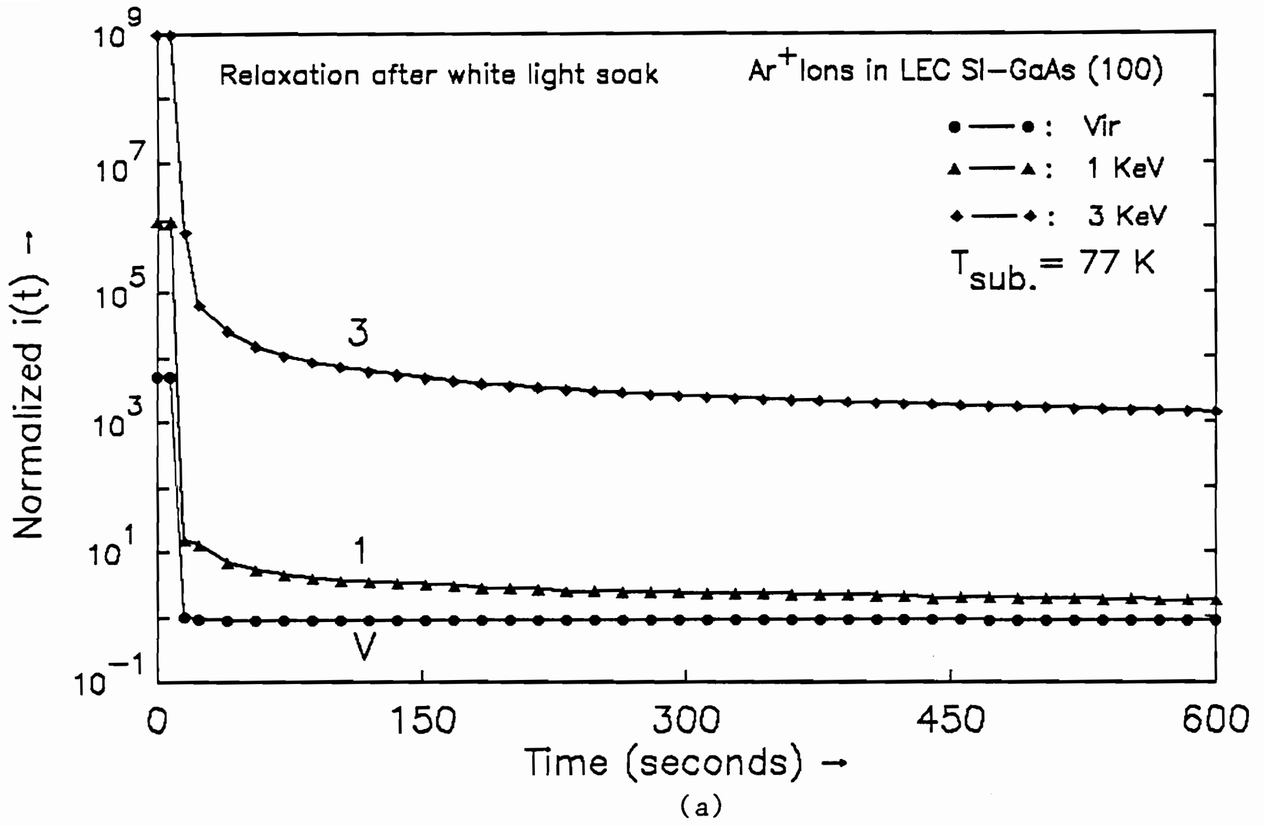

(a)

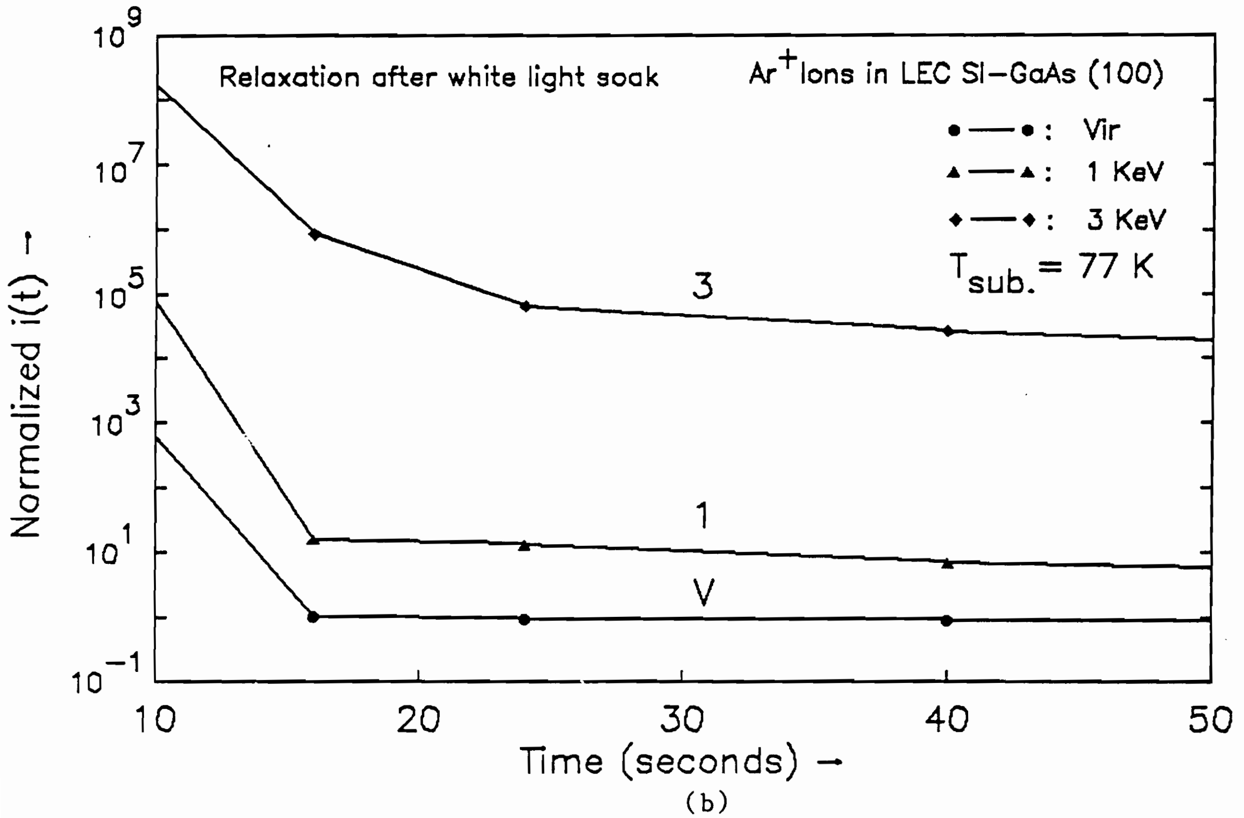

(b)

Figure 4.13 (a) i(t) of virgin, 1 KeV etched and 3 KeV etched SI-GaAs upon termination of white light excitation, (b) Same as (a) on expanded time scale.

4.1.3 Thermally Stimulated Conductivity

Thermally stimulated conductivity (TSC) is a powerful technique to detect and characterize the localized levels in the forbidden band gap. TSC investigations yields tremendous diversity of activation energies. The PVMD system had the capability of temperature excursion between liquid nitrogen temperature (LNT) to 400 K, hence the corresponding activation energies between 0.2 - 0.6 eV only, could be detected. The conductivity peaks widely overlap each other since the resolution of the classical TSC technique allows detection of only the dominant peaks. Appropriate precautions such as good contacts were observed. Also TSC spectra were recorded under constant current condition to prevent minority carrier bulk injection by contact and influence of field sensitive traps. Figure 4.14 (a) shows the conductivity of the samples in the dark and Figure 4.14 (b) shows the response of these samples after irradiation with 1300 nm. Laser diode for 30 min. at 77 K. While no substantial change was observed in the virgin sample, several traps are seen in 1 KeV etched and 3 KeV etched samples. The values of activation energies can be deduced from the Urbach's approximate formula;

$$E_T = 23\ k\ T_m \qquad (4.4)$$

where E_T is the trap depth, T_m is the temperature of the peak and k is the Boltzamann constant. The mixed contribution of neighboring traps leads to a mixed activation energy and mixed extrapolated cross-section, especially in the case when a weak cross-section and low energy trap lies close to a large cross-section high energy trap. The traps location found at 0.26 eV and 0.4 eV are consistent with the other experiments.

A fundamental limitation of TSC is that it cannot distinguish between levels which lie very close to the metal-semiconductor surface and those deeper into the depletion region of a Schottky barrier, because it is not possible to perform TSC measurements with a junction operating in forward bias. Large current in forward biased junction type devices would completely swamp the TSC signal.

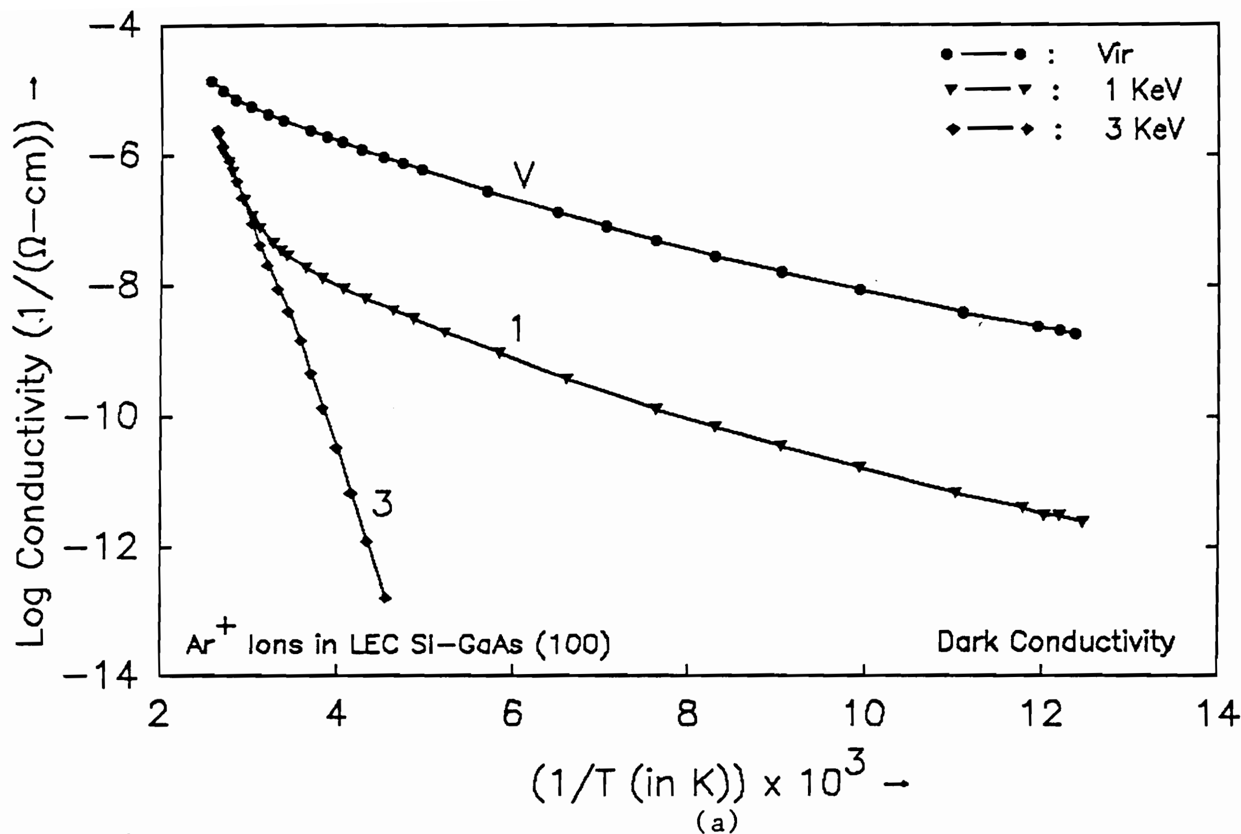

(a)

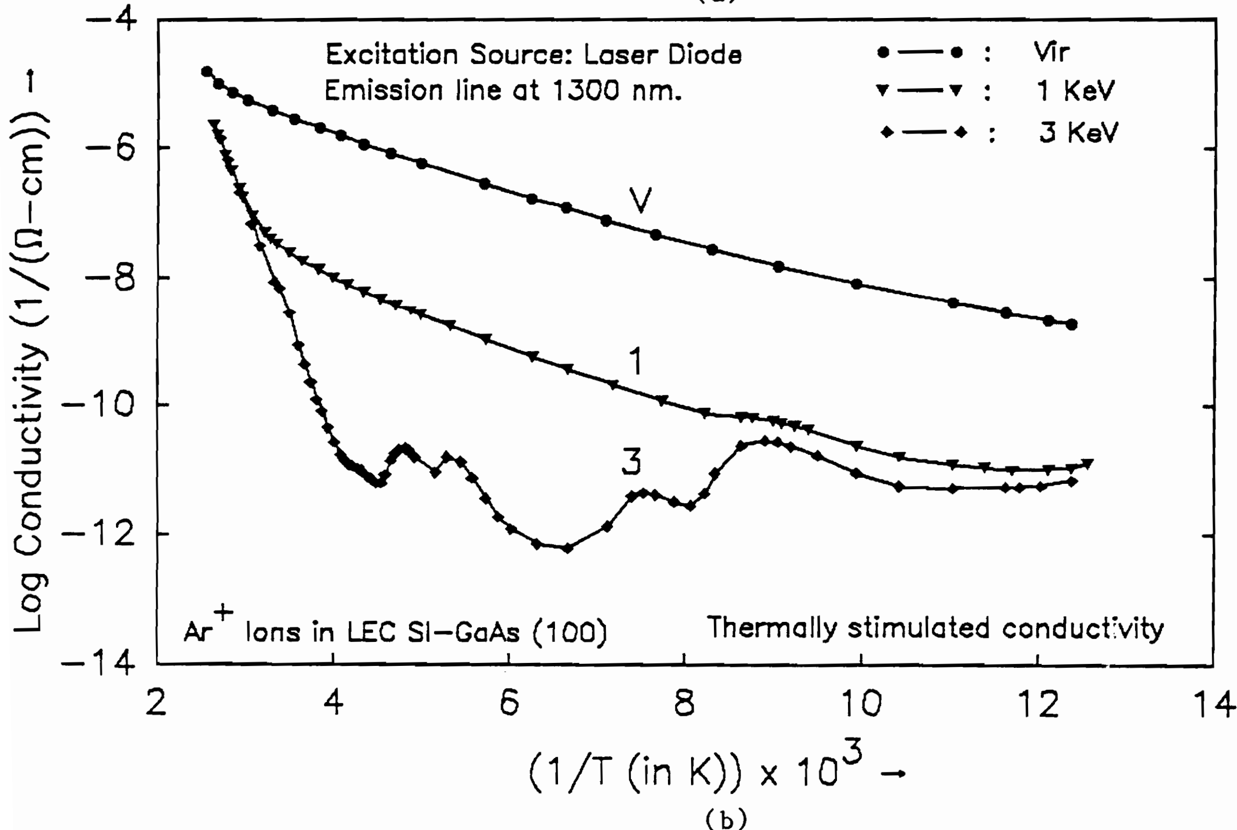

(b)

Figure 4.14 Comparison of thermal cycle of Virgin, 1 KeV etched, and 3 KeV etched SI (100) GaAs, (a) Under dark, and (b) Under monochromatic light absorption relaxation - Thermally stimulated conductivity.

Several light induced parasitic effects such as variation in parasitic channel resistance, power-delay variation, cross-talk and back-gating in ion-implanted GaAs MESFETs have also been reported [197,198]. Arrhenius plots reported by Subramanian et al [198], obtained by pulsing the back gate and analyzing the drain current transients, indicated two sets of traps. One is a well-defined linear region due to EL2, and the other showing overlapping time constants, possibly due to ion beam induced complex defects - identified as [(X, EL2)]. In summary:

Ar^+ ion etching in the 1-3 KeV energy range causes significant changes in the photoconductive response of semi-insulating GaAs. Some of the salient features were:

a) Substantial reduction in dark conductivity and increased photosensitivity in IBE GaAs.

b) Observation of persistent photoconductivity, with none evident in the unetched samples

A model was suggested for the observed PPC effect in low energy Ar^+ ion bombarded GaAs samples. Formation of optically induced metastable defect states having large relaxation times in absence of optical excitation was suggested. This model explains the present finding and some other anomalies observed earlier in ion beam processed devices. D. C. spectral conductivity response at liquid nitrogen temperature also indicated the formation of metastable defect state in the 0.9 eV to 1.4 eV range, and is consistent with the literature.

4.2 Diode and Photodiode Characteristics

MIS Schottky diodes and photodiodes were fabricated using thermally and anodically grown oxides and were characterized in terms of dark current-voltage, barrier height, capacitance-volatge and light current-voltage characteristics to determine the effect of IBE as a function of energy on the electrical diode parameters.

4.2.1 Dark Current-Voltage (I-V) Characteristics

Room temperature diode characteristics of virgin and IBE diodes, measured in dark are shown in Figure 4.15. The substrates for this investigation were: (a) MBE grown n^- on an n^+ substrates and a thermal oxide was grown on these substrates, (b) n-type GaAs procured from Morgan Semiconductor and an anodic oxide layer was deposited on these substrates. Before irradiation, the IV relationship closely follows the diode equation of a Schottky barrier dominated by thermionic emission:

$$I=I_o[\exp\{q(V - R_sI)/nkT\} - 1] \qquad (4.5)$$

where the terms have their usual meanings. Plots of ln(I) vs. qV/kT for IBE devices show a significant deviation from the near ideal behavior. By taking an inverse of the slope of ln(I) vs. qV/kT plot, yields the ideality factor. A decrease in slope, or increase in ideality factor indicated deviation from the normal ideal diode behavior, suggesting the formation of an ion beam induced damage layer at the interface where the depletion layer is formed. The increase in the ideality factor is attributed to ion beam induced damage at the interface where depletion region is formed. The penetration depth of 3 KeV ion is more than the 1 KeV and hence n for 3 KeV is higher than for 1 KeV etched sample. . The surface disorder and/or Ar inclusion introduced by ion bombardment during etching also leads to large reverse saturation current. The increase in I_s was due to the trap-assisted tunneling transport. At low forward voltage, the current is more due to excess recombination while at higher voltage the current tails off due to the large series resistance. The lower value of I_s for 3 KeV etched diodes than 1 KeV etched diodes is consistent with the observation of Wang and Holloway [28,40] that 3 KeV etched surface has lesser number of As related traps. A striking observation in both thermal and anodically oxide Schottky diodes was the observation of lower value of I_o for 3 KeV etched diodes than 1 KeV etched diodes, which indicates smaller number of ion induced traps at the interface. Several observations, by other studies were considered. According to Wang and Holloway, the GaAs has $\approx$ 3 Å of Ga rich surface for energies $\approx$ 1.5 KeV, while ion sputtering at $\geq$ 3 KeV

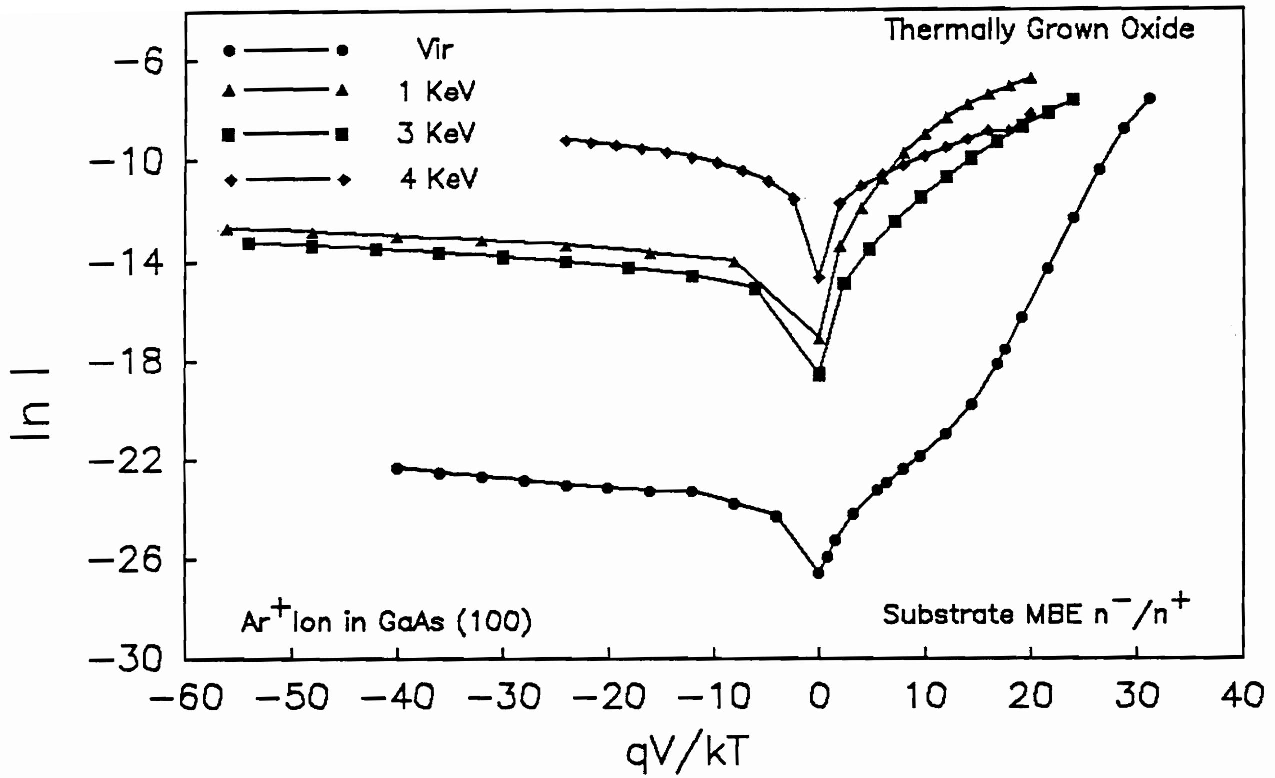

(a)

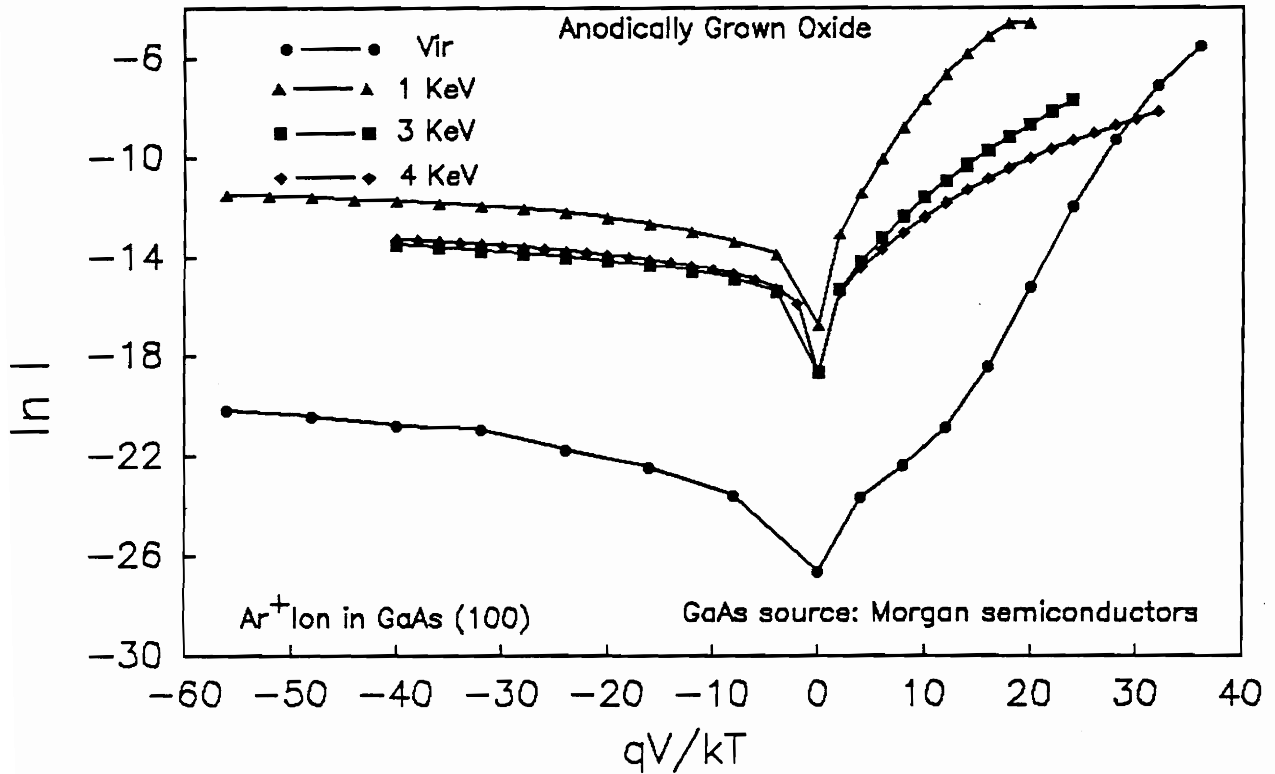

(b)

Figure 4.15 Characteristics of Virgin, 1 KeV, 3 KeV, and 4 KeV etched MIS Schottky diodes, as a function of ion beam energy, (a) thermally grown oxide, and (b) anodically grown oxides.

caused the outermost ≈ 3 Å of GaAs to be rich in As, even though over the Auger sampling depth the surface was depleted in As. The variation in the outermost surface composition could lead to the decrease in reverse saturation current, I_0. Similar observations was made by Freeouf[95,97,123], who attributed an increase in barrier height at 3 KeV to a nearly stoichiometric outer layer. The increase in reverse saturation current density indicates presence of near surface defects providing tunneling/hopping conduction paths through the barrier. Similar studies have also suggested the trap-assisted tunneling in radiation damaged devices.

Anodic oxides are generally considered to have more defect states as compared to the thermal oxide. A comparison of control samples of anodic oxide and thermal oxide Schottky barrier diode at 270 K is shown in Figure 4.16. At lower forward voltage, anodic oxide clearly displayed larger ideality factor than the thermal oxide. In anodic oxide, a large number of surface states remain unsatisfied and dangling due to different oxide growth mechanism than thermal growth mechanisms where the surface atoms are oxidized and are passivated.

The activation energy method, as described in a previous chapter was employed to calculate the barrier height on these devices. Figure 4.17 shows the activation energy plots for the Schottky diodes, (a) thermal oxide, and (b) anodically grown oxide, as a function of ion beam energy. Appropriate corrections were applied for the ideality factor and were calculated from the ln(I) vs. qV/kT plots.

Figure 4.17 shows the degradation in the barrier height by ion beam etching. The decrease in the barrier height is attributed to the high density of donor-like-traps with a depth distribution dependent on the energy of the incident ions. The traps are positively charged and create surface layer of very high electric field. The tunneling probability of electrons through this narrowed barrier increases, and, consequently a reduced barrier height results. It is observed from both kinds of diodes that the barrier height for 3 KeV etched diodes is greater than the 1 KeV etched diodes. This observation lends credence to

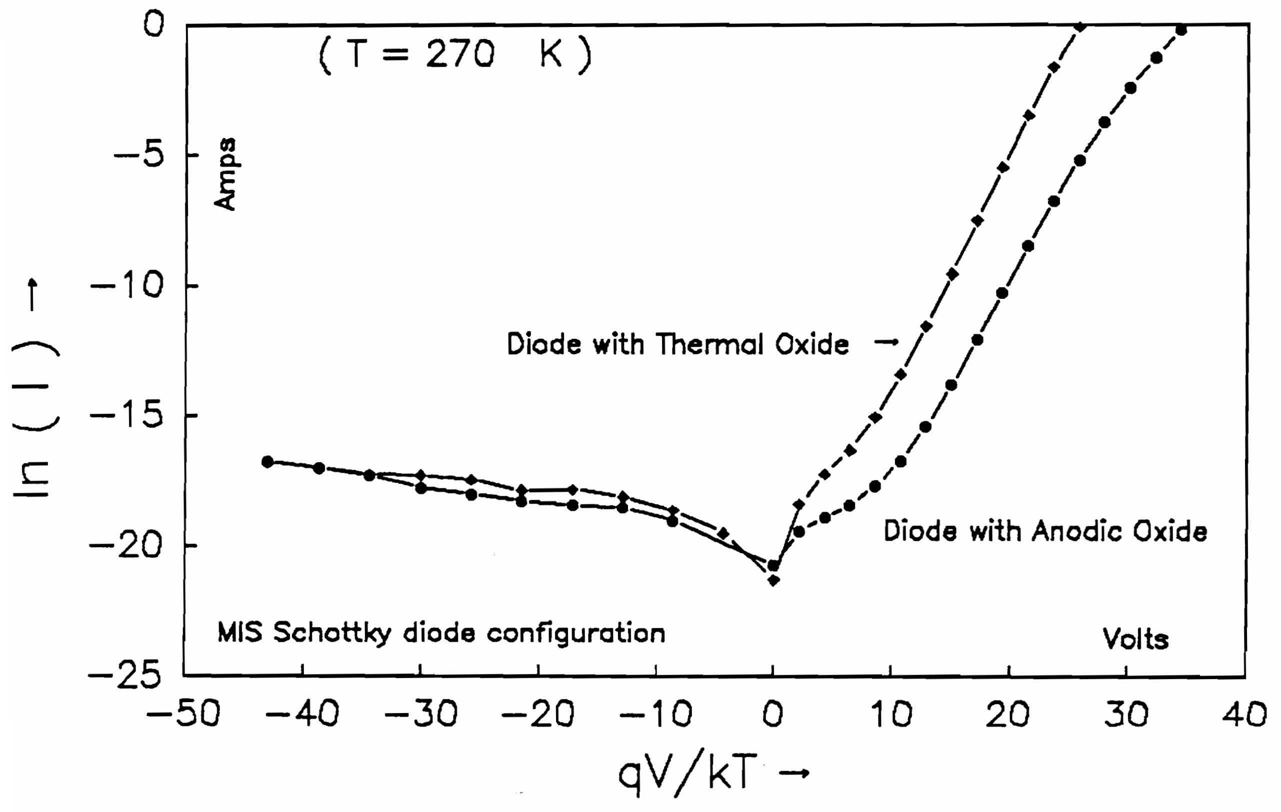

Figure 4.16 Comparison of MIS Schottky diode with thermal and diode oxide at 270 K.

(a)

(b)

Figure 4.17 ln (I_f/T^2) vs. q/kT or activation energy method to determine the barrier height for (a) Thermally grown oxides, and (b) Anodically grown oxide, as a function of ion beam energy.

the model proposed by Freeouf. Recently a multibarrier model was proposed by Chekir et al.[199] which invalidates the existing barrier height determination methods. The model suggests a coexistence of a low barrier and a high barrier diode, having different influences as a function of temperature. Appropriate corrections such as image force lowering, chemical reactivity of the metal are recommended, in their model. Barrier heights were also computed from the C-V plots (shown later). The barrier height values obtained by the C-V were different than I-V, primarily because of (a) different probing regions, and (b) the assumptions in C-V analysis that the N_D is constant. The conductance vs. temperature variation is shown in Figure 4.18, for MIS Schottky barrier diodes fabricated on (a) thermally grown oxides on MBE n^-/n^+, and (b) anodically grown oxides on Morgan Semiconductor wafers. Several striking features were noticed. The conductance of the virgin diodes fabricated on the Morgan Semiconductor substrates was relatively flat, while the conductance of diodes fabricated on MBE grown substrates stayed flat till about 300 K and then dropped a little. This is contrary to what is expected. The only plausible explanation according to Taylor et al[41] is that at lower temperature the surface conduction dominates due to surface states, creating a strong leakage component. It will be seen later that MBE material is usually defect free, hence as the temperature increases the surface leakage component decreases, while I_0 does not change much and hence overall conductance decreases. To cross check the above finding, several diodes, fabricated on MBE grown materials in various configurations, were characterized and similar observations was made, as shown in Figure 4.19. The diodes bombarded with ion beam showed increase in conductance as a function of temperature because the surface defects provide conduction conduits, with increased thermal activation.

In summary:

An increase in diode ideality factor (deviation from ideal behavior), reverse saturation current and decrease in barrier height was observed with increase in ion beam energy.

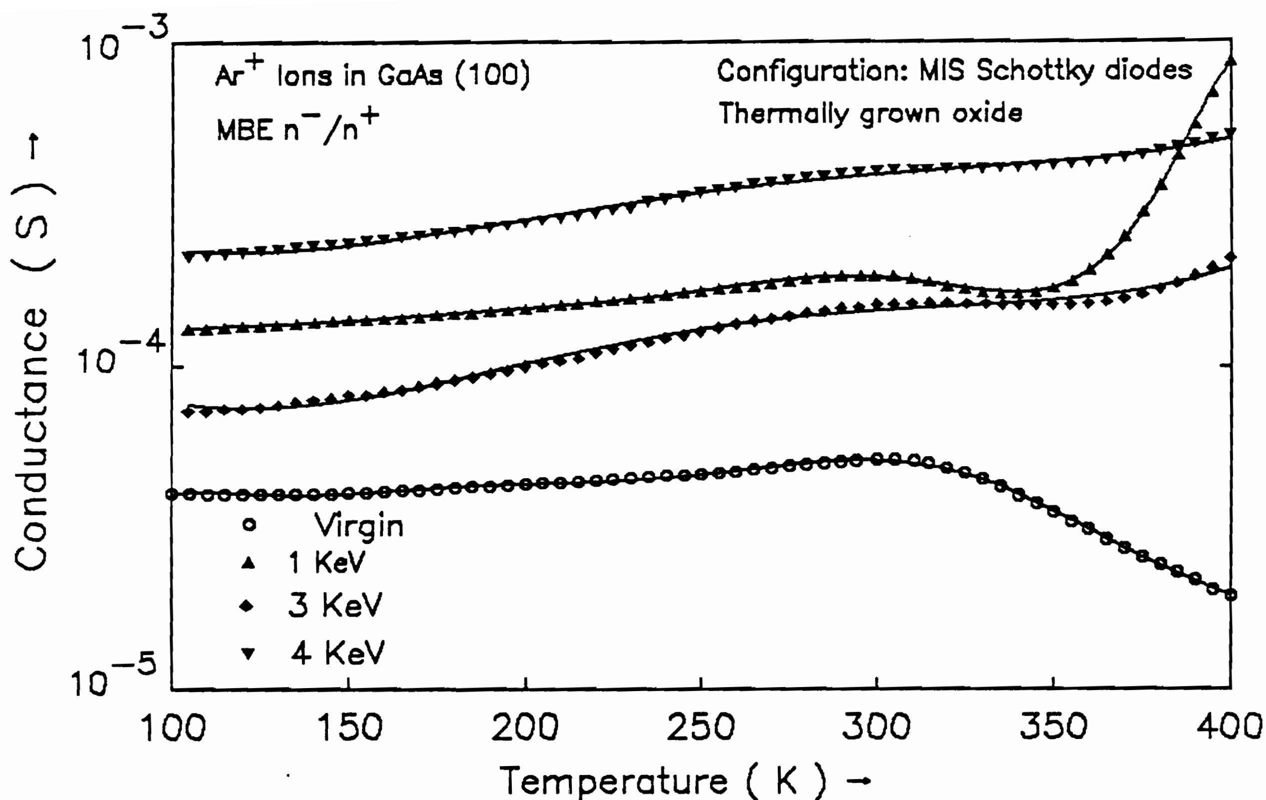

(a)

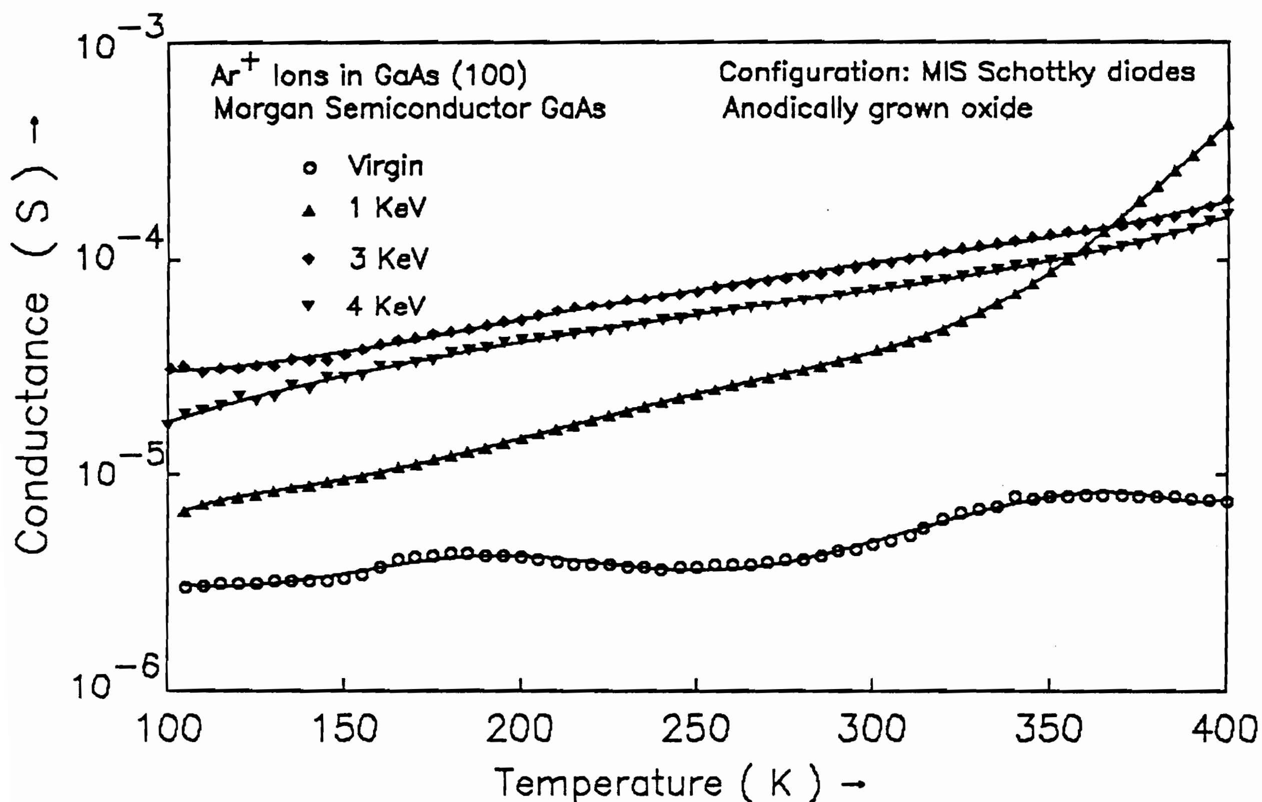

(b)

Figure 4.18 Conductance variation as a function of temperature for Virgin, 1 KeV etched , 3 KeV etched, and 4 KeV etched MIS Schottky barrier diodes, (a) Thermally grown oxides, and (b)Anodically grown oxides.

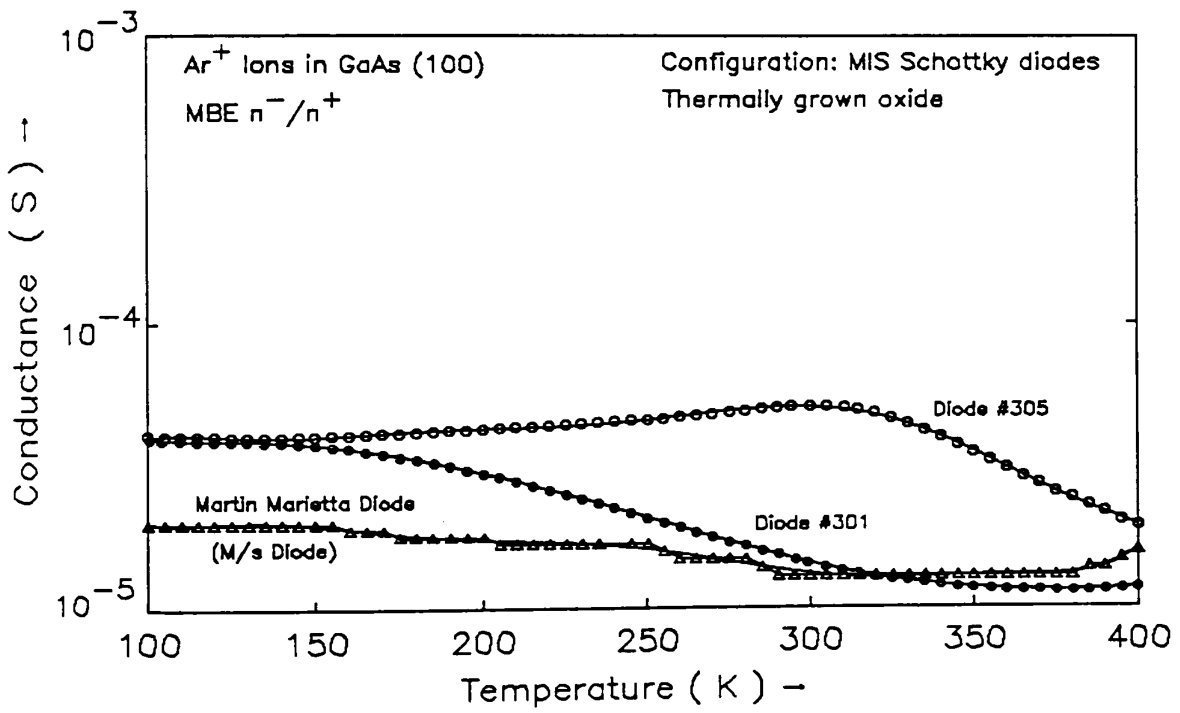

Figure 4.19 **Conductance variation as a function of temperature for virgin diodes fabricated on MBE grown materials.**

4.2.2 Light Current-Voltage (I-V) Characteristics

Illuminated current-voltage (I-V) characteristics of the Schottky photodiodes fabricated on MBE grown substrates are shown in Figure 4.20. The temperature of the diodes was maintained at 20 C using a Cambion Bipolar Temperature Controller. It was clearly observed, as expected that both the open circuit voltage and fill factor of solar cells on IBE diodes deteriorated significantly with increase in ion beam energy. The open circuit voltage is given by;

$$V_{OC}=nkT/q \ln[(1 + J_{SC}/J_O)] \qquad (4.6)$$

where J_{SC} is the short circuit current density and J_O is the saturation current density. The increase in J_O, as indicated by the dark I-V characteristics accounts for the deterioration in open circuit voltage. It is worth noticing that open circuit voltage of 3 KeV etched photodiodes is higher than for 1 KeV etched photodiodes due to lower reverse saturation current, and is consistent with the theory. According to Ghandhi et al.[56] the decrease in open circuit voltage and fill factor are attributed to the increase in reverse saturation current at the interface due to IBE, rather than by a decrease in the barrier height. The thesis to this recommendation was based upon the fact that the slope of $1/C^2$ vs. V plot was different from the control sample, which is attributed to non-uniform doping in this text. Table 4.2 list some photovoltaic performance data obtained under simulated AM1 conditions of control and IBE Schottky photodiodes.

In summary-IBE causes an increased reverse saturation current and hence significant drop in Voc of photodiodes

4.2.3 Capacitance-Voltage Characteristics

The swept (30 mV/sec) 1 MHz. C-V characteristics at room temperature are shown in Figure 4.21. For control, 1 KeV etched, 3 KeV etched, and 4 KeV etched Schottky diodes fabricated on (a) thermally grown oxide, and (b) anodically grown oxides were used. The C-V relation to access the doping concentration on uniformly doped substrates for MS

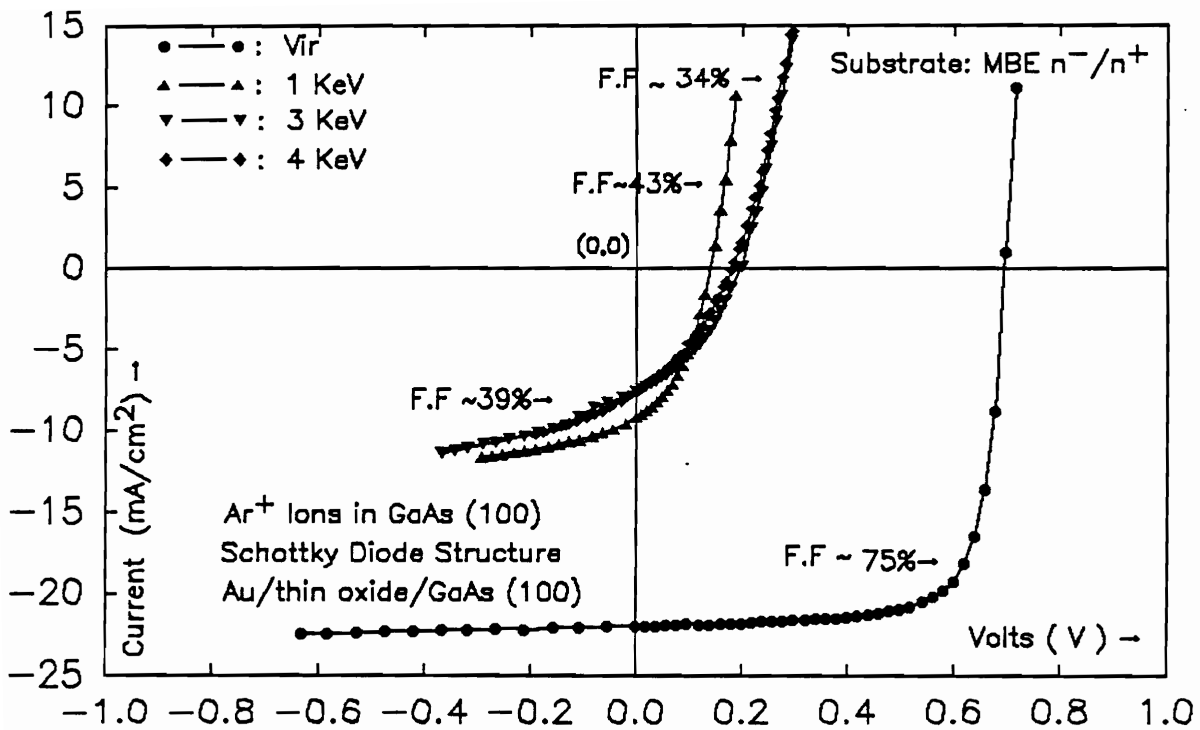

Figure 4.20 **Schottky diode characteristics under AM1 (simulated using GE Gemini 300 Arc Lamp) as a function of ion beam energy; Virgin, 1 KeV, 3 KeV, and 4 KeV etched.**

Table 4.2 Typical photodiode parameters.

sample	V_{oc} (volts)	F.F. %	R_s (Ω/cm^2)
vir	0.665	75	2.54
1 KeV	0.160	43	4.34
3 KeV	0.192	38	11.46
4 KeV	0.181	34	12.34

Schottky barrier diode is given by the relation;

$$\frac{1}{C^2} = \left[\frac{2(V_R + V_I)}{A^2 \, q \, \varepsilon_s \, N_D} \right] \qquad (4.7)$$

and holds true for MIS devices also as long as the device is operated in depletion or deep-depletion mode. The symbols have their usual meanings and V_I is the magnitude of the voltage intercept and includes terms involving flat band voltage and oxide capacitance. The donor concentration as calculated from the slope of the curves and is very close to the doping of the epitaxial layer ($\approx$ 4-5x10^{16}/cm^3). This indicates that active dopant concentration practically remains unchanged after IBE. However, near zero bias a slight decrease in slope is observed for ion etched diodes which indicates an increase in effective donor concentration in the ion beam damaged layer and is consistent with the literature. The technique is rather insensitive to the effects of surface damage, possibly due to the fact that the region being probed is away from the damage.

In order to qualitatively and quantitatively identify the damage, capacitance vs. frequency experiments were performed on the MIS Schottky barrier diodes fabricated for the present investigation. Figure 4.22 shows capacitance vs. frequency for the virgin, 1 KeV etched, 3 KeV etched, and 4 KeV etched Schottky diodes fabricated on MBE grown substrates at (a) zero-bias, and (b) at -1 V. Figure 4.23 shows similar response on substrates procured from Morgan Semiconductors. Capacitance of the devices fabricated on virgin (unetched) samples is practically constant. However, IBE samples show a frequency dispersion at low frequencies. Such low frequency dispersion can be attributed to the capacitance contribution of traps in the damaged surface region acting in series with the space charge region capacitance [46]. As hypothesized earlier, longer lifetime electron traps in the damaged and partly amorphous near-surface regions can possibly contribute to the low frequency dispersion in the IBE samples. The frequency dispersion effect is expected to be smaller at a large reverse bias because of shift of space charge region to a less damaged

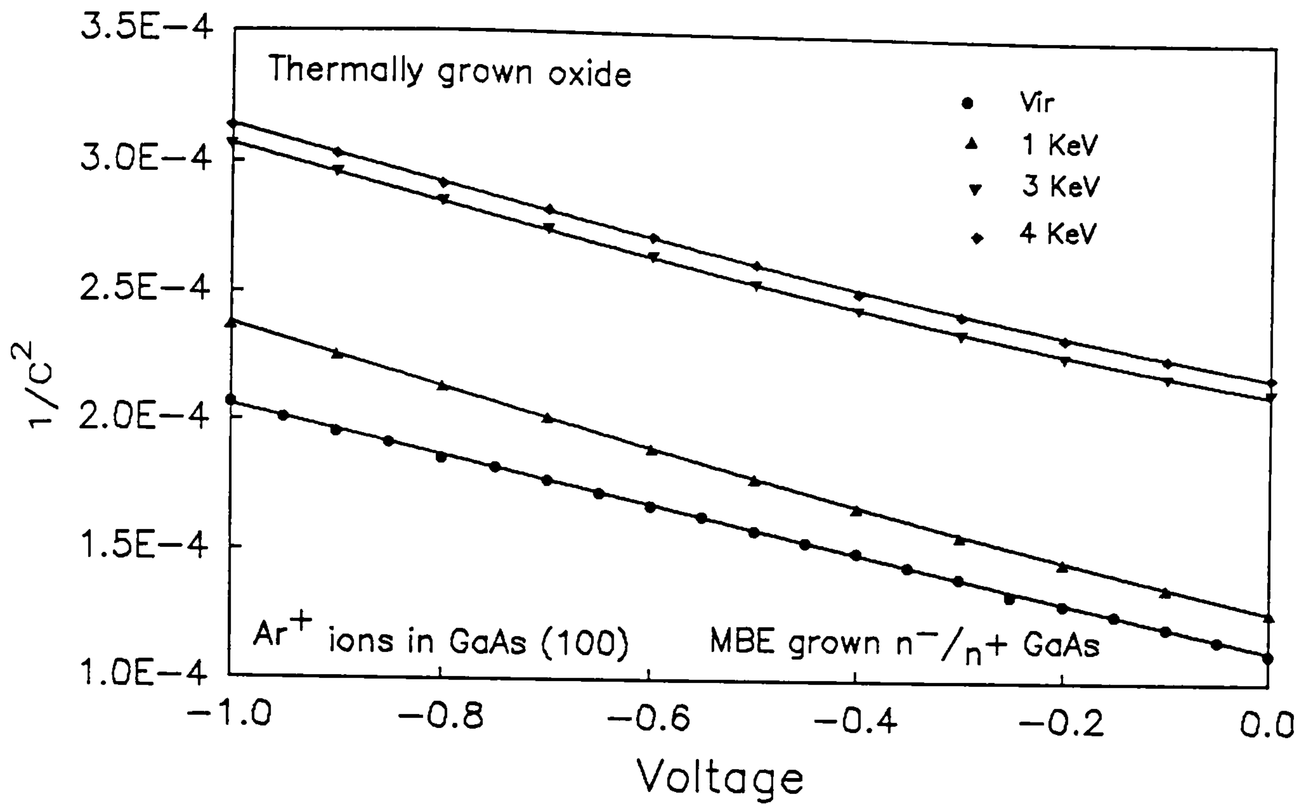

(a)

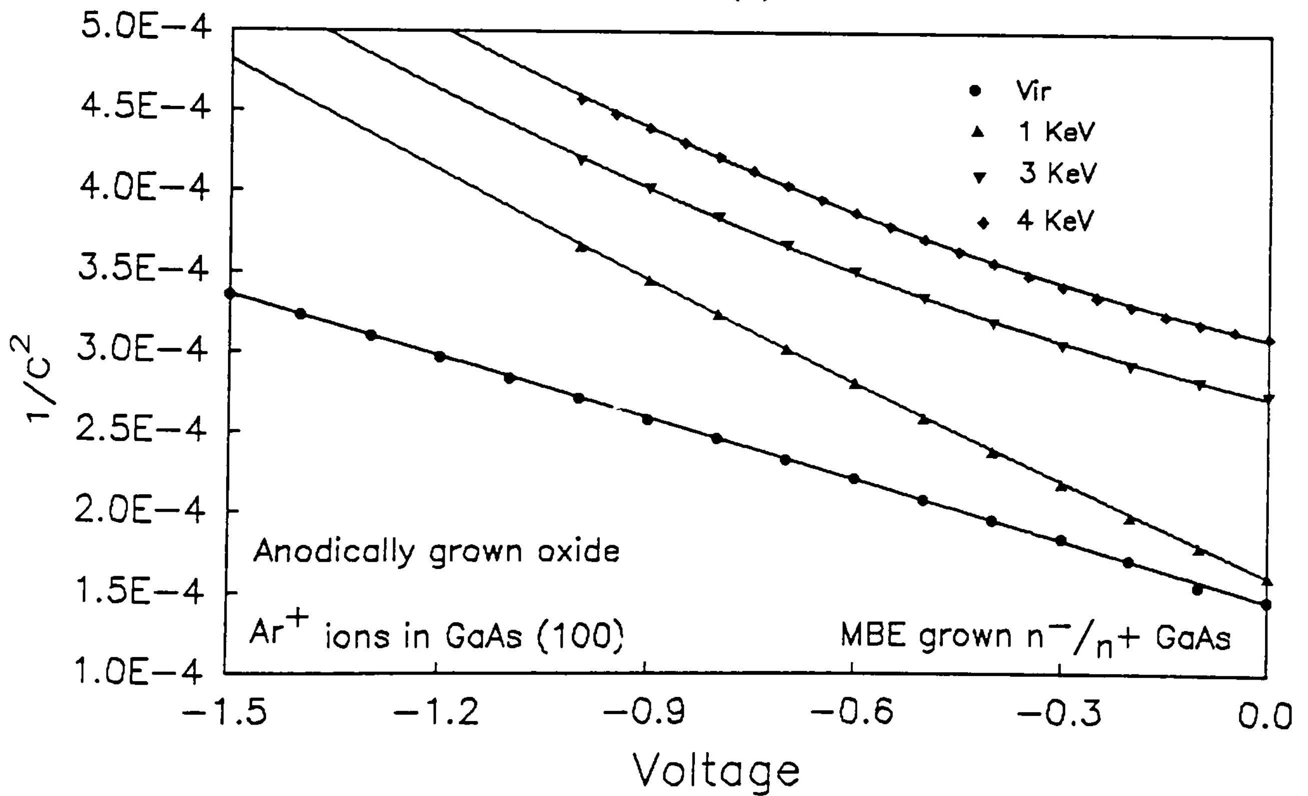

(b)

Figure 4.21 $1/C^2$ vs. reverse voltage characteristics of virgin, 1 KeV, and 3 KeV etched Schottky diodes, (a) Thermally grown oxides, and (b) Anodically grown oxides.

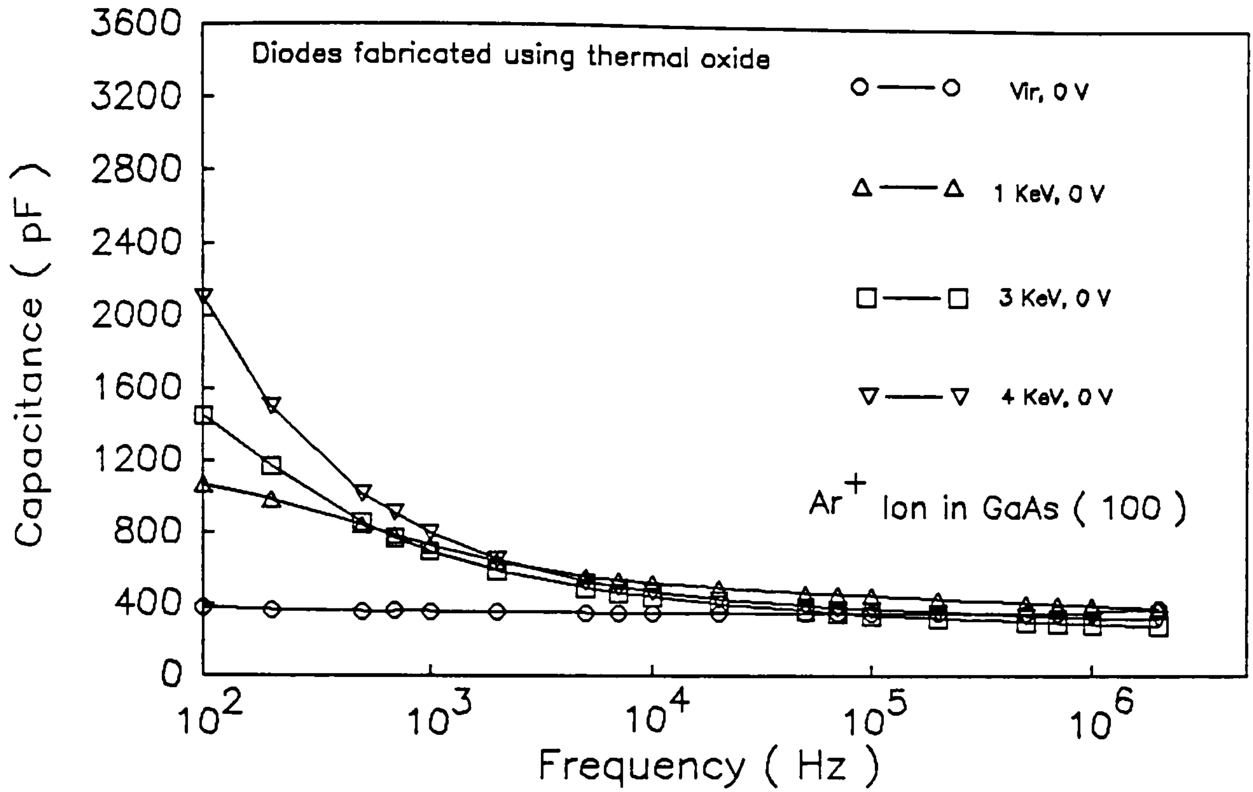

(a)

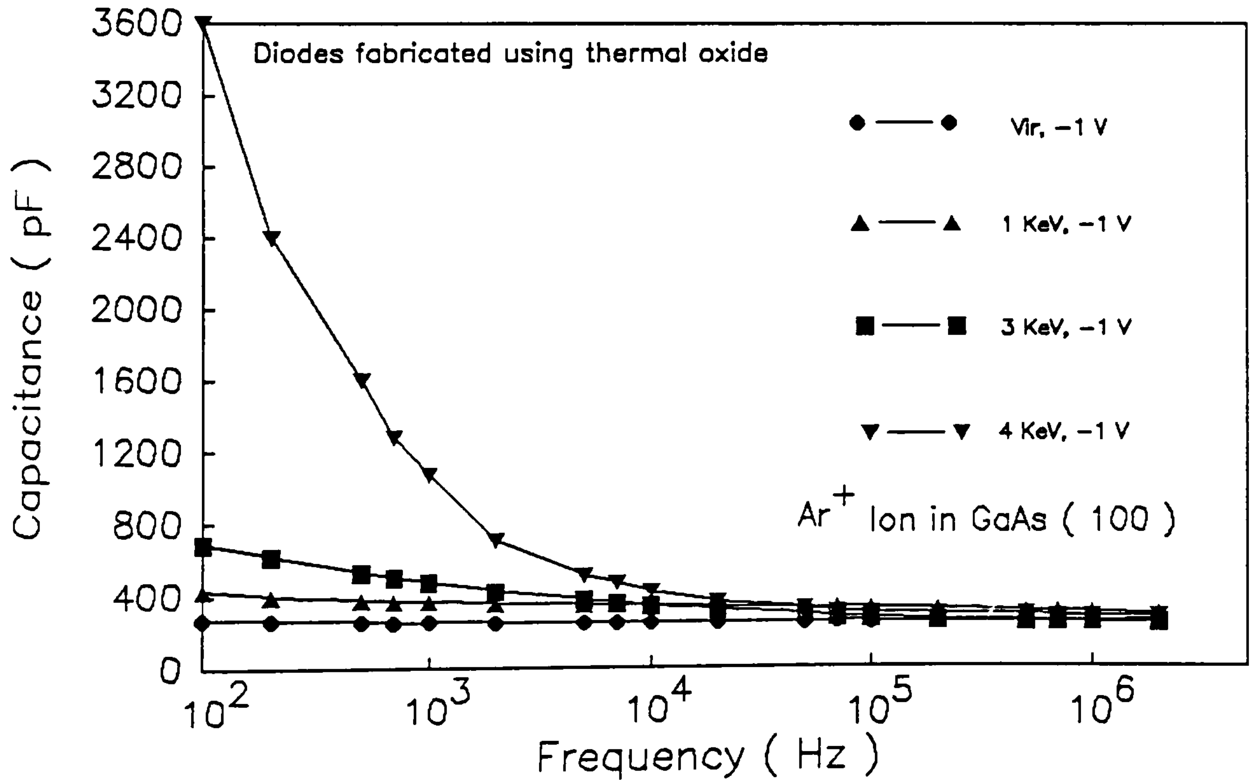

(b)

Figure 4.22 Capacitance vs. frequency for virgin, 1 KeV, 3 KeV, and 4 KeV etched Schottky diodes with thermally grown oxides at (a) zero bias, and (b) at -1 V.

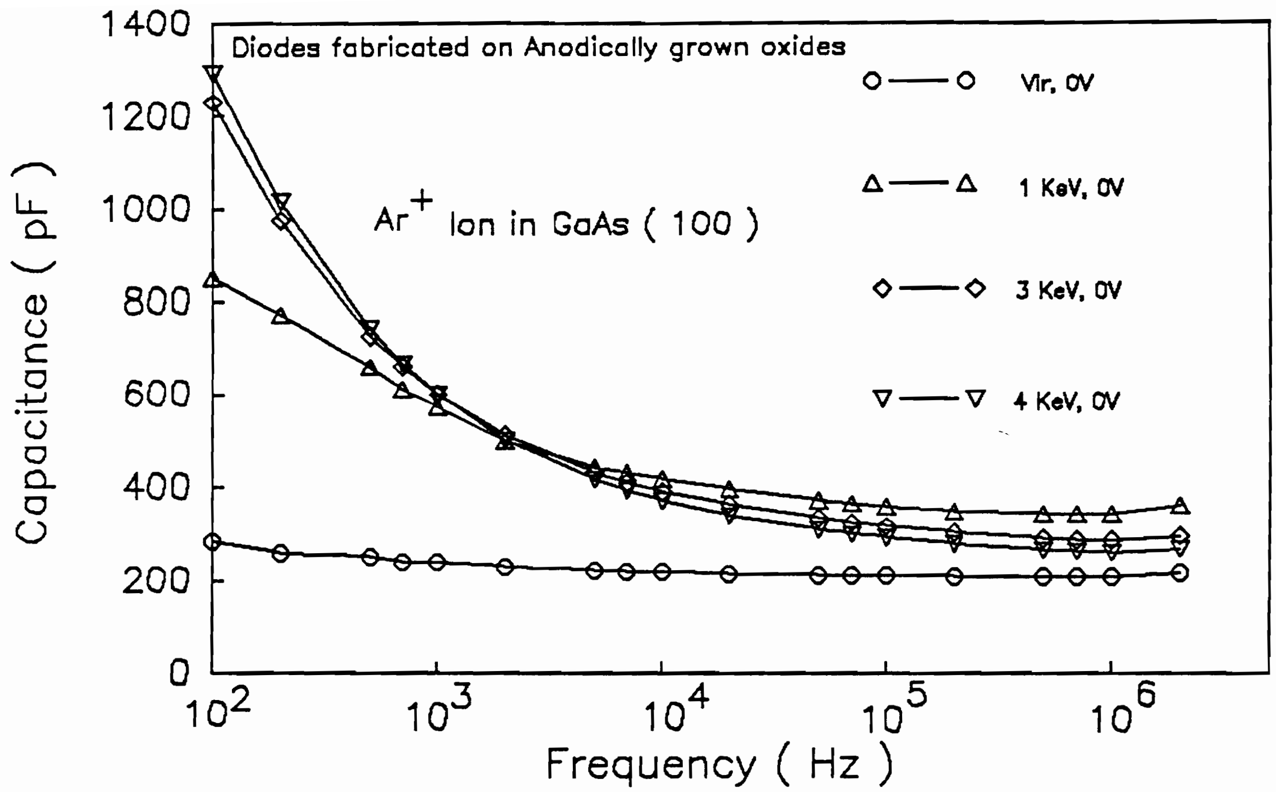

(a)

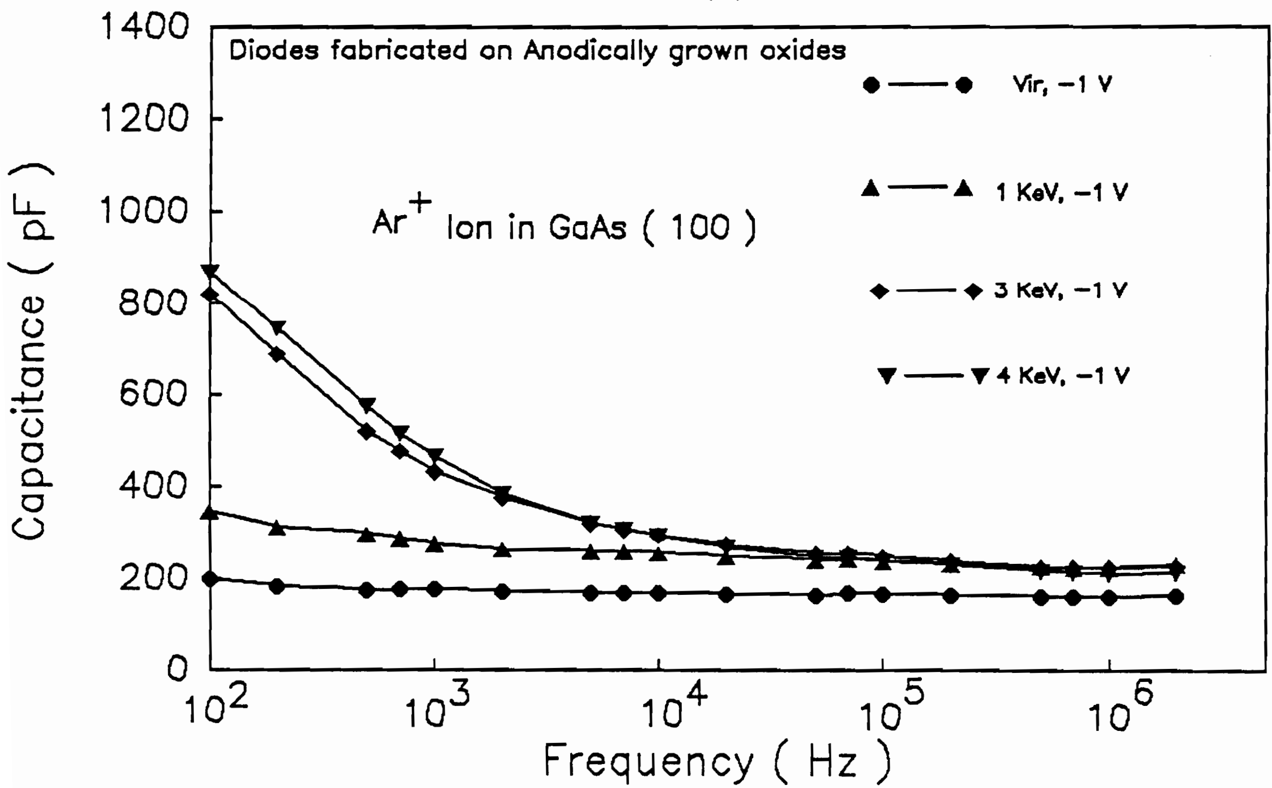

(b)

Figure 4.23 Capacitance vs. frequency for virgin, 1 KeV, 3 KeV, and 4 KeV etched Schottky diodes with anodically grown oxides at (a) zero bias, and (b) at -1 V.

region, where the ion induced trap density is lower than the dopant concentration. According to Sen et. al.[47] the total capacitance can be expressed as;

$$C = C(\omega) + C_D \tag{4.8}$$

where,

$$C(\omega) = \frac{2\varepsilon q^2}{kT} N_t \left[\frac{\omega_1}{\omega} \right]^{\frac{1}{2}} \tag{4.9}$$

with $\omega_1 = A \exp(-qE_t/kT)$, and A = constant

where E_t is the trap depth. It was proposed that the damaged and partly amorphized layer near the surface has large effective electron concentration at low frequencies, and controls capacitance. This large electron concentration clamps the depletion layer thickness, as long as frequency is low enough and temperature high enough so that the traps can respond. Under these conditions, the diode capacitance can be disregarded because the space charge is confined to the top amorphized layer. Under reverse bias, low temperature and/or high frequency conditions, the space charge extends into the lower, less damaged region, and the capacitance of the diode dominates. For high frequency capacitance, the traps cannot respond fast enough and also the damage in the bulk material partly compensates the background donors in IBE devices resulting in large space charge width, such that the capacitance is less and does not change appreciably with increasing ion beam energy.

In summary; capacitance-voltage technique was found be quite insensitive to ion beam induced damage. The IBE introduces a strong low-frequency dispersion in the Schottky devices. A quantitative analysis can furnish the trap density.

A summary of MIS Schottky diode parameters obtained from the dark current-voltage, capacitance-voltage, and capacitance dispersion experiments is provided in Table 4.3 (a) for thermally grown oxides, and (b) for anodically grown oxides.

Table 4.3 **Diode parameters as a function of ion beam energy - (a) Thermal Oxides, (b) Anodic oxides.**

Sample Description	ϕ_b (eV)	A^{**} Amp/K^2-cm^2	Isat (A)	$n^{\dagger}$	Cap @ 1 KHz (pf)
Vir	0.880	0.6	$1.6\text{-}4.7\times10^{-14}$	1.25 - 1.28	360
1 KeV	0.535	0.942	$3.35\text{-}8.76\times10^{-7}$	1.33 - 1.72	687
3 KeV	0.589	1.207	$1.72\text{-}2.3\times10^{-7}$	1.76 - 2.57	670
4 KeV	—	—	$4.04\text{-}7.2\times10^{-6}$	2.87 - 4.784	815

(a)

Sample Description	ϕ_b (eV)	A^{**} Amp/K^2-cm^2	Isat (A)	$n^{\dagger}$	Cap @ 1 KHz (pf)
Vir	0.9169	10.666	5.601×10^{-13}	1.631	198
1 KeV	0.5845	2.9152	$0.113\text{-}7.83\times10^{-7}$	1.675	280
3 KeV	0.6343	5.834	$1.21\text{-}1.7\times10^{-7}$	1.705 - 2.22	450
4 KeV	0.5785	0.6	1.24×10^{-7}	1.917 - 2.68	430

(b)

† :Values are reported for two different exponential regions.
(a) Diodes fabricated using room temperature water-vapor saturated oxide
(b) Diodes fabricated using anodically grown oxide

4.3 Spectral Response and Quantum Efficiency

The usefulness of solar cell spectral response data as a design parameter and diagnostic tool stem from the fact that relative contribution of photons of different energy to that relative contributions of photons of different energy to the short circuit photocurrent, can readily be obtained. The external quantum efficiency η_{ext} can be defined as;

$$\eta_{ext} = \left[\frac{I_{sc}(\lambda)}{q \, N_{ph}(\lambda)} \right] \qquad (4.10)$$

where the symbols have their usual meanings. A plot of η_{ext} vs. λ will provide the absolute spectral response which along with an appropriate solar spectrum yields the total short circuit current of the cell. Since the damage resides at the interface, the spectral response toward the blue end of the spectrum must deteriorate. Hence, the external quantum efficiency of the virgin and IBE MIS Schottky photodiodes was measured as a function of the wavelength, and is shown in Figure 4.24. It was evident that the response towards the blue end of the visible spectrum reduced as compared to the virgin diode. It was interesting to note that ratio increased continuously with the wavelength indicating that damage extends into the bulk, in agreement with Pang. The zero bias spectral response ratio drops at lower wavelengths due to lower mobility in the partly amorphous and damaged surface region. The ratio is significantly lower for 3 KeV etched samples. The response also drops towards the absorption band edge of the GaAs. The drop is 19% for 1 KeV etched diodes as compared to 26% for 3 KeV etched diodes and is linked to the higher degree of disorder. The noisy response was due to the rather small area of the device. In a different context, experiments were performed where traps were saturated using a second illumination source and observing the spectral response. Hence as a concluding remark for this section, substantial reduction in mobility in surface region is indicated by near-blue region of the spectral response.

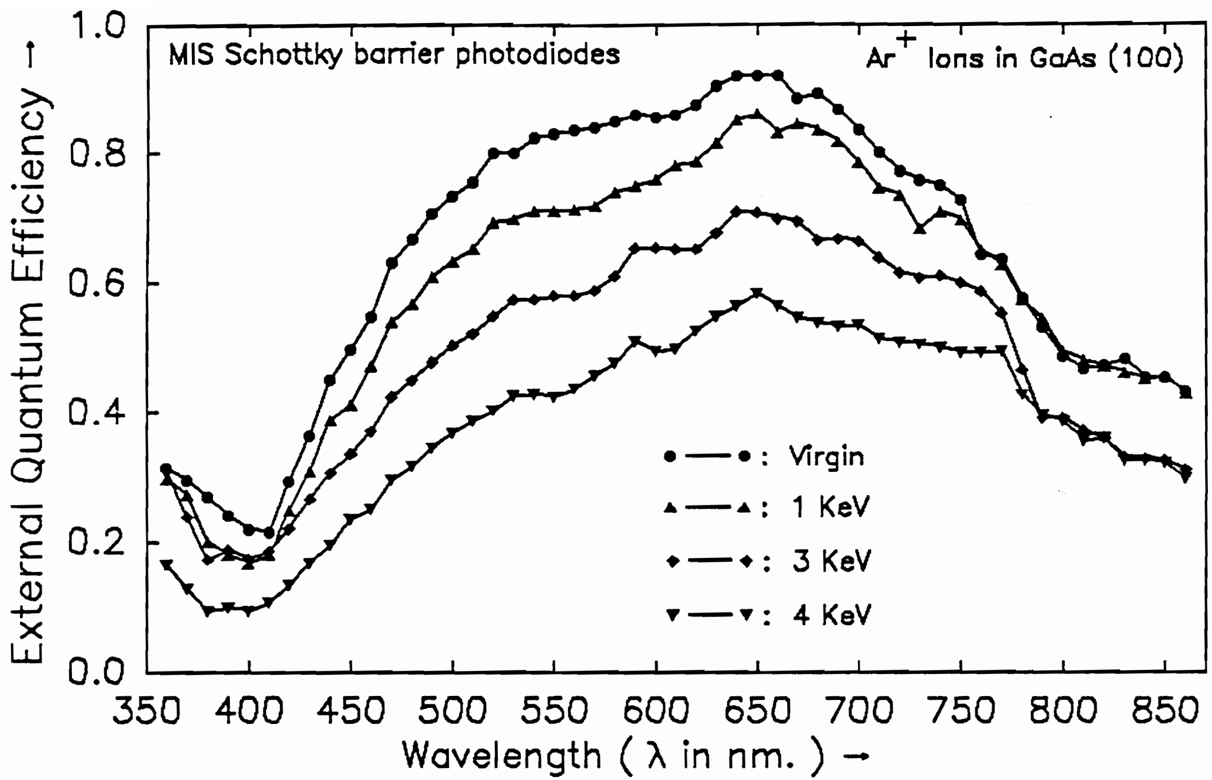

(a)

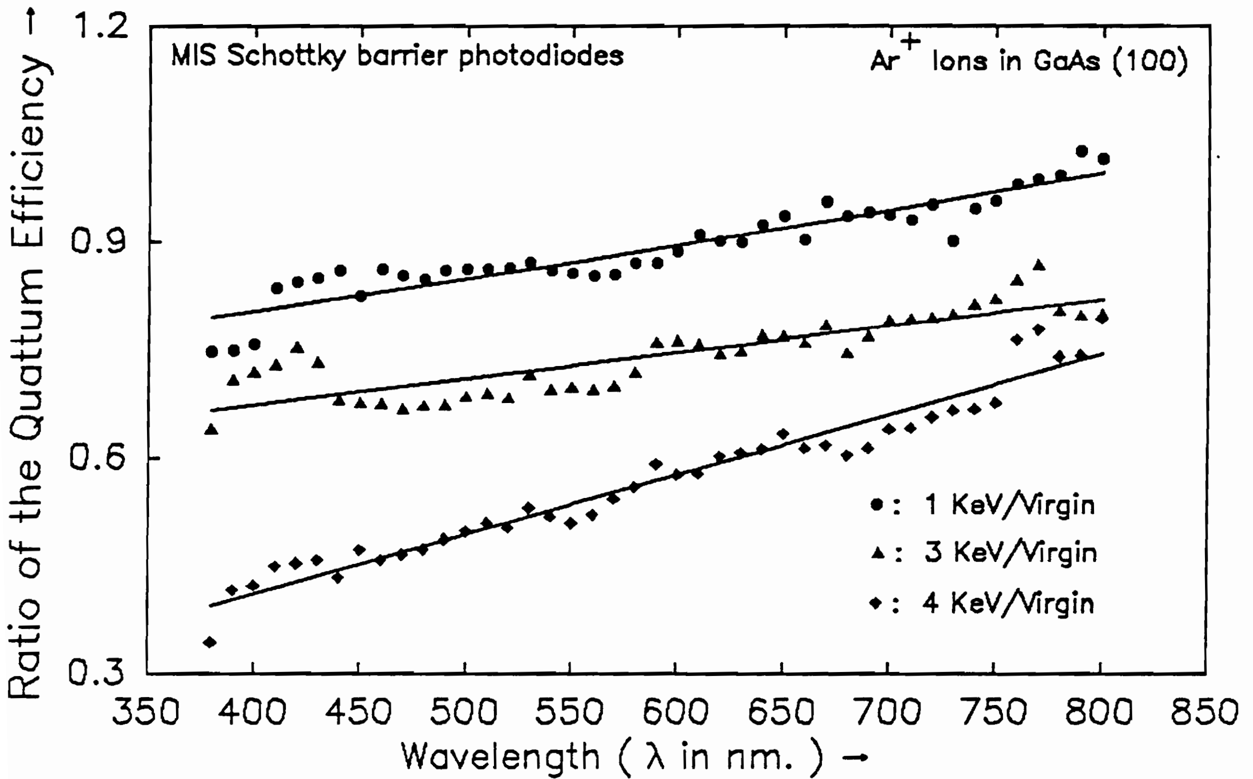

(b)

Figure 4.24 (a) External quantum efficiency of MIS Schottky barrier photodiodes as a function of ion beam etch energy (virgin, 1 KeV, 3 KeV, and 4 KeV), (b) Ratio of external quantum efficiency of 1 KeV, 3 KeV, and 4 KeV etched photodiodes to External Q.E. of virgin diode.

4.3.1 Sub-bandgap Absorption and Internal Photoelectric Emission

In disordered semiconductors, the periodic potential is greatly distorted causing the density of states in the conduction and valence bands to tail exponentially into the forbidden gap. As a result of this band-tailing, the absorption coefficient falls off exponentially, because sub or near band gap photons can excite localized defect sites to the conduction band. Thus an exponential current response vs. photon energy (for sub band gap photons) yields the tail absorption coefficient (Urbach tail) and hence, degree of disorder. Since generally speaking, sub-bandgap absorption occurs from valence band tail states to the conduction band, or $\alpha \propto \exp(E / E_0)$, where, E is the photon energy, and E_0 is the characteristic slope of the Urbach tail. E_0 is a measure of disorder, and a small slope would indicate a sharp valence band tail and hence low mid gap defects. In Figure 4.25 (a), a plot of log(QE) vs. E, for the virgin and 1 KeV etched diodes are shown. Lower slope of the virgin diode as compared to the I KeV bombarded sample indicates fewer defects in the virgin sample. It needs to be emphasized that such measurements in GaAs Schottky photodiodes represent a preliminary investigation. Also extremely small current response prevented measurement of 3 KeV etched and 4 KeV etched photodiodes. As described in section 2.4.2, when the photon energy of the incident beam is reduced below the smallest gap in the junction device, the current due to the internal photoelectric emission of carriers over junction barriers less than the band gap can be detected. Figure 4.25 (b) shows the square root of quantum efficiency vs. energy and was used to estimate the barrier height. Barrier heights of approximate 0.9 eV for virgin and 0.8 eV for 1 KeV were seen from these curves and are different from the activation energy method. The primary reason for such a discrepancy was attributed to the small signal-to-noise ratio for such small area devices.

4.4 Deep Level Transient Spectroscopy (DLTS)

DLTS spectra of Control and Ar^+ ion beam etched MIS Schottky barrier photovoltaic devices fabricated using, (a) thermal oxides on MBE grown n^-/n^+, and (b)

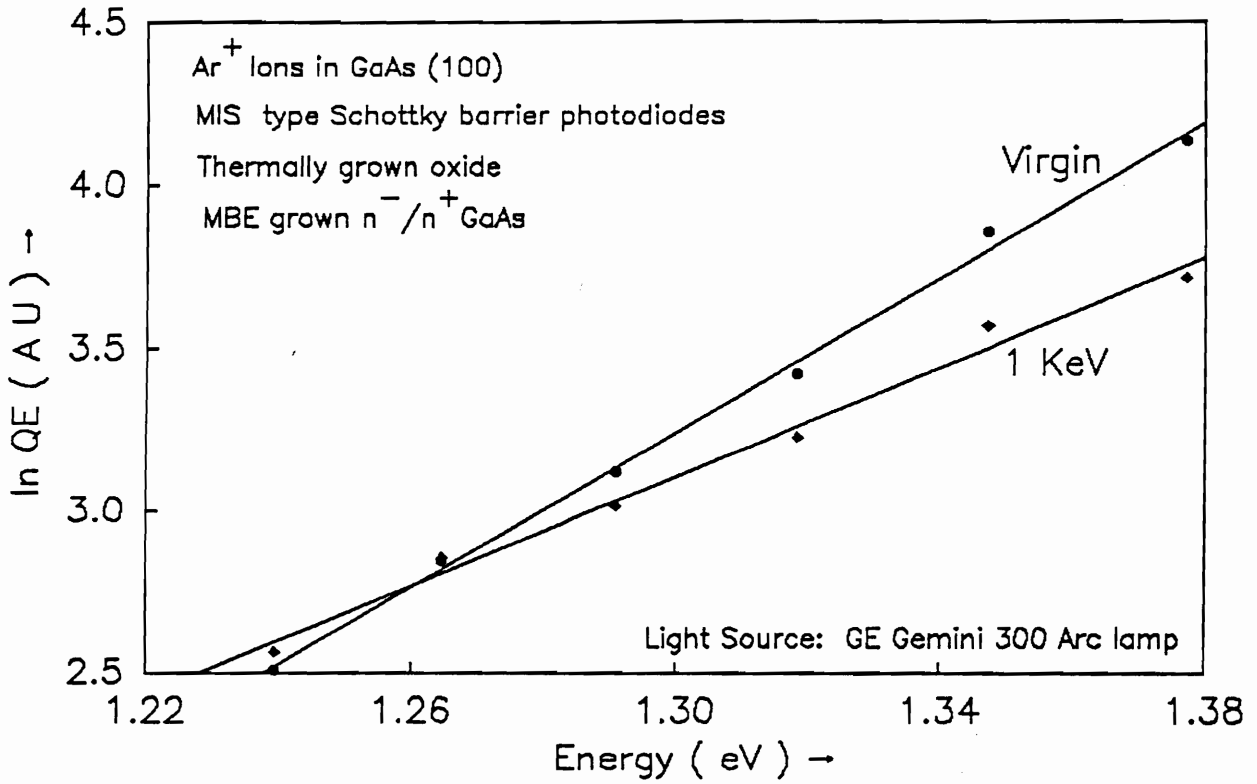

(a)

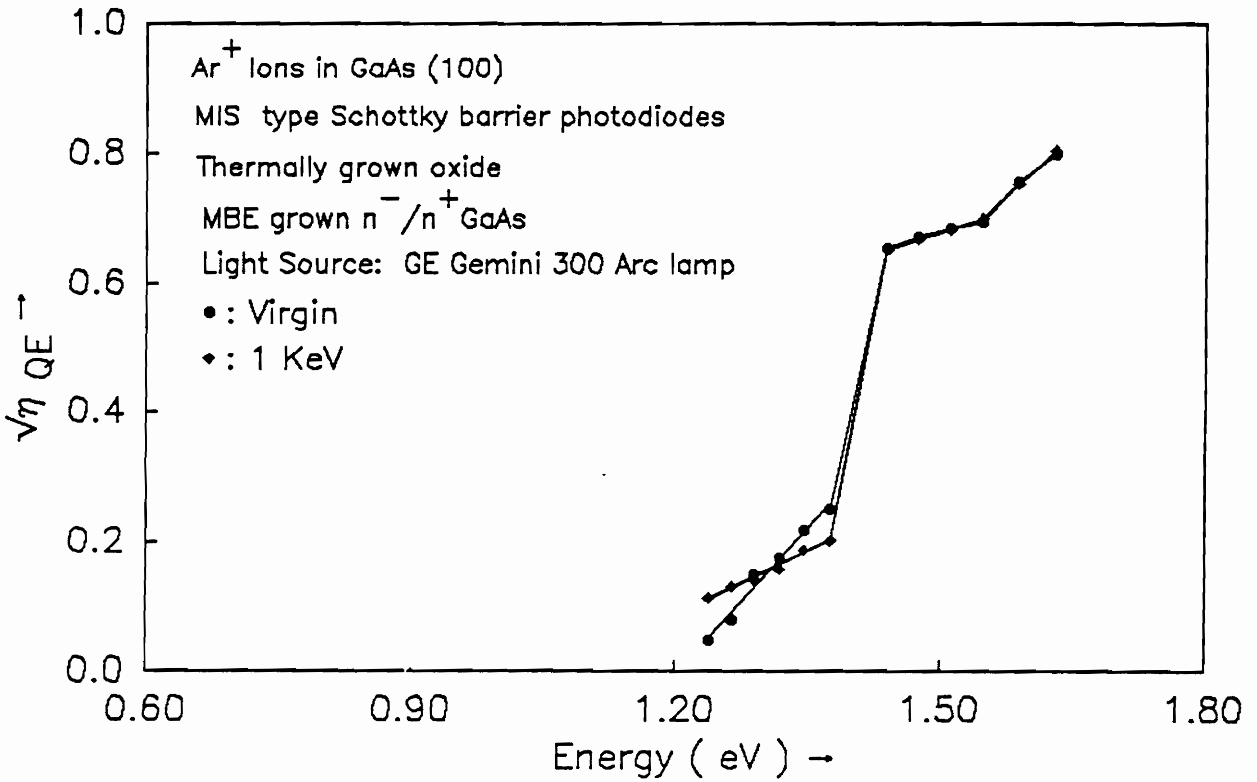

(b)

Figure 4.25 (a) Plot of ln(QE) vs. photon (sub band gap) energy for virgin and 1 KeV MIS Schottky photodiodes. (b) Square root of the collection efficiency as a function of photon energy for virgin and 1 KeV MIS Schottky photodiodes.

anodically grown oxides on Morgan Semiconductor material are shown in Figure 4.26. A DLTS system using 'MEDUSA' software acquires the data and has the lowest defect concentration detectability limit (typically ≈ 10^{-4} N_D). However, in the literature, much higher resolution of the constant capacitance DLTS (CC-DLTS) apparatus[200] has been reported. The CC-DLTS takes into consideration the edge-effects corrections (termed as lamda region corrections), increasing the sensitivity limit by about 1000. Several common activation energies, e.g. at 0.03 eV, 0.19 eV, 0.31 eV, and at 0.53 eV were reported for MBE grown materials[36]. It is evident from Figure 4.26 (a) that the unetched diodes fabricated on MBE material used for the present investigation was defect free, within the detectability limit of the apparatus. IBE introduces two distinct peaks with activation energies at 0.3 eV and at 0.52 eV below the conduction band edge and the trap concentration of different defects enhances significantly with increasing ion beam energy. The position of EL2, however, was not observed.

In anodic samples, two dominant peaks appear at 0.4 eV and 0.76 eV (the EL2) in the control devices. Upon ion bombardment, a peak at 0.3 eV and a broad peak at 0.52 eV appear, EL2 diminishes, and the 0.4 eV peak stays. The defect concentrations increase with ion beam energy. Hence, it appears that IBE introduces two distinct peaks, the first one at E_c - 0.3 eV and other at E_c - 0.52 eV. Loss of EL2 signal is in agreement with our previously reported model that EL2 forms a complex defect state and hence is not evident in the DLTS spectrum. At 4 KeV the increase in conductance reduces the resolution of the DLTS signal and hence correct estimation of the peak and defect density is difficult, because of incorrect estimate of $|dC/C|$. Table 4.4 lists the location and density of traps as a function of ion beam energy for (a) thermally grown oxides, and (b) Anodically grown oxides.

In summary, it was observed by DLTS that IBE introduced two distinct peaks in the GaAs samples; one at 0.30 eV and the other at 0.52 eV below the conduction band edge. These peaks are irrespective of the substrates and previous processing conditions,

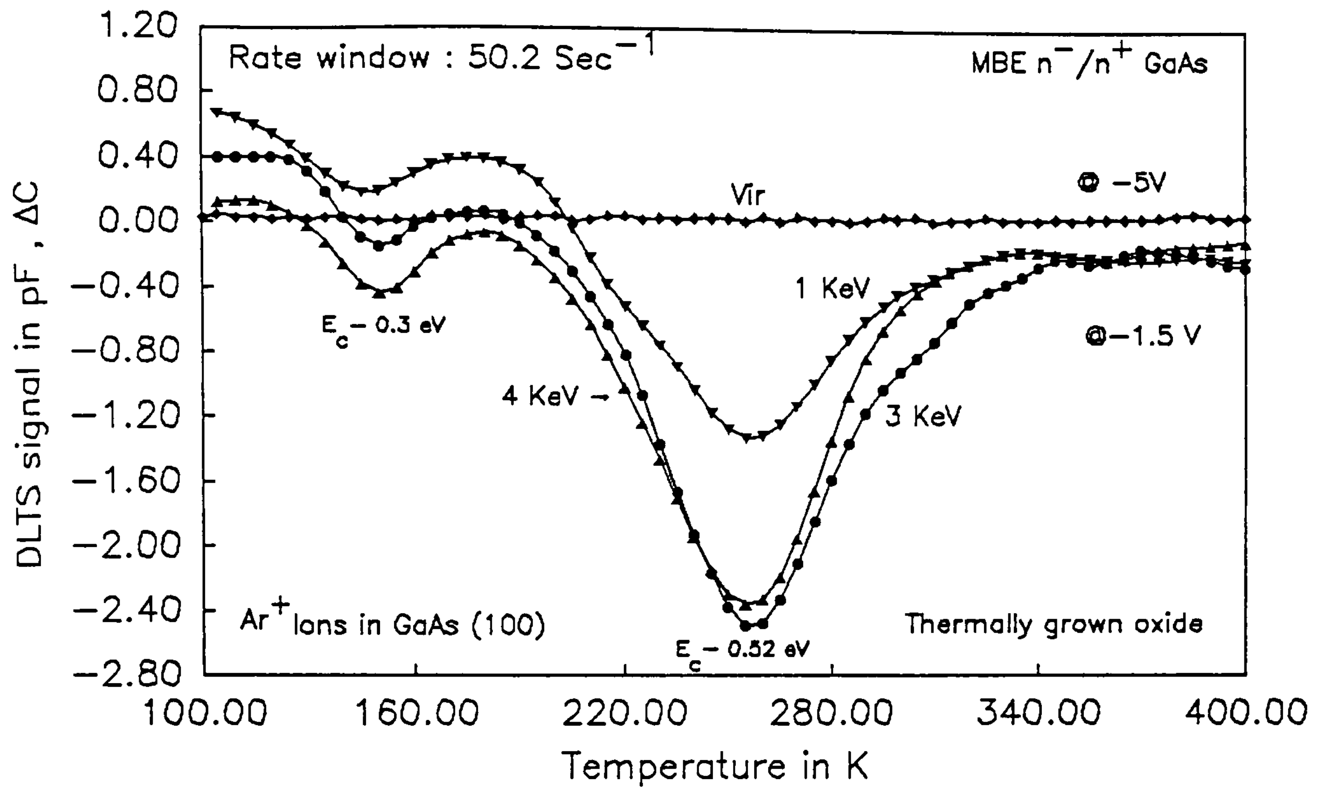

(a)

Rate window : 50.2 Sec^{-1}

Morgan semiconductor GaAs

Vir

1 KeV

@ −5V

@−1.5 V

@ −1 V

E_c−0.32 eV

E_c − 0.4 eV

E_c − 0.52 eV

← Vir

1 KeV →

3 KeV →

4 KeV →

3 KeV →

← 4 KeV

EL_2→

E_c − 0.76 eV

Ar$^+$ Ions in GaAs (100)

Anodically grown oxide

DLTS signal in pF , ΔC

1.5, 0.5, −0.5, −1.5, −2.5, −3.5, −4.5, −5.5, −6.5, −7.5, −8.5

0.5, 0.0, −0.5, −1.0, −1.5, −2.0, −2.5, −3.0

100.00, 160.00, 220.00, 280.00, 340.00, 400.00

Temperature in K

(b)

Figure 4.26 DLTS spectrum of the MIS Schottky diodes fabricated on virgin, 1 KeV, 3 KeV, and 4 KeV Ar^+ etched surfaces, (a) Thermally grown oxides, (b) Anodically grown oxides.

Table 4.4 **Location and density of traps as a function of ion beam energy - Thermal oxides and Anodic oxides.**

Schottky Diode	Trap Density, N_T			
Oxide & Beam Energy	0.3	0.41	0.52 (eV)	0.76
Thermal, Vir	≫ Below the detectability limit ≪			
Thermal, 1 K	4.163×10^{13}	—	5.9243×10^{14}	—
Thermal, 3 K	1.24×10^{14}	—	1.048×10^{15}	—
Thermal, 4 K	3.314×10^{14}	—	1.05×10^{15}	—
Anodic, Vir	—	5.02×10^{15}	—	3.72×10^{15}
Anodic, 1 K	2.4×10^{14}	3.4×10^{15}	2.74×10^{15}	—
Anodic, 3 K	$\approx5\times10^{14}$	3.0×10^{15}	6.1×10^{15}	—
Anodic, 4 K	$\approx5\times10^{14}$	4×10^{14}	5.2×10^{15}	—

ascertaining that these peaks were indeed resulted from DLTS. The EL2 peak vanished in Morgan Semiconductor wafer, favoring a hypothesis suggested earlier in the text that the IBE forms a defect complex with EL2.

DLTS data manipulation: The DLTS signal tends to be noisy at elevated temperatures due to increased leakage current of the diode. The shunt conductance increases rendering interpretation of capacitative signal difficult. Several data smoothing algorithms were considered for frequency domain filtering of the noisy signal. The basic Fourier transform and inverse procedures are commonly implemented as data filters and to deconvolute the measured data to enhance resolution. For the present purpose, an algorithm was selected in which convolution weights could be varied to have minimal side lobes. Data smoothing algorithms involve abrupt truncation of the spectrum, thereby introducing ripples (referred to as the Gibbs phenomena) into the smoothed data, especially near places where the data values change rapidly. The smoothing function involves multiplication by the square modulus $|\mathbf{W}|^2$ of a "window" function **W** that is chosen to be close to 1 in frequency bands that are predominantly signal, and close to zero in frequency bands that are predominantly noise. An appropriate choice for the smoothing window is a "low pass filter" that truncates the frequency spectrum at some intermediate frequency f_o. The windows that have extremely small side lobes are the ones called by R. B. Blackman's "lucky guess" [201] and is given by:

$$W(f)=0.42=\left[0.5\ \cos\left[\pi\ \frac{f}{f_o}\right]+\ 0.08\ \cos\left[2\pi\ \frac{f}{f_o}\right]\right] \quad (4.11)$$

Hence, the smoothing function implements the filtering procedure using the inverse Fourier transform of the Blackman window for the convolution weights.

As observed by DLTS and further evidenced by the transient experiments, it is possible that EL2 forms a complex defect state upon Ar^+ ion bombardment and hence the EL2 is not visible in the DLTS spectrum while in the virgin case its presence in well

pronounced. This is further explained in our proposed model that EL2 forms a complex which upon illumination forms a metastable defect state with forbidden transitions to either allowed band.

Anodically grown oxides have large density of states as compared to thermally activated grown oxides because of dangling bonds and incomplete oxidation at the interface.

4.5 X-ray Photoelectron Spectroscopy (XPS)

The XPS results taken at 15° take-off angle (toa: the angle between the sample and the photoelectron analyzer) for the ion-bombarded samples are shown in Figure 4.27. The surface atomic composition and the relative amounts of Ga(GaAs) and As(GaAs) on the surface of GaAs following chemical cleaning and Ar^+ ion bombardement determined from the XPS measurements at 15° toa are summarized in Table 4.5 for (a) thermally grown oxides, and (b) anodically grown oxides. A 15° toa probes approximately 22 Å into GaAs surface. Following chemical cleaning procedure, the surface was arsenic rich and no chemical shifts are detected in the Ga 3d or As 3d photopeaks that would indicate the presence of oxides on the surface. The traces of oxygen discovered in the XPS spectra were more likely due to the oxygen adsorbed during oxidation. The cleaning solution however indicated no trace in the spectra.

The XPS data indicate that oxide grown on the ion-bombarded samples consists of Ga_2O_3, As_2O_3, and As_2O_5; the quantities are indicted in the Table 4.5. Ga_2O_3 was preferentially formed on the ion bombarded material; nearly equivalent amounts of both gallium (Ga_2O_3) and arsenic (As_2O_3 and As_2O_5) were formed on the non-bombarded material. The Ga/As atomic ratio at 15° toa increases as a function of ion beam energy, indicating loss of As from ion bombarded surfaces rendering them Ga rich. Substantial changes were discovered on the surfaces of the thermally grown oxides and anodically grown oxides and could be linked to oxidation kinetics. The non-bombarded surface has

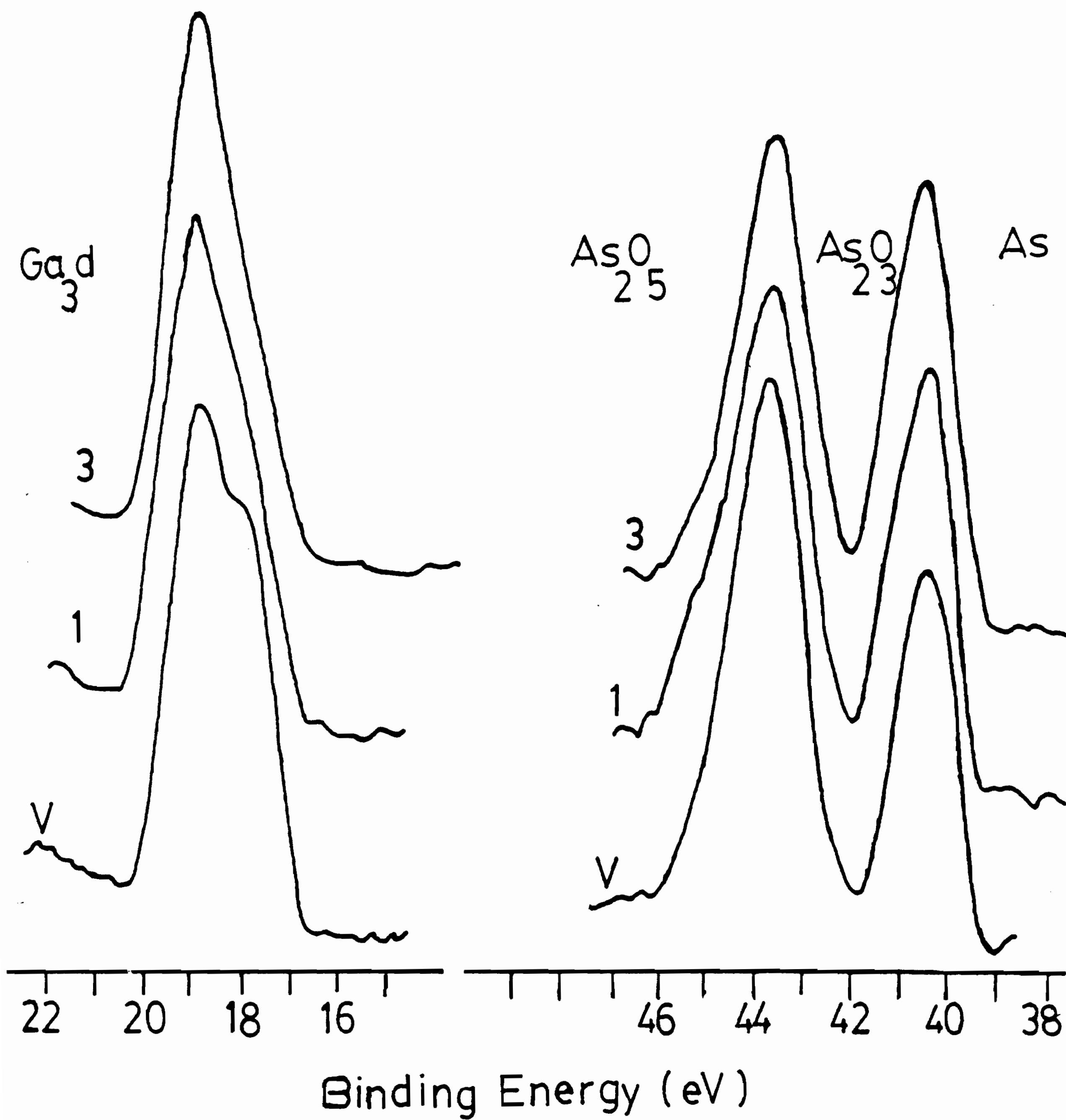

Figure 4.27 XPS spectra for oxide grown on Ar^+ ion etched GaAs using water vapor saturated oxygen at room temperature.

Table 4.5 **Ga and As oxide ratios as a function of ion beam energy for (a) Thermal oxides, (b) Anodic oxides.**

		Ga(GaAs)	Ga_2O_3	As(GaAs)	As_2O_3	As_2O_5	O	Ga/As
	BE	18.8	20.0	40.7	44.1	45.4	531.4	
Virgin	AC%	7.5	14.5	7.2	11.7	1.9	57.2	1.03
1 KeV	AC%	7.7	17.6	6.1	9.5	2.9	56.1	1.26
3 KeV	AC%	8.5	19.2	5.4	8.9	1.8	56.2	1.57
4 KeV	AC%	13.4	5.4	5.49	2.3	5.7	31.99	2.42

(a) Room temperature water-vapor saturated oxide

		Ga(GaAs)	Ga_2O_3	As(GaAs)	As_2O_3	As_2O_5	O	Ga/As
	BE	18.8	20.0	40.7	44.1	45.4	531.4	
Virgin	AC%	4.4	5.85	4.38	14.88	3.8	19.26	1.0
1 KeV	AC%	6.2	12.42	5.56	11.2	8.46	53.4	1.15
3 KeV	AC%	8.2	11.53	6.46	11.1	8.02	52.9	1.26
4 KeV	AC%	7.8	11.52	6.45	10.2	7.47	53.5	1.21

(b) Anodically grown oxides

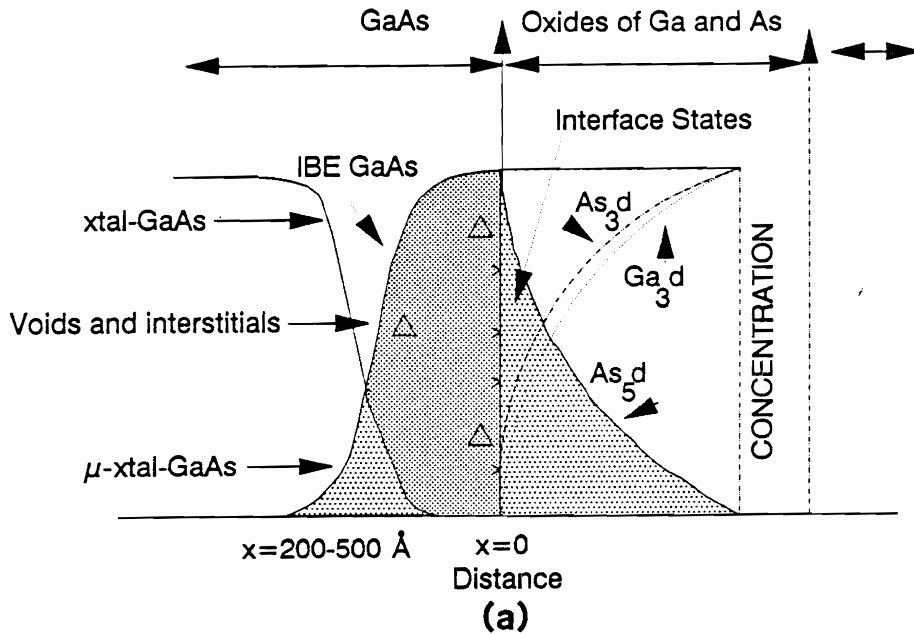

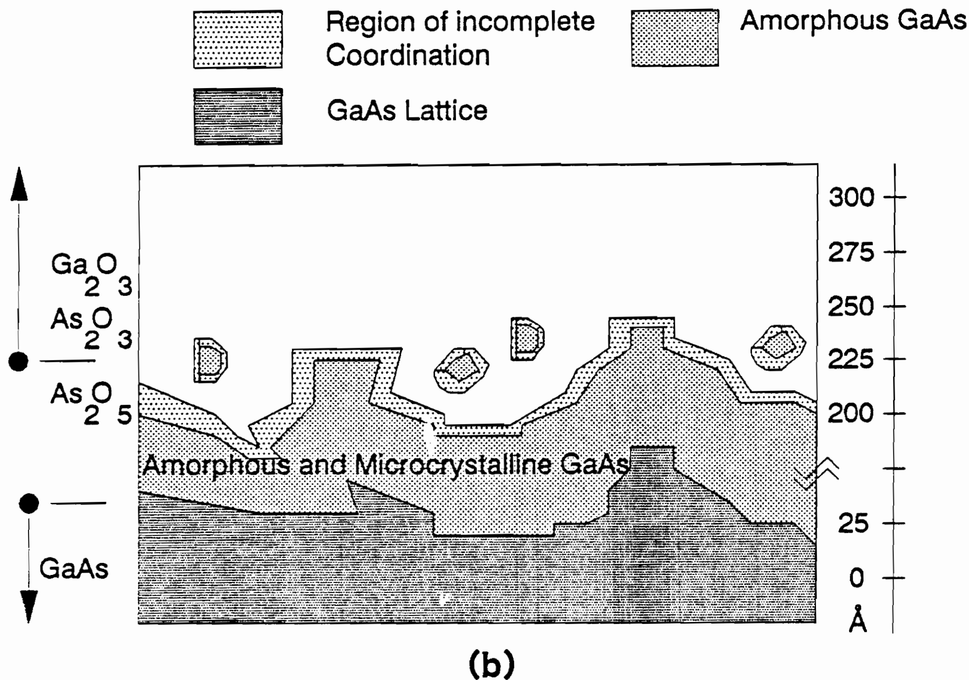

Figure 4.28 Hypothetical representation of oxides formation on an IBE GaAs surface, (b) Side view of the above model for clear representation.

Ga/As atomic ratio near unity. The Ga/As atomic ratio can be utilized to estimate the depth of the damage caused by the ion bombardment. The Ga/As atomic ratio for chemically cleaned GaAs is less than 1.0 at 15° and 90° toa, indicating that an As rich surface extends to at least 60 Å into the surface.

Chemical analyses by Epp and Dillard of the ion bombarded disordered regions indicates As deficiency as a result of preferential sputtering of arsenic and increased surface chemical reactivity[23]. Since the anodic oxidation process is field dependent, it is likely that it lowers the surface chemical reactivity and hence results in low Ga/As ratio. Various model providing insight into the reactions altering the chemical reactivity of GaAs surfaces have been reported in literature. While an exhaustive critical survey is the beyond the scope of the thesis, however, it is emphasized that disruption of the surface structure by IBE results in singly occupied dangling bonds. These dangling bonds participate in adsorption and/or dissociation of reactant molecules depending upon the extent that each reactant molecule interacts.

In summary, ion beam introduces a variation in Ga/As ratio i.e. a change in stoichiometric composition. The chemical reactivity of the GaAs surfaces changes as a result of ion beam bombardement, however no significant deviation in two oxidation procedures of these surfaces was observed.

Electro-optical devices fabricated using dry processing are more than likely to have radiation damage in the near surface region, causing parasitic absorption. The increased absorption on the GaAs side is due to formation of high refractive index region, and interstitials, amorphized region, etc. On the other side of the interface, increased absorption occurs due to the presence of poor native oxide, and oxides of Ga and As. This concept has been depicted in Figure 4.28 (a,b), which shows a conceptual schematic of the possible formation of the interface.

— ¤ —

Chapter 5

Computer Simulation and Device Analysis

To gain a better understanding of the experimental results and several anomalies, a theoretical investigation was carried out by physical simulation of some of the experimental results. Physical models were developed to analyze, simulate and model the results as close as possible to those observed experimentally. Many effects were treated in a very heuristic manner for the purpose of simulation, describing the underlying physics in a qualitative way.

5.1: Physical Model of the Damage.

Implantation of the energetic particles cause lattice damage and introduces defects in the crystal, causing amorphization of the crystal lattice at or near the surface and sub-surface region. Several techniques are reported in the literature to investigate the damage profile . Among these techniques is Rutherford back-scattering, which estimates the thickness of the highly disordered region. It is based upon the difference in back -scattering properties of the probing ions between ordered and disordered layer. It can reveal the damage; however the technique may itself introduce damage, rendering analysis difficult. Since structural damage accompanies the electrical damage, electrical measurements such as DLTS, IV, C-V-(ω), LEED, and Hall effect have been employed to study the effect of radiation damage, and damage profiles. The radiation damage also changes the optical properties of the damaged layer. Therefore, optical probes such as Raman spectrocopy, photoluminescence, UV reflectivity, ellipsometry are commonly employed to study the damaged region. Most of the characterization techniques lack resolution, in that, a combined effect of crystalline and amorphous region is usually obtained. Generally, a layer stripping technique, such as chemical etching, is required

for profiling the radiation damage. Since measurements are performed after each layer stripping step, the depth resolution is usually limited to by stripping technique.

Figure 5.1 shows a conjectural, physical model of the ion beam damaged GaAs surface and sub-surface regions, based on an exhaustive literature review. The depth distribution is dependent on the ion mass, energy, and process dependent variables. From the surface of GaAs, the top region mostly consists of the amorphized GaAs, which was experimentally verified by etch (chemical) and measure (UV reflectivity) experiment. This highly amorphized layer is followed by a thin transition region, where fine-grain mixture of the microcrystals of GaAs and amorphous GaAs coexist. The characteristic microcrystal size, L, according to Feng and Zallen[77], decreases with increasing fluence. This microcrystalline component gradually disappears into the GaAs bulk.

The sequence of structural changes that occur during conversion of a crystalline to an amorphous state, when subjected to ion damage, is not a well understood phenomena. Two models for eventual amorphization are reported in literature: (a) Heterogeneous model - which suggests that the individual damage clusters are amorphous and complete amorphization occurs as a result of accumulation and merging of individual damage clusters, and (b): Homogeneous model: which suggests that when the defect concentration reaches some critical value in a single crystal, the crystal becomes unstable and transforms to an amorphous state.

It is yet unclear if relaxation to an amorphous state results in a sharp interface. There is contradictory evidence in the literature, indicating that (a) a sufficiently damaged crystal relaxes to an amorphous state at some critical point defect concentration, indicating an abrupt transition from amorphous to crystalline state, and (b): the microstructure of the near-surface implantation induced damage layer consists of a fine grain mixture of the amorphous GaAs and GaAs microcrystals. Hence, this rather simple model proposed in the text is not without controversy. A theoretical analysis will be presented later to justify the proposed model.

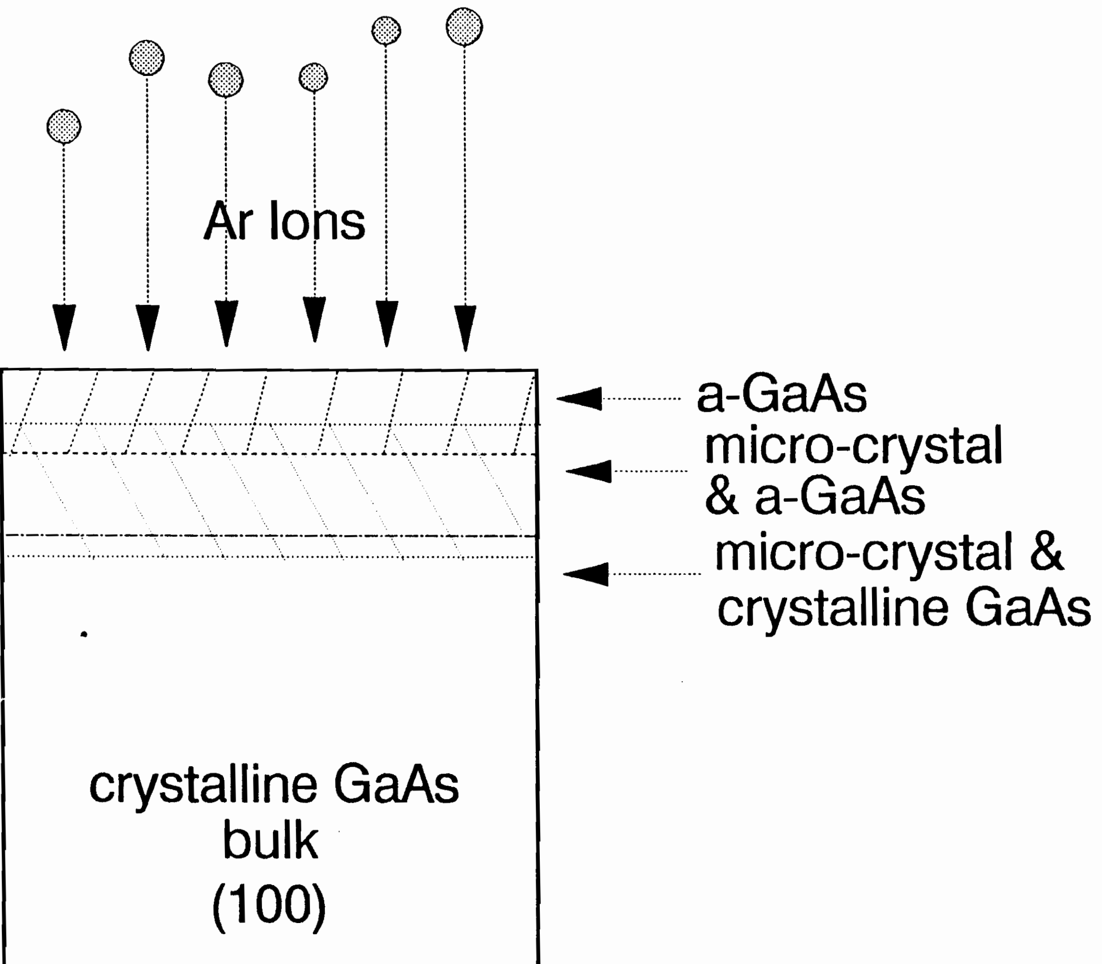

Figure 5.1 Physical model of the ion beam damaged GaAs surface and subsurface regions.

5.2: Calculation of the Depth of IBE Induced Damage in GaAs.

In this section a theoretical profile of the ion beam induced radiation damage is presented using the range parameters calculated from LSS theory. When the energetic ions penetrate a semiconductor, damage occurs to the host lattice because of the inelastic collision between the incident ion and the host lattice atom. The spatial rate of the energy loss is a function of the energy of the incident ions, resulting in the depth dependence to the damage. High energy ions have a reduced nuclear scattering cross-section and are slowed down, primarily through elastic scattering. As the ions loose energy, collision with the substrate atoms becomes more frequent, resulting in the structural disorder. Depending upon the implant conditions (ion energy and mass, target and its temperature etc.) a near surface amorphous and/or microcrystalline and/or disordered region is formed. If the energy required to displace one atom from its lattice site is constant, then the profile of the lattice damage is the same as that of the ion energy deposited via nuclear scattering processes. The ion energy deposition profile introduced during the time interval t' and $t' + \Delta t'$ can be approximated as[202];

$$F(Z')dt' = \frac{E_{ion}\Gamma I}{\sqrt{2\pi}\ \Delta R_p} \exp\left[-\exp\left[\frac{Z - R_p}{\sqrt{2\Delta}\ R_p}\right]^2\right]dt' \qquad (5.1)$$

where E_{ion} is the energy of per incident ion, Γ is the fraction of the total ion energies leading to the damage, R_p is the mean damage depth, ΔR_p is the standard deviation of R_p, and I is the flux of the incident ion. The above equation is derived from the standard implantation range distribution theory, where the implanted profile is given by[203];

$$N(z) = \frac{N_{\Box}}{\sqrt{2\pi}\ \Delta R_p} \left[-\frac{(x - R_p)^2}{\sqrt{2\Delta}\ R_p^2}\right] \qquad (5.2)$$

where $N_{\Box}$ is the implanted dose, and N(x) represents the spatial distribution of implanted species measured along the axis of the incidence.

Defining the sputtering yield Y, as the number of atoms sputtered per incident ion, the sputtering rate β, can be defined as the thickness of the target materials sputtered per unit time, and is proportional to the sputtering yield Y, by $\beta = YI/N_S$, where N_S is the density of the target. To calculate the ion energy deposition profile, accumulated over a period of time t, the ion energy deposition profile can be integrated as follows;

$$E(z) = \int_0^t F(z') \, dt' \tag{5.3}$$

If $z = 0$ corresponds to the target surface, then $z' = z + \beta(t - t')$, and Eq. 5.1 becomes;

$$E(z) = \frac{E_{ion} \, \Gamma \, I}{\sqrt{2\pi} \, \Delta R_p} \int_0^t \exp\left[- \left(\frac{z + \beta \, (t - t') - R_p}{\sqrt{2}\Delta \, R_p} \right)^2 \right] dt' \tag{5.4}$$

By an appropriate change of variable and integration, the Eq. 5.4 can be written as

$$E(z) = \frac{E_{ion} \, \Gamma \, N_S}{2 \, Y} \left[\operatorname{erf} \left(\frac{z + \beta t - R_p}{\sqrt{2}\Delta \, R_p} \right) - \left(\frac{z - R_p}{\sqrt{2}\Delta \, R_p} \right) \right] \tag{5.5}$$

Using the error function, viz.,

$$\operatorname{erf}(z) = \frac{2}{\sqrt{\pi}} \int_0^z \exp(-\alpha^2) \, d\alpha$$

In the limit of $z \to \infty$, $\operatorname{erf}(z) = 1$. Hence for $(\beta t - R_p) \gg \sqrt{2}\Delta \, R_p$, Eq. 5.5 can be written as;

$$E(z) = \frac{E_{ion}\,\Gamma\,N_s}{2Y}\ \mathrm{erfc}\left[\frac{z - R_p}{\sqrt{2}\Delta R_p}\right] \qquad (5.6)$$

It is interesting to note that the time dependence in Eq.(5.6) is eliminated. This indicates that the ion energy deposition profile E(z) is saturated, when the incident ion dose is very high.

Eq. (5.5) is employed to calculate the deposition profile for a given combination of incident ion and target. Projected range and straggle parameters for Ar^+ ions were chosen for Ge, whose mass and atomic number are the average of Ga and As atoms. The atomic radius assumed for the above calculations is 0.9 Å, and curve fitted for the ion beam energies used for IBE, from ref.[204,205]. In order to obtain the deposition profile for the surfaces under investigation, the experimental parameters were utilized for the calculations and are listed in Table 5.1 (a). The sputtering yield and Γ were extrapolated from the Ref.[263], and are presented in Table 5.1 (b). Figure 5.2 shows the calculated deposition profile for the Ar^+ ions in GaAs for the IBE conditions used for the investigation. The Figure 5.2 shows a demarcation line from amorphous to crystalline phase. This line was drawn based on the assumption, that if N_s for GaAs $\approx 4.42 \times 10^{22}$ /cm^3, and the average energy to displace one atom from its lattice site E_d, is equivalent to 9.4 eV for GaAs, then the energy which is needed to displace all the atoms in a unit volume of the crystal, ie. to cause randomization, is $E_d N_s \approx 4.15 \times 10^{23}$ eV/cm^3. From Figure 5.2, it can be seen that for ion beam energies of interest the depth of amorphization is 75 Å, 108 Å, and 150 Å for 1 KeV, 3 KeV and 4 KeV energies, respectively. The depth of amorphization thicknesses were smaller than the chemical etch profiles and those measured using Raman spectrocopy, (see Table 5.2). The discrepancy can be explained due to several reasons. Since the theoretically calculated thickness value is only for the amorphized region, the calculated value is smaller than the experimentally observed, from Raman spectroscopy which is very sensitive to very small deviations from crystallinity and measures a combined effect of amorphous and microcrystalline region. This suggests that beneath amorphized layer,

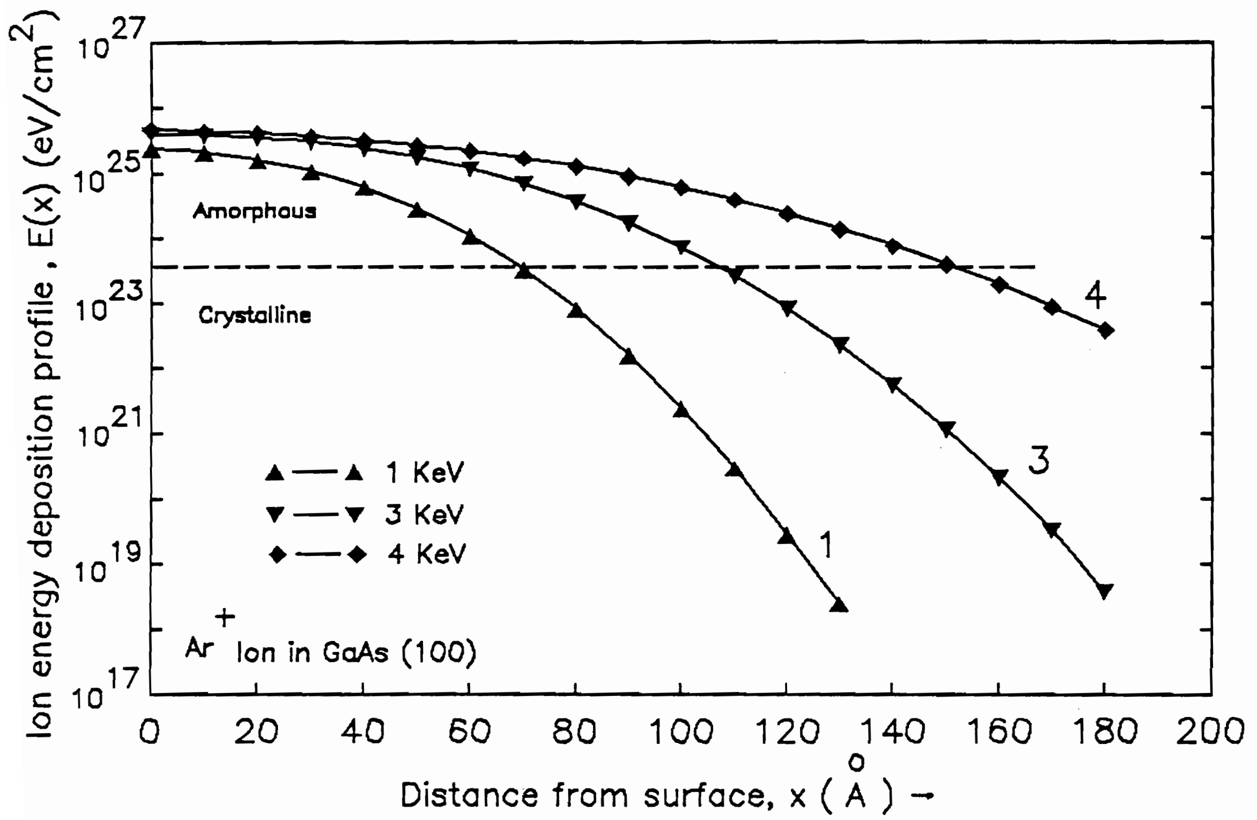

Figure 5.2 **Computed plot of depth of ion induced damage in the host lattice.**

Table 5.1 **Theoretical and experimental parameters used for the calculation of depth of ion beam induced damage in GaAs host lattice. (a) conditions of Ar^+ ion beam milling. (b) Parameters used for the calculation of the depth of damage.**

E_{ion} (eV)	Ar^+ Flux ($sec^{-1}cm^{-2}$)	Milling Time (min)	Milling Rate* (Å min^{-1})
1 KeV	10^{16}	14.83	≈ 1791
2 KeV	10^{16}	10.33	≈ 2810
3 KeV	10^{16}	7.85	≈ 3393
4 KeV	10^{16}	4.05	≈ 3665

(a) Conditions of Ar^+ beam milling on GaAs

E_{ion}	γ	R_p (Å)♀	ΔR_p (Å)♀	Y †
1 KeV	0.82	25	20	1.32
2 KeV	0.81	37	28	2.07
3 KeV	0.80	45	26	2.5
4 KeV	0.79	53	40	2.7

(b) Parameters used for the calculation of the depth of the damage

* Values calculated from sputtering yield Y listed in table (b).

♀ Projected range is calculated for the Ge target (Average of Ga and As atoms. The atomic radius used for the calculation is 0.9 Å.

† Polyatomic targets were considered with $M_1 = M_2$ and the values of K, for such targets changed to agree with the corresponding monoatomic values.

Table 5.2 **Depth of damage comparison computed from the LSS theory and the experimental parameters, and from reflectivity and Raman spectroscopy measurements for Ar^+ ion bombarded GaAs.**

ENERGY (eV)	DAMAGE DEPTH IN Å	
	Calculated ¤	Measured ♀
1000	73	200
3000	108	--
4000	153	500

♀ All values are approximate within 20%.

¤ Assumptions made in the calculations are mentioned in the text.

there exists a layer having an inhomogeneous mixture of amorphous and microcrystalline phase, lending credence to the hypothetical model suggested above. It is also obvious from the collision cascade theory that ionic distribution in the target is statistical and depends upon the collisional probability events. This, again suggests that transition from amorphous to crystalline phase is gradual, rather than abrupt.

5.3: Modelling Optical Effects-Photogeneration Rate.

The optical effects are fundamental in calculating the photocurrent response of the photonic devices. In view of the fact that IBE introduces nonlinearities in the near surface regions of the semiconductors, changing optical constants, it was appropriate to compute the depth distribution of the optical generation rate. The optical generation generation rate is commonly described in terms of a phenomenological model containing experimentally observed effects. For simplicity, impurity-assisted generation, multiphonon processes generation, and photothermal generation are assumed to occur with very small probability. For modelling purposes, the solar spectrum of Bird and Hulstrom[206] for air mass 1.5 (AM1.5) was utilized.

Several factors must be considered in finding light intensity within the GaAs substrates. The first loss suffered by the incident light is the reflection, $R(\lambda)$. The reflectance of a thin, uniform dielectric layer on a semi-infinite GaAs substrate can be calculated by considering the impedance mismatch resulting from the changes in refractive index of the propagation media. The resulting power reflection coefficient for normally incident light is given by the expression;

$$R(\lambda) = \left[\frac{R_{ox} + R_{GaAs} e^{-j2\theta}}{1 + R_{ox} R_{GaAs} e^{-j2\theta}} \right]^2 \qquad (5.7)$$

where,

$$\theta = \frac{2\pi n_{ox} T_{ox}}{\lambda}, \quad R_{ox} = \frac{1 - n_{ox}}{1 + n_{ox}}; \quad R_G = \left[\frac{n_{ox} - n_{ox}}{n_{ox} + n_{ox}} \right]$$

the parameters have their usual meaning. n_{GaAs} is the complex refractive index for GaAs and is given by the expression;

$$n_{GaAs}(\lambda) = n_{GaAs}(\lambda) - j\kappa_{GaAs}(\lambda) \qquad (5.8)$$

and,

$$\kappa(\lambda) = \left[\frac{\lambda \ \alpha(\lambda)}{4\pi} \right]$$

where $\kappa_{GaAs}(\lambda)$ is the extinction coefficient for GaAs. For most wavelengths, n_{GaAs} is essentially real. However, at ultraviolet wavelengths, $\alpha(\lambda)$ is large and $\kappa(\lambda)$ must be included for accurate results. For MIS structures, the optical density of the oxide layer is usually very small and the optical losses can be neglected to a first approximation.

In GaAs, due to the presence of surface states, the possibility of some attenuation of light at the interface must be considered. In IBE GaAs structures, the presence of the amorphized layer introduces significant deviations in an otherwise periodic lattice structure. Optical constants of c-GaAs [207], and a-GaAs [208] were studied by several investigations and the results are summarized in Figure 5.3. Figure 5.3(a) shows the refractive index, the absorption coefficient, and the extinction coefficient, as a function of energy for c-GaAs, and optical penetration depth in c-GaAs and a-GaAs is shown in Figure 5.3 (b). The photon flux entering the semiconductor is given by the expression, $[1 - R(\lambda)]xF(\lambda)$, where $F(\lambda)$ is the incident photon flux per square centimeter per second per unit bandwidth. The generation of electron-hole pairs due to the incident photons can be described as;

$$g(x) = \int_0^\infty F(\lambda)\alpha(\lambda)\exp^{-\alpha(\lambda)x} d\lambda \qquad (5.9)$$

This equation assumes that internal quantum efficiency is unity and free carrier

Absorption Coefficient ($\alpha(\lambda)$ x 1000) cm^{-1}

n

$\alpha(\lambda)$

k (ω)

by Aspnes & Studna ,
& Sell, Cassey & Wetch

(eV)

Energy

(a)

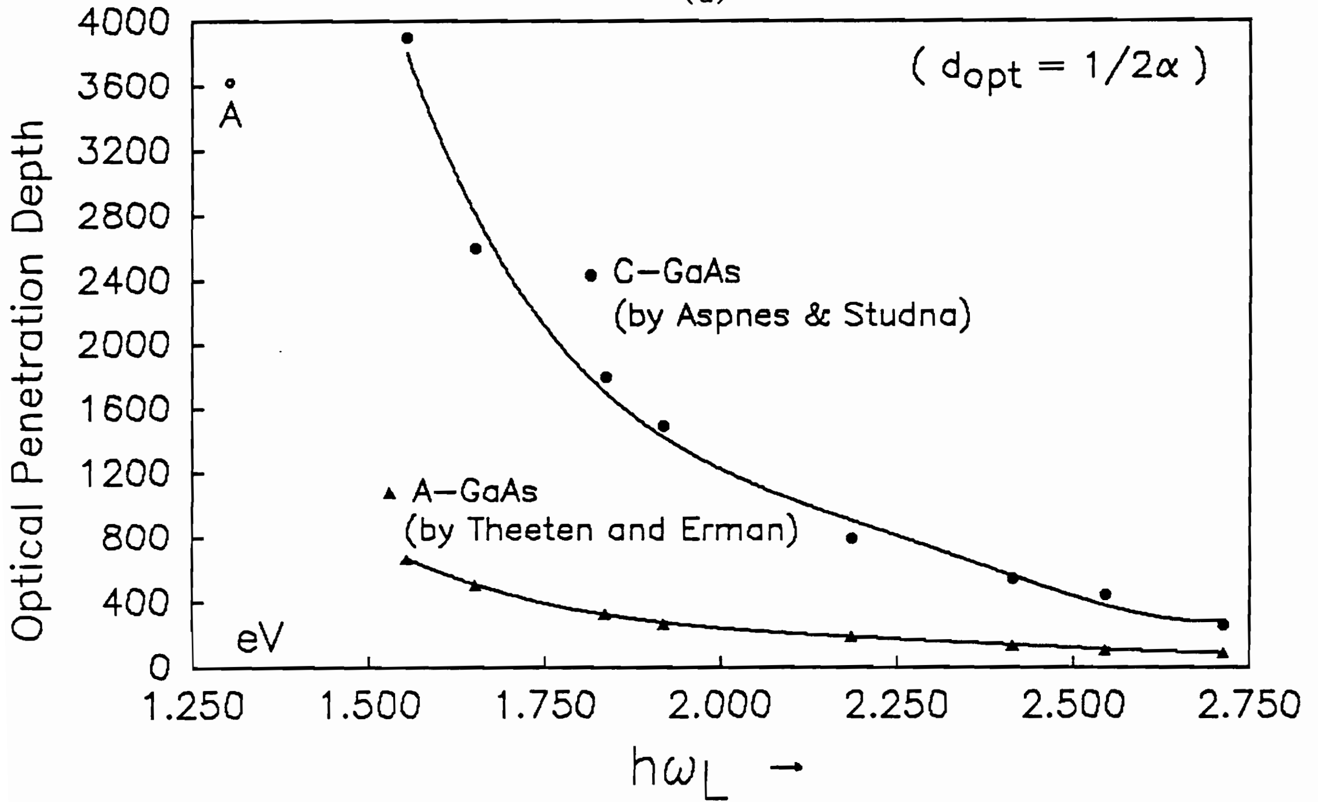

(b)

Figure 5.3 (a) Optical Constants of GaAs. (b) Optical penetration depth in c-GaAs and a-GaAs.

absorption is negligible. Several techniques have been used in the literature to compute the generation rate in semiconductors and are based on the piecewise construction and numerical integration of the generation in the bulk. Among several analytical techniques to perform the integration of the generation rate, mentioned in the literature, a new technique, introduced by Chen and Burton, [209] was utilized to compute the generation rate for GaAs. The generation rate can be written in a summation form, using the by Gauss-Quadrature (G-Q) method, and is expressed as;

$$g(x)=\left[\frac{b-a}{2}\right]\sum_{i=1}^{n} W_i \; F(k_i)\alpha(k_i)\exp(-\alpha(k_i)x) \quad (5.10)$$

where a, b are the integral limitations of the integration, k_i is the "key point" (representative point used for the calculation) of G-Q method, which can be expressed by,

$$k_i = \frac{Z_i\,(b-a) + b + a}{2} \quad (5.11)$$

and Z_i and W_i are the roots and weight factors respectively. Generation rate can be written in a reduced form as;

$$g(x) = \sum C_i \; e^{-D_i x} \quad (5.12)$$

where;

$$C_i = \frac{b-a}{2} \; W_i \; F(k_i)\alpha(k_i)$$

and,

$$D_i = \alpha(k_i)$$

Figure 5.4 (a) shows a physical model of IBE GaAs structure and possible mechanism which can lead to attenuation in the surface region of the semiconductor. Figure 5.4 (b) shows generation rate calculation in GaAs with unetched structure. The generation rate profile calculated for silicon substrates employing the G-Q technique [209] fits reasonably well with those calculated using extensive, piecewise numerical integration methods. However, since $\alpha(\lambda)$ increases rapidly in the first few layers for IBE structures, the product $[\alpha(\lambda)\exp\{-\alpha(\lambda)x\}]$ increases in the front surface regions, instead of decreasing, indicating a drawback of the numerical integration technique.

5.4: Effect of IBE on the Conductivity of SI and Doped GaAs Materials

The electrical conductivity is by far the most sensitive probe to detect and identify the trap centers in semiconductors. The resultant conductivity under a given set conditions encompasses numerous physical phenomena, and thus far inclusion of these effects in a unified solution has not been possible. For the present investigation, a broad outline of conductivity and steady state photoinduced conductivity phenomena is presented, in order to understand, and possibly relate to some of the results observed in the IBE devices.

Invoking the relevant transport equation, by substituting the current densities into the continuity equation, we obtain;

$$\frac{\partial n}{\partial t} = D_n \nabla^2 n + \mu_n(E \bullet \nabla_n + n\nabla \bullet E) + g_n - r_n$$

and, (5.13)

$$\frac{\partial p}{\partial t} = D_p \nabla^2 p - \mu_p(E \bullet \nabla_p + p\nabla \bullet E) + g_p - r_p$$

most symbols have their text book meaning. n and p are the free electron and hole densities and in subscripts, represent the carrier type. g and r are the volume generation

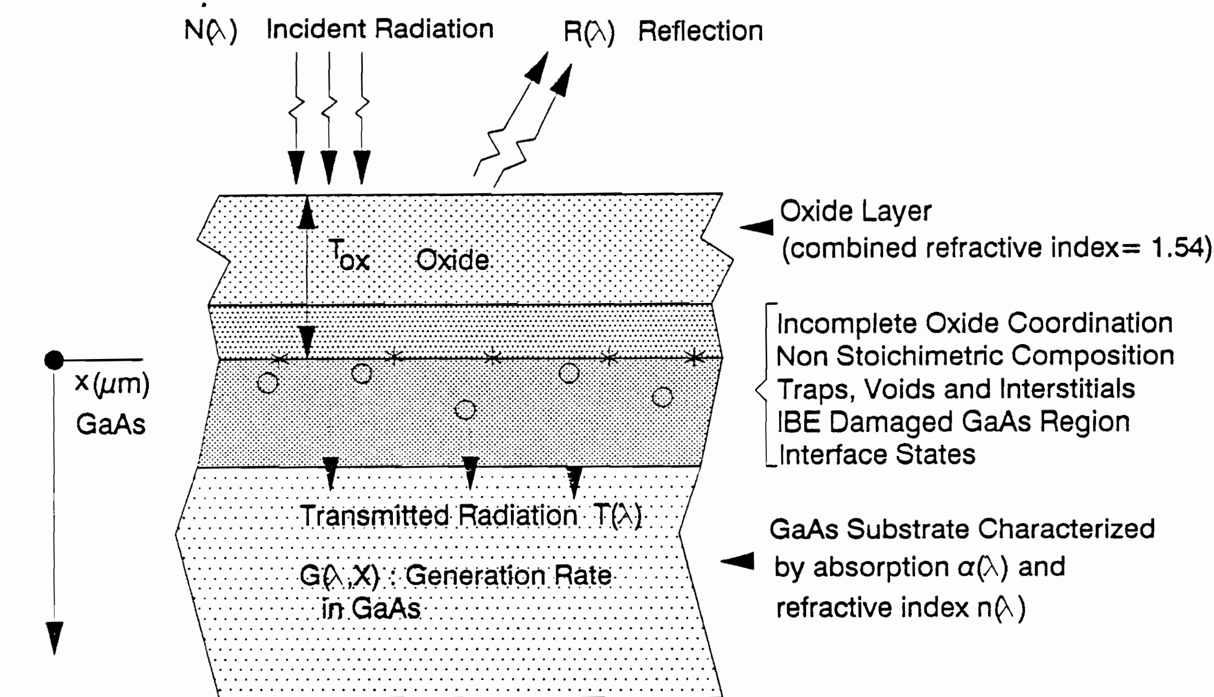

(a)

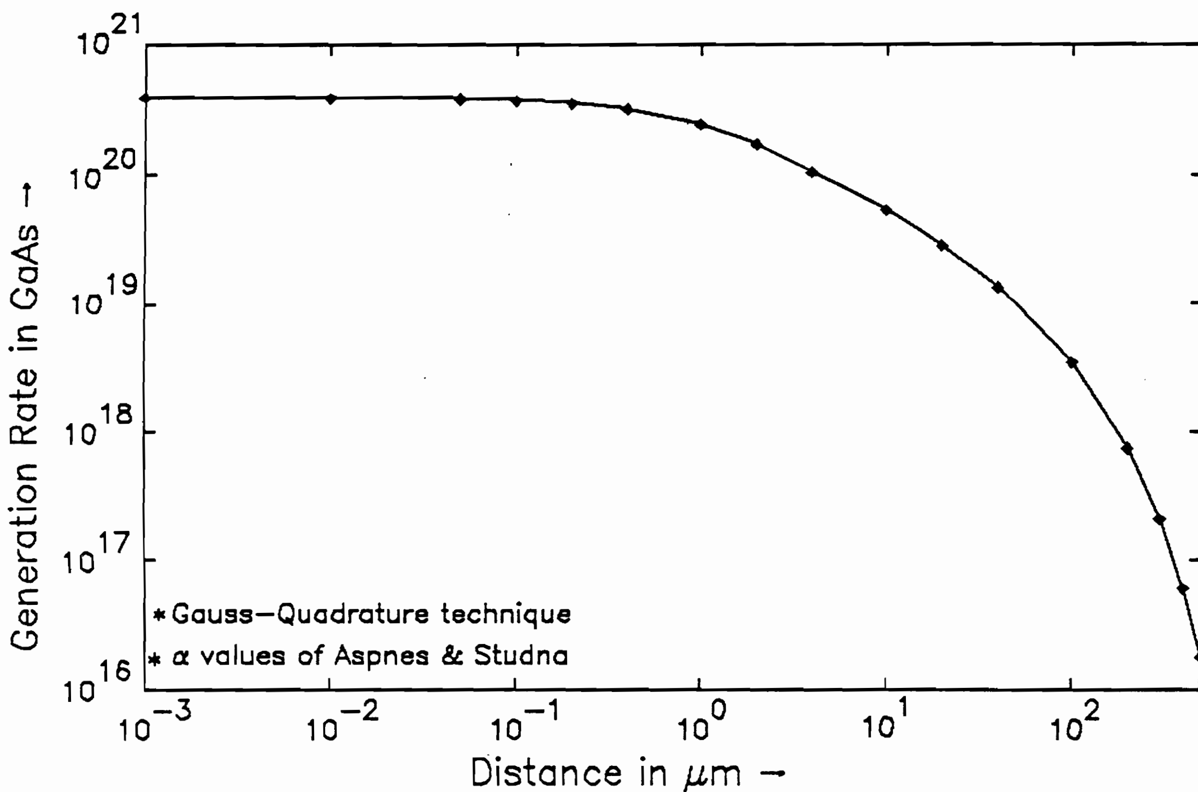

(b)

Figure 5.4 (a) Proposed model of the parasitic absorption at the interfacial region of IBE GaAs structures. (b) Optical generation rate in GaAs substrates.

and recombintion rates, respectively. It is implicitly assumed that generation rates are comprised of thermal and optical processes only. Auger and radiative recombination mechanisms are assumed to be insignificant, as compared to the impurity-assisted recombination process.

Under nondegenerate conditions, the net rate of recombination of electrons r_{ni}, and holes r_{pi}, are expressed, according to Shockley and Read, by,

$$r_{ni} = c_{ni}(1-f_{ti})N_{ti}n - e_{ni}f_{ti}N_{ti}$$

and, (5.14)

$$r_{pi} = c_{pi}f_{ti}N_{ti}p - e_{pi}(1-f_{ti})N_{ti}$$

where the rates are determined by the probability of emission and capture by the trap, (i represents an arbitrary trap, The emission rate for electron to the conduction band is denoted by e_{ni}, while the emission rate of the holes to the VB is e_{pi}. The electron and hole capture rates, c_{ni} and c_{pi}, are equal to the product of the carrier thermal velocity v, and the average trap capture cross-section, σ, for electrons and holes are expressed by,

$$c_{ni} = \sigma_{ni} v_{ni}$$

and, (5.15)

$$c_{pi} = \sigma_{pi} v_{pi}$$

In thermal equilibrium, the probability, f_{ti}, that a trap level is occupied by an electron, is given by the Fermi function,

$$f_{ti} = \left[1 + g_i \exp\left[\frac{E_{ti} - E_f}{kT}\right]\right]^{-1} \quad (5.16)$$

where E_f is the Fermi level and g_i is the degeneracy factor. In thermal equilibrium, the net recombination rates are zero and emission rates are expressed by,

$$e_{ni} = \frac{c_{ni}N_c}{g_{ci}} \exp\left[\frac{E_{ti} - E_c}{kT}\right]$$

and, (5.17)

$$e_{pi} = c_{vi}N_v g_{vi} \exp\left[\frac{E_v - E_{ti}}{kT}\right]$$

where the degeneracy factor for electrons is replaced by $[1/g_{ci}]$ and for hole $[g_{vi}]$. N_c, N_v, E_c, and E_v have their usual meanings.

The complete continuity equation can be written for electrons as;

$$\frac{\partial n}{\partial t} = D_n\nabla^2 n + \mu_n(E\bullet\nabla_n + n\nabla\bullet E) + g_n - \sum_{1=1}^{m}(c_{ni}(N_{ti}-n_{ti})n - e_{ni}n_{ti})$$

and for holes, (5.18)

$$\frac{\partial p}{\partial t} = D_p\nabla^2 p - \mu_p(E\bullet\nabla_p + p\nabla\bullet E) + g_p - \sum_{i=1}^{m}(c_{ni}n_{ti}p - e_{pi}(N_{ti}-n_{ti}))$$

where the trap occupancy probability is replaced by the ratio of the trapped electron density to total trap density, $(f_{ti} = n_{ti}/N_{ti})$. Equations above have m+3 unknowns: n, p, E and m-equations for n_{ti}.

The generation of carriers under an optical excitation can be described by Eq.(5.9), and is shown schematically in Figure 5.5 (a) for the photoconductivity element, used for the present experiments. The recombination can occur by photon emission, by phonon emission, or by the transfer of kinetic energy to other charge carriers (Auger effect). Auger process is a dominant recombination mechanism at high carrier densities.

The radiative recombination rate, under nondegenerate conditions can be expressed by, $r_r = \partial n/\tau_r$, where τ_r is the radiative recombination lifetime, and can be neglected for the present purpose because at low carrier densities recombination via impurities occur faster than either Auger and/or radiative recombination. Using Eq.(5.14) and (5.18), it can be easily be shown that,

$$r = \frac{np - \frac{g_v}{g_c} n_i^2}{\tau_p \left[n + \frac{e_n}{c_n}\right] + \tau_n \left[p + \frac{e_p}{c_p}\right]} \tag{5.19}$$

which for low resistivity materials can be reduced to; $r = \partial n/\tau$. Under these circumstances, the transport equations defined by Eqs. 5.13 become;

$$\frac{\partial n}{\partial t} = D_n \nabla^2 n + \mu_n(E \bullet \nabla_n + n\nabla \bullet E) + g_n - \frac{\partial n}{\tau}$$

and (5.20)

$$\frac{\partial p}{\partial t} = D_p \nabla^2 p - \mu_p(E \bullet \nabla_p + p\nabla \bullet E) + g_p - \frac{\partial p}{\tau}$$

trapping is neglected in the above equations, and $\partial n = \partial p$ is assumed to hold. For above bandgap photons, there is band-to-band generation, such that $g_n = g_p$. From Eq. 5.20, the ambipolar transport equation can be determined and expressed as;

$$\frac{\partial \delta n}{\partial t} = D^* \nabla^2 \delta n - \mu E \bullet \nabla \delta n + g_n - \frac{\delta n}{\tau} \tag{5.21}$$

Where the ambipolar diffusivity, $D^* = 2D_n D_p/(D_n + D_p)$, and the ambipolar mobility,

$$\mu = \frac{(n_o - p_o)\mu_n \mu_p}{\delta n \mu_n + \delta p \mu_p}$$

are used. It is worth a mention, that ambipolar mobility is negligible in nearly intrinsic material. In one dimension and for the steady state Eq. 5.21, reduces to;

$$\frac{\partial^2 \delta n}{\partial x^2} - \frac{\delta n}{L^2} = \frac{-g' \tau e^{-\alpha x}}{L^2} \qquad (5.22)$$

The diffusion length is defined as $L = (D^* \tau)^{1/2}$. A generalized form of solution of the above equation is given as;

$$\delta n(x) = Ae^{x/L} + Be^{-x/L} - \frac{g' \tau \; e^{-\alpha x}}{(\alpha L)^2 - 1} \qquad (5.23)$$

The constants A and B are determined by the boundary conditions. For the photoconductivity element shown in Figure 5.5 (a), light is incident normal to the wafer and the excess carriers are collected at the two tunnel type contacts. For unetched sample, at $x = 0$, there is negligible surface recombination, and hence $(\partial \delta n / \partial x)$ can be approximated to 0. For the IBE surface the surface recombination velocity will play a dominant role. A second boundary condition is that at $y = s/r$, where 's' is the separation between two electrodes of the photoconductivity element, $\delta n(0) = 0$.

Since IBE surfaces have a depth distribution of amorphized layer, a piecewise, cumulative photogeneration effect should be considered. Such an effect can be obtained by finite element technique. Such a piecewise construct is shown in Figure 5.5 (b) for photoconductivity element and Schottky photodiode. The schematic shows, (a) for conductivity element: a region of carrier pair generation and conductivity elements distributed spatially in parallel to the top amorphized region, (b) for photodiodes: the top photodiode and shunting paths distributed spatially and in parrallel to the top region. The individual elements can be considered equivalent to the mesh points in the

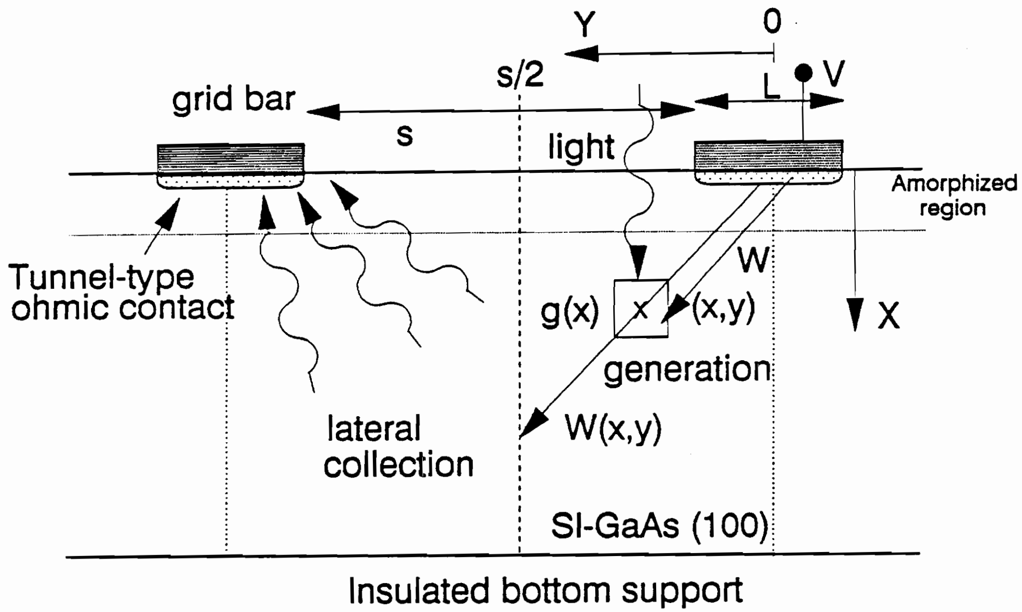

(a)

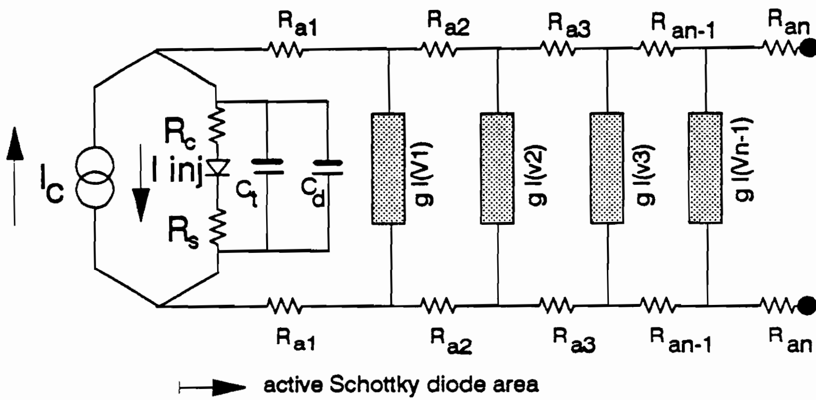

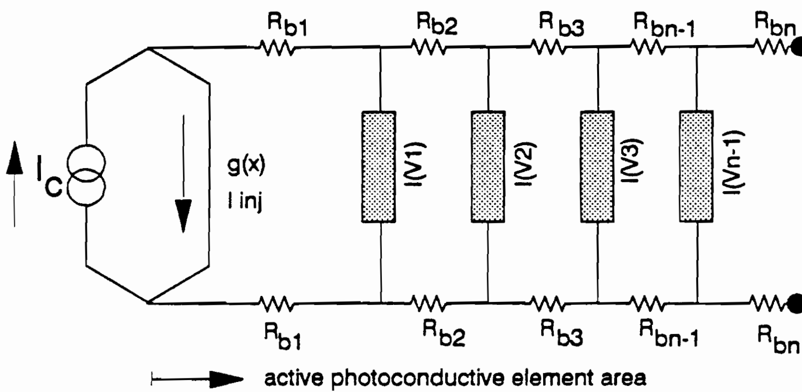

(b)

Figure 5.5 (a) A theoretical, two dimensional model for carrier-pair generation in the photoconductivity element. (b) Lumped electrical component equivalent of Schottky diodes and photoconductivity element.

finite element analysis. The results may be accurate but the technique is cumbersome. A boundary condition subjected to $\delta n(W) = 0$, ie zero current at the back contact, holds true in photovoltaic structures and is given by,

$$\delta n(x) = \frac{g'\tau}{(\alpha L)^2 - 1}\left[\frac{e^{-\alpha W}\cosh(x/L) + (\alpha L)\sinh(W-x)/L}{\cosh(W/L)}\exp^{-\alpha x}\right] \tag{5.24}$$

This generalized from can be simplified for to suit specific conditions of a device. The temperature dependence in this equation arises primarily due to the lifetime term. In the derivation of the above equation, effect of multicharged center [210,211], though important for GaAs, has been neglected. Such a multi-ionized center can exhibit different activation energies depending on its ionization state.

The equations 5.24 can be generalized for the time dependence of the photo conductivity by taking into consideration a two-level model, which consists of a fast recombination center, E_r, which accounts for the initial rapid recombination of carriers observed after illumination has been turned off, and a trap E_t, which changes its occupation by capturing predominantly one type of carriers during the illumination period and emits that carrier back after the light is turned off.

The continuity equation above can be written as

$$\frac{dn_t}{dt} = -e_{nt}n_t + e_{pt}(N_t - n_t) + c_{nt}n(N_t - n_t) - c_{pt}pn_t$$

and, (5.25)

$$\frac{dn_r}{dt} = -e_{nr}n_r + e_{pr}(N_r - n_r) + c_{nr}n(N_r - n_r) - c_{pr}pn_r$$

for trapping and recombination respectively. These equations can be solved for excess electron and hole densities to model the slow return to the equilibrium after the optical excitation source terminates. Several conditions must hold true such as, the

free carrier density returns to its equilibrium concentration in a time faster than the trapping centers release their trapped carriers. The capture processes for the deep trap must be negligible. Such equations have been solved by Yoshie and Kamihara[212] for the excess electron and hole densities and the solutions are given by,

$$\delta n(t) = e_n \tau_n \delta n_t(0) e^{-(e_n + e_p)t}$$

and, (5.26)

$$\delta p(t) = \delta n_t(0) e^{-(e_n + e_p)t}$$

In life-time controlled surfaces, since $e_n \tau_n << 1$, the excess electron density is much less than the excess hole density. The total conduction current density J_T is dominated by the hole current component. By an appropriate substitution of the experimental parameters, the mathematical analysis presented here can be modelled to discern the dominant conduction mechanism in photoconductivity and phototransients.

— ¤ —

Chapter 6

Summary, Conclusions and Future Recommendation

6.1 Summary and Conclusions

This investigation was directed towards discerning the effects of the ion bombardment in the surface and sub-surface regions of GaAs. Several electrical, optical, and analytical techniques are treated in the literature to evaluate the depth and extent of such damage. The probing region, in most of these techniques, is a few hundred Angstroms deep into the bulk. Since the damage is concentrated near the surface, the measurement techniques employed in this investigation are surface sensitive, and probe the semiconductor in the near surface regions, which is comparable to the depth of the damage.

A considerable amount of effort was expended toward the design and development of an integrated photovoltaic materials and devices characterization facility. The automated facility not only increases the characterization efficiency, it greatly enhances the precision, and reduces any possibility of human error in the measurements. With a few experiments presently operational, the set up offers tremendous potential for performing several other experiments by employing the already established procedures, and should support future investigations.

For the present investigation, the study primarily was concentrated in the following different, but closely associated areas:

1. To develop surface sensitive inspection devices and experimental methods to accurately discern the effects in the disordered surface regions.
2. To examine the IBE substrates and evaluate the distribution of the traps in the band gap, introduced as a consequence of ion beam processing.
3. To gain understanding of the process by proposing phenomenological physical and equivalent electrical models of the effects of ion beam induced damage.

To accomplish the research objectives, several photonic structures were introduced. A fully automated photovoltaic materials and devices (PVMD) characterization facility was established. Asyst, a Forth based scientific data acquisition and reduction software was selected to write the source codes to dynamically characterize the devices. The inherent fast execution times of the software allows real time data acquisition. Several electrical and optical evaluation procedures were developed and employed for the present investigation.

One of the striking results of the ion beam bombardment on semi-insulating (SI) GaAs samples was the observation of persistent photoconductivity. A phenomenological model for optically generated, ion beam induced, metastable defect state formation was proposed to explain such an effect. Spectral conductivity measurements show some interesting phenomena. The unquenched spectra are similar for ion-etched and virgin samples and show one peak at 0.76 eV and a broad central peak between 0.9 eV and 1.5 eV. The broad central peak can be quenched by soaking with photons and restoring by thermal activation. The peak is attributed to a complex defect formation with EL2 at 77 K. Another interesting feature of ion beam etching was increased photosensitivity. In the conductivity relaxation mode, the presence of two or more exponentially decaying mechanisms indicated the distributed nature of the electrical traps within the band gap of the material.

Metal-Insulator-Semiconductor (MIS) Schottky diodes were fabricated using both thermal and anodic oxides. Diode parameters were evaluated as a function of ion-beam energy. An increase in reverse saturation current density accompanied by an increase in the ideality factor is observed, indicating the presence of trap-assisted tunneling and a region of high recombination. The effective barrier height is lowered with increasing ion beam energy, but no monotonic correlation was established. We propose that the mechanisms described in previous studies (e.g. tunneling, stoichiometry effects, ion penetration depth) are superimposed by the effect of Fermi level pinning at the electronic states of process induced defects.

Deep Level Transient Spectroscopy (DLTS) indicates the presence of two trap levels, at 0.32 eV and 0.52 eV below the conduction band edge, as a consequence of ion beam etching. The EL2 peak is evident in the virgin sample and vanishes in the ion beam etched samples. This is in agreement with our proposed model that ion bombardment produces a complex defect state with EL2, having forbidden transitions to the allowed bands.

The photovoltaic response was measured using light current-voltage characteristics and spectral response. The ratio of the spectral responses indicated the regions and relative extent of the damage. Damage has a profound impact on the surface generation and band-bending due to excess carrier generation, hence sub-band gap absorption in the damaged region indicated the degree of disorder.

XPS results show an increased surface sensitivity and an increase in Ga/As ratio, indicating depletion of As atoms.

The depth of amorphization was calculated using the Lindhard-Scharff-Schiott (LSS) theory and the standard projected range, and straggle parameters, and experimental parameters. There exists a large difference in the values as calculated using LSS theory and experimentally measured values using optical probes. The difference was explained in light of the Collision-Cascade model.

6.2 Future Recommendations

With the continually increasing complexity and precision of current microelectronics technology, more etch process versatility is needed, such as: (a) Vertical etches to allow tight packing of micron and submicron circuit elements; also tapered etches to give subsequent step coverage. (b) Highly selective etches to prevent damage to very thin underlying layers, and multimaterial etches in a single process for patterns. (c) Etching the standard semiconductor materials, such as high speed GaAs devices.

Due to the immense potential of this step in microelectronics processing, more elaborate research is needed. While the results presented in this dissertation are far from

complete, they suggest several new directions of research. Hence, it is highly recommended that research efforts in the following areas be expanded:

- The observation of persistent photoconductivity in ion beam etched surfaces leaves many questions unanswered. It will be interesting to observe the mobility under identical experimental conditions using a photo-Hall technique. It would be relevant to find out the effect of thermal activation of the proposed optically-generated ion beam induced metastable defect states.
- It is necessary to perform similar studies on samples after annealing. Low temperature anneal ($\approx$ 200° C) is a viable temperature since the samples can be annealed without protective "cap". Excimer laser annealing is recommended, because by an appropriate adjustment of energy density and duration of irradiation, only the surface regions are recrystallized. Extension of the annealing study employing lasers would allow selective area annealing of the processed devices using automated rastering equipment.
- It was interesting to note that MBE grown material had the native defect EL2, with density below the detectability limit of the DLTS technique. It would be instructive to grow undoped GaAs layers employing MBE and verify the validity of the proposed model. If indeed the native defect forms a complex with ion beam process induced defects at low temperature, then the conductivity would rapidly drop back to its dark level. This would verify participation of EL2 in the persistent conductivity.
- MIS structures were chosen primarily because of the fact that atomically clean surfaces could not be achieved, in practice. An in-situ deposition of Schottky metal immediately after IBE would eliminate the native oxide growth and hence "true" M/S structure can be obtained.
- Electroabsorption measurement, viz. Franz-Keldysh effect is recommended. Such measurements can easily identify the increase in the absorption due to lattice disorder.

- A more detailed modelling based on finite element analysis is recommended. As proposed in the text, the damage is extended into the bulk through several layers of amorphous and/or micro-crystal GaAs layers. An analytic expression may not truly represent the physical phenomena and hence piecewise construct modelling, such as use of finite element analysis, may be more appropriate.
- A damage depth profile using ellipsometer is recommended. There is a possibility that data may vary depending upon the sensitivity of a given equipment to the damage, and change in surface charge and morphology of the sample.

It is gratifying to note that the study of the electrical, physical and chemical effects of this rather unique and technologically beneficial process are actively perused by Electronic Materials, Condensed Matter Physics and Surface Analysis Laboratories at Virginia Tech. It is hoped that under the impetus of this investigation and with the joint efforts of the co-workers, a significant understanding can be achieved, leading to the successful implementation of dry processing for semiconductor device fabrication.

— ¤ —

Appendix A: Fabrication Procedures and Process Variables.

Over a period of time, certain procedures were developed and optimized to fabricate samples for the IBE characterization. The procedures, along with their function are provided below.

A.1 Substrate Cleaning: Procedure adopted to clean As-recieved GaAs Wafers.

Organic Clean
Clean in Tetrachloroethylene [1 min.]
Clean in warm Tetrachloroethlyne [1 min.]
Clean in Acetone [1 min.]
Clean in warm Acetone [1 min.]
Clean in Methanol [1 min.]
Clean in warm methanol [1 min.]
Rinse in De-ionized water.

Inorganic Clean
Rinse in warm De-ionized water
Dip in $HCl:H_2O$ (1:1) solution @ 40° C. [10 min.]
Rinse in warm De-ionized water.
Dip in $H_2SO_4:H_2O_2:H_2O$ (8:1:1) [5 min.] ... agitation required
Rinse in cold/warm/cold De-ionized water.
Dip in $HCl:H_2O$ (1:1) solution @ 40° C. [5 min.]

A.2 Lift-Off Process: Procedure adopted to generate pattern using photolithography.

Pre-bake samples at 95° in inert atmosphere.
Coat a thin layer of Microposit positive photoresist #1400-27 (modified with ® Monazoline; see text for details) at 3500 rpm. [1 min.]
Post-bake the sample for @ 95° C [10 min.]
Align the mask with the Iron-oxide high-resolution patterned plate
Expose the sample under a UV-lamp [6.5 sec.]
Develop in Microposit developer #353 for [90 sec.]
Bake the sample at 95° C [30 mins.]
Evaporate the desired material onto the sample.
Use acetone to lift the photoresist. Clean the sample in transene 100 and jet dry.
[Microposit Photoresist #1400-27 and Microposit Developer #353 procured from Shipley, Mass.]

A.3 Chemical Etching: Procedures for controlled etching of the samples.

As recieved samples are etched with $H_2SO_4:H_2O_2:H_2O$ (8:1:1) solution at approximately 1.1 μm/min.
An (1:1:100) solution of $H_2SO_4:H_2O_2:H_2O$ etches GaAs at a rate of approximately 60 Å/min. as determined using a Tencor instruments, Sigmascan Profilometer.
A dilute solution of Ammonium hyroxide and hydrogen peroxide was also used. However such solution often caused random distribution etch pits (strongly depended upon time and agitation rate) and was not employed for the test devices.

A.4 Oxidation: Procedures adopted to grow oxide on the GaAs samples.

Thermal Oxidation:

GaAs samples were cleaned and oxide etched in HCl:H_2O (1:1) solution [10 min.]
sample loaded in the tube. Oxygen saturated with water at 45° C at 200 c.c./min is introduced in the tube. [48-60 hrs.]

Anodic Oxidation:

Anodic Oxide Electrolytic solution composition:

40 gm. Ammonium Pentaborate
400 ml. Ethylene Glycol [Heat and Dissolve the solute]
Filter the solution.

Platinum: Cathode and GaAs sample: Anode
Apply the voltage till the current density ≈ 1 mA/cm^2
Time is adjusted to obtain a desired thickness.

A.5 Contact Formation: Procedure followed to establish contacts on the devices.

Typical base pressure ≈ 1 x 10^{-6} torr.
Au-Ge ≈ (2400 Å) and Ni ≈ (800 Å). Ohmic Contacts were annealed at 440° C in a Forming gas (95% Nitrogen and 5 % Hydrogen) ambient. Cycle [5 min. at entrance/2.5 min. in the center zone / 5 min. at the entrance].
Aluminum or Gold are used as typical Schottky contact material.
[All metals obtained from Puratronic, England, and are 99.999% pure]

— ¤ —

Appendix B: Photovoltaic Materials and Devices Characterization Software

Several source codes for the data acquisition were written in Forth to characterize GaAs materials and devices. Asyst, a Forth based scientific language from Asyst Software Technologies, Rochester, N.Y., utilizes threaded-code interpreter for jump routine situations. Several procedures (routines), common to most of the data acquisition programs, are provided below. The procedures , termed as colon definitions, as each procedure starts with : and ends with ; . Following is a brief compendium of the procedures which can be intertwined together according to a specific task in a data-acquisition source code. The procedures, along with their function are provided below. The words enclosed in square parentheses can be appropriated to suit a specific application.

```
: FIRST.CHECK                        Comment:  Procedure for execution interruption.
          NORMAL.DISPLAY
          BELL
      047 VIDEO.ATTRIBUTE
       ." PROGRAM NAME.. "
       ." LOADING OF THIS PROGRAM MAY CAUSE FEW AUTOMATIC ADJUSTMENTS . PLEASE ENSURE THAT " CR
       ." INITIAL SETTINGS ARE ESTABLISHED. " CR
       ." OK TO PROCEED?  [Y/N]  ." CR
          KEY DUP EMIT
          DUP > 90 IF 32 - THEN 89 = THEN NOT IF CR CR
       ." TRANSFER " BLINK.TOGGLE ." INCOMPLETE" BLINK.TOGGLE ." EXECUTION ABORTED" CR
       57 ERROR
          THEN
          SCREEN.CLEAR ;

: BEEP               Comment:  A typical beep pattern, indication of a specific activity.
         40 , 4000  TUNE
         30 , 7000  TUNE
         20 , 10000 TUNE
         30 , 12000 TUNE
         40 , 4500  TUNE ;

: RED.LETTERS                        Comment:  Custom tailoring the graphics display.
          RED MIX FOREGROUND
          GREEN BLUE MIX BACKGROUND
          INTEN.ON ;
: CLEAR.WINDOWS                      Comment:  Screen space allocation for certain activity.
          NORMAL.DISPLAY
         ?GRAPHICS.DISPLAY NOT
```

```
         IF
         {WINDOW}                        Predefined window name.
          BLUE MIX FOREGROUND
          GREEN MIX BACKGROUND
          186 205 201 200 188 187 BORDER.CHARS {BORDER} ;

: ?SWITCH.TO.{WINDOW}   Comment:  Switches cursor to a predefined window.
         ?GRAPHICS.DISPLAY
          NOT
          IF {WINDOW} {BORDER} THEN ;

: WAIT.FOR.KEY                           Comment:  Halts execution for manual interruption.
            TEXT.CURSOR.OFF
        030 VIDEO.ATTRIBUTE
      01 01 GOTO.XY
         ." CONTINUE ? [Y/N] "
            KEY 0 = IF KEY DROP THEN
            TEXT.CURSOR.ON ;

: GET.Y/N                                Comment:  Awaits for a Y(es) or N(o) command.
            BEGIN
           ?REL.COL ?REL.ROW
            PCKEY NOT
            IF DUP > 90 IF 32 - THEN
            DUP 89 = NOT
            DUP 78 = NOT AND
            ELSE
            TRUE
            THEN
            WHILE
            BEEP
            DROP
            RED.LETTERS . Y or N  Only Please !!! " BEEP
       1000 MSEC.DELAY
           ?REL.COL 3 PICK -1 +
          3 PICK 3 PICK GOTO.XY
            SPACES GOTO.XY
            REPEAT UNROT 2 DROP *DROP 89 = ;

: #INPUT&CHECK                           Comment:  Evaluates if a valid number is registered.
            BEGIN
           ?REL.COL ?REL.ROW
           #INPUT
            NOT
            WHILE
            BEEP
           ?REL.COL 3 PICK - 1 +
          3 PICK 3 PICK GOTO.XY
            SPACES
            GOTO.XY
            REPEAT
            UNROT
         2 *DROP ;
```

```
: "INPUT&CHECK                          Comment:  Evaluates if a valid string is registered.
             BEGIN
            "INPUT
            "LEN 0 =
             WHILE
             BEEP
            "DROP
             REPEAT ;

: GET.NUMBER                            Comment:  Waits for a manual input of a number.
            #INPUT
             IF
             DEF.#
             THEN ;

: IEEE.488                              Comment:  Activates and resets the GPIB devices.
             SEND.INTERFACE.CLEAR
             REMOTE.ENABLE.ON
             BEEP ;

: IEEE.488.OFF                          Comment:  Deactivates the GPIB bus.
             SEND.INTERFACE.CLEAR
             REMOTE.ENALBLE.OFF
             BEEP ;

: SET.###                               Comment:  Initializes and sets field for a ### device.
            [DEVICE.NAME]
             EOS.ON
             ASCII : EOS.CHARACTER
             EOI.ON
             IEEE.488
             COMMAND.OUT GPIB.WRITE ;

: LN2.ON                                Comment:  Turns on the liquid nitrogen flow into Cryostat.
        -100 D/A.OUT
         100 MSEC.DELAY
        -200 D/A.OUT
             BEEP ;

: LN2.OFF                               Comment:  Turns off the liquid nitrogen flow into Cryostat.
             RCHNL/3OT
        -150 D/A.OUT
         100 MSEC.DELAY
        -100 D/A.OUT
         100 MSEC.DELAY
         -50 D/A.OUT
         100 MSEC.DELAY
           0 D/A.OUT
             BEEP ;

: HEAT.ON                               Comment:  Turns Heater on to a certain level of power.
             DASH16
             DCHNL/1OT
        1000 D/A.OUT
```

```
        60000 MSEC.DEALAY
              BEEP ;

: HEAT.OFF                               Comment:  Turns Heater off.
              DASH16
              DCHNL/1OT
          250 D/A.OUT
          100 MSEC.DELAY
          100 D/A.OUT
          100 MSEC.DELAY
            0 D/A.OUT BEEP ;

: READ.TEMP                              Comment:  Reads temperature from the Resistance Temperature
                                         Detector,  based upon Calendar-Van Dusen Equation.
              DASH16
          0.3 CONVERSION.DELAY
              DCHNL/1IN A/D.INIT
           10 SYNC.PERIOD
          6 1 DO
              SYNCHRONIZE
              A/D.IN
              TEMP.DAT [ I ] :=
              LOOP
            0 X1% :=
          6 1 DO
              X1% TEMP.DAT [ I ] + X1% :=
              LOOP
              X1% 5 / Y1% :=
              Y1%
         -5 5 A/D.SCALE
              100 -1 * *
              0.838 + RESATT :=
              0.0011401 RESATT RESATT * *
              2.2328 RESATT * + 243.706 -
              CUR.TEMP :=
              CUR.TEMP 273.2 + TINK :=
              TINK ABS TINK := ;

: SET.LN2.TEMP                           Comment:  Sets the Cryostat temperature at Liquid Nitrogen.
             ?SWITCH.TO.{WARNING}
             {WARNING} SCREEN.CLEAR
        01 01 GOTO.XY
              BLINK.TOGGLE
           01 SPACES
              RED.LETTERS
      .     " Warning..."
              BLINK.TOGGLE
              YELLOW.LETTERS
             {WARNING} 01 01 GOTO.XY
           ." The Diffusion Pump Must Be On... "
             ?SWITCH.TO.{TOP3}
             ?SWITCH.TO.{TOP1}
             {TOP1} SCREEN.CLEAR
              BLINK.TOGGLE
```

```
        {TOP3}
         SCREEN.CLEAR
    5000 MSEC.DELAY
         READ.TEMP
         BEGIN
    5000 MSEC.DELAY
    -1 4 FIX.FORMAT
         RED.LETTERS
         TINK TSET > IF
       5 SPACES
      ." CURRENT TEMPERATURE : " TINK . ." K " CR
         LN2ON
   40000 MSEC.DELAY
         LN2OFF
         READ.TEMP
   10000 MSEC.DEALY
         LN2OFF
         READ.TEMP
   10000 MSEC.DELAY
        ?DROP
         ELSE
         LN2OFF
         READ.TEMP
        ?SWITCH.TO.{BOTLINE}
        {BOTLINE} 01 01 GOTO.XY
      ." CURRENT TEMPERATURE : " TINK . . " K "
      ." Done Setting... "
         LN2ON
  120000 MSEC.DELAY
         LN2OFF
         EXIT
         THEN
         AGAIN
        ?SWITCH.TO.{BOTLINE}
        {BOTLINE} SCREEN.CLEAR ;

: INITIAL.ANNEAL                    Comment:  Performs initial vacuum anneal of the samples.
        ?SWITCH.TO.{WARNING}
        {WARNING}
         BLINK.TOGGLE
      01 SPACES
         RED.LETTERS
      ." WARNING..."
         BLINK.TOGGLE
         YELLOW.LETTERS
      ." The diffusion pump must be on..."
        ?SWITCH.TO.{TOP1}
        {TOP1} 02 SPACES
      ." INPUT MAXIMUM BAKE TEMPERATURE IN DEGREES C : "
        #INPUT&CHECK ANNEAL.TEMP :=
         ANNEAL.TEMP 273.2 + ANNEAL.TEMP :=
        ?SWITCH.TO.{BOTLINE}
        {BOTLINE}
      01 SPACES
```

```
       RED.LETTERS
       BLINK.TOGGLE
    15 SPACES
    ." WARNING..."
       BLINK.TOGGLE
       YELLOW.LETTERS
    ." SAMPLE IS HEATING..."
      ?SWITCH.TO.{TOP3}
      {TOP3} {BORDER}
       SCREEN.CLEAR
      {TOP1}
       BLINK.TOGGLE
       SCREEN.CLEAR
    01 SPACES
       WHITE INTEN MIX FOREGROUND
    ." SETTING ANNEALING TEMPERATURE..."
       BLINK.TOGGLE
      {TOP3}
  1000 MSEC.DELAY
       DASH16
       DCHNL/1OT
       BEGIN
  5000 MSEC.DELAY
       READ.TEMP
   -1 4 FIX.FORMAT
       ANNEAL.TEMP TINK > IF
       HEAT.ON
       ANNEAL.TEMP TINK - ABS
   35. * POWER :=
       POWER D/A.OUT
       YELLOW.LETTERS
    ." CURRENT TEMPERATURE IS :" TINK . ." DEGREES K :" CR CR BEEP
 10000 MSEC.DELAY
       ELSE
       HEAT.OFF
      ?SWITCH.TO.{BOTTOM}
      {BOTTOM}
       SCREEN.CLEAR
    ." ANNEAL DONE..."
  2000 MSEC.DELAY
       BEEP BEEP
      ?SWITCH.TO.{BOTTOM}
      {BOTTOM}
       SCREEN.CLEAR
       BLINK.TOGGLE
       YELLOW.LETTERS
    ." COOLING: PLEASE STAND BY... "
       WAIT.FOR.KEY
       BEEP
       EXIT
       THEN
       AGAIN
      {BOTLINE} SCREEN.CLEAR
       NORMAL.DISPLAY ;
```

```
: CHECK.ANNEAL                         Comment:  Decides if anneal should be done
           ?SWITCH.TO.{TOP1}
           {TOP1}
            SCREEN.CLEAR
            YELLOW.LETTERS
         ." IS AN INITIAL VACUUM BAKE NECESSARY ? " GET.Y/N
            IF
            INITIAL.ANNEAL
            ELSE
           {TOP1}
         ." ANNEAL NOT NECESSARY..."
       2000 MSEC.DELAY
            THEN ;

: FIRST.SCREEN                         Comment:  Connection scheme instructions.
           ?SWITCH.TO.{TOP} SCREEN.CLEAR {BORDER}
           ?SWITCH.TO.{TOP3} SCREEN.CLEAR {TOP3}
       05 07 GOTO.XY
          ." >>> [PROGRAM NAME] <<< " CR
       05 09 GOTO.XY
      ." _________________________ " CR
       05 11 GOTO.XY
         ." [HOOK UP SCHEME #1] " CR
       05 13 GOTO.XY
          ." [ANY RELEVANT ADJUSTMENT] " CR
       05 15 GOTO.XY
         ." [CAUTION FOR A SPECIFIC CONDITION] " CR ;
```

{PROCEDURES FOR MONOCHROMATOR ADJUSTMENT}

```
: START.MOTOR                          Comment:  Resets monochromator to the start position.
              {RESET} SCREEN.CLEAR
         01 00 GOTO.XY
               BLINK.TOGGLE
           169 VIDEO.ATTRIBUTE
               INTEN.ON
            ." >>> RESETTING <<< "
             " T5 A0.020 V0.50 D80000 G " GPIB.WRITE
         75000 MSEC.DELAY
              {RESET} SCREEN.CLEAR
               BLINK.TOGGLE BEEP ;

: GOUP.POSITION                        Comment:  Increments monochromator counter reading.
              {RESET} SCREEN.CLEAR
         01 01 GOTO.XY
           169 VIDEO.ATTRIBUTE
               BLINK.TOGGLE INTEN.ON
        ." >>> STEPPING UP <<< "
               SCANBEGINPOS CURRENTPOS - X1 :=
               X1 5000 * -1 *
               A :=
               A
              "."
```

```
              BETA ":=
            " T5 "
            " D" BETA 32 "COMPRESS "CAT
            " G " GPIB.WRITE
      115000 MSEC.DELAY
             {RESET} SCREEN.CLEAR BLINK.TOGGLE
           ." ALL DONE... "
        3000 MSEC.DELAY
             {RESET} SCREEN.CLEAR
              WAIT.FOR.KEY
             {RESET} SCREEN.CLEAR ;

: GODOWN.POSITION                    Comment:  Decreases monochromator counter value.
             {RESET}
              SCREEN.CLEAR
          169 VIDEO.ATTRIBUTE
        01 00 GOTO.XY
              BLINK.TOGGLE INTEN.ON
      ." >>> STEPPING DOWN <<< "
              CURRENTPOS SCANBEGINPOS - X1 :=
              X1 5000 *
              B :=
              B
             "."
              ALPHA ":=
            " T5 "
            " D" ALPHA "CAT 32 "COMPRESS "CAT
            " G " "CAT GPIB.WRITE
      115000 MSEC.DELAY
             {RESET} SCREEN.CLEAR BLINK.TOGGLE
       01 01 GOTO.XY
          ." ALLDONE.. " BEEP 1000 MSEC.DELAY
            {RESET} SCREEN.CLEAR BLINK.TOGGLE ;

: DECIDE.POSITION                    Comment:  A decision making routine.
            {RESET} SCREEN.CLEAR 01 01 GOTO.XY
         169 VIDEO.ATTRIBUTE
          ." *** THINKING *** "
        2000 MSEC.DELAY
             CURRENTPOS
         520 < IF GOUP.POSITION
             ELSE GODOWN.POSITION THEN
        5000 MSEC.DELAY ;

: GOTO.POSITION                      Comment:  Directs monochromator to any desired position.
            ?SWITCH.TO.{TOP}
            {TOP} 05 05 GOTO.XY SCREEN.CLEAR
           " E " GPIB.WRITE
           " A0.25 V0.4 MN G C " GPIB.WRITE
       05 01 GOTO.XY
          ." SET MONOCHROMATOR AT (*10) POSITION, IF NOT THERE ALREADY" CR
       05 03 GOTO.XY
          ." INPUT THE CURRENT POSITION " #INPUT&CHECK BEEP CR
             CURRENTPOS :=
```

```
            CURRENTPOS 520 = IF ELSE DECIDE.POSITION THEN ;

: PRINT.DATA                          Comment:  Prints data summary after program execution.
           ?SWITCH.TO.{BOTTOM} {BOTTOM}
          ." HIT ANY KEY WHEN READY... "
          ." ANY OTHER KEY MAY ABORT IT."  BEEP PCKEY ?DROP 13 <> BEEP
            IF ELSE
          ." >>> PRINTING DATA <<< "
            OUT>PRINTER CR CR
        -1 4 FIX.FORMAT
           4 SPACES ." DATE :" .DATE 5 SPACES ." TIME :" .TIME CR CR
           4 SPACES ." EXPERIMENTER : " OP.NAME "TYPE CR CR
           4 SPACES ." SAMPLE # : " FILENAME " .DAT" "CAT 32 "COMPRESS "TYPE CR CR
           4 SPACES ." AIM : " AIMEXP "TYPE CR CR
           4 SPACES ." HISTORY " SPECIFICS "TYPE CR CR
           4 SPACES ." TOTAL JSC " TOTJSC . ." mA/CM2" CR CR
          ." [PARAMETER1]     [PARAMETER2]     [PARAMETER3]    [PARAMETER4]" CR
         ." ____________     ___________     ____________    ___________ " CR CR
            MAXPOINTS 1 + 1 DO
        -1 4 FIX.FORMAT
           [PARAMETER1] . 8 SPACES
           [PARAMETER2] . 8 SPACES
           [PARAMETER3] . 8 SPACES
           [PARAMETER4] . 8 SPACES
            LOOP
            CONSOLE THEN BEEP ;
```

DATA FILE CREATING AND SAVING PROCEDURES

```
: DIR.CHECK                           Comment:  Displays data directory
           SCREEN.CLEAR
         ." THE CURRENT DIRECTORY OF THE SPECTRAL/DATA IS :"
           CHDIR C:\PVMD\SPECTRAL\DATA
           DIR *.*
           CHDIR C:\PVMD\SPECTRAL ;

: CHECK.CREATE                        Comment:  Determines if a new data file be created."
         ." NEED TO LOOK AT THE DIRECTORY [Y/N]" CR
         ." ANY OTHER KEY WILL NOT ACCESS THE DIRECTORY " CR
           PCKEY DUP EMIT
           DUP 90 > IF
       32 - THEN
           DUP
       89 = IF
           DIR.CHECK
           DROP CR CR ;

: CREATE.DATA.FILE Comment:  Allocates spaces for data file.
           STACK.CLEAR
           FILE.TEMPLATE
         2 COMMENTS
           REAL DIM[ NNN ] SUBFILE
         3 TIMES
           INTEGER DIM[ MM ] SUBFILE
           END
           CHDIR C:\PVMD\[PATHNAME]\DATA
```

```
           FILENAME DEFER> FILE.CREATE ;

: WRITE.DATA.FILE                          Comment:  Writes data into a specified file .
           FILENAME DEFER> FILE.OPEN
          [SPECIFICS #1] 1 >COMMENT
          [SPECIFICS #2] 2 >COMMENT
         1 SUBFILE [DATA1] ARRAY>FILE
         2 SUBFILE [DATA2] ARRAY>FILE
         3 SUBFILE [DATA3] ARRAY>FILE
         4 SUBFILE NDATA ARRAY>FILE
           FILE.CLOSE
           CHDIR C:\PVMD\[DIR. NAME]
          {WARNING} 030 VIDEO.ATTRIBUTE SCREEN.CLEAR
      01 00 GOTO.XY
         ." Done... "

: READ.DATA.FILE                          Comment:  Retrieves the data file.
           CHDIR C:\PVMD\[FILENAME]
          [PATH NAME] [FILENAME]
         " .DAT" "CAT 32 "COMPRESS
          "CAT 32 "COMPRESS
           DEFER> FILE.OPEN
         1 SUBFILE [DATA1] FILE>ARRAY
         2 SUBFILE [DATA2] FILE>ARRAY
         3 SUBFILE [DATA3] FILE>ARRAY
         4 SUBFILE NDATA   FILE>ARRAY
           FILE.CLOSE
           CHDIR C:\PVMD\[FILENAME] ;

: SAVE.DATA                               Comment:  Manual Interruption to check if the data be saved.
          ?SWITCH.TO.{BOTLINE} {BOTLINE} SCREEN.CLEAR
         ." DO YOU WANT TO SAVE THE DATA [CAPITALS ONLY] !! "
           GET.Y/N
           IF 89 EMIT
           CREATE.DATA.FILE
          {BOTLINE}
           SCREEN.CLEAR
          {BOTLINE}
           BLINK.TOGGLE
         ." Creating..." FILENAME "TYPE
           WRITE.DATA.FILE BLINK.TOGGLE THEN SCREEN.CLEAR ;

: ACCESS.DATA                             Comment:  Retrieves the data.
           STACK.CLEAR
          ?SWITCH.TO.{BOTTOM} {BOTTOM}
         ." DO YOU NEED TO LOOK AT THE DIRECTORY.. [Y/N] ? " CR
           GET.Y/N
           IF 89 EMIT
           SCREEN.CLEAR
           DIR.CHECK
           THEN CR BEEP2
         ." PRINT NAME OF THE FILE TO RETRIEVE... "
          "INPUT&CHECK FILENAME ":= BEEP2 CR
          ?SWITCH.TO.{BOTLINE} {BOTLINE} YELLOW.LETTERS
```

```
          ." Reading... " RED.LETTERS FILENAME "TYPE
             READ.DATA.FILE
            {BOTLINE} SCREEN.CLEAR    ;

: BACK_UP                              Comment:  Backs up the diskette in a specified drive.
            ?SWITCH.TO.{BOTLINE} {BOTLINE} SCREEN.CLEAR
          ." IS BACK UP DISKETTE IN B: DRIVE PRESENT ? "
             GET.Y/N IF
             CHDIR C:\PVMD\[DIR NAME]\DATA
             FILENAME
             DEFER> COPY
             FILEPATHB
             DEFER> TO
             CHDIR C:\PVMD\[DIR NAME]
             THEN ;
```

Graphics and dataplotting procedures:

```
: SET.GRAPHICS                         Comment:  Sets the viewport and text window.
          ." PRINT MAXIMUM Y-VALUE" #INPUT&CHECK YMAX := CR BEEP
          ." PRINT MINIMUM Y-VALUE" #INPUT&CHECK YMIN := CR BEEP
            ?SWITCH.TO.{BOTTOM}
             GRAPHICS.DISPLAY
            {BOTTOM}
             0.0 0.25 VUPORT.ORIG
             1.0 0.75 VUPORT.SIZE
             VUPORT.CLEAR
             OUTLINE
             AXIS.DEFAULTS
             VERTICAL
             AXIS.FIT.OFF GRID.OFF
             LABEL.SCALE.OFF
             HORIZONTAL
             AXIS.FIT.OFF GRID.ON
             LABEL.SCALE.OFF
             NORMAL.COORDS
             0.20 0.15 AXIS.ORIG
             0.75 0.75 AXIS.SIZE
             0.20 0.15 AXIS.POINT
             VERTICAL AXIS.OFF NO.LABELS
             HORIZONTAL X[MAX] X[MIN] WORLD.SET
             00 00 LABEL.POINTS
             -.5 -.9 4. LABEL.FORMAT
             XY.AXIS.PLOT
             NORMAL.COORDS
             0.20 0.15 AXIS.POINTS
             HORIZONTAL AXIS.OFF NO.LABELS
             VERTICAL AXIS.ON
             VERTICAL 0.0 1.0 WORLD.SET
             0.0 0.1 LABEL.POINTS
             -1.2 0. 6.0 LABEL.FORMAT
             027 AXIS.COLOR
             XY.AXIS.PLOT ;
```

```
: SET.LABELS                              Comment:  Assigns labels to the axis.
              NORMAL.COORDS
            6 LABEL.COLOR
              0.05 0.23 POSITION
           90 LABEL.DIR
           90 CHAR.DIR
           "  [Y-AXIS LABEL] " LABEL
              0.42 0.05 POSITION
              0 LABEL.DIR
              0 CHAR.DIR
           "  [X-AXIS LABEL] " LABEL
              NORMAL.COORDS
              0.80 0.05 POSITION
              0. 0. CHAR.JUST
              17 ASCII" " X-AXIS" 16 ASCII" "CAT "CAT
              0 LABEL.DIR 0 CHAR.DIR
              LABEL
              0.07 0.6 POSITION
              17 ASCII" " Y-AXIS" 16 ASCII" "CAT "CAT
              90 LABEL.DIR 90 CHAR.DIR
              LABEL
              0 LABEL.DIR 0 CHAR.DIR
              0.45 0.95 POSITION
              FILENAME LABEL
              NORMAL.COORDS ;

: CHANGE.SYMBOL                           Comment:  Changes the data symbol.
              ?SWITCH.TO.{BOTTOM} {BOTTOM}
              10 01 ." CHANGE DATA SYMBOL FROM' DATASYMB "TYPE
              10 03 ." TO [ENTER NEW DATA SYMBOL HERE] :-"
             "INPUT "LEN 0 <>
              IF DATASYMB ":=
              ELSE "DROP THEN ;

: EXPAND.GRAPH                            Comment: Zooms on a specified portion of the graph.
              HORIZONTAL
              AXIS.DEFAULTS
              LABEL.SCALE.ON
              SOLID
             ?SWITCH.TO.{BOTTOM}
              {BOTTOM}
              SCREEN.CLEAR BEEP2
           ." KEYPAD CURSOR MOVES POSITION OF LINES " CR
           ." HOME KEY INDICATES POSITION & INS EXPANDS GRAPH " CR
           ." DEL KEY HALTS THE OPTION. HIT ANY KEY TO CONTINUE" CR
              ARRAY.READOUT
              LINE.POSITIONS
              READOUT>ARRAY
           ." # OF READOUT POINTS ARE : " #READOUT .
              NORMAL.COORDS
              BEGIN
             ?KEY
              UNTIL ;
```

Main Programs

```
: REF.SCAN                                   Comment:  Data acquisition program for reference cell response.
             {DEF}
              STACK.CLEAR
              CLEAR.WINDOWS
              FIRST.SCREEN
             {BOTLINE}
              01 01 GOTO.XY
              WAIT.FOR.KEY
             {BOTLINE}
              01 01 GOTO.XY SCREEN.CLEAR
             ?SWITCH.TO.{TOP1} {TOP1}
              WHITE.LETTERS
              01 01 GOTO.XY
           ." ENTER LOCK-IN RANGE OF SIGNAL AMPLIFIER: " BEEP2
              YELLOW.LETTERS
             #INPUT&RANGE LOCK_RANG := CR
              WHITE.LETTERS
              01 01 GOTO.XY
           ." ENTER SENSITIVITY RANGE: THE DEFAULT IS" SVTY . BEEP2
              1E-4 DEF.# :=
              GET.NUMBER
              DEF.# SVTY := CR
              {BOTLINE} SCREEN.CLEAR
              SEND.INTERFACE.CLEAR
              SET.175
              SET.175.1
              SET.MOTOR
              GOTO.POSITION
              START.POSITION
              5000 MSEC.DEALY
             {PROGRESS}
              01 00 GOTO.XY
          234 VIDEO.ATTRIBUTE
           ." EXPERIMENT IS IN PROGRESS..."
             {TOP1} SCREEN.CLEAR
              08 05 GOTO.XY
           ." WAVELENGTH UDT.CURRENT #.PHOTONS "
             ?SWITCH.TO.{TOP3} SCREEN.CLEAR
             ?SWITCH.TO.{TOP} SCREEN.CLEAR
             {TOP3}
              QEREF_VS_LAMDA SUB[ 1 , MAXPOINTS , 2 ] DATAX :=
              MAXPOINTS 1 + 1 DO
              COMPARE.MM2
             {TOP3}
              ME.LISTENER
              MM2 TALKER
              BUFFER.LISTEN
              REF.CUR.IN "[ I ]
           0 "NUMBER
              ABS
              IF REF.CUR [ I ] := THEN "DROP
              LOCK_RANG SVTY REF.CUR [ I ] * * REF.CUR [ I ] :=
```

```
            I 10 * 350 + WVLNT [ I ] :=
        1.24 WVLNT [ I ] / 1000 *
            ENERGY [ I ] :=
        -1 4 FIX.FORMAT
          1 SPACES
            WVLNT [ I ] .
          8 SPACES
         9 3 SCI.FORMAT
            REF.CUR [ I ]
          6 SPACES
            REF.CUR [ I ] CHARGE
            DATAX [ I ] * /
           #PHOTON [ I ] :=
           #PHOTON [ I ] . CR
            WVLNT [ I ] 540 = IF
           {CHANGE} SCREEN.CLEAR 01 00 GOTO.XY
         027 VIDEO.ATTRIBUTE
          ." INSERT LONG PASS FILTER... "
       01 03 GOTO.XY
            WAIT.FOR.KEY
           {CHANGE} SCREEN.CLEAR
            THEN
           {BOTLINE} 01 00 GOTO.XY SCREEN.CLEAR
            MOTOR
          " A0.2 V0.5" GPIB.WRITE
           "T1 D-50000 MN G C " GPIB.WRITE
       10000 MSEC.DELAY BEEP
            LOOP
            MOTOR
           {RESET}
       01 00 GOTO.XY
         169 VIDEO.ATTRIBUTE
          ." >>> RESETTING <<< "
         "  T5 10.20 V0.50 D175000 G" GPIB.WRITE
     150000 MSEC.DELAY
          {WARNING} SCREEN.CLEAR
          {BOTLINE} SCREEN.CLEAR
      00 00 GOTO.XY
        078 VIDEO.ATTRIBUTE
         ." ALLDONE... " BEEP
           STACK.CLEAR REF.SAVE
          {BOTLINE} SCREEN.CLEAR
          {TOP1} SCREEN.CLEAR ;

: DO.SPECTRAL                         Comment: This procedure does spectral response.
          {DEF} STACK.CLEAR
          ?SWITCH.TO.{TOP3} SCREEN.CLEAR
          ?SWITCH.TO.{TOP} SCREEN.CLEAR
          {TOP3}
           SAMPLE.INFO
           SECOND.SCREEN
          {BOTLINE}
           01 00 GOTO.XY
           WAIT.FOR.KEY
```

```
     {BOTLINE} 01 01 GOTO.XY SCREEN.CLEAR
     ?SWITCH.TO.{TOP1} {TOP1}
      01 01 GOTO.XY
   ." PLEASE INPUT THE SCAN TEMPERATURE :-"
     #INPUT&CHECK YELLOW.LETTERS TSET := BEEP2 CR
      TSET 90 < IF
      SET.LN2.TEMP
      THEN
     {TOP1}
      01 01 GOTO.XY
   ." PLEASE INPUT THE BIAS VOLTAGE :"
     #INPUT&CHECK VIN% := BEEP2 CR
      RCHNL/10T
      VIN% -10 10 D/A.SCALE D/A.OUT
     {TOP1}
      01 00 GOTO.XY
   ." ENTER LOCK IN RANGE OF SIGNAL CHANNEL "
     #INPUT&CHECK LOCK_RANG := BEEP CR
      01 00 GOTO.XY
   ." SENSITIVITY RANGE IS :" SVTY . BEEP2
      1E-4 DEF.# :=
      GET.NUMBER
      DEF.# SVTY := CR
     {BOTLINE} SCREEN.CLEAR
      SET.175
      SET.175.2
      SET.MOTOR
      GOTO.POSITION
      START.POSITION
5000 MSEC.DELAY
     {PROGRESS}
 234 VIDEO.ATTRIBUTE
      01 00 GOTO.XY
   ." EXPERIMENT IN PROGRESS..."
     ?SWITCH.TO.{TOP}
     {TOP1} YELLOW.LETTERS
      08 05 GOTO.XY
   ." WAVELENGTH  ENERGY  DUT.CURRENT  DUT QE "
     ?SWITCH.TO.{TOP3} SCREEN.CLEAR
     ?SWITCH.TO.{TOP} SCREEN.CLEAR
     {TOP3} WHITE.LETTERS
      MAXPOINTS 1 + 1 DO
      COMPARE.MM2
     {TOP3}
      ME LISTENER
      MM2 TALKER
      BUFFER.LISTEN
      DUT.CUR.IN "[ I ]
  0 "NUMBER
      ABS
      IF DUT1.CUR [ I ] := THEN "DROP
      LOCK_RANG SVTY DUT1.CUR [ I ] * * DUT1.CUR [ I ] :=
      I 10 * 350 + WVLNT [ I ] :=
1.24 WVLNT [ I ] / 1000 *
```

```
          ENERGY [ I ] :=
      -1 4 FIXX.FORMAT 1 SPACES
          WVLNT [ I ] .
        4 SPACES
          ENERGY [ I ] .
        4 SPACES
          ENERGY [ I ] .
       9 3 SCI.FORMAT
        4 SPACES
          DUT1.CUR [ I ] .
        4 SPACES
          DUT1.CUR [ I ] CHARGE #PHOTON [ I ] * /
          QE [ I ] :=
          QE [ I ] . CR
          WVLNT [ I ] 540 = IF
         {CHANGE} SCREEN.CLEAR 01 00 GOTO.XY
       027 VIDEO.ATTRIBUTE
          BLINK.TOGGLE
        ." INSERT LONG PASS FILTER... "
          WAIT.FOR.KEY
         {CHANGE} SCREEN.CLEAR
          THEN
          MOTOR
        "  A0.20 V0.50 " GPIB.WRITE
        "  T1 D-50000 MN G C " GPIB.WRITE
     10000 MSEC.DELAY BEEP
          LOOP
          MOTOR
         {RESET}
       169 VIDEO.ATTRIBUTE
     01 01 GOTO.XY
        ." >>> RESETTING <<< "
        "  T5 A0.20 V0.50 D1750000 G " GPIB.WRITE
    150000 MSEC.DELAY
         {WARNING}
     01 01 GOTO.XY SCREEN.CLEAR
         {BOTLINE} 01 01 GOTO.XY
        ." ALLDONE..." BEEP
          STACK.CLEAR
          DAT.SAVE
          IEEE.488.OFF ;
```

```
: DO.SR                                   Comment: A typical data acquisition program.
          ?SWITCH.TO.{TOP1} {TOP1}
       08 SPACES
       ." [ARE A SET OF CONDITIONS ESTABLISHED]" BEEP
          GET.Y/N IF 89 EMIT
          REF.SCAN
          THEN
          DO.SPECTRAL
          SUM_JSC
          PRINT.DATA
          SET.GRAPHICS
          WVLNT
```

```
            QE
        030 COLOR
            XY.DATA.PLOT
            SET.GRAPHICS2
            SAVE.DATA.FILE
            BACK.UP ;

: DO:DARK                              Comment: Procedure does dark conductivity.
            CLEAR.WINDOWS
            INIT.ARRAYS
            STACK.CLEAR
            SET.VOLTMETER
          " T4XC0X" GPIB.WRITE
            DARK.CONDUCTIVITY
           ?SWITCH.TO.{TOP1}
         12 SPACES
         ." TEMP IN K 1000/T  DC VOLT  CONDUCTIVITY "
           ?SWITCH.TO.{TOP3}
           ?SWITCH.TO.{TOP}
           {TOP3}
            SCREEN.CLEAR
      301 1 DO
            READ.TEMP
            ME LISTENER
            VOLTMETER TALKER
            BUFFER.LISTEN
            VOLDAT "[ I ]
        0. "NUMBER
            ABS
            IF DCV [ I ] := THEN "DROP
           ?DROP
            INVTINK TINVK [ I ] :=
            DCV [ I ] 0.0 > IF
            CONSTI DCV [ I ] / LTOS * 450 * 1E-4 * INV
            DCOND [ I ] :=
            ELSE DCOND [ I ] 1.0 :=
            THEN
          1 SPACES
       -1 4 FIX.FORMAT
            TINK TINKD [ I ] :=
            TINKD [ I ] . 3 SPACES
            TINKV [ I ] . 3 SPACES
       11 3 SCI.FORMAT
            DCV [ I ] . 3 SPACES
            DCOND [ I ] . CR
       11 3 SCI.FORMAT
            TINK 200 < IF
            TINK 70. - 360 *
            ELSE
            TINK 77. - 110 *
            THEN
            ABS
            MSEC.DELAY
            DASH16
```

```
          DCHNL/10T
          TINK TMAX% > IF
          BEEP1
          LEAVE
          ELSE
    1 4 * POWER
          POWER D/A.OUT
        " X " GPIB.WRITE
          THEN
          BEEP
          LOOP
          BEEP
          HEAT.OFF
        0 D/A.OUT
          VOLTMETER
        " T4XC1X" GPIB.WRITE
          SEND.INTERFACE.CLEAR
          REMOTE.ENABLE.OFF ;   Comment: The photo conductivity part is identical.

: DO.ACCOND Comment: This procedure does the A.C Conductivity.
          SAMPLE.INFO
          FIRST.SCREEN
         {BOTLINE}
          RED.LETTERS
          RED.LETTERS
          WAIT.FOR.KEY
          SCREEN.CLEAR
          YELLOW.LETTERS
         ?SWITCH.TO.{TOP1}
         {TOP1}
          SCREEN.CLEAR
          YELLOW.LETTERS
       ." PLEASE INPUT THE LOW TEMPERATURE SET LIMIT"
         #INPUT TSET :=
          CHECK.ANNEAL
          SET.LN2.TEMP
          SCREEN.CLEAR
         ?SWITCH.TO.{TOP1}
          SCREEN.CLEAR
         {TOP1}
       ." INPUT MAX. TEMP IN k [350] FOR ~ 100 C"
         #INPUT&CHECK TMAX% := BEEP2
         {TOP1} SCREEN.CLEAR ;

: ACIMPED   Comment: Continuation of the above procedure.
          SET.TOY
          CLEAR.WINDOWS
          INIT.ARRAYS
          STACK.CLEAR
          DARK.CONDUCTIVITY
          STACK.CLEAR
         ?SWITCH.TO.{TOP1}
       12 SPACES
       ." TEMP IN k 1000/T  AC_RES (OHMS) AC_CONDUCT "
```

```
     ?SWITCH.TO.{TOP3}
     ?SWITCH.TO.{TOP}
     {TOP3}
      SCREEN.CLEAR
 301 1 DO
      READ.TEMP
      TOY
      SEND.INTERFACE.CLEAR
   255 SERIAL.POLL DROP
     " SO1, 2" GPIB.WRITE
     " CZO" GPIB.WRITE
     " OP2, 1" GPIB.WRITE
     " SI" GPIB.WRITE
   8 3 SCI.FORMAT
    34 LISTEN.LIMIT
      DATA1 GPIB.READ \ FOR FREQUENCY
      DATA1
     1 B := 0 INFOR :=
      BEGIN
  44. "NUMBER
      WHILE INFOR [ B ] :=
     1 B + B :=
      REPEAT "DROP
      INFOR [ 1 ] FREQU [ I ] :=
      INFOR [ 2 ] IMPED [ I ] :=
      INFOR [ 3 ] PHASE [ I ] :=
   255 SERIAL.POLL DROP
      INVTINK TINVK [ I ] :=
      IMPED [ I ]  0.0 > IF
      IMPED [ 625 ] 625.0 * LTOS / 1E-4 *
      ACCOND [ I ] :=
      ELSE ACCOND [ I ] :=
      THEN
  -1 4 FIX.FORMAT
      TINK TINKD [ I ] :=
      TINKD [ I ] . 2 SPACES
      TINVK [ I ] . 3 SPACES
  11 4 SCI.FORMAT
      IMPED [ I ] . 3 SPACES
      ACCOND [ I ] . 1 SPACES
  11 3 SCI.FORMAT
      PHASE [ I ] . CR
   8 3 FIX.FORMAT
     " RE" GPIB.WRITE
      TINK 175 < IF
 I 7 * POWER :=
40000  ELSE
      I 4 * POWER :=
 20000 THEN
      MSEC.DELAY
      DASH16
      DCHNL/1OT
      TINK TMAX% > IF
      BEEP1
```

```
        LEAVE
        ELSE
        POWER D/A.OUT
        THEN
        BEEP
       ?DROP
        LOOP
        BEEP
        HEAT.OFF
        SEND.INTERFACE.CLEAR
        REMOTE.ENABLE.ON     ;
```

Lines below initialize screen and set screen colors

```
       {BOTTLINE}
    075 VIDEO.ATTRIBUTE
        SCREEN.CLEAR
        BLINK.TOGGLE
     ." DONE LOADING..."
   3000 MSEC.DELAY
       {BOTLINE}
        SCREEN.CLEAR
       {FULL}
        SCREEN.CLEAR
```

```
: SELECT.ACTION                          Comment: Sets the initial screen and provides options.
        SCREEN.CLEAR
       ?SWITCH.TO.{TOP}
    075 VIDEO.ATTRIBUTE {TOP} SCREEN.CLEAR
  05 02 GOTO.XY INTEN.ON ."  [PROGRAM NAME] "
  05 05 GOTO.XY ." TYPE                    PROGRAM DOES "
  05 07 GOTO.XY ." ____                    ____________ "
  05 10 GOTO.XY ." [EXPERIMENT #1] "   INTEN OFF
  30 10 GOTO.XY ." Details of the Ist experiment." INTEN.ON
  05 12 GOTO.XY ." [EXPERIMENT #2] "   INTEN.OFF
  30 12 GOTO.XY ." Details of the 2nd experiment." INTEN.OFF ;
        CR CR CR BEEP2 {BORDER}
        NORMAL.DISPLAY
        SELECT.OPTION
       {BOTLINE}
    030 VIDEO.ATTRIBUTE
```

■ Please note that the procedures mentioned above do not constitute a full program. The sections, however can be utilized along with proper variable declaration, towards a data acquisition program.

— ¤ —

Appendix C: Grid Design Considerations for Schottky Barrier Photodiodes.

In Schottky barrier photodiodes, the grid serves a dual purpose of providing a low resistance in the external circuit and maintaining a high transmission of the incident light to the active layer beneath it. Generally, a thin and transparent layer of metal of suitable Schottky barrier height is deposited and a grid pattern is further deposited on it. The grid then adds its own contribution to the series resistance. Hence, it is imperative that a grid pattern be selected which offers negligible series resistance and shadowing. One of the contact grid geometry under consideration is depicted in Figure C.1. The grid contains, say n lines/cm. The sheet resistance of the first thin metal is, say R_S Ω/cm. For the parallel grid lines as shown in Figure (C.1) the finger width is assumed to be smaller than the spacing in between grid lines. Also, the conditions of short circuit current flow are maintained i.e. voltage $\lesssim V_{oc}/2$, is the voltage at the junction.

The power dissipated in the sheet resistance in a segment dx long and 1 cm. wide is given by;

$$p(x,\ x + dx) = [I(x)]^2 dR$$

where;

$$dR = r_s\ dx$$

The total power dissipation in the segment under consideration is given by

$$P_T = \int_0^{1/2n} I_{sc}^2 (\ 1/2n - 1\ )^2\ r_s\ dx$$

$$= I_{sc}^2 r_s/(24\ n^3)$$

Hence power dissipated per square per cm. of cell area at short circuit can be written as

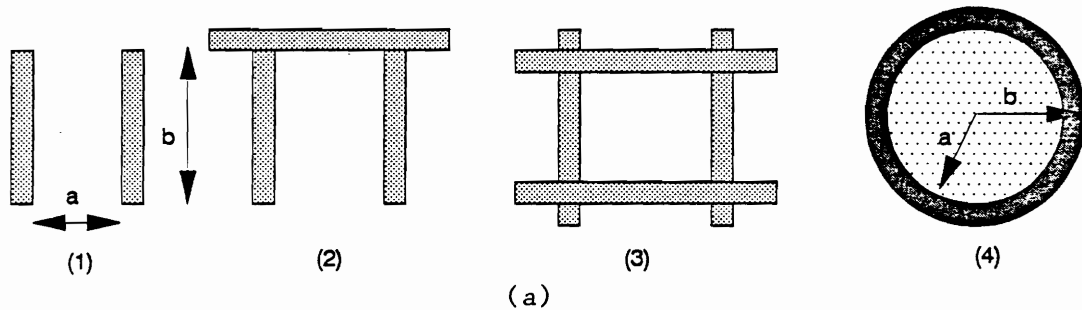

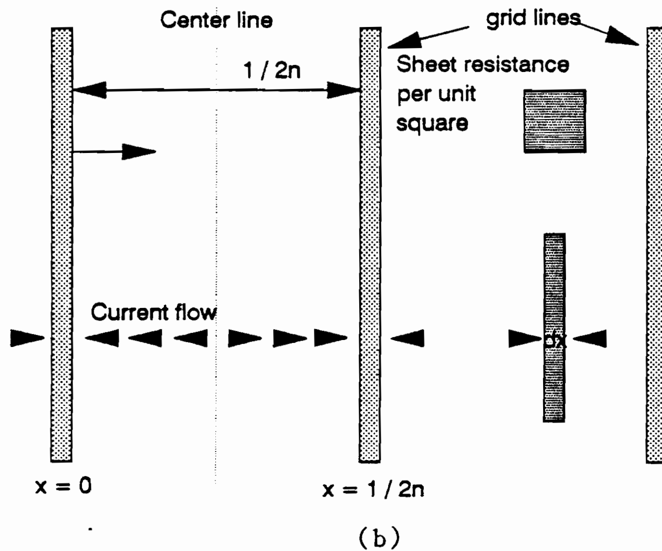

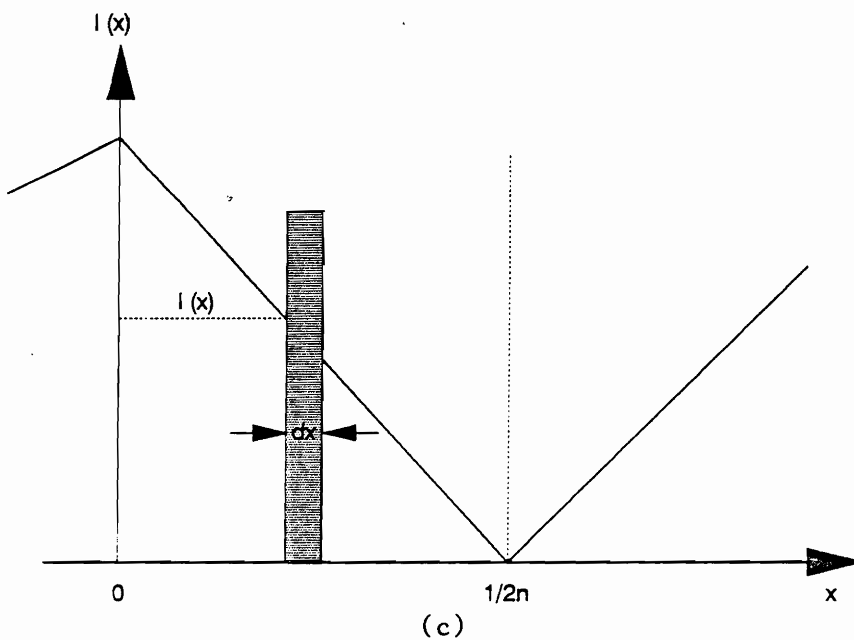

Figure C.1 (a) A Units of (1) parallel grid lines, (2) parallel grid lines with one bus bar, (c) rectangular mesh grid, and (4) circular grid. (b) current flow considerations in the grid fingers, and (c) lateral current flow in the thin metal layer at short circuit.

$$P_T = I_{sc}^2 R_L$$

where R_L is the effective lumped series resistance, and can be written as

$$R_L = r_s / (12 n^2)$$

Substituting more common terms such as shown in figure 5.5a

$$R_L = 1/12 \; (a/b) \; (\rho/t)$$

For geometry in Figure C.1 [a(2]), the expression has been calculated and is given by

$$R_L = \left[1/12(a/b) - (a/b)^2 8/\pi \sum (2n+1)^{-5} \tanh(2n+1)\pi \; (b/a) \right] (\rho/t)$$

and for circular grid geometry, the resistance is given by

$$R_L = 1/8\pi \; (\rho/t)$$

while for the circular grid with an electrode of infinitesimal thickness along one of the diameter of the circle

$$R_L \approx 7.382 \times 10^{-2} \; (\rho/t)$$

It is instructive from the above equations that the sheet resistivity should be low, thickness of the film should be high while maintaining a good transmission.

— ¤ —

References

1. B. K. Gilbert, Gallium Arsenide Technology, Ed. D. K. Ferry, H. W. Sams Co. Inc. (1985).
2. R. L. Jacobson and G. K. Wehner, J. Appl. Phys.36, 2674 (1965).
3. M. Kawabe, N. Kanazaki, K. Masuda, and S. Namba, Appl. Opts., 17, 2556 (1978).
4. R. S. Williams, Solid State Commun. 41, 153 (1983).
5. J. M. Epp and J. G. Dillard, Chem. Mater, 1, 325 (1989).
6. G. E. McGuire, Surf. Sci. 76,130 (1978).
7. J. L. Singer, J. S. Murday, and L. R. Cooper, Surf. Sci., 108, 7 (1981).
8. R. S. Berg and P. Y. Yu, Phys. Rev. B, 35, 2205 (1987).
9. G. F. Feng, M. Holtz, R. Zallen, J. Epp, J. Dillard, E. Cole, P. Johnson, S. Sen, and L. C. Burton, Proc. of Fall Mtg. MRS, (1987).
10. J. Feng, Optical studies of ion-bombarded Gallium arsenide, Ph. D. Thesis, VPI and State University, 1989.
11. J. Bonafe, J. Jimnez, M. Gonzalez, and M. Castagne, Physica Scripta, 30, 198 (1984).
12. P. K. Chatterjee, W. V. McLevige, K. V. Vaidyanathan, and B. G. Streetman, Appl. Phys. Lett.,28, 509 (1976).
13. S. Namba, M. Kawabe, N. Kanazaki, and K. Masuda, J. Vac. Sci. & Technol., 12(6), 1348 (1975).
14. J. R. Chelikowsky and M. L. Cohen, Phys. Rev. B, 14, 556 (1976).
15. M. Skowronski, J. Lagoswski, and H. C. Gatos, Phys. Rev. B, 32, 4264 (1985).
16. G. A. Baraff, M. Lannoo, and M. Schluter, Phys. Rev. B, 38, 6003 (1988).
17. H. J. Van Bardeleben, D. Stievenard, D. Deresmes, A. Hubard, and J. C. Boorgoin, Phys. Rev. B, 34, 7192 (1986).
18. J. F. Wagner and J. A. Vechten, Phys. Rev. B, 35, 2330 (1987).
19. G. Jacob, Journal of Crystal Growth, 58, 455 (1982).

20. K. Terashima, T. Katsumata, F. Orita, T. Kikuta, and T. Fukada, Jap. J. Appl. Phys., 22, 2325 (1983).

21. W. J. Anderson and Y. S. Park, J. Appl. Phys., 8, 4568 (1978).

22. D. K. Sadana, T. Sands and J. Washburn, Appl. Phys. Lett., 44, 623 (1984).

23. J. M. Epp, The effects of ion bombardment on the chemical reactivity of GaAs (100), Ph. D. Thesis, VPI & State University, (1989).

24. J. P. Ponpon, Surf. Sci. 162, 687 (1985).

25. T. Naffati, G. N. Lu and C. Barrett, Sol. Stat. Elecron, 31(8), 1335 (1988).

26. S. W. Pang, D. D. Rathman, D. J. Silversmith, R. W. Mountain, and P. D. DeGraff, J.Appl. Phys., 54(6), 3272 (1983).

27. E. D. Cole, S. Sen and L. C. Burton, J. Electron. Mater. 4, 527 (1989).

28. Y. X. Wang and P. H. Holloway, J. Vac. Sci. and Technol., B2(4), 613 (1984).

29. P. Kwan, K. N. Bhat, J. M. Borrego and S. K. Ghandhi, Solid Stat. Electron, 26, 125 (1983).

30. C. S. Wu, D. M. Scott, Wei-Xi-Chen and S. S. Lau, J. Electrochem. Soc. 132, 918 (1985).

31. K. Yamasaki, K. Asai, K. Shimada and T. Makimura, J. Electrochem. Soc., 129, 2760 (1982).

32. T. Hara, H. Suzuki and A. Suga, J. Appl. Phys., 62(10), 4109 (1987).

33. P. Robinzohn, G. Gautherin, B. Agius and C. Cohen, J. Electrochem. Soc., 131, 905 (1984).

34. Y. G. Wang and S. Ashok, J. Vac. Sci. Technol., A6(3), 1548 (1988).

35. S. W. Pang, M. W. Gois, N. N. Eferemow and G. A. Lincoln, J. Vac. Sci. Technol. B3, 398 (1985).

36. G. M. Martin, A. Mitonneau and A. Mircea, Electronics Lett., 13, 190 (1977).

37. S. W. Pang, Solid Stat Technol. 4, 249 (1984).

38. Y. Chung, D. W. Langer, R. Becker and D. Look, IEEE Trans. Electron Devices,

ED-32, 40 (1984).

39. D. W. E. Allsopp and A. R. Peaker, Solid Stat Electron, 29(4), 467 (1986).

40. Y. X. Wang and P. H. Holloway, J. Vac. Sci. & Technol., A2, 567 (1984).

41. P. D. Taylor and D. V. Morgan, Solid State Electron., 19, 481 (1980).

42. F. K. Moghadam and X. C. Mu, IEEE Trans. Electron Device, ED-36, 1602 (1989).

43. E. Meyer and G. Heymann, J. Vac. Sci. Technol. B7(3), 491 (1989).

44. J. M. Palau, E. Testemale, A. Ismail and L. Lassabarere, Solid Stat. Electron, 25, 285 (1982).

45. O. Aina and K. P. Pande, J. Appl. Phys, 56, 1717 (1984).

46. A. Vaseashta, J. M. Epp, S. Sen and L. C. Burton, 24th IEEE, IECEC (1989).

47. S. Sen, E. D. Cole and L. C. Burton, Proc. of the Spring Mtg. of MRS (1988).

48. S. Sen, "Electrical Studies on Ion Etched (100) n-GaAs Surfaces" M.S. Thesis, VPI & State University (1988).

49. E. D. Cole, "Electrical Analysis of Low Energy Ar^+ Ion Bombarded GaAs", Ph. D. Thesis, VPI & State University, (1988).

50. A. Amith and P. Park, J. Vac. Sci. Technol., 15(4), 1344 (1978).

51. W. D. Devlin, Electron Lett., 15, 92 (1980).

52. D. J. Stirland and B. W. Straugh, Thin Solid Films, 31, 139 (1976).

53. R. Singh, S. J. Fonash, S. Ashok, P. J. Caplan, J. Shappiro, M. Hage-Ali and J. Ponpon, J. Vac. Sci. Technol, 1, 334 (1983).

54. L. P. Anderson and A. O. Emwaraye, Vacuum, 28, 1 (1978).

55. J. M. Borrego and R. J. Gutmann, Appl. Phys. Lett, 28, 280 (1976).

56. S. K. Ghandhi, P. Kwan, K. N. Bhat and J. M. Borrego, IEEE Electron Device Lett. EDL-3, 48 (1982).

57. G. A. Sarov, Vacuum, 34, 1027 (1984).

58. F. R. Mullins and A. Brunnschweiler, Solid Stat. Electron., 19, 47 (1976).

59. B. Pistoulet, P. Girard and G. Hamadjian, J. Appl. Phys., 56, 2275 (1984).

60. Y. Mita, Defect Recognition and Image Processing in III-V compounds, Ed. J. P. Fillard, 185 (1985).

61. A. Goltzene, B. Meyer and C. Schwab, Appl. Phys. Lett., 54, 907 (1989).

62. E. Kamieniecki, J. Lagowski and H. C. Gatos, J. Appl. Phys.51(3), 1863 (1980).

63. P. M. Mooney, T. N. Theis and S. L. Wright, Intl. Symp. GaAs and Related Compounds, Greece, Inst. Phys. Conf. Ser, #91, 359 (1987).

64. A. Vaseashta and L. C. Burton, Proc. of the Spring Mtg. MRS (1989).

65. J. Jimnez, P. Hernandez, and J. A. de Saja and J. Bonnafe, Solid Stat Commun., 55, 459 (1985).

66. S. Nojima, J. Appl. Phys., 58, 3485 (1985).

67. S. Nojima, J. Appl. Phys. 57, 621, (1985).

68. S. Nojima, H. Asahi and T. Ikoma, J. Appl. Phys., 61, 1073 (1987).

69. Y. Mita, J. Appl. Phys., 61, 5325 (1987).

70. M. Tajima, H. Sato, T. Iino and K. Ishida, Jap. J. of Appl. Phys., 27, L101 (1988).

71. G. Vincent, D. Bois and A. Chantre, J. Appl. Phys., 53, 3643 (1982).

72. J. Tauc, R. Grigorovici and A. Vancu, Phy. Stat. Sol., 15, 627 (1966).

73. R. S. Crandall, Phys. Rev. Lett., 44, 749 (1980).

74. H. M. Welsh, W. Fuhs, K. H. Greeb and H. Mell, J. De Physique, 42, C-4, 567 (1981).

75. C. R. Wronski, B. Ables, G. D. Cody and T. Tiedje, Appl. Phys. Lett., 37, 96 (1980).

76. G. Cody, T. Tiedge, B. Ables, T. Moustakas, B. Brooks and Y. Goldstein, J. De Physique, 42, C-4, 301 (1981).

77. J. Feng and R. Zallen, Phys. Rev. B (accepted for publication, 1989).

78. M. Holtz, Raman-scattering studies of the structure of ion-implanted GaAs, Ph. D. Thesis, VPI & State University, (1987).

79. J. Lindhard and M. Scharff, Phys. Rev., 124, 128 (1961).

80. P. Sigmund, Sputtering by Particle Bombardment I: Physical Sputtering of Single

Element Solids, Ed. R. Behrisch, Springer Verlag (1981).

81. P. Sigmund, Appl. Phys. Lett., 14, 114 (1969), & J. Vac. Sci. Technol. A7(3), 585 (1989).

82. P. Sigmund, Phys. Rev, 184, 383 (1969).

83. F. Morehead, Jr. and B. L. Crowder, Rad. Effects, 6, 27 (1970).

84. W. E. Spicer, P. W. Chye, P. E. Gregory, T. Sukegawa and I. A. Babaloa, J. Vac. Sci. Technol., 13, 231 (1976).

85. W. E. Spicer, I. Lindau, R. R. Skeath and C. Y. Su, Applic. Surf. Sci., 9, 83 (1981).

86. N. Newmann, M. Van Schilfgaarde, T. Kendelwicz, M. D. Williams, and W. E. Spicer, Phy. Rev. B, 33(2), 1146 (1986).

87. S. J. Eglash, N. Newmann, S. Pan, D. Mo, K. Shenai, W. E. Spicer, F. A. Ponce and D. M. Collins, J. Appl. Phys., 61, 5159 (1987)

88. R. Ludeke, Surf. Sci, 132, 143 (1983).

89. R. Ludeke, Phys. Rev. B40, Preprint (1989)

90. R. Ludeke, J. Jezequel and A. Taleb-Ibrahimi, J. Vac. Sci. Technol. B6(4), 1277 (1988).

91. R. Ludeke, G. Jezequel and A. Taleb-Ibrahimi, Phys. Rev. Lett, 61(5), 601 (1988).

92. W. E. Spicer, Z. Liliental-Weber, E. Weber, N. Newmann, T. Kendelewicz, R. C. Rao, C. McCants, P. Mahowald, K. Miyano and I. Lindau, J. Vac. Sci. Technol., B6(4), 1245 (1988).

93. W. E. Spicer, N. Newmann, T. Kendelewicz, W. G. Petro, M. D. Williams, C. E. McCants and I. Lindau, J. Vac. Sci. & Technol., B3(4), 1178 (1985).

94. O. F. Sankey, R. E. Allen, S. F. Ren and J. D. Dow, J. Vac. Sci. & Technol., B3(4), 1162 (1985).

95. J. L. Freeouf, App. Phys. Lett, 41(3), 285 (1982).

96. B. W. Lee, D. C. Wang, R. K. Ni, G. Xu and M. Rowe, J. Vac. Sci. and Technol., 21(2), 577 (1982).

97. J. M. Woodall and J. L. Freeouf, J. Vac. Sci. Technol., B2(3), 610 (1984).

98. W. Gudat, D. E. Eastmann and J. L. Freeouf, J. Vac. Sci. and Technol., 13(1), 250 (1976).

99. J. E. Rowe, J. Vac. Sci. Technol., 13(1), 248 (1976).

100. J. D. Levine, J. App. Phys., 42(10), 3991 (1971).

101. N. Newmann, Z. Liliental-Weber, E. R. Weber, J. Washburn and W. E. Spicer, App. Phys. Lett., 53(2), 145 (1988).

102. E. R. Weber, H. Ennen, U. Kaufmann, J. Windscheif, J. Schneider, and T. Wosinski, J. Appl. Phys., 53, 6140 (1982); E. R. Weber and J. Schneider, Physica, B116, 398 (1983).

103. V. Heine, Phys. Rev., 138, 1689 (1965).

104. J. Tersoff, J. Vac. Sci. Technol, B3(4), 1157 (1985).

105. S. J. Eglash, N. Newman, S. Pan, D. Mo, K. Shenai, W. E. Spicer, F. A. Ponce, and D.M. Collins, J. Appl. Phys., 61, 5159 (1987).

106. E. H. Nicollian, B. Schwartz, D. J. Coleman, R. M. Ryder and J. R. Brews, J. Vac. Sci. Technol., 13, 1047 (1976).

107. S. J. Fonash, J. Appl. Phys., 47, 3597 (1976).

108. S. Ashok, J. M. Borrego and R. J. Gutmann, Electron. Lett., 14, 332 (1978).

109. H. S. Tseng and C. Y. Wu, Solid Stat Electron., 30(4), 383 (1987).

110. A. Piotrowska, A. Guivarch and G. Pelous, Solid State Electron., 26(3), 779 (1983).

111. A. K. Kulkarni and J. T. Lukowski, J. Appl. Physics, 59(8), 2901 (1986).

112. Y. C. Shih, M. Murakami, E. L. Wilkie and A. C. Callegari, J. App. Phys. 62(2), 582 (1987).

113. A. Callegari and Y. C. Shih, CASTA, Bari Itali (1987)

114. F. Lonnum and J. S. Johannessen, Electron. Lett., 22(12), 632 (1986).

115. N. Braslau, J. Vac. Sci & Technol., 19(3), 803 (1981).

116. W. Dingfen and K. Heina, Electron. Lett., 18(22), 940 (1982).

117. G. Y. Robinson, J. Vac. Sci. Technol., 13(4), 884 (1976).

118. J. G. Werthen and D. P. Scifres, J. App. Phys., 52(2), 1127 (1981).

119. R. P. Gupta and W. S. Khokle, IEEE Trans. Electron Devices Letters, EDL-6, 300 (1985).

120. V. L. Rideout, Solid State Electronics, 18, 541 (1975).

121. G. Y. Robinson, Solid State Electron, 18, 331 (1975).

122. H. Paria and H. Hartnagel, Appl. Phys., 10, 97 (1976).

123. J. M. Woodall and J. L. Freeouf, J. Vac. Sci. & Technol., 19(3), 794 (1981).

124. J. L. Freeouf and M. Woodall, Appl. Phys. Lett., 39, 727 (1981).

125. H. Ito, T. Ishibashi and T. Sugata, Jap. J. of Appl. Phys., 23(8), L635 (1984).

126. J. Gyulai, J. W. Mayer, V. Rodriguez, A. Y. C. Yu. and H. J. Gopen. J. Appl. Phys., 42, 3578 (1971).

127. R. S. Popovic, Solid Stat Electron., 21, 1133 (1978).

128. M. Jaros and H. L. Hartnagel, Solid Stat Electron., 18, 1029 (1975).

129. J. I. Pankove, Optical Processes in Semiconductors (Dover) (1975).

130. M. Castagne, J. Bonnafe, J. C. Manifacier and J. P. Fillard, J. Appl. Phys., 51, 4891 (1980).

131. J. P. Fillard, M. Castagne, J. Bonnafe and M. de Murcia, J. Appl. Phys., 54, 6767 (1983).

132. J. Bonnafe, J. JImnez, M. Gonzalez and M. Catagne, Physica Scripta, 30, 198 (1984).

133. J. P. Fillard, J. Bonnafe and M. Castagne, Phys. Sta. Sol., 72, K65 (1982).

134. J. P. Fillard, J. Bonnafe and M. Castagne, J. Appl. Phys., 56, 3020 (9184).

135. P. Bräunlich, P. Kelly and J. P. Fillard, Thermally Stimulated Relaxation in Solids, Ed: P. Bräunlich

136. T. N. Theis, Int. Symp. GaAs and Related Compounds, (Int. Phys. Conf. Ser.) 91, 1 (1987).

137. P. I. Nathan, Solid State Electron. 29, 167 (1986).

138. D. V. Lang, Deep centers in semiconductors, Gordon and Breach, 1986.

139. T. Wosinski, Appl. Phys. A36, 213 (1985).

140. M. Taniguchi, Y. Mochizuki, and T. Ikoma, Semi-Insulating III-V materials, Ed. D. C. Look and J. S. Blakemore, Kahneeta (1984).

141. W. L. Wang, S. S. Li, and D. H. Lee, J. Electrochem Soc., 133, 196 (1986).

142. U. Kaufmann, Phys. Rev. Lett., 54, 1332 (1985).

143. J. Lagowski, D. G. Lin, T. P. Chen, M. Skowronski, and H. C. Gatos, Appl. Phys. Lett. 49(9), 929 (1985).

144. Y. Bar-lam and J. D. Joannoupoulous, Phys. Rev. Lett., 56, 1213 (1986).

145. M. Kaminska, M. Skowronski, and W. Kuszko, Phys. Rev. Lett., 55, 2204 (1985).

146. G. A. Baraff, M. Lannoo, and M. Schluter, Phys. Rev., B38, 6003 (1988).

147. J. Jimnez, P. Hernandez, J. A. de Saja and J. Bonnafe, Solid State Commun., 55, 459 (1985).

148. J. Lagowski, M. Skowronski and H. C. Gatos, Jap. J. Appl. Phys. 25, L194 (1986).

149. A. L. Lin, E. Omelianovski and R. H. Bube, J. Appl. Phys., 47, 1852 (1976).

150. A. L. Lin and R. H. Bube, J. Appl. Phys. 47, 1859 (1976).

151. D. V. Lang, R. A. Logan, and M. Jaros, Phys. Rev., B19, 1015 (1979).

152. M. Levinson, Phys. Rev. B 28, 3660 (1983).

153. D. C. Look, Electrical Characterization of GaAs Materials and Devices, John Wiley and Sons, (1989).

154. L. C. Burton, Fourth international summer college on physics and contemporary needs (1979).

155. K. W. Böer, J. Appl. Phys., 50, 5356 (1979).

156. A. L. Fahrenbruch and R. H. Bube, Fundamentals of solar cells (Academic Press) (1983).

157. R. O. Bell, Silicon processing for photovoltaics (Elsevier) (1985).

158. H. K. Charles, R. J. King, and A. P. Ariotedjo, Solar cells, 1, 327 (1980).

159. K. L. Chopra and S. R. Das, Thin film solar cells (Plenum Press) (1983).

160. J. R. Hauser and Dunbar, Solid Stat Electron., 18, 715 (1975).

161. A. Vaseashta et al. Proc. 25th IEEE Intl. Elect. Dev. Mtg., 666 (1979).

162. A. R. Moore, Appl. Phys. Lett., 40(5), 403-405 (1982).

163. A. Vaseashta, J. D. Arora and P. C. Mathur, Intl. J. Electron., 5, 529 (1980).

164. N. C. Wyeth and A. Catalano, A. J. Appl. Phys., 50, 344 (1979).

165. P. Swarup and V. K. Jain, IEEE Elect. Dev. Lett. EDL-3(9), 259 (1982).

166. H. C. Card, Solid Stat. Electron., 18, 881 (1975).

167. R. J. Stirn and Y. C. M. Yeh, Appl. Phys. Lett, 27, 95 (1975).

168. Y. C. M. Yeh and R. J. Stirn, Proc. 11th Photovoltaic Specialists Conference record, 391 (1975).

169. S. J. Fonash, J. Appl. Phys., 47, 3597 (1976).

170. R. J. Stirn and Y. C. M. Yeh, IEEE Trans. Electron Devices, ED-24, 476 (1977).

171. W. A. Anderson, J. K. Kim and A. E. Delahoy, IEEE Trans. Electron Devices. ED-24, 453 (1977).

172. B. R. Pruniaux and A. C. Adams, J. Appl. Phys., 43, 1980 (1972).

173. C. A. Mead, Solid Stat. Elecron., 9, 1023 (1966).

174. C. R. Crowell, W. G. Spitzer, L. E. Howarth, and E. Labate, Phys. Rev., 127, 2006 (1962).

175. Y. Mori and N. Watanabe, J. Electrochem Soc., 125, 1510 (1978).

176. S. Iida and K. Ito, Electrochem Soc., 118, 768 (1971).

177. L. I. Maissel and R. Glang, Handbook of Thin Film and Technology, McGraw Hill Books Company, (1970).

178. H. Moritz, IEEE Trans. Electron Devices, 32, 672 (1985).

179. S. P. Tobin, M. B. Spitzer, C. Bajgar, L. Geoffroy and C. J. Keavney, 19th Proc. of the Photovoltaic Specialists Conference, 70 (1987).

180. P. W. Che, C. Y. Su, I. Lindau, P. Skeath and W. E. Spicer, J. Vac. Sci. Technol.,

16(5), 1191 (1979).

181. K. A. Bertness, D. J. Friedman, P. H. Mahowald, J. J. Yeh, A. K. Wahi, I. Lindau and W. E. Spicer, J. Vac. Sci. Technol. B4(4), 1102 (1986).

182. G. Hughes and R. Ludeke, J. Vac. Sci. Technol., B4(4), 1109 (1986).

183. G. Landgren, R. Ludeke, Y. Jugnet, J. F. Morar, and F. J. Himpsel, J. Vac. Sci. Technol., B2(3), 352 (1984).

184. K. D. Childs and M. G. Legally, Phys. Rev., B(30), 5742 (1984).

185. L. G. Meiners, J. Vac. Sci. Technol., 21, 655 (1982).

186. K. K. Kan, M. C. Petty, and G. G. Roberts, The Physics of MOS Insulators, Eds. G. Lucovsky, S. T. Pantelides, and F. L. Galeener, Oxford, Pergamon Press (1980).

187. F. A. Putnam, Res. & Dev., 106-111 (1989).

188. K. L. Ratzlaff, Introduction to computer-assisted experimentation (John Wiely) (1985).

189. R. E. Dessey, Analytical Chemistry (I), 55, 650 (1983).

190. L. Brodie, Thinking Forth (Prentice Hall Software series) (1987).

191. J. Gillard, Byte, 181 (1981).

192. G. Wyszecki and W. S. Stiles, Color Science: Concept and Methods, Quantitative Data and Formula (John Wiley and Sons Inc.) (1982).

193. S. J. Fonash, J. Appl. Phys. 54(4), 1966 (1983).

194. E. Kamieniecki, J. Lagowski, and H. C. Gatos, J. Appl. Phys., 51(3), 1863 (1980).

195. J. Epp, J. G. Dillard, A. Siuochi, R. Zallen, S. Sen, E. D. Cole, A. Vaseashta, and L. C. Burton, Proc. MRS, Fall Mtg. (1989).

196. U. V. Desnica and B. Santic, Appl. Phys. Lett. 54, 810 (1989).

197. H. Goronkin, M. S. Birrittella, W. C. Seelbach and R. S. Viatkus, IEEE Trans. Electron Devices, ED-29, 845 (1982).

198 S. Subramanian, P. B. Bhattacharya, K. J. Staker, C. L. Gosh and M. H. Badawi, IEEE Trans. Electron Devices, ED-32, 28 (1985).

199. F. Chekir, G. N. Lu and C. Barret, Solid State Electron., 29, 519 (1986).

200. R. Y. DeJule, M. A. Haase, G. E. Stillman, S. C. Palmateer, and J. C. M. Hwang, J. Appl. Phys., 57, 5287 (1985).

201. R. B. Blackman and J. W. Tuckey, The measurement of power spectra, Dover 1958)

202. H. Ryssel, Ion implantation Techniques, Ed. H. Ryssel and H. Glawischnig, Springer-Verlag, New York (1982).

203. K. B. Winterbon, Ion implantation range and energy deposition distribution; Vol. 2, Low incident ion energies, IFI/Plenum Press, New York (1975).

204. A. P. Webb and C. D. C. Wilkinson, Vacuum, 34, 159 (1984).

205. A. F. Burenkov, F. F. Komarov, M. A. Kumakhov, and M. M. Temkin, Tables of Ion Implantation Spatial Distributions, Gordon and Breach Science Publishers (1986).

206. Data obtained from Solar Energy Research Institute, Golden, CO.

207. D. E. Aspnes and A. A. Studna, Phys. Rev. B27, 985 (1983).

208. J. B. Theeten and M. Erman, J. Vac. Sci. & Technol., 20, 471 (1982).

209. Z. Chen and L. C. Burton, (in communication) (1989).

210. D. C. Look, Phys. Rev., B24, 5852 (1981).

211. J. S. Blakemore, Semiconductor Statistics (Dover) (1987).

212. O. Yoshie and M. Kamihara, Jap. J. Appl. Phys., 22, 621 (1983).

— ¤ —

Vita

Ashok K. Vaseashta received B. Sc (Honors) in Physics, M. Sc (Honors) in Physics from University of Delhi and M. Tech (Solid State Devices) in Physics from Indian Institute of Technology, Delhi. He initiated MOS Solar cell program at Center of Advanced Research in Electronics and Center for Energy Studies, Indian Institute of Technology, Delhi. He then joined corporate research center of Chronar Corporation, Princeton, N. J. as Research scientist. After that he held a joint appointment as Staff Scientist and Principal Investigator at Spire Corporation, Bedford, MA., and Polaroid Corporation, Waltham, MA., working towards a U. S. Department of Energy program of the 'Fabrication and Characterization of Hydrogenated amorphous silicon tandem junction solar cells'. In 1986, he joined Virginia Polytechnic Institute and State University for Ph. D. program in Materials Engineering Science. He is now with Kobe Steel microelectronic research laboratory at Research Triangle Park, N.C. He is member of AIP, AVS, IEEE, ISHM, MRS and Microbeam Analysis Society.

List of Publications

The research at Virginia Tech resulted in the following publications:

Journal Publication:

1. **Computer Assisted Photovoltaic Characterization and Analyses using Asyst, A Forth based Scientific language.** (with P. Johnson and L. C. Burton)
   Measurements and Control, Vol. 3, 165 (1989).

Refereed Conference Papers

2. **Characterization of Si-implanted (211) vs. (100) GaAs.** (with J. Epp, S. Sen, E. Cole, A. Siochi, R. Zallen, J. Dillard and L. C. Burton)
   Proceedings of the Materials Research Society, Fall (1988).
3. **Characterization of Ion damaged photovoltaic devices.** (with J. Epp, S. Sen and L. C. Burton)
   Proceeding of the Inter Society Energy Conversion Conference, D. C. Aug. (1989)
4. **New features of the Dark and photoconductivity response of Low energy Ar^+ ion bombarded GaAs.** (with L. C. Burton)
   Proceedings of the Materials Research Society, Spring (1989).

Conference Papers:

5. **Automated Photovoltaic Characterization System Using Asyst.** (with P. Johnson and L. C. Burton)
   Asyst'88: Proceeding of the International Conference of Users and Applications. Rochester, N. Y. (1988).

6. **Amorphous SiC: Diamond like films:** (with L. C. Burton)
   6th Annual Graduate Research Symposium, VPI and State University, Blacksburg, Oct., (1989).

7. **Characterization of Ion beam processed GaAs.** (with S. Sen and L. C. Burton)
   6th Annual Graduate Research Symposium, VPI and State University, Blacksburg, Oct., (1989).

— ¤ —